Microstrip phased-array antennas : a finite-array approach

DOI:
10.6100/IR423038

Document status and date:
Published: 01/01/1994

Document Version:
Publisher's PDF, also known as Version of Record (includes final page, issue and volume numbers)

Microstrip Phased-Array Antennas: A Finite-Array Approach

PROEFSCHRIFT

ter verkrijging van de graad van doctor aan de
Technische Universiteit Eindhoven, op gezag van
de Rector Magnificus, prof.dr. J.H. van Lint,
voor een commissie aangewezen door het College
van Dekanen in het openbaar te verdedigen op
woensdag 5 oktober 1994 te 16.00 uur

door

Adrianus Bernardus Smolders

geboren te Hilvarenbeek

Dit proefschrift is goedgekeurd
door de promotoren
prof.dr. A.G. Tijhuis
en
prof.dr.ir. G. Brussaard

copromotor:
dr. M.E.J. Jeuken.

CIP-DATA KONINKLIJKE BIBLIOTHEEK, DEN HAAG

Smolders, Adrianus Bernardus

Microstrip phased-array antennas: a finite-array approach / Adrianus Bernardus Smolders - Eindhoven University of Technology. - Ill., fig., photos, tab.
Thesis Eindhoven. - With ref. - With summary in Dutch.
ISBN 90-386-0010-0
NUGI 832
Subject headings: microstrip antennas / microstrip arrays / phased arrays

To study, to finish, to publish

Benjamin Franklin (1706-1790)

Aan Annet en mijn Ouders

This study was performed as part of the research program of the Electromagnetics Division, Department of Electrical Engineering, Eindhoven University of Technology, P.O. Box 513, 5600 MB Eindhoven, The Netherlands. This work was supported by the Technology Foundation (STW)

Abstract

In this thesis, the results are presented of a theoretical and experimental investigation of isolated microstrip antennas and of finite microstrip phased-array antennas. Microstrip antennas have several features, including light weight, conformability and low production costs, which make them interesting candidates for several applications where a phased-array antenna is required. The theoretical analysis of finite arrays of microstrip antennas is based on a rigorous spectral-domain method-of-moments procedure. The electromagnetic field is expressed in terms of the exact spectral-domain dyadic Green's function. Mutual coupling and surface wave effects are automatically included in the analysis. Small arrays and array elements near the edge of an array can also be analysed with this finite-array approach. In addition, a sophisticated model for the feeding coaxial cables is developed. In this way, electrically thick and thus broadband microstrip configurations can be analysed. An analytical extraction technique is proposed to reduce the required CPU time. The theoretical model is validated by comparing the calculated results with measured data from several experiments. Generally, a good agreement between theory and experiment is obtained. Some techniques to improve the available bandwidth of microstrip antennas are discussed. Bandwidths ranging from 20% to 50% have been obtained for isolated microstrip antennas. When such broadband elements are used in an array of microstrip antennas, the bandwidth is reduced significantly due to mutual coupling.

Contents

List of abbreviations

AR	Axial Ratio,
BW	Bandwidth,
CPU	Central Processing Unit,
EMC	ElectroMagnetically Coupled,
EUT	Eindhoven University of Technology,
GaAs	Gallium Arsenide,
INMARSAT	INternational MARitime SATellite organisation,
MMIC	Monolythic Microwave Integrated Circuit,
SAR	Synthetic Aperture Radar,
TE	Transverse Electric,
TEM	Transverse ElectroMagnetic,
TM	Transverse Magnetic,
T/R module	Transmitter/Receiver module,
VSWR	Voltage Standing Wave Ratio

Chapter 1

Introduction

1.1 General introduction

History

One of the principal characteristics of human beings is that they almost continually send and receive signals to and from one another. The exchange of meaningful signals is the heart of what is called communication. In its simplest form, communication involves two people, namely the signal transmitter and the signal receiver. These signals can take many forms. Words are the most common form. They can be either written or spoken. Before the invention of technical resources such as radio communication or telephone, long-distance communication was very difficult and usually took a lot of time. Proper long-distance communication was at that time only possible by exchange of written words. Couriers were used to transport the message from the sender to the receiver. Since the invention of radio and telephone, far-distance communication or *tele*communication is possible, not only of written words, but also of spoken words and almost without any time delay between the transmission and the reception of the signal. Antennas have played an important part in the development of our present telecommunication services. Antennas have made it possible to communicate at far distances, without the need of a physical connection between the sender and receiver. Apart from the sender and receiver, there is a third important element in a communication system, namely the propagation channel. The transmitted signals may deteriorate when they propagate through this channel. In this thesis only the antenna part of a communication system will be investigated.

In 1886 Heinrich Hertz, who was a professor of physics at the Technical Institute in Karlsruhe, was the first person who made a complete radio system [33]. When he produced sparks at a gap of the transmitting antenna, sparking also occurred at the gap of the receiving antenna. Hertz in fact visualised the theoretical postulations of James Clerk Maxwell. Hertz's first experiments used wavelengths of about 8 meters. After Hertz an Italian called Guglielmo Marconi became the motor behind the development of practical radio systems [46]. He was not a famous scientist like Hertz, but he was obsessed with the idea of sending messages with a wireless communication system. He was the first who performed wireless communications across the Atlantic. The antennas that Marconi used were very large wire antennas mounted onto two 60-meter wooden poles. These antennas had a very poor efficiency, so a lot of input power had to be used. Sometimes the antenna wires even glowed at night. In the 93 years after Marconi's first transatlantic wireless communication in 1901, a huge amount of research and development has been performed concerning antennas and complete communication systems. In later years antennas were also used for other purposes such as radar systems and radio astronomy. In 1953 Deschamps [18] reported for the first time about planar microstrip antennas, also known as patch antennas. It was only in the early eighties that microstrip antennas became an interesting topic among scientists and antenna manufacturers. It will probably take another 5 to 10 years before microstrip antennas will be used on a large scale in a variety of telecommunication products.

Antenna concepts

Figure 1.1 shows some well-known antenna configurations which are nowadays in use in a variety of applications. Both reflector antennas and wire antennas have become mass products. Reflector

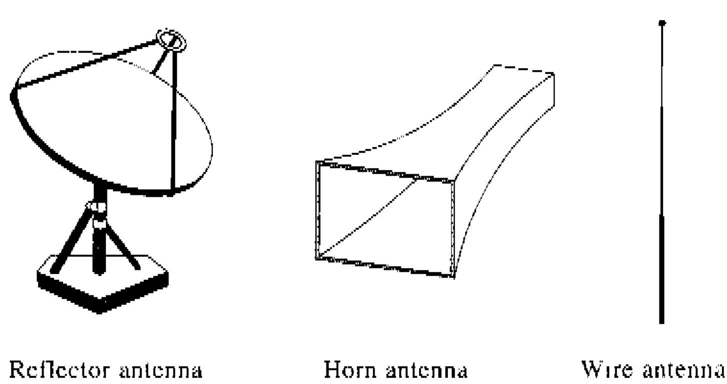

Figure 1.1: *Some conventional antenna concepts.*

antennas are for example used for the reception of satellite television, whereas wire antennas are often used to receive radio signals with a car or portable radio receiver. Reflector and horn antennas usually have a high gain, but have the disadvantage that the main lobe of the antenna has to be steered in the desired direction by means of a highly accurate mechanical steering mechanism. This means that simultaneous communication with several points in space is not possible. Wire antennas are omni-directional, but have a very poor antenna gain. There are certain applications where these conventional antennas cannot be used. These applications often require a phased-array antenna. A phased-array antenna has the capability to communicate with several targets which may be anywhere in space, simultaneously and continuously, because the main beam of the antenna can be directed electronically into a certain direction. Another advantage of phased-array antennas is the fact that they are relatively flat. Figure 1.2 shows the general phased-array antenna concept. Three essential layers can be distinguished 1) an antenna layer,

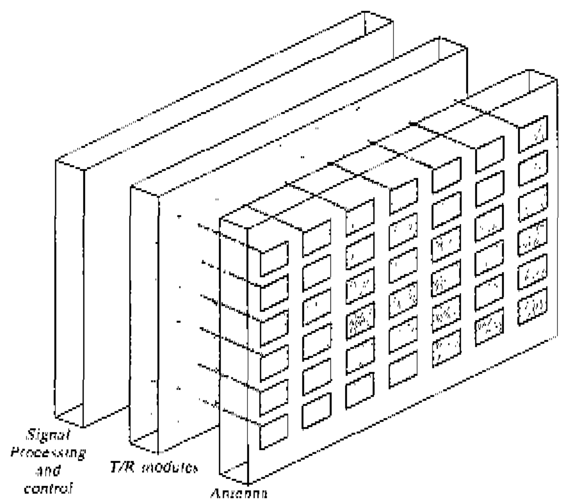

Figure 1.2: *Phased-array antenna*

2) a layer with transmitter and receiver modules (T/R modules) and 3) a signal-processing and control layer that controls the direction of the main beam of the array. The antenna layer consists of several individual antenna elements which are placed on a rectangular or on a triangular grid. Open-ended waveguide radiators are often used as array elements, but also microstrip antennas seem to become interesting candidates [61, 65]. The total gain of a phased-array antenna depends on the number of array elements and on the gain of a single array element. With M denoting the number of array elements, the theoretical gain at broadside of a phased-array antenna is given by

$$G_t = 10 \log_{10} M + G_e \qquad (\mathrm{dB}), \tag{1.1}$$

where G_a is the element gain in dB. Note that the antenna gain in a real phased-array antenna is reduced due to losses in the feeding network [43]. Each array element or a small cluster of elements (subarray) is connected with one T/R module. Arrays can be as large as 5000 elements, so it is essential to keep the production costs of a single array element or subarray as low as possible. The price of one T/R module can be minimised if most of its functions are integrated into only a few low-cost MMIC's (Monolithic Microwave Integrated Circuits) [26].

Microstrip antennas and microstrip phased-array antennas

Microstrip antennas or patch antennas have several interesting features, such as low production costs, light weight and conformability, which make them very interesting candidates for use in a phased-array configuration. Figure 1.3 shows an example of a single-layer isolated microstrip antenna. The patch is made of copper and is situated on top of a dielectric substrate. The substrate

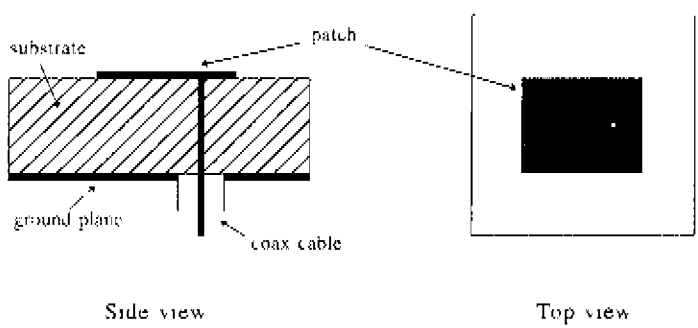

Figure 1.3. *Isolated single-layer microstrip antenna*

is mounted on a metal ground plane. A rectangular patch shape is shown in this figure. Other patch shapes are possible as well, but seem to have no significant advantages over the rectangular form. Sometimes the antenna is covered with a second dielectric layer. This dielectric cover could serve as a protection layer for the antenna. Sometimes a second patch is placed on top of this dielectric cover. Such a structure is called a two-layer stacked microstrip antenna [60]. Stacked microstrip antennas have two closely spaced resonant frequencies, which may be useful in obtaining a larger bandwidth or dual-frequency operation. The (lower) patch is fed with one or two coaxial cables in order to establish a linearly or circularly polarised far field. The inner conductor of the coaxial cable is usually connected with the patch, while the outer conductor of the coaxial cable is attached to the backside of the metal ground plane. Other feeding configurations, for example with microstrip lines, can be used as well. Figure 1.4 shows the geometry of a finite array of rectangular microstrip antennas placed on a rectangular grid. The array elements can have a stacked configuration of the patches and the substrate can be built up of several layers (multilayer structure). Each array element is fed with one or two coaxial cables, depending on the polarisation requirements of the antenna.

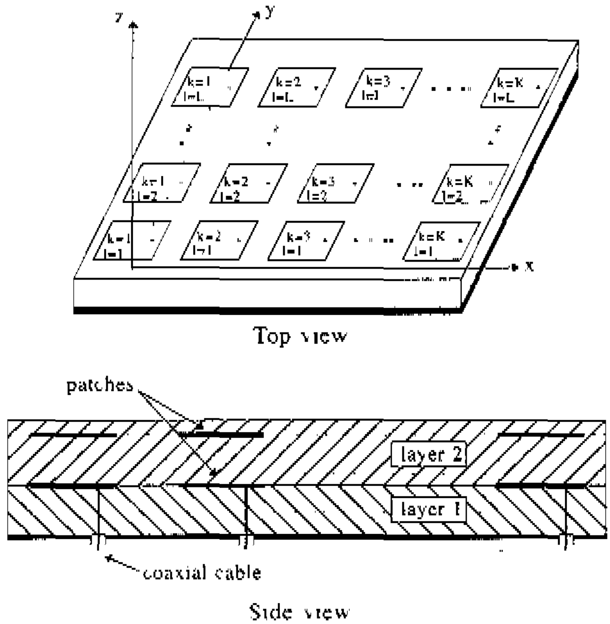

Figure 1.4: *Finite array of (stacked) microstrip antennas embedded in a grounded two-layer dielectric slab with $k = 1, 2, \ldots, K$ and $l = 1, 2, \ldots, L$*

Applications of microstrip antennas and microstrip phased arrays

Some typical (future) applications where microstrip antennas or microstrip phased-array antennas can be used are land-mobile communications and mobile satellite communications [41], active phased-array radars, Synthetic Aperture Radar (SAR) [24] and medical systems [48]. Especially mobile communication is becoming a huge and important market where low-cost microstrip antennas can be used. At the present time, INMARSAT (INternational MARitime SATellite organisation) has four operational systems for mobile satellite communication at L-band frequencies (≈ 1.5 GHz), i.e. INMARSAT system A, B, C and M [14, 77]. The antenna of a mobile user of the INMARSAT M system can be mounted on top of a car, truck, train, aeroplane or in an attaché case. In the near future, it is expected that the need for individual world-covering telecommunication devices will grow. These devices should have the same ease of use and transport as our own means of communication, i.e. our mouths, ears and eyes. Ideally, where the person goes, the communication device should accompany her/him. Telecommunication devices should therefore be miniaturized as much as possible to improve their transportability. This implies that future communication systems need the use of higher frequencies, which results in a smaller antenna size. In the United States, a study has been performed on a mobile satellite communication system at a frequency of 20 GHz (receive) and 30 GHz (transmit) [22]. These high frequencies make it possible to use real personal-access communication systems, because the antenna size is small. Figure 1.5 shows an example of such a personal access system. Microstrip antennas

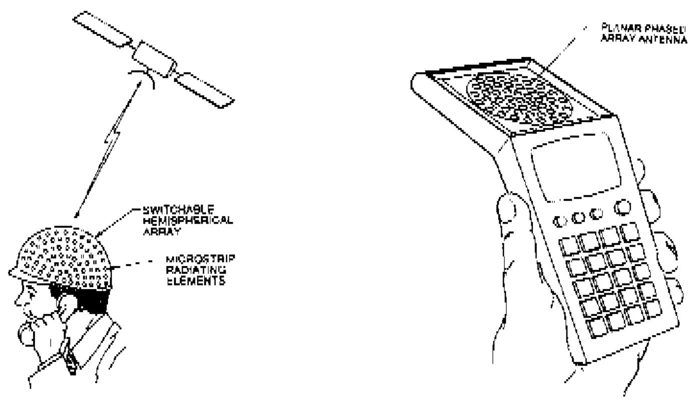

Figure 1.5: *Future mobile satellite communication with microstrip antennas* [21]

are expected to be used in these future communication systems, because they can be integrated with the T/R modules if, for example, MMIC fabrication techniques on GaAs substrates are used [40]. This would reduce the total production costs dramatically. Table 1.1 shows some typical antenna requirements for some (future) applications of microstrip (array) antennas. The most important observation from table 1.1 is probably that the required bandwidth of these applications varies from a minimum of 3 percent to approximately 50 percent for certain radar applications. The bandwidth is defined as the frequency band for which the input reflection coefficient of the antenna is lower than a certain value r_{max}. Usually $r_{max} = 1/3$ is used, which corresponds to a Voltage Standing Wave Ratio (VSWR) of 2.

Application	*Bandwidth*	*Antenna Gain*	*Polarisation*
INMARSAT data	7%	1 dB	circular
INMARSAT voice	7%	12 dB	circular
SAR	3%	21 dB	linear
radar	10-50%	20-40 dB	linear/circular

Table 1.1 *Some typical antenna requirements.*

Bandwidth of microstrip antennas

When the present research was started in 1991, most microstrip antennas that had been described in the literature had a bandwidth of only a few percent. The research activities since 1991 have therefore concentrated on the development of a theoretical model for the design of large-bandwidth microstrip antennas and microstrip phased-array antennas. The bandwidth of a microstrip antenna can be improved if electrically thick substrates are being used. Figure 1.6 shows the bandwidth of several microstrip antennas as a function of the electrical thickness of the substrate h/λ_e, where h is the thickness of the substrate and where λ_e is the wavelength in the substrate. Four antennas have been designed and measured at the antenna laboratory of the Eindhoven University of Technology. More details about these four antennas can be found in section 3.9. From figure 1.6 it is obvious that the bandwidth of a microstrip antenna increases with increasing thickness of the substrate on which the patch is mounted. However, electrically thick substrates often give rise to an inductive shift in the input impedance, which means that a good impedance match can only be achieved if a complicated and expensive input network is used. There are some techniques to avoid this problem. One of the configurations with an enhanched bandwidth is a stacked microstrip antenna. A stacked microstrip antenna has two closely-spaced resonant frequencies, which results in an improved bandwidth. The two antennas specified in figure 1.6 with a bandwidth between 20% and 30% have such a stacked configuration of the patches. Another technique to improve the bandwidth will be presented in chapter 3 of this thesis. The antenna in figure 1.6 with $h/\lambda_e = 0.22$ is made with this new technique and has a bandwidth of approximately 50%.

The enlargement of the bandwidth of a microstrip antenna usually has a negative effect on the radiation pattern and the radiation efficiency [36]. This is mainly due to surface wave generation and radiation from the coaxial feed.

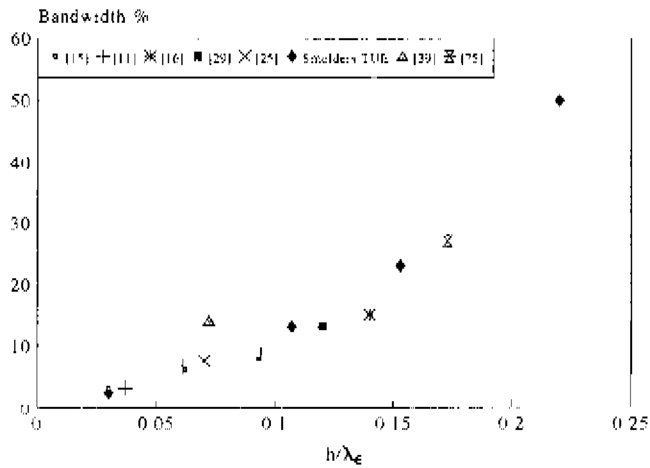

Figure 1.6: *Bandwidth of microstrip antennas (VSWR< 2), $Z_0 = 50\Omega$.*

1.2 Modelling approach

Several theoretical models for the analysis of microstrip antennas have been introduced during the past two decades. Among the first models were the transmission-line model [17, 9] and the cavity model [45]. Both approaches are relatively easy to implement into a computer program and require relatively short computation times. However, the predicted antenna characteristics are not very accurate and are usually limited to the case of isolated, narrow-band, microstrip antennas. Later, more rigorous methods have been proposed [56, 49]. The current distribution on the antenna is determined by solving an integral equation. The integral-equation methods are not restricted to the case of isolated microstrip antennas, but can also be applied to microstrip arrays and to multilayer configurations. However, a major drawback of these methods is the long computation time and the relatively large computer memory requirements. This seems to become less important nowadays since the computing power of even the cheapest computer system is growing more and more.

In this thesis, the current distribution on the electric conductors (patches and coaxial probes) of each array element is found by solving the integral equation for the unknown currents with the method of moments [31]. The method of moments reduces an integral equation into a matrix equation by expanding the unknown current distribution into a set of *basis functions* and weighting the equation with a set of *testing functions*. The resulting matrix equation can be solved with standard numerical techniques. In the analysis the electromagnetic field is written in terms of the dyadic Green's function The Green's function is the response due to a point current source embedded in the layered medium. Because the current distribution on the patches as well as on the coaxial probes needs to be determined, the Green's function of a horizontal point current source and the Green's function of a vertical point current source have to be known. Once the current distribution on the antenna is known, the input impedance or scattering matrix and the radiation characteristics can be determined. Most publications in the literature concern narrow-band and thus electrically thin microstrip antennas. Because of this thin substrate, the current distribution along the coaxial probe will be almost constant and therefore a simple feed model can be used. In case of an electrically thick substrate, however, a more sophisticated model for the feeding coaxial cables must be used which accounts for the variation of current along the probes and which ensures continuity of current along the patch-probe transitions. An accurate feed model was developed that includes all these effects.

In general, one could say that there are two ways to analyse microstrip arrays with a method-of-moments procedure [3]: (1) element-by-element approach (finite-array approach) and (2) infinite-array approach. In the case of a very large array, the infinite-array approach will be more efficient, while small arrays and elements near the edge of an array can only be properly analysed with an element-by-element approach. The best and probably most efficient design strategy for microstrip arrays is a combination of both approaches. In this thesis finite arrays of microstrip antennas are investigated. Much effort has been put into the development of special analytical and numerical techniques to reduce the computation time and to improve the accuracy of the method-of-moments formulation. The theoretical model has been implemented in a software package.

1.3 Organisation of the thesis

As stated earlier, the current distribution on a microstrip antenna or on an array of microstrip antennas is calculated by solving the integral equation for the currents with the method of moments. The electromagnetic field which appears in the integral equation is written in terms of the dyadic Green's function. The dyadic Green's function needs therefore to be determined before the currents on the antenna can be calculated. In chapter 2 the point-source problem for a grounded three-layer medium is solved. The exact spectral-domain dyadic Green's function is determined for a horizontal as well as for a vertical point current source embedded in this three-layer medium. In chapter 3 a method is presented for an efficient and rigorous analysis of a single, linearly polarised, microstrip antenna. Calculated results are compared with measured data from several experiments. In addition, the bandwidth of several microstrip configurations will be investigated in chapter 3. It is shown that microstrip antennas with a bandwidth varying from 20% to 50% can be constructed. In chapter 4 the method of chapter 3 is extended to the case of a finite array of linearly or circularly polarised microstrip antennas. Some numerical and analytical techniques are introduced in order to reduce the required CPU time. Several designs of microstrip arrays are discussed and compared with experiments. Special attention is devoted to the influence of mutual coupling on the input reflection coefficient of each array element and on the radiation pattern of the total array.

Chapter 2

Green's functions of a grounded two-layer dielectric structure

2.1 Introduction

In this chapter, we will start the analysis of microstrip antennas and microstrip arrays by developing an essential mathematical tool that will be used in chapter 3 and chapter 4, where the characteristics of microstrip antennas and microstrip arrays are determined with the method of moments. The Green's function will there be used to calculate the electromagnetic fields caused by a certain current distribution. Figure 2.1 shows the coordinate system that will be used throughout this thesis.

We are interested in finding the electromagnetic fields due to a certain electric current distribution $\vec{\mathcal{J}}(\vec{r})$ and a magnetic current distribution $\vec{\mathcal{M}}(\vec{r})$. The electric field $\vec{\mathcal{E}}(\vec{r})$ and magnetic field $\vec{\mathcal{H}}(\vec{r})$ satisfy Maxwell's equations

$$\begin{aligned} \nabla \times \vec{\mathcal{E}}(\vec{r}) &= -j\omega\mu\vec{\mathcal{H}}(\vec{r}) - \vec{\mathcal{M}}(\vec{r}), \\ \nabla \times \vec{\mathcal{H}}(\vec{r}) &= j\omega\varepsilon\vec{\mathcal{E}}(\vec{r}) + \vec{\mathcal{J}}(\vec{r}), \end{aligned} \tag{2.1}$$

where an $e^{j\omega t}$ dependence of the fields is assumed (time-harmonic solution). ε denotes the permittivity of the medium and μ denotes the permeability of the medium. The medium is assumed to be isotropic, linearly reacting and homogeneous. In this chapter only electric source currents are considered, so $\vec{\mathcal{M}}(\vec{r}) = \vec{0}$ in equation (2.1). In chapter 3 both electric and magnetic sources will be investigated.

For most problems, including our microstrip antenna problem, it is not possible to obtain a closed-form solution of equation (2.1). Therefore Green's functions will be introduced. A

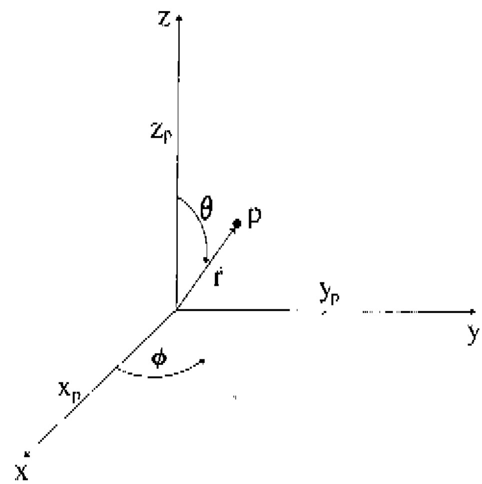

Figure 2.1 *Coordinate system.*

Green's function is the response due to a point source. Sometimes the Green's functions are directly related to the electric and magnetic field. However, we will make use of the magnetic vector potential. With $\vec{\mathcal{M}} = \vec{0}$ in equation (2.1), the divergence of the magnetic field equals zero, i.e. $\nabla \cdot \vec{\mathcal{H}} = 0$. This implies that the magnetic field $\vec{\mathcal{H}}$ can be represented as the curl of another vector

$$\vec{\mathcal{H}}(\vec{r}) = \nabla \times \vec{\mathcal{A}}(\vec{r}), \tag{2.2}$$

in which $\vec{\mathcal{A}}(\vec{r})$ is the magnetic vector potential. Substituting this relation into the first equation of (2.1) with $\vec{\mathcal{M}} = \vec{0}$ yields

$$\nabla \times (\vec{\mathcal{E}}(\vec{r}) + j\omega\mu\vec{\mathcal{A}}(\vec{r})) = \vec{0} \tag{2.3}$$

Hence

$$\vec{\mathcal{E}}(\vec{r}) + j\omega\mu\vec{\mathcal{A}}(\vec{r}) = -\nabla\Phi(\vec{r}), \tag{2.4}$$

where Φ is a scalar potential. The scalar potential Φ satisfies the Lorentz gauge [32, p. 77]

$$\nabla \cdot \vec{\mathcal{A}}(\vec{r}) = -j\omega\varepsilon\Phi(\vec{r}) \tag{2.5}$$

Substituting the Lorentz gauge into equations (2.2) and (2.4) yields

$$\begin{aligned} \vec{\mathcal{H}}(\vec{r}) &= \nabla \times \vec{\mathcal{A}}(\vec{r}), \\ \vec{\mathcal{E}}(\vec{r}) &= -j\omega\mu\vec{\mathcal{A}}(\vec{r}) - \nabla\left[\frac{j\omega\mu}{k^2}\nabla\cdot\vec{\mathcal{A}}(\vec{r})\right], \end{aligned} \tag{2.6}$$

where $k = \omega\sqrt{\varepsilon\mu}$ denotes the wave number in the medium. With $\vec{\mathcal{A}} = \mathcal{A}_x\vec{e}_x + \mathcal{A}_y\vec{e}_y + \mathcal{A}_z\vec{e}_z$, (2.6) takes the following form

$$\vec{\mathcal{H}}(x,y,z) = \begin{bmatrix} \partial_y\mathcal{A}_z - \partial_z\mathcal{A}_y \\ \partial_z\mathcal{A}_x - \partial_x\mathcal{A}_z \\ \partial_x\mathcal{A}_y - \partial_y\mathcal{A}_x \end{bmatrix} \tag{2.7}$$

and

$$\vec{\mathcal{E}}(x,y,z) = \frac{-j\omega\mu}{k^2}\begin{bmatrix} (k^2+\partial_x^2)\mathcal{A}_x + \partial_x\partial_y\mathcal{A}_y + \partial_x\partial_z\mathcal{A}_z \\ (k^2+\partial_y^2)\mathcal{A}_y + \partial_x\partial_y\mathcal{A}_x + \partial_y\partial_z\mathcal{A}_z \\ (k^2+\partial_z^2)\mathcal{A}_z + \partial_x\partial_z\mathcal{A}_x + \partial_y\partial_z\mathcal{A}_y \end{bmatrix}, \tag{2.8}$$

The Green's function is now defined as the magnetic vector potential created by a unit electric-current source or electric dipole. The magnetic vector potential resulting from a certain current distribution $\vec{\mathcal{J}}(\vec{r}_0)$ can then be found by dividing this current distribution into an infinite number of elementary unit sources, and integrating the contributions of all these elementary sources. The vector potential at $\vec{r} = (x, y, z)$ can be expressed in terms of the dyadic Green's function $\bar{\bar{\mathcal{G}}}(\vec{r},\vec{r}_0)$

$$\vec{\mathcal{A}}(\vec{r}) = \iiint \bar{\bar{\mathcal{G}}}(\vec{r},\vec{r}_0)\cdot\vec{\mathcal{J}}(\vec{r}_0)\,dV_0, \tag{2.9}$$

where V_0 is a volume that encloses the source currents. The dyadic Green's function can be represented by a square 3×3 matrix of which the general form is given by

$$\bar{\bar{\mathcal{G}}}(\vec{r},\vec{r}_0) = \begin{pmatrix} \mathcal{G}_{xx} & \mathcal{G}_{xy} & \mathcal{G}_{xz} \\ \mathcal{G}_{yx} & \mathcal{G}_{yy} & \mathcal{G}_{yz} \\ \mathcal{G}_{zx} & \mathcal{G}_{zy} & \mathcal{G}_{zz} \end{pmatrix} \tag{2.10}$$

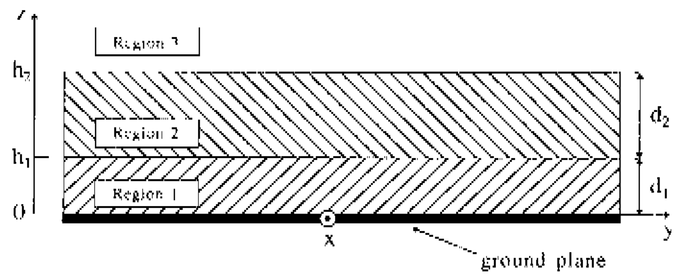

Figure 2.2: *Geometry of the grounded two-layer configuration (side view)*

The matrix element $\mathcal{G}_{xy}$ is the x-component of the Green's function at $\vec{r} = (x, y, z)$ due to a y-directed unit current source located at $\vec{r}_0 = (x_0, y_0, z_0)$. The electric and magnetic field can now be expressed in terms of the current distribution $\vec{\mathcal{J}}(\vec{r}_0)$ and the dyadic Green's function by substituting (2.10) and (2.9) in (2.8) and (2.7).

2.2 Boundary-value problem

In this section, we will formulate the boundary-value problem for the magnetic vector potential $\vec{A}$ in a grounded two-layer dielectric structure due to the exitation by an electric unit current source. The geometry of the layered structure is shown in figure 2.2. It consists of two dielectric layers (regions 1 and 2) with thickness d_1 and d_2, respectively, mounted on a perfectly conducting infinite ground plane. Region 3 consists of free space. The ground plane is located at $z = 0$.
In the frequency domain, the electromagnetic properties in each region of figure 2.2 can be represented by the permeability μ_i and the permittivity ε_i, with $i = 1, 2, 3$. The permittivity is complex and is given by

$$\varepsilon_i = \varepsilon_i' + \frac{\sigma_i}{j\omega} = \varepsilon_i'(1 - j\tan\delta_i) = \varepsilon_{ri}\varepsilon_0, \tag{2.11}$$

where ε_i' is the real part of ε_i, σ_i is the conductivity in region i, $\tan\delta_i$ denotes the loss tangent and ε_{ri} denotes the relative permittivity in region i. The permittivity in free space is represented by $\varepsilon_0 \approx 1/(36\pi 10^9)$ Fm^{-1}. The permeability in each region, is taken as the free-space permeability $\mu = \mu_0 = 4\pi 10^{-7}$ Hm^{-1}.

Let $\vec{\mathcal{A}}_i$ be the magnetic vector potential in region i. Then $\vec{\mathcal{A}}_i$ can be found by substituting relation (2.6) into Maxwell's equations (2.1). Note that ε_{ri} is constant within each region i. This results in the well-known Helmholtz equation for the magnetic vector potential that has to be satisfied in each region

$$\nabla^2\vec{\mathcal{A}}_i(\vec{r}) + \varepsilon_{ri}k_0^2\vec{\mathcal{A}}_i(\vec{r}) = -\vec{\mathcal{J}}_i(\vec{r}), \quad \text{with } i = 1,2,3\,, \tag{2.12}$$

where $\vec{\mathcal{J}}_i$ is the electric current distribution in region i and $k_0 = \omega\sqrt{\varepsilon_0\mu_0}$ is the wave number in free space. At the interfaces of the three regions and at the ground plane, the tangential components of the fields are subject to the following boundary conditions:

$$\begin{array}{lll} \vec{e}_z \times \vec{\mathcal{E}}_1 = \vec{0} & & z = 0, \\ \left.\begin{array}{lll} \vec{e}_z \times \vec{\mathcal{E}}_1 & = & \vec{e}_z \times \vec{\mathcal{E}}_2 \\ \vec{e}_z \times \vec{\mathcal{H}}_1 & = & \vec{e}_z \times \vec{\mathcal{H}}_2 \end{array}\right\} & & z = h_1, \\ \left.\begin{array}{lll} \vec{e}_z \times \vec{\mathcal{E}}_2 & = & \vec{e}_z \times \vec{\mathcal{E}}_3 \\ \vec{e}_z \times \vec{\mathcal{H}}_2 & = & \vec{e}_z \times \vec{\mathcal{H}}_3 \end{array}\right\} & & z = h_2, \end{array} \tag{2.13}$$

in which $\vec{e}_z$ is the unit vector in the z-direction. In addition, we will also have to define a boundary condition as $z \to \infty$. According to the causality condition [38] the fields must represent waves that propagate away from the sources and/or waves that decay with distance from these sources. In chapters 3 and 4, we will only investigate microstrip antennas and microstrip arrays for which the patches are located inside region 2 and for which the inner conductor of the coaxial cables may be located inside region 1 and region 2. We therefore only need to consider the situation of horizontally directed sheet currents inside region 2 and vertical currents inside region 1 or region 2. The analysis in this chapter is restricted to the determination of the Green's function in region 1 and region 2, due to an x- or y-directed electric dipole in region 2 and the Green's function in region 1 and 2, due to a z-directed electric dipole in region 1 or region 2.

Horizontal dipole in region 2

The electric dipole is located at $\vec{r}_0 = (0, 0, z_0)$ inside region 2 and has only a component in the x-direction (see figure 2.3). Later in this section, the location of the electric dipole will be extended to the general case with $\vec{r}_0 = (x_0, y_0, z_0)$. The Green's function of a y-directed dipole can be

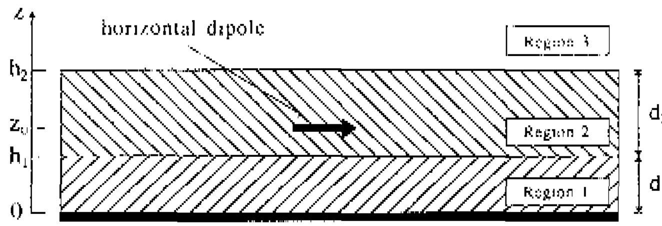

Figure 2.3 *An x-directed dipole in layer 2 at $\vec{r}_0' = (0,0,z_0)$*

found from the Green's function of an x-directed dipole by interchanging x and y in the resulting expressions. The volume current density associated with an x-directed dipole at $\vec{r}_0' = (0,0,z_0)$ is given by

$$\vec{\mathcal{J}}_2(\vec{r}) = \vec{e}_x\delta(x)\delta(y)\delta(z-z_0) \tag{2.14}$$

The Helmholtz equations in the three regions now take the form

$$\begin{aligned}
\nabla^2\vec{\mathcal{A}}_1 + \varepsilon_{r1}k_0^2\vec{\mathcal{A}}_1 &= \vec{0} & 0 < z < h_1,\\
\nabla^2\vec{\mathcal{A}}_2 + \varepsilon_{r2}k_0^2\vec{\mathcal{A}}_2 &= \vec{e}_x\delta(x)\delta(y)\delta(z-z_0) & h_1 < z < h_2,\\
\nabla^2\vec{\mathcal{A}}_3 + k_0^2\vec{\mathcal{A}}_3 &= \vec{0} & h_2 < z < \infty,
\end{aligned} \tag{2.15}$$

where the vector potential may be written in terms of the components of the dyadic Green's function

$$\begin{aligned}
\vec{\mathcal{A}}_i(\vec{r}) &= \iiint \bar{\bar{\mathcal{G}}}(\vec{r},\vec{r}')\cdot\vec{e}_x\delta(x')\delta(y')\delta(z'-z_0)\,dV'\\
&= \bar{\bar{\mathcal{G}}}(\vec{r},\vec{r}_0')\cdot\vec{e}_x\\
&= \mathcal{G}_{ixx}(\vec{r},\vec{r}_0')\vec{e}_x + \mathcal{G}_{iyx}(\vec{r},\vec{r}_0')\vec{e}_y + \mathcal{G}_{izx}(\vec{r},\vec{r}_0')\vec{e}_z
\end{aligned} \tag{2.16}$$

In a homogeneous medium the electromagnetic fields created by an x-directed electric dipole can be described with the x-component of the magnetic vector potential alone, i.e. with $\mathcal{G}_{xx}$. In a layered medium, however, a second component of the magnetic vector potential is required. Sommerfeld has shown [64, p. 257] that a solution can be found with $\mathcal{G}_{izx} \neq 0$ and $\mathcal{G}_{iyx} = 0$. Under the asumption that $\mathcal{G}_{iyx} = 0$, for $i = 1, 2, 3$, equation (2.15) takes the form

$$
\left.\begin{aligned}
\nabla^2 \mathcal{G}_{1xx} + \varepsilon_{r1} k_0^2 \mathcal{G}_{1xx} &= 0 \\
\nabla^2 \mathcal{G}_{1zx} + \varepsilon_{r1} k_0^2 \mathcal{G}_{1zx} &= 0
\end{aligned}\right\} \quad 0 < z < h_1,
$$

$$
\left.\begin{aligned}
\nabla^2 \mathcal{G}_{2xx} + \varepsilon_{r2} k_0^2 \mathcal{G}_{2xx} &= -\delta(x)\delta(y)\delta(z - z_0) \\
\nabla^2 \mathcal{G}_{2zx} + \varepsilon_{r2} k_0^2 \mathcal{G}_{2zx} &= 0
\end{aligned}\right\} \quad h_1 < z < h_2, \tag{2.17}
$$

$$
\left.\begin{aligned}
\nabla^2 \mathcal{G}_{3xx} + k_0^2 \mathcal{G}_{3xx} &= 0 \\
\nabla^2 \mathcal{G}_{3zx} + k_0^2 \mathcal{G}_{3zx} &= 0
\end{aligned}\right\} \quad h_2 < z < \infty
$$

$\mathcal{G}_{ixx}$ and $\mathcal{G}_{izx}$, with $i = 1, 2, 3$, have to be chosen such that the corresponding field satisfies the boundary conditions (2.13). Unfortunately, it is not possible to find a closed-form expression for $\mathcal{G}_{ixx}$ and $\mathcal{G}_{izx}$ in the spatial domain ((x, y, z)-domain). Therefore, a Fourier transformation with respect to the x- and y-coordinate is introduced, i.e. $(x, y, z) \to (k_x, k_y, z)$. The (k_x, k_y, z) domain is called the spectral domain. In the spectral domain, an analytical solution for the boundary-value problem can be obtained. This will be discussed in section 2.3.

Vertical dipole in region 1 or region 2

Figure 2.4 shows the configuration for this situation. The volume current distribution associated with this vertical dipole in region 1 or 2 is given by

$$\vec{J}(\vec{r}) = \vec{e}_z \delta(x)\delta(y)\delta(z - z_0) \tag{2.18}$$

It can be shown that only a single component of the vector potential is needed in order to solve the boundary-value problem for a z-directed dipole, i.e. $\vec{A}_i = \mathcal{G}_{izz}\vec{e}_z$ [64, p. 246]. In terms of

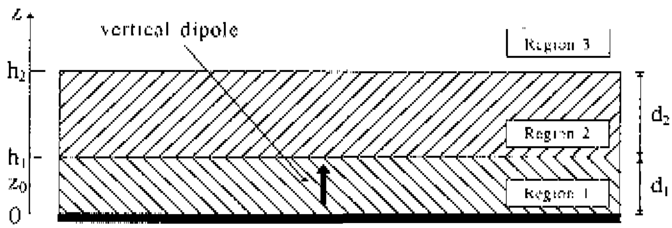

Figure 2.4 *A z-directed dipole at $\vec{r}_0 = (0, 0, z_0)$*

$\mathcal{G}_{izz}$, Helmholtz's equation (2.12) reads

$$
\begin{aligned}
\nabla^2 \mathcal{G}_{1zz} + \varepsilon_{r1} k_0^2 \mathcal{G}_{1zz} &= -\delta(x)\delta(y)\delta(z - z_0) & 0 < z < h_1, \\
\nabla^2 \mathcal{G}_{2zz} + \varepsilon_{r2} k_0^2 \mathcal{G}_{2zz} &= 0 & h_1 < z < h_2, \\
\nabla^2 \mathcal{G}_{3zz} + k_0^2 \mathcal{G}_{3zz} &= 0 & h_2 < z < \infty,
\end{aligned}
\tag{2.19}
$$

if the dipole is located in region 1 and

$$
\begin{aligned}
\nabla^2 \mathcal{G}_{1zz} + \varepsilon_{r1} k_0^2 \mathcal{G}_{1zz} &= 0 & 0 < z < h_1, \\
\nabla^2 \mathcal{G}_{2zz} + \varepsilon_{r2} k_0^2 \mathcal{G}_{2zz} &= -\delta(x)\delta(y)\delta(z - z_0) & h_1 < z < h_2, \\
\nabla^2 \mathcal{G}_{3zz} + k_0^2 \mathcal{G}_{3zz} &= 0 & h_2 < z < \infty,
\end{aligned}
\tag{2.20}
$$

if the dipole is located in region 2. Again, $\mathcal{G}_{izz}$ has to be chosen such that the corresponding field satisfies the boundary conditions (2.13). A Fourier transformation with respect to the transverse coordinates will be introduced in order to obtain a solution for $\mathcal{G}_{izz}$.

2.3 Spectral-domain solution

It has already been stated before that in the spectral domain an analytical expression of the dyadic Green's function can be obtained. The original spatial-domain Green's function can be determined by applying an inverse Fourier transformation. The Fourier transform with respect to x and y of a function $\mathcal{G}(x,y)$ and its corresponding inverse Fourier transform $G(k_x,k_y)$ are defined as

$$\begin{aligned}
G(k_x,k_y) &= FT\{\mathcal{G}(x,y)\} = \int_{-\infty}^{\infty}\int_{-\infty}^{\infty} \mathcal{G}(x,y)e^{jk_x x}e^{jk_y y}\,dxdy, \\
\mathcal{G}(x,y) &= FT^{-1}\{G(k_x,k_y)\} \\
&= \frac{1}{4\pi^2}\int_{-\infty}^{\infty}\int_{-\infty}^{\infty} G(k_x,k_y)e^{-jk_x x}e^{-jk_y y}dk_x dk_y.
\end{aligned} \tag{2.21}$$

Some useful properties of the Fourier transformation are

$$\begin{aligned}
&FT\{\nabla^2\mathcal{G}_{ixx}(x,y)\} = (-k_x^2 - k_y^2 + \partial_z^2)G_{ixx}(k_x,k_y,z), \\
&FT\{\delta(x-x_0)\delta(y-y_0)\delta(z-z_0)\} = e^{jk_x x_0}e^{jk_y y_0}\delta(z-z_0)
\end{aligned} \tag{2.22}$$

These properties will be used to find the spectral-domain Green's function of a horizontal dipole and of a vertical dipole.

Horizontal dipole in region 2

The spectral-domain form of the Helmholtz equations (2.17) is given by

$$\left.\begin{aligned}
\partial_z^2 G_{1xx} + k_1^2 G_{1xx} &= 0 \\
\partial_z^2 G_{1zx} + k_1^2 G_{1zx} &= 0
\end{aligned}\right\} \quad 0 < z < h_1,$$

$$\left.\begin{aligned}
\partial_z^2 G_{2xx} + k_2^2 G_{2xx} &= -\delta(z-z_0) \\
\partial_z^2 G_{2zx} + k_2^2 G_{2zx} &= 0
\end{aligned}\right\} \quad h_1 < z < h_2, \tag{2.23}$$

$$\left.\begin{aligned} \partial_z^2 G_{3xx} + k_3^2 G_{3xx} &= 0 \\ \partial_z^2 G_{3zx} + k_3^2 G_{3zx} &= 0 \end{aligned}\right\} \quad h_2 < z < \infty,$$

in which the vertical components of the wave vector in each region are given by

$$k_1^2 = \varepsilon_{r1} k_0^2 - k_x^2 - k_y^2 \quad (\mathrm{Im}(k_1) < 0 \text{ or } \mathrm{Im}(k_1) = 0 \wedge \mathrm{Re}(k_1) > 0),$$

$$k_2^2 = \varepsilon_{r2} k_0^2 - k_x^2 - k_y^2 \quad (\mathrm{Im}(k_2) < 0 \text{ or } \mathrm{Im}(k_2) = 0 \wedge \mathrm{Re}(k_2) > 0),$$

$$k_3^2 = k_0^2 - k_x^2 - k_y^2 \quad (\mathrm{Im}(k_3) < 0 \text{ or } \mathrm{Im}(k_3) = 0 \wedge \mathrm{Re}(k_3) > 0)$$

The solution of the inhomogeneous Helmholtz equation for G_{2xx} is a combination of a homogeneous solution and a particular solution. The particular solution can be found by means of variation of constants and is given by

$$G_{2xx}^{par} = \frac{1}{2jk_2} e^{-jk_2|z-z_0|} \qquad h_1 < z < h_2 \tag{2.24}$$

The other components of the spectral-domain Green's function satisfy a homogeneous Helmholtz equation. The general solution of (2.23) is a linear combination of elementary functions

$$\begin{aligned}
G_{1xx} &= C_{1xx} e^{-jk_1 z} + D_{1xx} e^{-jk_1(h_1-z)}, \\
G_{1zx} &= C_{1zx} e^{-jk_1 z} + D_{1zx} e^{-jk_1(h_1-z)}, \\
G_{2xx} &= C_{2xx} e^{-jk_2(z-h_1)} + D_{2xx} e^{-jk_2(h_2-z)} + \frac{1}{2jk_2} e^{-jk_2|z-z_0|}, \\
G_{2zx} &= C_{2zx} e^{-jk_2(z-h_1)} + D_{2zx} e^{-jk_2(h_2-z)}, \\
G_{3xx} &= C_{3xx} e^{-jk_3(z-h_2)}, \\
G_{3zx} &= C_{3zx} e^{-jk_3(z-h_2)},
\end{aligned} \tag{2.25}$$

where the radiation condition was used to eliminate the terms proportional to $e^{jk_3 z}$ in G_{3xx} and G_{3zx}. Note that $Im(k_3) \leq 0$. The physical interpretation of the general solution (2.25) is illustrated in figure 2.5 for the x-component G_{xx}. In region 1 and region 2, the general solution of

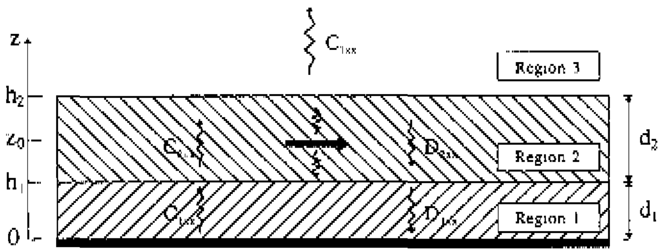

Figure 2.5: *Physical interpretation of the general solution of G_{ixx}.*

G_{ixx} is a combination of an upgoing wave in the $+z$-direction and a downgoing wave propagating in the $-z$-direction. In region 3 there is only an upgoing wave in the $+z$-direction.

The 10 unknown constants in (2.25) can be determined by applying the boundary conditions (2.13) for the electric and magnetic field at the interfaces between the layers. The Fourier transform of (2.13) gives rise to the following set of boundary equations in terms of the components of the spectral-domain Green's function

$$\left.\begin{aligned} G_{1xx} &= 0 \\ -jk_x G_{1zx} + \partial_z G_{1xx} &= 0 \end{aligned}\right\} \quad z = 0,$$

$$\left.\begin{aligned} G_{1xx} &= G_{2xx} \\ \varepsilon_{r2}\left[k_x^2 G_{1zx} + jk_x \partial_z G_{1xx}\right] &= \varepsilon_{r1}\left[k_x^2 G_{2zx} + jk_x \partial_z G_{2xx}\right] \\ G_{1zx} &= G_{2zx} \\ \partial_z G_{1xx} &= \partial_z G_{2xx} \end{aligned}\right\} \quad z = h_1, \tag{2.26}$$

$$\left.\begin{aligned}
G_{2xx} &= G_{3xx} \\
\left[k_x^2 G_{2zx} + jk_x \partial_z G_{2xx}\right] &= \varepsilon_{r2}\left[k_x^2 G_{3zx} + jk_x \partial_z G_{3xx}\right] \\
G_{2zx} &= G_{3zx} \\
\partial_z G_{2zx} &= \partial_z G_{3zx}
\end{aligned}\right\} \quad z = h_2$$

With the general solution (2.25) substituted in the boundary conditions (2.26), one obtains a set of 10 linear equations with 10 unknown coefficients. This set of linear equations can be solved analytically. A convenient way to determine the unknown coefficients is to use the Fresnel reflection coefficients at the interfaces between each region for TE and TM fields [12, p. 48]. These coefficients are given by

$$R_{ji}^{TE} = \frac{k_j - k_i}{k_j + k_i}, \tag{2.27}$$

and

$$R_{ji}^{TM} = \frac{\varepsilon_{ri} k_j - \varepsilon_{rj} k_i}{\varepsilon_{ri} k_j + \varepsilon_{rj} k_i}, \tag{2.28}$$

in which k_i is the vertical component of the wave vector in one of the three regions $i = 1, 2, 3$. As an example, we will take a closer look at the solution for C_{2xx} and D_{2xx} of G_{2xx} in region 2. At the interface $z = h_2$, the downgoing wave in region 2 can be expressed in terms of the upgoing wave in region 2

$$D_{2xx} = R_{23}^{TE}\left(C_{2xx}e^{-jk_2 h_2} + \frac{1}{2jk_2}e^{-jk_2(h_2 - z_0)}\right) \tag{2.29}$$

Similarly, at the interface $z = h_1$ the upgoing wave in region 2 can be expressed in terms of the downgoing wave. This gives the relation

$$C_{2xx} = \tilde{R}_{21}^{TE}\left(D_{2xx}e^{-jk_2 h_2} + \frac{1}{2jk_2}e^{-jk_2(z_0 - h_1)}\right), \tag{2.30}$$

where $\tilde{R}_{21}^{TE}$ is the generalised reflection coefficient, which includes the effect of multiple reflections and transmissions in region 2:

$$\tilde{R}_{21}^{TE} = R_{21}^{TE} + \frac{(1 + R_{21}^{TE})(-1)(1 + R_{12}^{TE})e^{-2jk_1h_1}}{1 - R_{21}^{TE}e^{-2jk_1h_1}}, \tag{2.31}$$

in which $T_{21}^{TE} = (1 + R_{21}^{TE})$ is the Fresnel transmission coefficient between layer 2 and layer 1. Note that the Fresnel reflection coefficient for TE-waves at the ground plane is equal to -1. If equation (2.29) is substituted into equation (2.30), a solution for C_{2xx} and D_{2xx} can be obtained:

$$\begin{aligned} C_{2xx} &= \frac{1}{2jk_2}\tilde{R}_{21}^{TE}\left[\frac{e^{-jk_2(z_0-h_1)} + R_{23}^{TE}e^{-jk_2(2h_2-h_1-z_0)}}{D^{TE}}\right], \\ D_{2xx} &= \frac{1}{2jk_2}R_{23}^{TE}\left[\frac{e^{-jk_2(h_2-z_0)} + \tilde{R}_{21}^{TE}e^{-jk_2(z_0+h_2-2h_1)}}{D^{TE}}\right], \end{aligned} \tag{2.32}$$

in which the denominator D^{TE} is given by

$$D^{TE} = 1 - \tilde{R}_{21}^{TE}R_{23}^{TE}e^{-2jk_2d_2} \tag{2.33}$$

The other 8 unknown coefficients in (2.25) can be calculated in a similar way.
To summarize, the expressions for the components of the spectral-domain Green's function due to an x-directed dipole are given by

$$\begin{aligned} G_{ixx} &= g_i, && \text{for } i = 1,2, \\ G_{iyx} &= 0, && \text{for } i = 1,2, \\ G_{izx} &= -k_x g_{i+2}, && \text{for } i = 1,2, \end{aligned} \tag{2.34}$$

with

$$g_1 = \frac{1}{2jk_2D^{TE}}\left(\frac{(1 + R_{21}^{TE})e^{-jk_1h_1}}{(1 - R_{21}^{TE}e^{-2jk_1h_1})}\right)2j\sin(k_1z)\cdot \left[e^{-jk_2(z_0-h_1)} + R_{23}^{TE}e^{jk_2(z_0-2h_2+h_1)}\right],$$

$$g_2 = \begin{cases} \dfrac{1}{2jk_2D^{TE}}\left[e^{-jk_2z_0} + R_{23}^{TE}e^{jk_2(z_0-2h_2)}\right]\cdot \\ \qquad \left[e^{jk_2z} + \tilde{R}_{21}^{TE}e^{-jk_2(z-2h_1)}\right] & h_1 \le z \le z_0, \\ \dfrac{1}{2jk_2D^{TE}}\left[e^{jk_2z_0} + \tilde{R}_{21}^{TE}e^{-jk_2(z_0-2h_1)}\right]\cdot \\ \qquad \left[e^{-jk_2z} + R_{23}^{TE}e^{jk_2(z-2h_2)}\right] & z_0 \le z \le h_2, \end{cases} \tag{2.35}$$

$$g_3 = \frac{-1}{2jk_2 D^{TE} D^{TM}} \frac{\cos(k_1 z)}{\cos(k_1 h_1)} \Big[(1 - \varepsilon_{r2})(1 + \bar{R}_{21}^{TM}) e^{-jk_2 d_2} F_1(z_0)$$
$$+ (\varepsilon_{r2} - \varepsilon_{r1})(1 + R_{23}^{TM} e^{-2jk_2 d_2}) F_2(z_0)\Big],$$

$$g_4 = \frac{-1}{2jk_2 D^{TE} D^{TM}} \Big[(1 - \varepsilon_{r2}) F_1(z_0)(e^{jk_2(z-h_2)} + \bar{R}_{21}^{TM} e^{-jk_2(z+h_2-2h_1)})$$
$$+ (\varepsilon_{r2} - \varepsilon_{r1}) F_2(z_0)(e^{-jk_2(z-h_1)} + R_{23}^{TM} e^{jk_2(z-2h_2+h_1)})\Big],$$

with

$$\bar{R}_{21}^{TM} = R_{21}^{TM} + \frac{(1 + R_{21}^{TM})(1 + R_{12}^{TM}) e^{-2jk_1 h_1}}{1 + R_{21}^{TM} e^{-2jk_1 h_1}}, \tag{2.36}$$

The functions $F_1(z_0)$ and $F_2(z_0)$ are given by

$$\begin{aligned} F_1(z_0) &= \left(\frac{1 + R_{23}^{TE}}{k_2 + k_3 \varepsilon_{r2}}\right) \left[e^{jk_2(z_0-h_2)} + \bar{R}_{21}^{TE} e^{-jk_2(z_0+h_2-2h_1)}\right], \\ F_2(z_0) &= \left(\frac{(1 + R_{21}^{TE})(1 - e^{-4jk_1 h_1})}{(1 - R_{21}^{TE} e^{-2jk_1 h_1})(1 + R_{21}^{TM} e^{-2jk_1 h_1})(k_2 \varepsilon_{r1} + k_1 \varepsilon_{r2})}\right) \cdot \\ &\quad \left[e^{-jk_2(z_0-h_1)} + R_{23}^{TE} e^{jk_2(z_0-2h_2+h_1)}\right], \end{aligned} \tag{2.37}$$

and the denominators D^{TM} and D^{TE} are given by

$$\begin{aligned} D^{TM} &= 1 - \bar{R}_{21}^{TM} R_{23}^{TM} e^{-2jk_2 d_2}, \\ D^{TE} &= 1 - \bar{R}_{21}^{TE} R_{23}^{TE} e^{-2jk_2 d_2} \end{aligned} \tag{2.38}$$

Note that we are only interested in the fields in region 1 an 2. Therefore, the expressions for $G_{3_{xx}}$ and $G_{3_{zx}}$ are not given here. The functions D^{TM} and D^{TE} can be rewritten in the following form

$$\begin{aligned} D^{TM} &= \left(\frac{4e^{-jk_1 d_1} e^{-jk_2 d_2}}{(1 + R_{21}^{TM} e^{-2jk_1 d_1})(k_1 \varepsilon_{r2} + k_2 \varepsilon_{r1})(k_2 + k_3 \varepsilon_{r2})}\right) T_m, \\ D^{TE} &= \left(\frac{4e^{-jk_1 d_1} e^{-jk_2 d_2}}{(1 - R_{21}^{TE} e^{-2jk_1 d_1})(k_1 + k_2)(k_2 + k_3)}\right) T_e, \end{aligned} \tag{2.39}$$

in which T_e and T_m are given by

$$\begin{aligned} T_e &= jk_2k_3\sin(k_1d_1)\cos(k_2d_2) + k_1k_2\cos(k_1d_1)\cos(k_2d_2) \\ &\quad -k_2^2\sin(k_1d_1)\sin(k_2d_2) + jk_1k_3\cos(k_1d_1)\sin(k_2d_2), \\ T_m &= k_2k_3\varepsilon_{r1}\varepsilon_{r2}\cos(k_1d_1)\cos(k_2d_2) + jk_2^2\varepsilon_{r1}\cos(k_1d_1)\sin(k_2d_2) \\ &\quad -k_1k_3\varepsilon_{r2}^2\sin(k_1d_1)\sin(k_2d_2) + jk_1k_2\varepsilon_{r2}\sin(k_1d_1)\cos(k_2d_2). \end{aligned} \tag{2.40}$$

The zeros of the functions T_e and T_m correspond to solutions of the characteristic equation for transverse electric (TE) and transverse magnetic (TM) surface waves, respectively, in a grounded two-layer dielectric structure [32, p. 168]. These zeros correspond to first-order poles in the spectral-domain Green's function and some care has to be taken in the numerical inverse Fourier transformation. In section 3.8, an analytical method will be proposed to avoid these numerical problems. The spectral-domain Green's function of a y-directed dipole can be found by interchanging k_x and k_y in the spectral-domain Green's function of an x-directed dipole, i.e.

$$\begin{aligned} G_{iyy} &= g_i, && \text{for } i = 1,2, \\ G_{ixy} &= 0, && \text{for } i = 1,2, \\ G_{izy} &= -k_y g_{i+2}, && \text{for } i = 1,2. \end{aligned} \tag{2.41}$$

Vertical dipole in region 1 or region 2

First, the situation of a vertical dipole located inside region 1 will be considered. Transforming Helmholtz's equations (2.19) to the spectral domain yields

$$\begin{aligned} \partial_z^2 G_{1zz} + k_1^2 G_{1zz} &= -\delta(z-z_0) && 0 < z < h_1, \\ \partial_z^2 G_{2zz} + k_2^2 G_{2zz} &= 0 && h_1 < z < h_2, \\ \partial_z^2 G_{3zz} + k_3^2 G_{3zz} &= 0 && h_2 < z < \infty \end{aligned} \tag{2.42}$$

The general solution of (2.42) is a combination of a homogeneous solution and a particular solution:

$$
\begin{aligned}
G_{1zz} &= C_{1zz}e^{-jk_1 z} + D_{1zz}e^{-jk_1(h_1-z)} + \frac{1}{2jk_1}e^{-jk_1|z-z_0|}, \\
G_{2zz} &= C_{2zz}e^{-jk_2(z-h_1)} + D_{2zz}e^{-jk_2(h_2-z)}, \\
G_{3zz} &= C_{3zz}e^{-jk_3(z-h_2)},
\end{aligned}
\tag{2.43}
$$

where again the radiation condition was used to eliminate the term proportional to $e^{jk_3 z}$ in G_{3zz}. From the boundary conditions (2.13), a set of restrictions for G_{izz} can be obtained

$$
\begin{aligned}
&\partial_z G_{1zz} = 0 && z = 0, \\
&\left.\begin{aligned} \varepsilon_{r2}\partial_z G_{1zz} &= \varepsilon_{r1}\partial_z G_{2zz} \\ G_{1zz} &= G_{2zz} \end{aligned}\right\} && z = h_1, \\
&\left.\begin{aligned} \partial_z G_{2zz} &= \varepsilon_{r2}\partial_z G_{3zz} \\ G_{2zz} &= G_{3zz} \end{aligned}\right\} && z = h_2
\end{aligned}
\tag{2.44}
$$

Substituting (2.43) into (2.44) results in a set of 5 linear equations with 5 unknown coefficients. At the interface between the ground plane and layer 1, i.e. at $z = 0$, the upgoing wave can be expressed in terms of the downgoing wave.

$$
C_{1zz} = D_{1zz}e^{-jk_1 h_1} + \frac{1}{2jk_1}e^{-jk_1 z_0}
\tag{2.45}
$$

From the boundary conditions at $z = h_1$ and $z = h_2$ we get

$$
D_{1zz} = \tilde{R}_{12}^{TM}\left(C_{1zz}e^{-jk_1 h_1} + \frac{1}{2jk_1}e^{-jk_1(h_1-z_0)}\right),
\tag{2.46}
$$

in which $\tilde{R}_{12}^{TM}$ is the generalised reflection coefficient from layer 1 to layer 2 and is given by

$$
\tilde{R}_{12}^{TM} = R_{12}^{TM} + \frac{(1+R_{12}^{TM})R_{23}^{TM}(1+R_{21}^{TM})e^{-2jk_2 d_2}}{1 + R_{12}^{TM}R_{23}^{TM}e^{-2jk_2 d_2}}
\tag{2.47}
$$

From (2.45) and (2.46) the coefficients C_{1zz} and D_{1zz} can be determined. The remaining 3 unknown coefficients in (2.43) can be found in a similar way. The final result is

$$
\begin{aligned}
G_{1zz} &= g_5, \\
G_{2zz} &= g_6,
\end{aligned}
\tag{2.48}
$$

with

$$
g_5 = \begin{cases}
\left(\dfrac{1 + R_{12}^{TM} R_{23}^{TM} e^{-2jk_2 d_2}}{2jk_1 D^{TM} (1 - R_{12}^{TM} e^{-2jk_1 h_1})} \right) 2\cos(k_1 z) \\
\qquad \left[e^{-jk_1 z_0} + \tilde{R}_{12}^{TM} e^{jk_1 (z_0 - 2h_1)} \right] & 0 \le z \le z_0, \\
\left(\dfrac{1 + R_{12}^{TM} R_{23}^{TM} e^{-2jk_2 d_2}}{2jk_1 D^{TM} (1 - R_{12}^{TM} e^{-2jk_1 h_1})} \right) 2\cos(k_1 z_0) \cdot \\
\qquad \left[e^{-jk_1 z} + \tilde{R}_{12}^{TM} e^{jk_1 (z - 2h_1)} \right] & z_0 \le z \le h_1,
\end{cases}
\tag{2.49}
$$

$$
g_6 = \frac{2\cos(k_1 z_0)(1 + R_{12}^{TM}) e^{-jk_1 h_1}}{2jk_1 D^{TM} (1 - R_{12}^{TM} e^{-2jk_1 h_1})} \left[e^{-jk_2 (z - h_1)} + R_{23}^{TM} e^{jk_2 (z - 2h_2 + h_1)} \right].
$$

The same procedure can be used if the vertical dipole is located inside region 2. The final expressions for G_{1zz} and G_{2zz} are also given by (2.48), where g_5 and g_6 now take the form

$$
g_5 = \frac{2\cos(k_1 z)(1 + R_{21}^{TM}) e^{-jk_1 h_1}}{2jk_2 D^{TM} (1 - R_{12}^{TM} e^{-2jk_1 h_1})} \left[e^{-jk_2 (z_0 - h_1)} + R_{23}^{TM} e^{jk_2 (z_0 - 2h_2 + h_1)} \right]
$$

$$
g_6 = \begin{cases}
\dfrac{1}{2jk_2 D^{TM}} \left[e^{-jk_2 z_0} + R_{23}^{TM} e^{jk_2 (z_0 - 2h_2)} \right] \\
\qquad \left[e^{jk_2 z} + \tilde{R}_{21}^{TM} e^{-jk_2 (z - 2h_1)} \right] & h_1 \le z \le z_0, \\
\dfrac{1}{2jk_2 D^{TM}} \left[e^{jk_2 z_0} + \tilde{R}_{21}^{TM} e^{-jk_2 (z_0 - 2h_1)} \right] \cdot \\
\qquad \left[e^{-jk_2 z} + R_{23}^{TM} e^{jk_2 (z - 2h_2)} \right] & z_0 \le z \le h_2,
\end{cases}
\tag{2.50}
$$

Summary

To summarize, the spectral-domain Green's function of a horizontal dipole in layer 2 or a vertical dipole in layer 1 or layer 2, located at the coordinates $\vec{r}_0 = (x_0, y_0, z_0)$, is given in matrix form by

$$\begin{aligned}\bar{\bar{G}}_i(k_x, k_y, z, \vec{r}_0) &= e^{jk_x x_0} e^{jk_y y_0} \begin{pmatrix} g_i & 0 & 0 \\ 0 & g_i & 0 \\ -k_x g_{i+2} & -k_y g_{i+2} & g_{i+4} \end{pmatrix} \\ &= e^{jk_x x_0} e^{jk_y y_0}\, \bar{\bar{G}}{}'_i(k_x, k_y, z, z_0)\end{aligned} \tag{2.51}$$

An additional factor of $e^{jk_x x_0} e^{jk_y y_0}$ occurs in the above expression, which is due to the displacement (x_0, y_0) of the dipole with respect to the origin of the coordinate system.

2.4 Electric and magnetic fields in the spatial domain

Once the dyadic Green's function of the microstrip structure has been determined, the fields in each region can be calculated with relations (2.6) and (2.9). The electric field in the spectral domain can be found from relation (2.8):

$$\vec{E}(k_x, k_y, z) = \frac{-j\omega\mu_0}{\varepsilon_{ri} k_0^2} \begin{bmatrix} (\varepsilon_{ri} k_0^2 - k_x^2) A_{ix} - k_x k_y A_{iy} - jk_x \partial_z A_{iz} \\ (\varepsilon_{ri} k_0^2 - k_y^2) A_{iy} - k_x k_y A_{ix} - jk_y \partial_z A_{iz} \\ (\varepsilon_{ri} k_0^2 + \partial_z^2) A_{iz} - jk_x \partial_z A_{ix} - jk_y \partial_z A_{iy} \end{bmatrix}, \tag{2.52}$$

and the spectral-domain magnetic field from relation (2.7)

$$\vec{H}(k_x, k_y, z) = \begin{bmatrix} -jk_y A_{iz} - \partial_z A_{iy} \\ \partial_z A_{ix} + jk_x A_{iz} \\ -jk_x A_{iy} + jk_y A_{ix} \end{bmatrix}, \tag{2.53}$$

with

$$i = 1 \quad \text{if } 0 \le z \le h_1,$$

$$i = 2 \quad \text{if } h_1 \le z \le h_2,$$

where $\vec{A}_i$ is the magnetic vector potential, with $\vec{A}_i = A_{ix}\vec{e}_x + A_{iy}\vec{e}_y + A_{iz}\vec{e}_z$. Now let us assume that there is a certain volume current distribution inside volume V_0, which is located in region 1 and/or in region 2. The magnetic vector potential caused by this current distribution can be written in terms of the spectral-domain Green's function, when relation (2.9) is used. This relation can be rewritten in the following way

$$\begin{aligned}
\vec{A}_i(\vec{r}) &= \iiint \bar{\bar{G}}(\vec{r}, \vec{r}_0) \cdot \vec{J}(\vec{r}_0)\, dx_0 dy_0 dz_0 \\
&= \iiint \left[\frac{1}{4\pi^2} \int_{-\infty}^{\infty} \int_{-\infty}^{\infty} \tilde{\bar{\bar{G}}}_i(k_x, k_y, z, \vec{r}_0) e^{-jk_x x} e^{-jk_y y}\, dk_x dk_y \right] \\
&\quad \cdot \vec{J}(\vec{r}_0)\, dx_0 dy_0 dz_0 \\
&= \frac{1}{4\pi^2} \int_{-\infty}^{\infty} \int_{-\infty}^{\infty} \int_{0}^{h_2} \tilde{\bar{\bar{G}}}_i'(k_x, k_y, z, z_0) \cdot \tilde{\vec{J}}(k_x, k_y, z_0) dz_0 \\
&\quad e^{-jk_x x} e^{-jk_y y}\, dk_x dk_y \\
&= FT^{-1}\{\tilde{\vec{A}}_i(k_x, k_y, z)\},
\end{aligned} \tag{2.54}$$

in which $\tilde{\bar{\bar{G}}}_i(k_x, k_y, z, \vec{r}_0) = e^{jk_x x_0} e^{jk_y y_0} \tilde{\bar{\bar{G}}}_i'(k_x, k_y, z, z_0)$ (see (2.51)). $\tilde{\vec{J}}(k_x, k_y, z_0)$ is the Fourier transform, with respect to x_0 and y_0, of the current distribution $\vec{J}(x_0, y_0, z_0)$, with

$$\tilde{\vec{J}}(k_x, k_y, z_0) = \int_{-\infty}^{\infty} \int_{-\infty}^{\infty} \vec{J}(x_0, y_0, z_0) e^{jk_x x_0} e^{jk_y y_0}\, dx_0 dy_0 \tag{2.55}$$

From (2.54) it follows that

$$\tilde{\vec{A}}_i(k_x, k_y, z) = \int_0^{h_2} \tilde{\bar{\bar{G}}}_i'(k_x, k_y, z, z_0) \cdot \tilde{\vec{J}}(k_x, k_y, z_0) dz_0 \tag{2.56}$$

If relation (2.56) is substituted in (2.52) and (2.53), an expression for the electric and magnetic fields in region 1 and region 2 can be determined:

$$\begin{aligned}\vec{\mathcal{E}}(x,y,z) &= \frac{1}{4\pi^2}\int_{-\infty}^{\infty}\int_{-\infty}^{\infty}\vec{E}(k_x,k_y,z)e^{-jk_x x}e^{-jk_y y}dk_x dk_y \\ &= \frac{1}{4\pi^2}\int_{-\infty}^{\infty}\int_{-\infty}^{\infty}\int_{0}^{h_2}\bar{\bar{Q}}_i^E(k_x,k_y,z,z_0)\cdot\vec{J}(k_x,k_y,z_0)dz_0 e^{-jk_x x}e^{-jk_y y}dk_x dk_y\end{aligned} \tag{2.57}$$

and

$$\begin{aligned}\vec{\mathcal{H}}(x,y,z) &= \frac{1}{4\pi^2}\int_{-\infty}^{\infty}\int_{-\infty}^{\infty}\vec{H}(k_x,k_y,z)e^{-jk_x x}e^{-jk_y y}dk_x dk_y \\ &= \frac{1}{4\pi^2}\int_{-\infty}^{\infty}\int_{-\infty}^{\infty}\int_{0}^{h_2}\bar{\bar{Q}}_i^H(k_x,k_y,z,z_0)\cdot\vec{J}(k_x,k_y,z_0)dz_0 e^{-jk_x x}e^{-jk_y y}dk_x dk_y\end{aligned} \tag{2.58}$$

with

$i = 1 \quad \text{if } 0 \leq z \leq h_1,$

$i = 2 \quad \text{if } h_1 \leq z < h_2,$

in which the dyadic function $\bar{\bar{Q}}_i^E$ is given by

$$\bar{\bar{Q}}_i^E(k_x,k_y,z,z_0) = \begin{pmatrix} Q_{ixx}^E & Q_{ixy}^E & Q_{ixz}^E \\ Q_{iyx}^E & Q_{iyy}^E & Q_{iyz}^E \\ Q_{izx}^E & Q_{izy}^E & Q_{izz}^E \end{pmatrix}, \quad \text{with } i = 1,2, \tag{2.59}$$

with

$$\begin{aligned}Q_{ixx}^E(k_x,k_y,z,z_0) &= -\frac{j\omega\mu_0}{\varepsilon_{ri}k_0^2}\left[(\varepsilon_{ri}k_0^2 - k_x^2)q_i + jk_x^2\partial_z q_{i+2}\right] & h_1 \leq z_0 \leq h_2, \\ Q_{iyy}^E(k_x,k_y,z,z_0) &= -\frac{j\omega\mu_0}{\varepsilon_{ri}k_0^2}\left[(\varepsilon_{ri}k_0^2 - k_y^2)q_i + jk_y^2\partial_z q_{i+2}\right] & h_1 \leq z_0 \leq h_2, \\ Q_{ixy}^E(k_x,k_y,z,z_0) &= Q_{iyx}^E = \frac{j\omega\mu_0}{\varepsilon_{ri}k_0^2}\left[-k_x k_y q_i + jk_x k_y\partial_z q_{i+2}\right] & h_1 \leq z_0 \leq h_2,\end{aligned}$$

$$
\begin{aligned}
Q^E_{ixz}(k_x, k_y, z, z_0) &= -\frac{j\omega\mu_0}{\varepsilon_{ri}k_0^2}\left[-jk_x\partial_z g_{i+4}\right] && 0 \leq z_0 \leq h_2, \\
Q^E_{iyz}(k_x, k_y, z, z_0) &= -\frac{j\omega\mu_0}{\varepsilon_{ri}k_0^2}\left[-jk_y\partial_z g_{i+4}\right] && 0 \leq z_0 \leq h_2, \\
Q^E_{izx}(k_x, k_y, z, z_0) &= \frac{j\omega\mu_0}{\varepsilon_{ri}k_0^2}\left[k_x\varepsilon_{ri}k_0^2 g_{i+2} + k_x\partial_z^2 g_{i+2} + jk_x\partial_z g_i\right] && h_1 \leq z_0 \leq h_2, \\
Q^E_{izy}(k_x, k_y, z, z_0) &= \frac{j\omega\mu_0}{\varepsilon_{ri}k_0^2}\left[k_y\varepsilon_{ri}k_0^2 g_{i+2} + k_y\partial_z^2 g_{i+2} + jk_y\partial_z g_i\right] && h_1 \leq z_0 \leq h_2, \\
Q^E_{izz}(k_x, k_y, z, z_0) &= -\frac{j\omega\mu_0}{\varepsilon_{ri}k_0^2}\left[\varepsilon_{ri}k_0^2 g_{i+4} + \partial_z^2 g_{i+4}\right] \\
&= \frac{j\omega\mu_0}{\varepsilon_{ri}k_0^2}\delta(z - z_0) - \frac{j\omega\mu_0(k_x^2 + k_y^2)}{\varepsilon_{ri}k_0^2} g_{i+4} && 0 \leq z_0 \leq h_2,
\end{aligned}
$$

and where the dyadic function $\bar{Q}_i^H$ is given by

$$
\bar{Q}_i^H(k_x, k_y, z, z_0) = \begin{pmatrix} Q^H_{ixx} & Q^H_{ixy} & Q^H_{ixz} \\ Q^H_{iyx} & Q^H_{iyy} & Q^H_{iyz} \\ Q^H_{izx} & Q^H_{izy} & Q^H_{izz} \end{pmatrix}, \quad \text{with } i = 1, 2\,, \tag{2.60}
$$

with

$$
\begin{aligned}
Q^H_{ixx}(k_x, k_y, z, z_0) &= jk_x k_y g_{i+2} && h_1 \leq z_0 \leq h_2, \\
Q^H_{iyy}(k_x, k_y, z, z_0) &= -jk_x k_y g_{i+2} && h_1 \leq z_0 \leq h_2, \\
Q^H_{ixy}(k_x, k_y, z, z_0) &= jk_y^2 g_{i+2} - \partial_z g_i && h_1 \leq z_0 \leq h_2, \\
Q^H_{iyx}(k_x, k_y, z, z_0) &= \partial_z g_i - jk_x^2 g_{i+2} && h_1 \leq z_0 \leq h_2, \\
Q^H_{ixz}(k_x, k_y, z, z_0) &= -jk_y g_{i+4} && 0 \leq z_0 \leq h_2,
\end{aligned}
$$

$$Q^H_{iyz}(k_x, k_y, z, z_0) = \quad jk_x g_{i+4} \quad 0 \leq z_0 \leq h_2,$$

$$Q^H_{izx}(k_x, k_y, z, z_0) = \quad jk_y g_i \quad h_1 \leq z_0 \leq h_2,$$

$$Q^H_{izy}(k_x, k_y, z, z_0) = \quad -jk_x g_i \quad h_1 \leq z_0 \leq h_2,$$

$$Q^H_{izz}(k_x, k_y, z, z_0) = \quad 0 \quad 0 \leq z_0 \leq h_2.$$

Chapter 3

Isolated microstrip antennas

3.1 Introduction

This chapter deals with the analysis of isolated, linearly polarised, microstrip antennas. The antenna is built up of two dielectric layers mounted on an infinite ground plane, and has one or two rectangular metallic patches. The lower patch is fed with a single coaxial cable, which results in a linearly polarised far field. Circular polarisation is discussed in chapter 4 of this thesis. From the electric-field boundary condition on the patches and on the coaxial probe of the microstrip antenna an integral equation for the unknown currents is derived. This integral equation is solved numerically with a Galerkin type of method-of-moment procedure, which includes the exact spectral-domain Green's function of chapter 2. Once this current distribution is known, the input impedance and radiation pattern can be determined. In the case of an electrically thick substrate, a very accurate model for the feeding coaxial cable has to be used that includes the variation of current along the coaxial probe and that ensures continuity of current at the patch-probe transition. In section 3.8 some techniques will be discussed to improve the numerical accuracy of the method and to reduce the total computation time.

3.2 Model description

3.2.1 Two-layer stacked microstrip antenna

The geometry of an isolated stacked microstrip antenna with rectangular patches and fed by a coaxial cable is shown in figure 3.1. The layered structure consists of two dielectric layers backed by a perfectly conducting infinite ground plane. This is exactly the same structure as discussed in chapter 2, section 2.2. Therefore, the notation introduced in section 2.2 will also be used here. From a practical point of view, we may assume that both patches are situated within region 2,

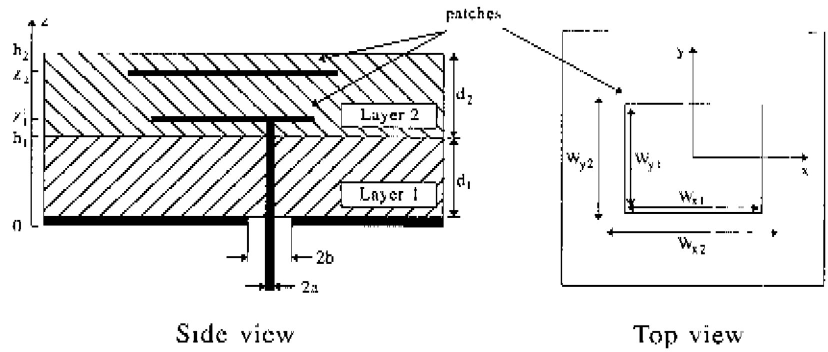

Figure 3.1: *Geometry of an isolated stacked microstrip antenna embedded in a two-layer dielectric structure.*

so $h_1 \leq z_1' \leq z_2' \leq h_2$. The x- and y-dimensions of the lower patch (located at $z = z_1'$) are denoted by W_{x1} and W_{y1}, respectively, and the x- and y-dimensions of the upper patch (located at $z = z_2'$) are denoted by W_{x2} and W_{y2}. Both patches are treated as perfect electric conductors and are assumed to be infinitely thin. The centres of both patches are located at $(x, y) = (0, 0)$. The feeding coaxial cable consists of an inner conductor with radius a and an outer conductor with radius b. The centre of the coaxial cable is located at (x_s, y_s). The inner conductor (also called probe) is usually connected to the lower patch and the outer conductor is connected to the ground plane. Another possible feeding structure that will be studied in this thesis is shown in figure 3.2. Now, the inner conductor of the coaxial cable is not physically connected to the lower patch, i.e., $z_P < z_1'$. This so-called electromagnetically coupled (EMC) microstrip structure has broadband characteristics if the dimensions of the antenna are chosen properly (see section 3.9).

3.2.2 Thin-substrate model

Microstrip antennas, for which the patches are printed on an electrically thin substrate, have a high quality factor, and therefore have a very small frequency bandwidth. If the distance between the lower patch and the ground plane is small compared to the wavelength in the substrate, i.e., if $z_1' \ll \lambda$, we may assume that the current distribution along the coaxial probe is constant. The

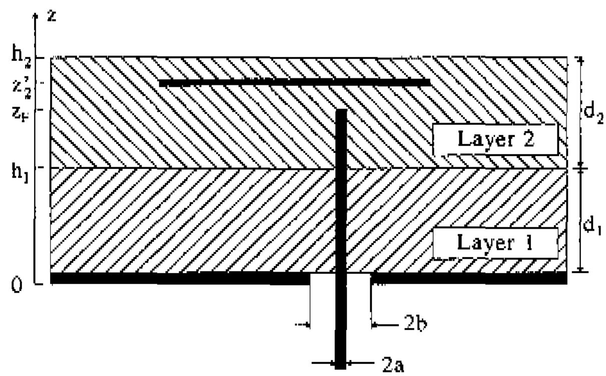

Figure 3.2: *Electromagnetically coupled (EMC) microstrip antenna.*

probe is represented by a cylinder with radius a. The z-independent current distribution on this cylinder is then given by

$$\begin{aligned} \vec{J}^{tot}_{probe}(x, y, z) &= I^p \vec{J}_{probe}(x, y, z) \\ &= \vec{e}_z \frac{I^p}{2\pi a} \delta\left(\sqrt{(x - x_s)^2 + (y - y_s)^2} - a\right), \quad 0 \leq z \leq z'_1, \end{aligned} \tag{3.1}$$

where I^p is the port current at $z = 0$ and z_F is the length of the coaxial probe. This current distribution is now used as a source exciting the two metallic patches of the antenna. Note that this model only works well if the probe is connected to the lower patch. Therefore, the configuration of figure 3.2 cannot be analysed with this simple source model. This thin-substrate source model has been often used succesfully in literature to analyse microstrip antennas [5, 28, 56], because most of these microstrip antennas are narrow-banded and therefore have a relative thin substrate. Microstrip antennas with a large bandwidth are usually fabricated on electrically thick substrates. This means that the simple source model, represented by formula (3.1), cannot be used any more, because the current distribution along the probe will not be constant. A second major drawback of the simple constant-current source model is the fact that the condition of continuity of current at the probe-patch transition is not fulfilled. A better and more general source model is presented in the next section.

3.2.3 Thick-substrate model

Figure 3.3 shows a detailed view of the feeding coaxial cable. The inner conductor of this cable is represented by a cylinder with radius a with perfectly conducting walls. It is assumed that

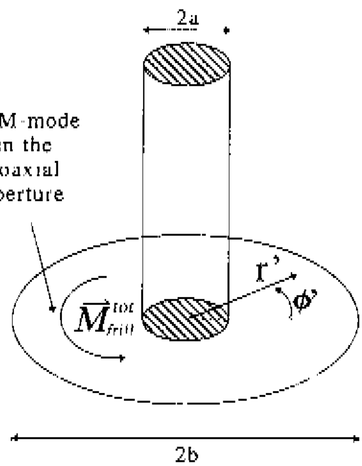

Figure 3.3: *Detailed view of the feeding coaxial structure.*

the z-directed surface current on the cylinder does not depend on the angular coordinate φ. This surface current is unknown and will be determined with the same procedure as the currents on both patches (see section 3.3). Further, a special attachment mode will be used to ensure the continuity of current at the probe-patch transition (see section 3.4). The electric field in the coaxial aperture at $z = 0$, act as a source exciting the antenna, i.e., the probe and the two patches.

From the analysis of wire antennas it was concluded that at frequencies for which $kb < 0.1$, with $k = 2\pi f \sqrt{\varepsilon \mu_0}$, accurate results are obtained if the field at the coaxial aperture is approximated by the fundamental mode only, i.e., the TEM-mode [54, p. 35]. The electric field of the TEM-mode in the coaxial cable is the same as the electric field of the corresponding electrostatic problem for the coaxial cable [32, p. 63]. When higher-order modes are neglected, the electric field in the aperture of the coaxial cable at $z = 0$ is given by

$$\vec{\mathcal{E}}_r(r') \approx \vec{\mathcal{E}}_{r,TEM}(r') = \frac{V^p}{r' \ln(b/a)} \vec{e}_{r'}, \quad a \le r' \le b, \tag{3.2}$$

where $\vec{r}' = \vec{r} - \vec{r}_s = (r' \cos\phi', r' \sin\phi', 0)$, with $\vec{r}_s = (x_s, y_s, 0)$. V^p is the impressed port voltage between the inner and outer conductor of the coaxial cable. So for a given port voltage V^p, we have to determine the corresponding port current I^p. From the equivalence principle [32, p. 111] it follows that the original problem of figure 3.4a can be replaced by the equivalent problem of figure 3.4b. In figure 3.4b a surface magnetic current $\vec{\mathcal{M}}_{frill}^{tot}$ is placed at the former coaxial opening, immediately above an infinite ground plane. The approximated magnetic current

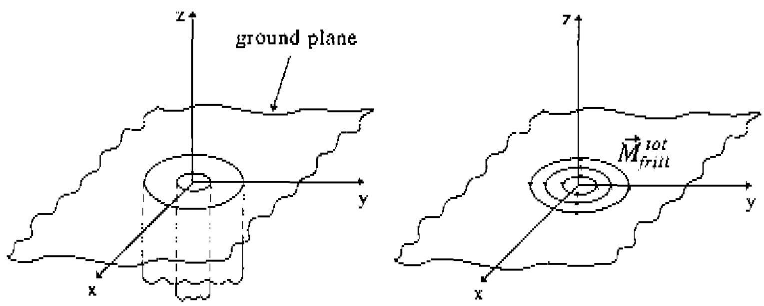

a) original problem *b) equivalent problem*

Figure 3.4. *Equivalent magnetic surface current at the coaxial opening.*

distribution at the coaxial opening is now given by

$$\vec{\mathcal{M}}^{tot}_{frill}(r) = \vec{\mathcal{M}}_{frill}(r)V^p = \vec{\mathcal{E}}_r(r) \times \vec{e}_z = -\frac{V^p}{r' \ln(b/a)}\vec{e}_{\phi'}, \quad a \leq r' \leq b \tag{3.3}$$

In the literature this source model is often called the "magnetic frill excitation model" [54, p. 35].

3.3 Method-of-moments formulation

In this section the thick-substrate source model of section 3.2.3 will be used. The magnetic current distribution (3.3) in the coaxial aperture is used as a source. The current distribution on the probe and on both patches of the microstrip antenna are the unknown quantities that have to be determined. At the end of this section the equations for the case of the thin-substrate model of section 3.2.2 are given. The boundary conditions on the two patches and on the coaxial probe are used to formulate a system of integral equations for the unknown current distribution $\vec{\mathcal{J}}$ on the antenna. These integral equations are solved by applying the method of moments [31]. We will start with the boundary condition that on both patches and on the probe the total tangential electric field has to vanish

$$\vec{e}_\nu \times \vec{\mathcal{E}}^{tot}(\vec{r}) = \vec{e}_\nu \times (\vec{\mathcal{E}}^{ex}(\vec{r}) + \vec{\mathcal{E}}^{s}(\vec{r})) = \vec{0}, \quad \vec{r} \epsilon S_0, \tag{3.4}$$

in which the surface S_0 denotes the surface of the patches and the probe and where $\vec{E}^{ex}(\vec{r})$ and $\vec{E}^{s}(\vec{r})$ represent the excitation field and the scattered field, respectively, and where $\vec{e}_\nu$ is the unit normal vector on the metallic surface under consideration. The scattered field results from the induced currents on both patches and on the probe. The excitation field is the electric field due to the magnetic current distribution in the coaxial aperture at $z = 0$. The scattered field can be expressed in terms of the unknown current distribution $\vec{\mathcal{J}}$ and the dyadic Green's function $\bar{\bar{\mathcal{G}}}$ by using relations (2.6) and (2.9). Equation (3.4) then takes the following form

$$\begin{aligned} \vec{e}_\nu \times \vec{E}^{ex}(\vec{r}) &= \vec{e}_\nu \times j\omega\mu \iint \bar{\bar{\mathcal{G}}}(\vec{r}, \vec{r}_0) \cdot \vec{\mathcal{J}}(\vec{r}_0) dS_0 \\ &\quad + \vec{e}_\nu \times \nabla \left(\frac{j\omega\mu}{k^2} \nabla \cdot \iint \bar{\bar{\mathcal{G}}}(\vec{r}, \vec{r}_0) \cdot \vec{\mathcal{J}}(\vec{r}_0) dS_0 \right), \vec{r} \epsilon S_0 \end{aligned} \tag{3.5}$$

Integral equation (3.5) can be solved numerically with the method of moments. The first step in the method of moments is the expansion of the unknown currents into a set of basis functions:

$$\vec{\mathcal{J}}(x, y, z) = \sum_n I_n \vec{\mathcal{J}}_n(x, y, z), \tag{3.6}$$

where I_n are mode coefficients that have to be determined. $\vec{\mathcal{J}}_n(x, y, z)$ is called a basis function or mode. If one wants to obtain an exact solution for the current distribution on the antenna, (3.6) has to be an infinite summation and the set of basis functions have to form a complete set. In practice, the summation in (3.6) is truncated at a maximum value $n = N_{max}$ and thus an approximation of the exact solution is obtained. The current distribution on the patches and on the probe is now given by

$$\begin{aligned} \vec{\mathcal{J}}(x, y, z) &= \sum_n^{N_{max}} I_n \vec{\mathcal{J}}_n(x, y, z) \\ &= I_1 \vec{\mathcal{J}}^a(x, y, z) + \sum_{n=2}^{N_z+1} I_n \vec{\mathcal{J}}_n^f(x, y, z) \\ &\quad + \sum_{n=N_z+2}^{1+N_z+N_1+N_2} I_n \vec{\mathcal{J}}_n^p(x, y, z_n), \end{aligned} \tag{3.7}$$

with

$$z_n = \begin{cases} z_1', & \text{if } N_z + 2 \le n \le N_z + 1 + N_1, \\ z_2', & \text{if } n > N_z + 1 + N_1, \end{cases}$$

where the basis function $\vec{\mathcal{J}}^a(x,y,z)$ represents the attachment mode at the transition between the probe and the lower patch, $\vec{\mathcal{J}}_n^f(x,y,z)$ is a basis function on the feeding coaxial probe and $\vec{\mathcal{J}}_n^p(x,y,z_n)$ is a basis function on one of the patches. An attachment mode is used to ensure continuity of current along the patch-probe transition. More details about this attachment mode will be given in section 3.4.3. There are N_z basis functions on the probe, N_1 basis functions on the lower patch and N_2 basis functions on the upper patch and there is 1 attachment mode. The total number of basis functions is therefore $N_{max} = 1 + N_z + N_1 + N_2$. More details about the type of basis functions that we will use are given in section 3.4. The scattered electric field $\vec{\mathcal{E}}^s(x,y,z)$ can be expressed in terms of the current distribution $\vec{\mathcal{J}}(x,y,z)$

$$\vec{\mathcal{E}}^s(x,y,z) = L\{\vec{\mathcal{J}}(x,y,z)\}, \tag{3.8}$$

where L is a linear operator. Combining (3.8) with (3.7) gives

$$\vec{\mathcal{E}}^s(x,y,z) = \sum_{n=1}^{N_{max}} I_n L\{\vec{\mathcal{J}}_n(x,y,z)\} = \sum_{n=1}^{N_{max}} I_n \vec{\mathcal{E}}_n^s(x,y,z) \tag{3.9}$$

Substituting the expansion (3.9) in equation (3.4) gives

$$\vec{e}_\nu \times \left(\sum_{n=1}^{N_{max}} I_n \vec{\mathcal{E}}_n^s(x,y,z) + \vec{\mathcal{E}}^{ex}(x,y,z) \right) = \vec{0} \quad , \tag{3.10}$$

on each patch and probe. Now, we introduce a residue according to

$$\vec{R}(x,y,z) = \vec{e}_\nu \times \left(\sum_{n=1}^{N_{max}} I_n \vec{\mathcal{E}}_n^s(x,y,z) + \vec{\mathcal{E}}^{ex}(x,y,z) \right) \tag{3.11}$$

This residue has to be zero at all points of the two patches and on the probe. This condition will be relaxed somewhat. The residue is *weighted* to zero with respect to some weighting functions $\vec{\mathcal{J}}_m(x,y,z)$, such that

$$(\vec{R}\,;\,\vec{\mathcal{J}}_m) = \iint_{S_m} \vec{R}(x,y,z)\cdot\vec{\mathcal{J}}_m(x,y,z)\,dS = 0 \quad , \tag{3.12}$$

for $m = 1,2,\ldots,N_{max}$, where S_m is the surface on which the weighting function $\vec{\mathcal{J}}_m$ is nonzero. Note that the set of weighting functions, also called test functions, is the same as the set of expansion functions. This particular choice is known as Galerkin's method [31]. Inserting (3.11) into (3.12) gives a set of linear equations

$$\sum_{n=1}^{N_{max}} I_n \iint_{S_m} \vec{\mathcal{E}}_n^s(x,y,z)\cdot\vec{\mathcal{J}}_m(x,y,z)\,dS + \iint_{S_m} \vec{\mathcal{E}}^{ex}(x,y,z)\cdot\vec{\mathcal{J}}_m(x,y,z)\,dS = 0, \tag{3.13}$$

for $m = 1, 2, \ldots, N_{max}$. This set of linear equations can be written in the more compact form

$$\sum_{n=1}^{N_{max}} I_n Z_{m\,n} + V_m^{ex} V^p = 0, \tag{3.14}$$

for $m = 1, 2, \ldots, N_{max}$. In matrix notation we get.

$$[Z][I] + [V^{ex}]V^p = [0], \tag{3.15}$$

in which V^p is the input port voltage at the base of the coaxial cable and where the elements of the matrices $[Z]$ and $[V^{ex}]$ are given by

$$\begin{aligned}
Z_{m\,n} &= 4\pi^2 \iint_{S_m} \vec{\mathcal{E}}_n^s(x, y, z) \cdot \vec{\mathcal{J}}_m(x, y, z)\, dS, \\
V_m^{ex} &= \frac{4\pi^2}{V^p} \iint_{S_m} \vec{\mathcal{E}}^{ex}(x, y, z) \cdot \vec{\mathcal{J}}_m(x, y, z)\, dS \\
&= -4\pi^2 \iint_{frill} \vec{\mathcal{H}}_m^s(x, y, 0) \cdot \vec{\mathcal{M}}_{frill}(x, y, 0)\, dx dy,
\end{aligned} \tag{3.16}$$

where the reaction concept [59] was used to rewrite V_m^{ex}. $\vec{\mathcal{M}}_{frill}(x, y, 0)$ is the magnetic current distribution in the coaxal aperture given by expression (3.3). The matrix $[Z]$ contains $N_{max} \times N_{max}$ elements, $[I]$ is a vector containing the N_{max} unknown mode coefficients and $[V^{ex}]$ is the excitation vector with N_{max} elements. If an expansion of the form (3.7) is used, the method-of-moments matrix $[Z]$ and the excitation vector $[V^{ex}]$ have the following structure

$$[Z] = \begin{pmatrix} Z^{aa} & [Z^{af}] & [Z^{ap}] \\ [Z^{fa}] & [Z^{ff}] & [Z^{fp}] \\ [Z^{pa}] & [Z^{pf}] & [Z^{pp}] \end{pmatrix}, \tag{3.17}$$

and

$$[V^{ex}] = \begin{pmatrix} V^{ex\,a} \\ [V^{ex\,f}] \\ [V^{ex\,p}] \end{pmatrix}, \tag{3.18}$$

where the superscript a denotes the attachment mode, f a basis function on the coaxial probe (feed) and p a basis function on one of the patches. $[Z]$ is a symmetrical matrix, because Galerkin's method is used, i.e., the expansion functions and test functions are identical. In chapter 2 of this thesis a closed-form expression was derived for the spectral-domain dyadic Green's function in a grounded two-layer configuration. Therefore, we will express the elements of $[Z]$ and $[V^{cx}]$ in terms of this spectral-domain Green's function. If we look for example at an element of the submatrix $[Z^{pp}]$, i.e., expansion and test function pertaining to the surface current on one of the patches, we get

$$\begin{aligned}
Z^{pp}_{m\,n} &= 4\pi^2 \iint_{S_m} \vec{E}^{s}_{n}(x,y,z_m) \cdot \vec{J}^{p}_{m}(x,y,z_m)\, dx dy \\
&= 4\pi^2 \iint_{S_m} \left[\frac{1}{4\pi^2} \int_{-\infty}^{\infty}\int_{-\infty}^{\infty} \bar{\bar{Q}}^{E}_{2}(k_x,k_y,z_m,z_n) \cdot \tilde{J}^{p}_{n}(k_x,k_y,z_n) \right. \\
&\qquad \left. e^{-jk_x x} e^{-jk_y y} dk_x dk_y \right] \cdot \vec{J}^{p}_{m}(x,y,z_m) dx\, dy \\
&= \int_{-\infty}^{\infty}\int_{-\infty}^{\infty} \left[\bar{\bar{Q}}^{E}_{2}(k_x,k_y,z_m,z_n) \cdot \tilde{J}^{p}_{n}(k_x,k_y,z_n) \right] \\
&\qquad \cdot \left[\iint_{S_m} \vec{J}^{p}_{m}(x,y,z_m) e^{-jk_x x} e^{-jk_y y} dx dy \right] dk_x dk_y \\
&= \int_{-\infty}^{\infty}\int_{-\infty}^{\infty} \left[\bar{\bar{Q}}^{E}_{2}(k_x,k_y,z_m,z_n) \cdot \tilde{J}^{p}_{n}(k_x,k_y,z_n) \right] \cdot \tilde{J}^{p*}_{m}(k_x,k_y,z_m) dk_x dk_y,
\end{aligned} \tag{3.19}$$

with

$$z_m = \begin{cases} z_1', & \text{if domain } m \text{ is located on the lower patch,} \\ z_2', & \text{if domain } m \text{ is located on the upper patch,} \end{cases}$$

in which $\tilde{J}^{p}_{m}(k_x,k_y,z_m)$ is the Fourier transform of the m-th basis function on the patch located at $z = z_m$ and where $\bar{\bar{Q}}^{E}_{2}(k_x,k_y,z,z_0)$ is the electric-field dyadic Green's function in the spectral domain, given by (2.59). The definition of the Fourier transformation is given in (2.21). Only real-valued basis functions will be used, so $\vec{J}^{p*}_{m}(x,y,z) = \vec{J}^{p}_{m}(x,y,z)$, where $\vec{J}^{p*}_{m}(x,y,z)$ denotes the complex conjugate of $\vec{J}^{p}_{m}(x,y,z)$. The other elements of the method-of-moments matrix $[Z]$

can also be expressed in terms of the spectral-domain electric-field Green's function $\bar{\bar{Q}}_{\nu}^{E}$:

$$
\begin{aligned}
Z^{aa} &= \int_{-\infty}^{\infty}\int_{-\infty}^{\infty}\int_{0}^{z_1'}\int_{0}^{z_1}\left[\bar{\bar{Q}}_{\nu}^{E}(k_x,k_y,z,z_0)\cdot\vec{J}^{a}(k_x,k_y,z_0)\right]dz_0\cdot\vec{J}^{a*}(k_x,k_y,z)dz\,dk_x\,dk_y,\\
Z_{m}^{fa} &= \int_{-\infty}^{\infty}\int_{-\infty}^{\infty}\int_{0}^{z_1'}\int_{0}^{z_1}\left[\bar{\bar{Q}}_{\nu}^{E}(k_x,k_y,z,z_0)\cdot\vec{J}^{a}(k_x,k_y,z_0)\right]dz_0\cdot\vec{J}_{m}^{f*}(k_x,k_y,z)dz\,dk_x\,dk_y,\\
Z_{mn}^{ff} &= \int_{-\infty}^{\infty}\int_{-\infty}^{\infty}\int_{0}^{z_1'}\int_{0}^{z_1}\left[\bar{\bar{Q}}_{\nu}^{E}(k_x,k_y,z,z_0)\cdot\vec{J}_{n}^{f}(k_x,k_y,z_0)\right]dz_0\cdot\vec{J}_{m}^{f*}(k_x,k_y,z)dz\,dk_x\,dk_y, \qquad (3.20)\\
Z_{m}^{pa} &= \int_{-\infty}^{\infty}\int_{-\infty}^{\infty}\int_{0}^{z_1}\left[\bar{\bar{Q}}_{2}^{E}(k_x,k_y,z_m,z_0)\cdot\vec{J}^{a}(k_x,k_y,z_0)\right]dz_0\cdot\vec{J}_{m}^{p*}(k_x,k_y,z_m)dk_x\,dk_y,\\
Z_{mn}^{pf} &= \int_{-\infty}^{\infty}\int_{-\infty}^{\infty}\int_{0}^{z_1}\left[\bar{\bar{Q}}_{2}^{E}(k_x,k_y,z_m,z_0)\cdot\vec{J}_{n}^{f}(k_x,k_y,z_0)\right]dz_0\cdot\vec{J}_{m}^{p*}(k_x,k_y,z_m)dk_x\,dk_y,
\end{aligned}
$$

with

$$
\nu = \begin{cases} 1 & \text{if } 0 \le z \le h_1,\\ 2, & \text{if } h_1 < z < h_2, \end{cases}
$$

In (3.20) $\vec{J}^{a}(k_x,k_y,z)$ is the Fourier transform of the attachment mode and $\vec{J}_{n}^{f}(k_x,k_y,z)$ represents the Fourier transform of the n-th basis function on the probe. The integrations over z and z_0 in (3.20) can be carried out analytically. Furthermore, it can be shown that the two-dimensional integral over k_x and k_y in Z^{aa}, Z_{m}^{fa} and Z_{mn}^{ff} can be reduced to a single, one dimensional integral. More details can be found in section 3.5 and appendix A. The elements of the excitation vector $[V^{ex}]$ can be expressed in terms of the spectral-domain magnetic-field Green's function $\bar{\bar{Q}}_{1}^{H}$:

$$
\begin{aligned}
V^{exa} &= -4\pi^2 \iint_{frill} \vec{H}_{a}^{*}(x,y,0)\cdot\vec{\mathcal{M}}_{frill}(x,y,0)\,dx\,dy\\
&= -4\pi^2 \iint_{frill}\left[\frac{1}{4\pi^2}\int_{-\infty}^{\infty}\int_{-\infty}^{\infty}\int_{0}^{z_1}\bar{\bar{Q}}_{1}^{H}(k_x,k_y,0,z_0)\cdot\vec{J}^{a}(k_x,k_y,z_0)dz_0\right.\\
&\qquad\left. e^{-jk_x x - jk_y y}dk_x dk_y\right]\cdot\vec{\mathcal{M}}_{frill}(x,y,0)dx\,dy\\
&= \int_{-\infty}^{\infty}\int_{-\infty}^{\infty}\left[\int_{0}^{z_1'}\bar{\bar{Q}}_{1}^{H}(k_x,k_y,0,z_0)\cdot\vec{J}^{a}(k_x,k_y,z_0)dz_0\right]\cdot\vec{M}_{frill}^{*}(k_x,k_y)dk_x\,dk_y \qquad (3.21)
\end{aligned}
$$

$$V_m^{ex,f} = -\int_{-\infty}^{\infty}\int_{-\infty}^{\infty}\left[\int_0^{z_1}\bar{\bar{Q}}_1^H(k_x,k_y,0,z_0) \quad \vec{J}_m^I(k_x,k_y,z_0)dz_0\right]\cdot \vec{M}_{frill}^*(k_x,k_y)dk_xdk_y,$$
$$V_m^{ex,p} = -\int_{-\infty}^{\infty}\int_{-\infty}^{\infty}\left[\bar{\bar{Q}}_1^H(k_x,k_y,0,z_m) \quad \vec{J}_m^p(k_x,k_y,z_m)\right]\cdot \vec{M}_{frill}^*(k_x,k_y)dk_xdk_y,$$

where $\vec{M}_{frill}(k_x, k_y)$ is the Fourier transform of the magnetic current distribution in the coaxial aperture of the antenna, given by

$$\begin{aligned}\vec{M}_{frill}(k_x,k_y) = \quad \vec{M}_{frill}(\beta,\alpha) = \frac{2\pi j}{k_0\beta\ln(b/a)}\left[J_0(k_0\beta b) - J_0(k_0\beta a)\right] \\ e^{jk_0\beta\cos\alpha x_s} e^{jk_0\beta\sin\alpha y_s}\left\{-\vec{e}_x\sin\alpha + \vec{e}_y\cos\alpha\right\}\end{aligned} \tag{3.22}$$

In (3.22) a transformation to cylindrical coordinates has been introduced with $k_x = k_0\beta\cos\alpha$ and $k_y = k_0\beta\sin\alpha$. $J_0(x)$ is the Bessel function of the first kind of order 0. Two of the three integrations in $V^{ex,a}$ and $V_m^{ex,f}$ can be carried out in closed form (see 3.5 and appendix B).
If the thin-substrate model of section 3.2.2 is used, no attachment mode and no basis functions on the probe are used. In this case the matrix $[Z]$ reduces to

$$[Z] = [Z^{pp}], \tag{3.23}$$

where the elements of $[Z^{pp}]$ are given by (3.19). In this case the method-of-moments matrix equation takes the form

$$[Z][I] + [V_i^{ex}]I^p = [0], \tag{3.24}$$

where I^p is the input port current. The excitation vector $[V_i^{ex}]$ differs from (3.21), because now an electric current source is used instead of a magnetic current source. Let $\vec{\mathcal{E}}^{ex}$ be the electric field due to the constant current source on the probe. Then from (3.16) we obtain

$$\begin{aligned}V_{i,m}^{ex} &= \frac{4\pi^2}{I^p}\iint \vec{\mathcal{E}}^{ex}(x,y,z_m) \quad \vec{\mathcal{J}}_m(x,y,z_m)\,dxdy \\ &= 4\pi^2\iiint_{probe} \vec{\mathcal{E}}_m^*(x,y,z)\cdot\vec{\mathcal{J}}_{probe}(x,y,z)\,dxdydz,\end{aligned} \tag{3.25}$$

where, again, the reaction concept was used in (3.25), and where $\vec{\mathcal{J}}_{probe}(x,y,z)$ is given by (3.1). Again the elements of $[V_\ell^{ex}]$ can be expressed in terms of the spectral-domain Green's function

$$
\begin{aligned}
V^{ex}_{\ell m} &= 4\pi^2 \iiint_{probe} \vec{\mathcal{E}}^{s}_{m}(x,y,z) \cdot \vec{\mathcal{J}}_{probe}(x,y,z)\, dx dy dz \\
&= 4\pi^2 \iiint_{probe} \left[\frac{1}{4\pi^2} \int_{-\infty}^{\infty} \int_{-\infty}^{\infty} \bar{\bar{Q}}^{k}_{\nu}(k_x,k_y,z,z_m) \cdot \vec{J}_m(k_x,k_y,z_m) \right. \\
&\qquad \left. e^{-jk_x x} e^{-jk_y y} dk_x dk_y \right] \cdot \vec{\mathcal{J}}_{probe}(x,y,z) dx dy dz \\
&= \int_{-\infty}^{\infty} \int_{-\infty}^{\infty} \left[\int_0^{z_l} \bar{\bar{Q}}^{k}_{\nu}(k_x,k_y,z,z_m) dz \cdot \vec{J}_m(k_x,k_y,z_m) \right] \cdot \vec{J}^{*}_{probe}(k_x,k_y) dk_x dk_y \\
&= \int_{-\infty}^{\infty} \int_{-\infty}^{\infty} \left[\int_0^{z_l} \bar{\bar{Q}}^{k}_{\nu}(k_x,k_y,z,z_m) dz \cdot \vec{J}_m(k_x,k_y,z_m) \right] \cdot \vec{e}_z \\
&\qquad J_0(a\sqrt{k_x^2+k_y^2}) e^{-jk_x x_s} e^{-jk_y y_s} dk_x dk_y,
\end{aligned}
\tag{3.26}
$$

with

$$
\nu = \begin{cases} 1, & \text{if } 0 < z \le h_1, \\ 2, & \text{if } h_1 < z < h_2, \end{cases}
$$

where $\vec{J}^{*}_{probe}(k_x,k_y)$ is the complex conjugate of the Fourier transform of the current distribution on the probe

$$
\vec{J}^{*}_{probe}(k_x,k_y) = \vec{e}_z J_0(a\sqrt{k_x^2+k_y^2}) e^{jk_x x_s} e^{jk_y y_s}
$$

3.4 Basis functions

In a method-of-moments procedure a proper choice of the set of basis functions is very important, because only a limited number of basis functions can be used due to the limited computer capacity. In general, two types of basis functions can be distinguished. The first type are the so-called entire-domain basis functions, which are non-zero over the entire domain of the unknown function. The second type are the subsectional or subdomain basis functions each of which exists only over a small subsection of the domain of the unknown function.

Subsectional basis functions are very flexible, so they could be used to analyse arbitrarily shaped microstrip antennas. A great disadvantage of subsectional basis functions, however, is the fact that they usually require a lot more computation time and computer memory than properly chosen entire domain basis functions. Normally, only a few entire-domain basis functions have to be used to obtain accurate results from a method-of-moments procedure. The latter is especially of great importance when arrays of microstrip antennas are considered (see chapter 4).

3.4.1 Basis functions on the patches

In this thesis it is assumed that the patches have a rectangular form. Other patch forms can, of course, be analysed with the same procedure as described in this thesis. The only difference is the set of basis functions that is employed. Several types of basis functions can be used to approximate the current distribution on the patches. We have studied three different types. In section 3.9 the results obtained with each type will be compared.

Entire-domain sinusoidal basis functions

This set of basis functions can be obtained from a cavity-model analysis of a microstrip antenna [10]. They form a complete and orthogonal set that exists on each patch of the antenna. The m-th x-directed basis function on the lower patch, with $(m = 1, \ldots, N_{x1})$, is given by

$$\vec{J}^{px}_{m}(x, y, z_1') = \vec{J}^{px}_{m_p m_q}(x, y, z_1') = \vec{e}_x \sin\left(\frac{m_p \pi}{W_{x1}}\left(x + \frac{W_{x1}}{2}\right)\right) \cos\left(\frac{m_q \pi}{W_{y1}}\left(y + \frac{W_{y1}}{2}\right)\right),$$
$$\text{with } |x| \leq \frac{W_{x1}}{2},\ |y| \leq \frac{W_{y1}}{2},\ m_p = 1, 2, \ldots,\ m_q = 0, 1, 2, \ldots, \tag{3.27}$$

and the m-th y-directed basis function on the lower patch, with $(m = N_{x1} + 1, \ldots, N_{x1} + N_{y1})$, is given by

$$\vec{J}^{py}_{m}(x, y, z_1') = \vec{J}^{py}_{m_p m_q}(x, y, z_1') = \vec{e}_y \cos\left(\frac{m_p \pi}{W_{x1}}\left(x + \frac{W_{x1}}{2}\right)\right) \sin\left(\frac{m_q \pi}{W_{y1}}\left(y + \frac{W_{y1}}{2}\right)\right),$$
$$\text{with } |x| \leq \frac{W_{x1}}{2},\ |y| \leq \frac{W_{y1}}{2},\ m_p = 0, 1, 2, \ldots,\ m_q = 1, 2, \ldots, \tag{3.28}$$

where for every m a certain combination (m_p, m_q) has to be chosen. Note that the total number of basis functions on the lower patch is equal to $N_1 = N_{x1} + N_{y1}$. On the upper patch at $z = z_2'$, a similar set of basis functions is used with W_{x1} and W_{y1} replaced by W_{x2} and W_{y2}, respectively, and z_1' replaced by z_2' in (3.27) and (3.28). Figure 3.5 shows the x-dependence of the first three x-directed basis functions of this set. The corresponding Fourier transforms of (3.27) and (3.28)

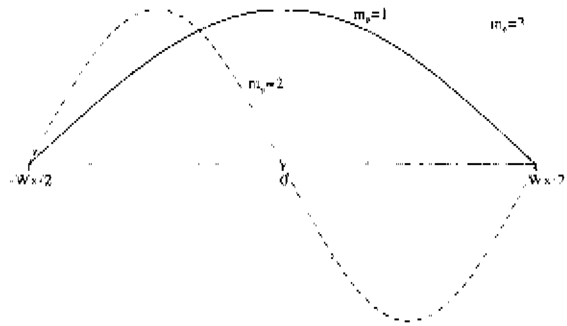

Figure 3.5 *x-dependence of x-directed entire-domain basis functions*

have the form

$$\begin{aligned}\vec{J}_m^{px}(k_x,k_y,z_1') &= \vec{J}_{m_p m_q}^{px}(k_x,k_y,z_1') = \vec{e}_x F_s(m_p,k_x,W_{x1})F_c(m_q,k_y,W_{y1}),\\ \vec{J}_m^{py}(k_x,k_y,z_1') &= \vec{J}_{m_p m_q}^{py}(k_x,k_y,z_1') = \vec{e}_y F_c(m_p,k_x,W_{x1})F_s(m_q,k_y,W_{y1}),\end{aligned} \tag{3.29}$$

with

$$F_s(m_p,k_x,W_{x1}) = \begin{cases} \dfrac{2m_p\pi W_{x1}\cos(k_xW_{x1}/2)}{(m_p\pi)^2-(k_xW_{x1})^2} & m_p \text{ odd},\\[2ex] \dfrac{-j2m_p\pi W_{x1}\sin(k_xW_{x1}/2)}{(m_p\pi)^2-(k_xW_{x1})^2} & m_p \text{ even},\end{cases}$$

and

$$F_c(m_q,k_y,W_{y1}) = \begin{cases} \dfrac{2jW_{y1}^2k_y\cos(k_yW_{y1}/2)}{(m_q\pi)^2-(k_yW_{y1})^2} & m_q \text{ odd},\\[2ex] \dfrac{-2W_{y1}^2k_y\sin(k_yW_{y1}/2)}{(m_q\pi)^2-(k_yW_{y1})^2} & m_q \text{ even}.\end{cases}$$

From convergence tests in [57] and from tests described in section 3.9 it became clear that by using a set of entire-domain basis functions with x-directed modes for which $m_q = 0$ and with y-directed modes for which $m_p = 0$, quite good results can be obtained for linearly polarised microstrip antennas. The other modes in (3.27) and (3.28) do not significantly improve the result. This sub-set of (3.27) and (3.28) is given by

$$\vec{\mathcal{J}}_m^{px}(x,y,z_1') = \vec{\mathcal{J}}_{m_p}^{px}(x,y,z_1') = \vec{e}_x \sin\left(\frac{m_p\pi}{W_{x1}}(x+\frac{W_{x1}}{2})\right), \tag{3.30}$$

$$\text{with } |x| \leq \frac{W_{x1}}{2},\ |y| \leq \frac{W_{y1}}{2},\ m=1,2,\ldots,N_{x1},\ m_p=1,2,\ldots,$$

and

$$\vec{\mathcal{J}}_m^{py}(x,y,z_1') = \vec{\mathcal{J}}_{m_q}^{py}(x,y,z_1') = \vec{e}_y \sin\left(\frac{m_q\pi}{W_{y1}}(y+\frac{W_{y1}}{2})\right), \tag{3.31}$$

$$\text{with } |x| \leq \frac{W_{x1}}{2},\ |y| \leq \frac{W_{y1}}{2},\ m=N_{x1}+1,\ldots,N_{x1}+N_{y1}\ m_q=1,2,\ldots$$

The Fourier transforms of these basis functions are given by

$$\begin{aligned}\tilde{J}_m^{px}(k_x,k_y,z_1') &= \tilde{J}_{m_p}^{px}(k_x,k_y,z_1') = \vec{e}_x F_s(m_p,k_x,W_{x1})F_c(0,k_y,W_{y1}),\\ \tilde{J}_m^{py}(k_x,k_y,z_1') &= \tilde{J}_{m_q}^{py}(k_x,k_y,z_1') = \vec{e}_y F_c(0,k_x,W_{x1})F_s(m_q,k_y,W_{y1}),\end{aligned} \tag{3.32}$$

$$\text{with } m_p=1,2,\ldots,\ m_q=1,2,\ldots$$

Entire-domain sinusoidal basis functions with edge conditions

The current normal to the edge of a patch behaves as $\sqrt{\Delta r}$ when the distance from the edge approaches zero, i.e., $\Delta r \rightarrow 0$. If the direction of current is parallel to the edge of the patch, the current behaves as $1/\sqrt{\Delta r}$ when the distance from the edge is nearly zero, i.e., $\Delta r \rightarrow 0$ [47]. It could be expected that when these edge conditions are explicitly included in the set of basis functions, a faster convergence of the method-of-moments procedure can be obtained. For that purpose, the set of basis functions given by (3.27) and (3.28) is modified with these edge conditions. The m-th x-directed basis function on the lower patch of this modified set, with $m=1,\ldots,N_{x1}$, is given by

$$\begin{aligned}\vec{\mathcal{J}}_m^{px}(x,y,z_1') &= \vec{\mathcal{J}}_{m_p m_q}^{px}(x,y,z_1')\\ &= \vec{e}_x \frac{\sin\left(\frac{m_p\pi}{W_{x1}}(x+\frac{W_{x1}}{2})\right)\cos\left(\frac{m_q\pi}{W_{y1}}(y+\frac{W_{y1}}{2})\right)}{\sqrt{1-(2x/W_{x1})^2}\sqrt{1-(2y/W_{y1})^2}},\end{aligned} \tag{3.33}$$

$$\text{with } |x| \leq \frac{W_{x1}}{2},\ |y| \leq \frac{W_{y1}}{2},\ m_p=1,2,\ldots,\ m_q=0,1,2,\ldots,$$

and the m-th y-directed basis function on the lower patch, with ($m = N_{x1}+1, \ldots, N_{x1}+N_{y1}$), is given by

$$
\begin{aligned}
\vec{J}^{1y}_m(x,y,z_1') &= \vec{J}^{py}_{m_pm_q}(x,y,z_1') \\
&= \vec{c}_y \frac{\cos\left(\frac{m_p\pi}{W_{x1}}(x+\frac{W_{x1}}{2})\right)\sin\left(\frac{m_q\pi}{W_{y1}}(y+\frac{W_{y1}}{2})\right)}{\sqrt{1-(2x/W_{x1})^2}\sqrt{1-(2y/W_{y1})^2}},
\end{aligned}
\tag{3.34}
$$

with $|x| \leq \frac{W_{x1}}{2}$, $|y| \leq \frac{W_{y1}}{2}$, $m_p = 0,1,2,\ldots$, $m_q = 1,2,\ldots$

A similar set of basis functions is used on the upper patch. The Fourier transform of (3.33) and (3.34) can be evaluated analytically as a sum of two zero-order Bessel functions of the first kind:

$$
\begin{aligned}
\tilde{J}^{1x}_m(k_x,k_y,z_1') &= \tilde{J}^{px}_{m_pm_q}(k_x,k_y,z_1') = \vec{c}_x F^{ed}_s(m_p,k_x,W_{x1})F^{ed}_c(m_q,k_y,W_{y1}), \\
\tilde{J}^{1y}_m(k_x,k_y,z_1') &= \tilde{J}^{py}_{m_pm_q}(k_x,k_y,z_1') = \vec{c}_y F^{ed}_c(m_p,k_x,W_{x1})F^{ed}_s(m_q,k_y,W_{y1}),
\end{aligned}
\tag{3.35}
$$

with

$$
F^{ed}_s(m_p,k_x,W_{x1}) = \begin{cases} \frac{\pi W_{x1}\epsilon^o_{m_p}}{4}\left\{J_0\left(\frac{m_p\pi}{2}+\frac{k_xW_{x1}}{2}\right)+J_0\left(\frac{m_p\pi}{2}-\frac{k_xW_{x1}}{2}\right)\right\} & m_p \text{ odd}, \\ \frac{j\pi W_{x1}\epsilon^e_{m_p}}{4}\left\{J_0\left(\frac{m_p\pi}{2}-\frac{k_xW_{x1}}{2}\right)-J_0\left(\frac{m_p\pi}{2}+\frac{k_xW_{x1}}{2}\right)\right\} & m_p \text{ even}, \end{cases}
$$

$$
F^{ed}_c(m_q,k_y,W_{y1}) = \begin{cases} \frac{j\pi W_{y1}\epsilon^o_{m_q}}{4}\left\{J_0\left(\frac{m_q\pi}{2}+\frac{k_yW_{y1}}{2}\right)-J_0\left(\frac{m_q\pi}{2}-\frac{k_yW_{y1}}{2}\right)\right\} & m_q \text{ odd}, \\ \frac{\pi W_{y1}\epsilon^e_{m_q}}{4}\left\{J_0\left(\frac{m_q\pi}{2}+\frac{k_yW_{y1}}{2}\right)+J_0\left(\frac{m_q\pi}{2}-\frac{k_yW_{y1}}{2}\right)\right\} & m_q \text{ even}, \end{cases}
$$

where $\epsilon^o_{m_p}$ and $\epsilon^e_{m_p}$ are given by

$$
\begin{aligned}
\epsilon^o_{m_p} &= (-1)^{(m_p-1)/2}, \\
\epsilon^e_{m_p} &= (-1)^{m_p/2}
\end{aligned}
$$

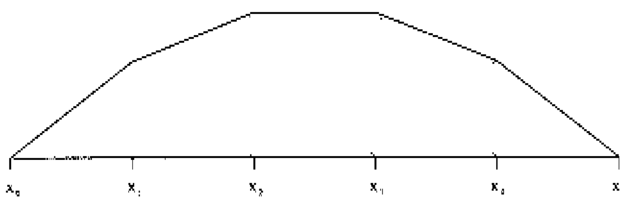

Figure 3.6 *Piecewise linear approximation of a function.*

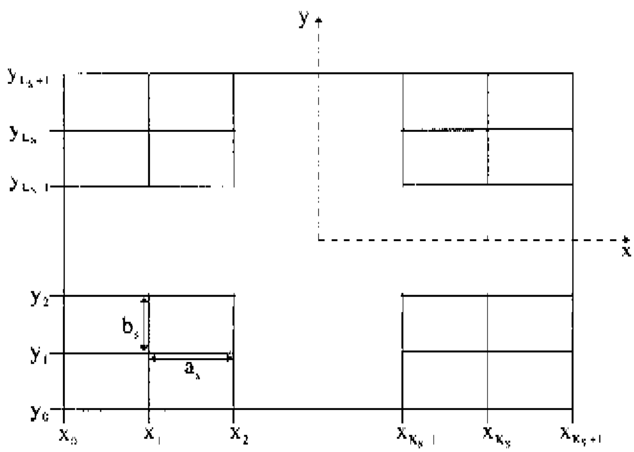

Figure 3.7 *Segmentation of the rectangular patch.*

Subsectional basis functions

With rooftop subsectional basis functions, a piecewise-linear approximation of a function can be obtained. Figure 3.6 shows an one-dimensional example of such an approximation. Figure 3.7 shows the segmentation into cells on one of the rectangular patches

The unknown currents on the patches are expanded in terms of overlapping piesewise-linear basis functions in the direction of current and in piecewise-constant functions in the direction orthogonal to the current, i.e., rooftop basis functions. On the lower patch we have N_{x1} x-directed basis functions and N_{y1} y-directed basis functions The Fourier transform of the m-th subsectional

x-directed rooftop basis function on the lower patch is given by ($m = 1, \ldots, N_{x1}$)

$$\tilde{J}^{px}_{m}(k_x, k_y, z_1') = \tilde{J}^{px}_{k_m l_m}(k_x, k_y, z_1')$$

$$= \vec{e}_x a_s b_s \mathrm{sinc}^2(k_x a_s/2)\mathrm{sinc}(k_y b_s/2) e^{jk_x x_{k_m}} e^{jk_y(y_{l_m}+y_{l_m-1})/2}, \tag{3.36}$$

with $k_m = 1, \ldots, K_s$ and $l_m = 1, \ldots, L_s + 1$,

and the Fourier transform of the m-th y-directed rooftop basis function on the lower patch is given by ($m = N_{x1} + 1, \ldots, N_{x1} + N_{y1} (= N_1)$)

$$\tilde{J}^{py}_{m}(k_x, k_y, z_1') = \tilde{J}^{py}_{k_m l_m}(k_x, k_y, z_1')$$

$$= \vec{e}_y a_s b_s \mathrm{sinc}(k_x a_s/2)\mathrm{sinc}^2(k_y b_s/2) e^{jk_x(x_{k_m-1}+x_{k_m})/2} e^{jk_y y_{l_m}}, \tag{3.37}$$

with $k_m = 1, \ldots, K_s + 1$ and $l_m = 1, \ldots, L_s$,

where basis function $\vec{\mathcal{J}}^{px}_m(x, y, z)$ is nonzero in the interval $x_{k_m-1} \leq x \leq x_{k_m+1}$ and $y_{l_m-1} \leq y \leq y_{l_m}$ and where $\vec{\mathcal{J}}^{py}_m(x, y, z)$ is nonzero in the interval $x_{k_m-1} \leq x \leq x_{k_m}$ and $y_{l_m-1} \leq y \leq y_{l_m+1}$ (see also figure 3.7). The dimensions of a subdomain in the x- and in the y-direction are equal to a_s and b_s, respectively. On the upper patch a similar set of basis functions can be used.

3.4.2 Basis functions on the coaxial probe

The coaxial probe is represented by a metallic cylinder with radius a with perfectly conducting walls. The current distribution on this metallic cylinder is expanded into a set of basis functions if the thick-substrate model of section 3.2.3 is used. Because the coaxial probe is very thin ($a \ll \lambda_0$), we may assume that the current distribution on the coaxial probe has only a z-directed component that depends solely on the z-coordinate. This z-directed current on the outer surface of the probe is expanded into a set of piecewise-linear (rooftop) basis functions. The m-th basis function of this set is given by

$$\vec{\mathcal{J}}^{I}_m(x, y, z) = \frac{1}{2\pi a}\delta\left(\sqrt{(x - x_s)^2 + (y - y_s)^2} - a\right) g_m(z)\vec{e}_z, \tag{3.38}$$

with

$$g_m(z) = \begin{cases} \frac{2}{h}(\frac{h}{2} - z), & m = 1, \quad 0 \leq z \leq \frac{h}{2}, \\ \frac{2}{h}(z - z_{m-1}), & m \geq 2, \quad z_{m-1} \leq z \leq z_m, \\ \frac{2}{h}(z_{m+1} - z), & m \geq 2, \quad z_m \leq z \leq z_{m+1}. \end{cases}$$

The first basis function at the base of the probe with $m = 1$, is a half rooftop function. In figure 3 8 the z-dependent part of the basis functions is shown. The total number of basis functions on the probe equals N_z

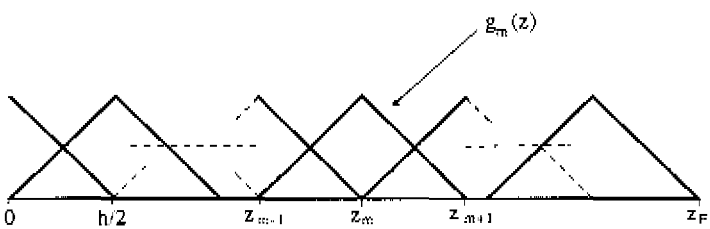

Figure 3 8: *Rooftop basis functions along the probe*

The Fourier transform of the m-th basis functions of this set is given by

$$\vec{J}^f_m(k_x, k_y, z) = \vec{e}_z J_0(a\sqrt{k_x^2 + k_y^2}) g_m(z) e^{jk_x x_s} e^{jk_y y_s}. \tag{3 39}$$

3.4.3 Attachment mode

The so-called attachment mode is a special basis function introduced to ensure continuity of the current at the transition from the probe to the lower patch. In addition, this mode describes the rapid variation of current on the lower patch near the connection point of the probe. The use of the attachment mode accelerates the convergence of the method-of-moments procedure. Note that the attachment mode is not needed if the EMC configuration of figure 3 2 is analysed, because in this case the inner conductor of the coaxial cable is not connected to the lower patch. The attachment mode is built up of two parts, namely a part on the lower patch and a part on the probe. The patch part of the attachment mode has a r^{-1} dependence near the patch-probe transition. On the probe, a half rooftop function is used. In formula form the attachment mode is given by:

$$\vec{J}^a(x, y, z) = \vec{J}^{ap}(x, y, z_1) + \vec{J}^{af}(x, y, z), \tag{3.40}$$

with

$$\vec{J}^{ap}(x,y,z_1') = \begin{cases} -\dfrac{r'}{2\pi b_a^2}\vec{e}_{r'}, & 0 \le r' \le a, \\ \left(-\dfrac{r'}{2\pi b_a^2} + \dfrac{1}{2\pi r'}\right)\vec{e}_{r'}, & a \le r' \le b_a, \\ 0, & r' \ge b_a, \end{cases}$$

and

$$\vec{J}^{af}(x,y,z) = \vec{e}_z \frac{1}{2\pi a}\delta\left(\sqrt{(x-x_s)^2+(y-y_s)^2} - a\right)\frac{2}{h}(z - z_1' + \frac{h}{2}),$$

$$\text{with} \quad z_1' - \frac{h}{2} \le z \le z_1',$$

where $\vec{r'} = (x - x_s, y - y_s, 0)$. A three-dimensional plot of the patch part of the attachment mode is shown in figure 3.9. A similar attachment mode (however, without a variation of current along the coaxial probe) was used in [53] for the analysis of circular microstrip antennas.

Tests in the literature [53, 63] show that excellent results can be obtained if b_a is chosen properly. The best results are obtained if $0.1\lambda \le b_a \le 0.2\lambda$, where λ is the wavelength in the medium of interest. A drawback of this attachment mode is the fact that it cannot be used if the probe connection is near the edge of the lower patch. In almost all practical microstrip configurations, however, this is not a severe problem, because the input impedance of an edge-fed microstrip antenna is very high and these configurations therefore have no practical interest. The Fourier transform of (3.40) is known in closed form and is given by

$$\tilde{J}^a(k_x,k_y,z) = \tilde{J}^{ap}(k_x,k_y,z_1') + \tilde{J}^{af}(k_x,k_y,z), \tag{3.41}$$

with

$$\tilde{J}^{ap}(k_x,k_y,z_1') = [\vec{e}_x\cos\alpha + \vec{e}_y\sin\alpha]e^{jk_xx_s}e^{jk_yy_s}\left\{\frac{-2jJ_1(k_0\beta b_a)}{b_ak_0^2\beta^2} + \frac{jJ_0(k_0\beta a)}{k_0\beta}\right\},$$

$$\tilde{J}^{af}(k_x,k_y,z) = \vec{e}_z J_0(k_0\beta a)e^{jk_xx_s}e^{jk_yy_s}\frac{2}{h}(z - z_1' + \frac{h}{2}), \quad z_1' - \frac{h}{2} < z < z_1,$$

where a transformation to cylindrical coordinates was introduced with $k_x = k_0\beta\cos\alpha$ and $k_y = k_0\beta\sin\alpha$. In the literature other attachment modes have also been studied. The attachment mode introduced by Pozar in [57] for the analysis of infinite arrays of microstrip antennas describes the variation of the current at the patch-probe transition more accurate, but is inefficient from a

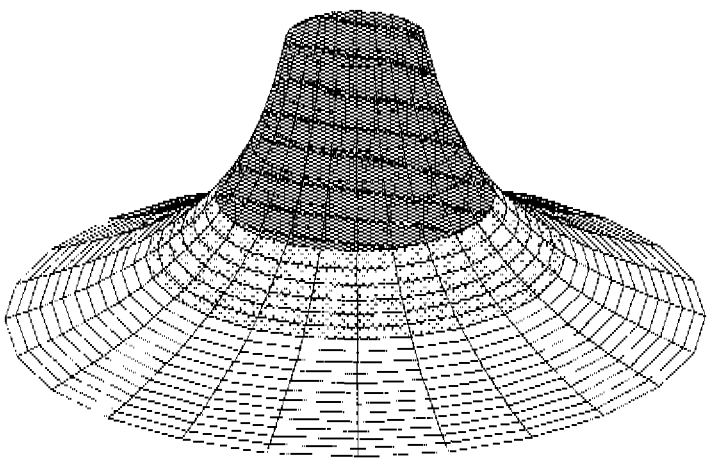

Figure 3.9. *Three dimensional representation of the patch-part of the attachment mode*

computational point of view, because it involves an infinite summation of cavity modes. Another disadvantage of this mode is the fact that it does not include a variation of current along the coaxial probe. This means that electrically thick microstrip antennas cannot be analysed properly with the mode of Pozar. In [30] another type of attachment mode is used, where the patch current near the probe-patch transition is approximated by means of a piecewise-linear function. Therefore, this mode does not account for the rapid variation of the patch current near the probe attachment.

3.5 Calculation of the method-of-moment matrix $[Z]$ and $[V^{ex}]$

The general structure of the method-of-moments matrix $[Z]$ is given by the expression (3.17) in the case where the thick-substrate model is used. Only 6 of the 9 submatrices need to be calculated, because of the symmetry in $[Z]$, i.e., $[Z^{af}] = [Z^{fa}]^T$, $[Z^{ap}] = [Z^{pa}]^T$ and $[Z^{fp}] = [Z^{pf}]^T$. The elements of the remaining six relevant submatrices can be calculated from (3.20) and (3.19). The submatrix $[Z^{aa}]$ has only one element, because there is only one attachment mode, $[Z^{fa}]$ is a vector with N_z elements, $[Z^{pa}]$ is a vector containing $N_1 + N_2$ elements, $[Z^{ff}]$ is a symmetric matrix with $N_z \times N_z$ elements, $[Z^{pf}]$ is a matrix with $(N_1 + N_2) \times N_z$ elements and finally $[Z^{pp}]$ is a symmetric matrix with $(N_1 + N_2) \times (N_1 + N_2)$ elements. The integrals in (3.20) and (3.19) can be simplified somewhat by introducing cylindrical coordinates:

$$k_x = k_0\beta\cos\alpha,$$
$$k_y = k_0\beta\sin\alpha, \tag{3.42}$$
$$\text{with } 0 \leq \beta \leq \infty \quad \text{and} \quad -\pi \leq \alpha \leq \pi.$$

When (3.42) is substituted in (3.20) and (3.19), it is possible to carry out the integration over α for the elements of Z^{aa}, $[Z^{fa}]$ and $[Z^{ff}]$ analytically. The α-integration interval of the other elements of the matrix $[Z]$, i.e., $[Z^{pa}]$, $[Z^{pf}]$ and $[Z^{pp}]$ can be reduced to the interval $[0, \frac{\pi}{2}]$. The integration over z and z_0 in (3.20) and (3.19) can be carried out analytically if rooftop basis functions on the probe are being used. The expressions for the elements of the matrix $[Z]$ are given in appendix A of this thesis. The resulting integrals in these expressions have to be evaluated numerically. The computational and numerical details are discussed in section 3.8, where some numerical and analytical techniques are introduced in order to calculate the elements of $[Z]$ and $[V^{ex}]$ with a computer program in an accurate and fast way.

The general structure of the excitation vector $[V^{ex}]$ is given by (3.18) when the thick-substrate model is used. It consists of three submatrices. Submatrix $[V^{ex,a}]$ has only one element, $[V^{ex,f}]$ contains N_z elements and $[V^{ex,p}]$ has $N_1 + N_2$ elements. The elements of $[V^{ex}]$ can be calculated from (3.21). Again a change to cylindrical coordinates (3.42) is introduced. The integration over α for $V^{ex,a}$ and for the elements of $[V^{ex,f}]$ can be carried out analytically and the α-integration interval for the elements of $[V^{ex,p}]$ can be reduced to the interval $[0, \frac{\pi}{2}]$. Again, the integrations over z and z_0 can be performed analytically if rooftop basis functions on the probe are used. The expressions for the elements of the vector $[V^{ex}]$ are given in appendix B of this thesis. In this appendix also the expressions for the elements of $[V_t^{ex}]$ are given if the thin-substrate model of section (3.2.2) is used.

3.6 Input impedance

As a result of the method-of-moments procedure, we obtain an approximation of the exact solution for the current distribution on the patches and on the coaxial probe. Engineers usually work with port currents and port voltages instead of current distributions or electric and magnetic fields. We will therefore represent the microstrip antenna by the one port of figure 3.10.

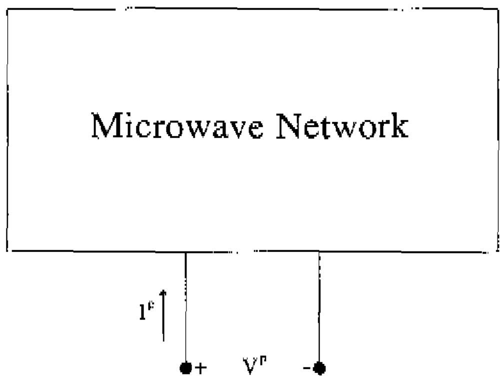

Figure 3.10: *One-port representation of an isolated microstrip antenna.*

The relation between the port current and the port voltage can be described in two ways:

$$V^p = Z_{\text{in}} I^p,$$
$$I^p = Y_{\text{in}} V^p, \tag{3.43}$$

where Z_{in} is the input impedance and Y_{in} is the input admittance. The relation between port current I^p and port voltage V^p can also be written in the following form [32, p. 96].

$$I^p = \frac{P_{\text{in}}^*}{V^{p*}}, \tag{3.44}$$

where P_{in} is the total complex power supplied by the sources. It is defined as

$$P_{\text{in}} = -\iiint \left(\vec{\mathcal{E}} \cdot \vec{\mathcal{J}}^*_{source} + \vec{\mathcal{H}}^* \cdot \vec{\mathcal{M}}_{source}\right) dV, \tag{3.45}$$

where $\vec{\mathcal{J}}_{source}$ and $\vec{\mathcal{M}}_{source}$ are the electric and magnetic current distibutions of the source, respectively. If we use the thick-substrate model of section 3.2.3, the source is a magnetic current distribution corresponding to the TEM-mode in the coaxial aperture. This magnetic current distribution is given by (3.3). Substituting this expression in (3.45) yields

$$I^p = \frac{P_{\text{in}}^{p*}}{V^{p*}} = -\iint_{feed} \vec{\mathcal{H}} \cdot \vec{\mathcal{M}}^*_{feed} dS \tag{3.46}$$

Note that $\vec{\mathcal{H}}$ is the total magnetic field due to the electric currents on both patches and due to the electric current on the probe. We may therefore write $\vec{\mathcal{H}}$ in terms of the mode coefficients I_m, with $m = 1, 2, \ldots, N_{mode}$:

$$\vec{\mathcal{H}} = I_1 \vec{\mathcal{H}}^a + \sum_{m=2}^{1+N_z} I_m \vec{\mathcal{H}}^f_m + \sum_{m=N_z+2}^{1+N_z+N_1+N_2} I_m \vec{\mathcal{H}}^p_m, \tag{3.47}$$

in which the supscript a refers to an attachment mode, f to a basis function on the coaxial probe (feed) and p to a basis function on one of the patches. If we substitute the above expansion of the magnetic field in (3.46) we get the relation

$$I^p = \frac{1}{4\pi^2}[V^{ex}]^T[I] = \frac{-1}{4\pi^2}[V^{ex}]^T[Z]^{-1}[V^{ex}]V^F, \tag{3.48}$$

where the matrix equation (3.15) has been used. The matrix $[Z]^{-1}$ is the inverse of the method-of-moments matrix $[Z]$ and $[V^{ex}]^T$ is the transpose of $[V^{ex}]$. Apparently, the input admittance can be calculated from

$$Y_{in} = \frac{I^p}{V^F} = \frac{-1}{4\pi^2}[V^{ex}]^T[Z]^{-1}[V^{ex}] \tag{3.49}$$

In the literature a different approach is sometimes used to calculate the input admittance [30], [54, p. 40]. One often uses the formula

$$Y_{in} = \frac{I(0)}{V^F}, \tag{3.50}$$

where $I(0)$ is the current at the base of the coaxial probe ($z = 0$), which can be determined by solving the matrix equation (3.15). Formula (3.50) can be derived from (3.49) if one uses the TEM approximation of the magnetic field in the coaxial opening:

$$\mathcal{H}_\phi(x, y, z) = \frac{I(0)}{2\pi\rho} \tag{3.51}$$

where ρ is the distance from the point (x, y, z) to the centre of the probe. The expression (3.50) is based on an approximation of both the electric and magnetic field at the coaxial aperture, whereas (3.49) is based on a TEM-approximation of the electric field, while the magnetic field is, essentially, assumed to contain higher-order modes. In the case of an electrically thick substrate, the approximation (3.50) gives fairly accurate results. However, from tests we have found that the relative difference between expressions (3.49) and (3.50) becomes very large ($> 20\%$) if the substrate of the antenna under consideration is electrically thin. To avoid errors, it is recommended to use expression (3.49). In addition, the overall computation time is not increased very much when (3.49) is used, because the inverse of $[Z]$ needs to be calculated anyway.

If the thin-substrate model of section 3.2.2 is used, the electric current distribution of the source, i.e., the constant current along the probe given by (3.1), is inserted into (3.45). The total electric field at the source is now expressed in terms of the mode coefficients I_m of the basis functions on the patches

$$\vec{\mathcal{E}}^p = \sum_{m=1}^{N_1+N_2} I_m \vec{\mathcal{E}}_m^p. \tag{3.52}$$

Substituting this expansion in (3.44) and (3.45) yields

$$V^p = \frac{-1}{4\pi^2}[V_t^{ex}]^T[I] = \frac{1}{4\pi^2}[V_t^{ex}]^T[Z]^{-1}[V_t^{ex}]I^p, \tag{3.53}$$

where the matrix equation (3.24) was used. Apparently, the input impedance is given by

$$Z_{\text{in}} = \frac{V^p}{I^p} = \frac{1}{4\pi^2}[V_t^{ex}]^T[Z]^{-1}[V_t^{ex}]. \tag{3.54}$$

At microwave frequencies one usually measures the reflection coefficient rather than the input impedance or the input admittance, because at higher frequencies it is easier to accurately measure the incident and reflected power quantities than to measure the impressed voltages and impressed currents. The incident power will usually remain constant under varying conditions, whereas it is very difficult to keep the impressed voltages or the impressed current constant [2, p. 51]. The reflection coefficient can be calculated by means of the well-known relation

$$R = \frac{Z_{\text{in}} - Z_0}{Z_{\text{in}} + Z_0}, \tag{3.55}$$

or

$$R = \frac{Y_0 - Y_{\text{in}}}{Y_0 + Y_{\text{in}}}, \tag{3.56}$$

in which $Z_0 = Y_0^{-1}$ is the characteristic impedance of the coaxial cable. Usually $Z_0 = 50\Omega$.

3.7 Radiation pattern

In addition to the port characteristics of antennas, one is usually also interested in the radiation pattern, since antennas are by definition made to radiate or receive electromagnetic power into/from free space. The method-of-moments procedure described in the previous sections, yields an approximation for the current distribution on the upper and lower patch and on the feeding coaxial probe. The easiest way to determine the far-field pattern is by using the equivalence principle. This means that the sources which are embedded in the grounded two-layer structure are replaced

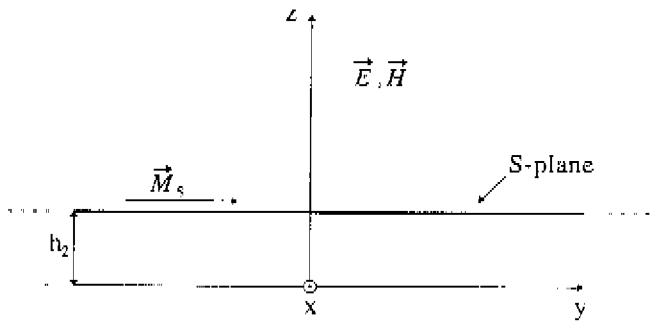

Figure 3.11: *Equivalent magnetic current source.*

by an equivalent electric and magnetic current distribution on the top surface S of the dielectric structure at $z = h_2$. Figure 3.11 shows the location of this surface S. These equivalent sources have to be chosen in such a way that the field above the plane S is equal to the field of the original problem, i.e., $\vec{\mathcal{E}},\vec{\mathcal{H}}$. We may postulate that the field in the region below the plane S is a null field. In this case the equivalent electric and magnetic sources on S must take the form

$$
\begin{aligned}
\vec{\mathcal{J}}_s(x,y,h_2) &= \vec{e}_z \times \vec{\mathcal{H}}(x,y,h_2), \\
\vec{\mathcal{M}}_s(x,y,h_2) &= \vec{\mathcal{E}}(x,y,h_2) \times \vec{e}_z,
\end{aligned}
\tag{3.57}
$$

where $\vec{\mathcal{H}}$ and $\vec{\mathcal{E}}$ are the magnetic and electric field of the original problem. This form of the equivalence principle is known as Love's equivalence principle [13, p. 35]. Since the field below S is a null field, we can place a perfectly conducting surface just below S. In this case the electric surface current $\vec{\mathcal{J}}_s$ vanishes. Therefore, the field above the perfectly conducting surface S, i.e. $\vec{\mathcal{E}},\vec{\mathcal{H}}$ above S, can be found from the magnetic surface current $\vec{\mathcal{M}}_s = \vec{\mathcal{E}} \times \vec{e}_z$ alone. The presence of the perfectly conducting infinite plane S can be eliminated by applying image theory, i.e., by replacing $\vec{\mathcal{M}}_s$ by $2\vec{\mathcal{M}}_s$ and removing the perfectly conducting plane S. The electric field at the point (x,y,z), with $z > h_2$, can now be calculated from [13, p. 36]

$$
\vec{\mathcal{E}}(\vec{r}) = \nabla \times \iint_S 2\vec{\mathcal{M}}_s(\vec{r}_0)\frac{e^{-jk_0|\vec{r}-\vec{r}_0|}}{4\pi|\vec{r}-\vec{r}_0|}dS, \tag{3.58}
$$

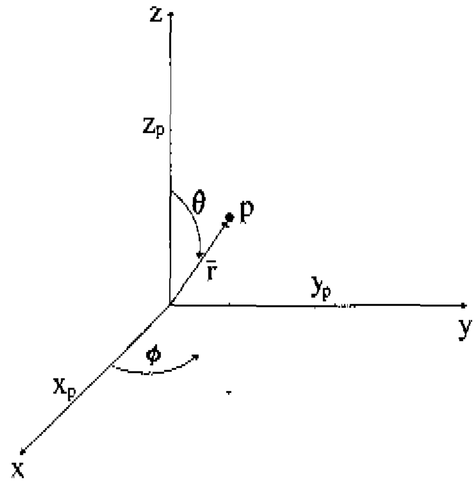

Figure 3.12: *Coordinate system.*

where $\vec{r}_0 = (x_0, y_0, z_0)$ represents a source point. In the far-field region it is assumed that $|\vec{r}| \gg |\vec{r}_0|$. Under far-field conditions relation (3.58) takes the form

$$\vec{\mathcal{E}}(\vec{r}) = \frac{jk_0 e^{-jk_0 r}}{2\pi r}\vec{e}_r \times \iint_S \vec{\mathcal{M}}_s(x_0, y_0, h_2) e^{jk_0 \vec{e}_r \cdot \vec{r}_0} dx_0 dy_0, \tag{3.59}$$

where $\vec{e}_r$ is a unit vector in the $\vec{r}$-direction. Far fields are normally expressed in terms of spherical coordinates (r, θ, ϕ) instead of Cartesian coordinates (x, y, z). The coordinate system is shown in figure 3.12. The inner product $\vec{e}_r \cdot \vec{r}_0$ can be written in the form

$$\vec{e}_r \cdot \vec{r}_0 = \frac{xx_0 + yy_0 + zz_0}{r} = x_0 \sin\theta\cos\phi + y_0 \sin\theta\sin\phi + z_0\cos\theta. \tag{3.60}$$

Combining relation (3.59) with this last expression yields

$$\begin{aligned}\vec{\mathcal{E}}(\vec{r}) = {} & \frac{jk_0 e^{-jk_0 r}}{4\pi r} e^{jk_0 h_2 \cos\theta}\vec{e}_r \times \\ & \iint_S 2\vec{\mathcal{M}}_s(x_0, y_0, h_2) e^{jk_0(x_0 \sin\theta\cos\phi + y_0 \sin\theta\sin\phi)} dx_0 dy_0\end{aligned} \tag{3.61}$$

Now introduce the spectral-domain coordinates k_x and k_y, with

$$\begin{aligned} k_x &= k_0 \sin\theta\cos\phi, \\ k_y &= k_0 \sin\theta\sin\phi. \end{aligned} \tag{3.62}$$

The integral over the surface S in (3.61) can now be expressed in terms of the spectral-domain electric field at $z = h_2$

$$\begin{aligned}
&\iint_S \vec{\mathcal{M}}_s(x_0, y_0, h_2) e^{j(k_x x_0 + k_y y_0)} dx_0 dy_0 \\
&= \int_{-\infty}^{\infty}\int_{-\infty}^{\infty} [\vec{\mathcal{E}}(x_0, y_0, h_2) \times \vec{e}_z] e^{j(k_x x_0 + k_y y_0)} dx_0 dy_0 \\
&= \vec{E}(k_x, k_y, h_2) \times \vec{e}_z
\end{aligned} \tag{3.63}$$

Using this result, we are able to construct a closed-form expression for the far field from (3.61)

$$\begin{aligned}
\vec{\mathcal{E}}(\vec{r}) &= \frac{jk_0 e^{-jk_0 r}}{2\pi r} e^{jk_0 h_2 \cos\theta} \vec{e}_r \times [\vec{E}(k_x, k_y, h_2) \times \vec{e}_z] \\
&= \frac{jk_0 e^{-jk_0 r}}{2\pi r} e^{jk_0 h_2 \cos\theta} \{\vec{e}_\phi [E_y(k_x, k_y, h_2) \cos\theta \cos\phi \\
&\quad - E_x(k_x, k_y, h_2) \cos\theta \sin\phi] + \vec{e}_\theta [E_y(k_x, k_y, h_2) \sin\phi + E_x(k_x, k_y, h_2) \cos\phi]\},
\end{aligned} \tag{3.64}$$

with $\vec{E} = E_x\vec{e}_x + E_y\vec{e}_y + E_z\vec{e}_z$. The electric field in the spectral domain can be written in terms of the current distribution on the lower and upper patches, i.e., $\vec{\mathcal{J}}^p(x, y, z_1')$ and $\vec{\mathcal{J}}^p(x, y, z_2')$, and the current distribution on the coaxial probe $\vec{\mathcal{J}}^f(x, y, z)$. At the plane $z = h_2$ the spectral-domain electric field is, according to (2.57), given by

$$\begin{aligned}
\vec{E}(k_x, k_y, h_2) &= \bar{\bar{Q}}_2^{L}(k_x, k_y, h_2, z_1') \cdot \vec{J}^p(k_x, k_y, z_1') \\
&+ \bar{\bar{Q}}_2^{L}(k_x, k_y, h_2, z_2') \cdot \vec{J}^p(k_x, k_y, z_2') + \int_0^{z_F} \bar{\bar{Q}}_2^{C}(k_x, k_y, h_2, z_0) \cdot \vec{J}^f(k_x, k_y, z_0) dz_0
\end{aligned} \tag{3.65}$$

Note that we have neglected the contribution of the magnetic current source in the coaxial aperture. Once an approximation of the current distribution on the patches and on the probe has been determined with the method of moments, the far-field pattern can be calculated without any numerical difficulties from (3.64). The remaining integration over z_0 in (3.65) can be performed analytically. The corresponding magnetic field in the far-field region can be calculated from the electric field by using the relation

$$\vec{\mathcal{H}} = \sqrt{\frac{\varepsilon_0}{\mu_0}} \vec{e}_r \times \vec{\mathcal{E}} \tag{3.66}$$

If the microstrip antenna under consideration has only a single patch ($z_1' = z_2'$) and is linearly polarised with $y_s = 0$, the far-field pattern can be approximated by a very simple closed-form expression. It is assumed that the current distribution on the patch is x-directed and that it has the same form as the first basis function of the set (3.30). The current on the patch and its corresponding Fourier transform are now given by

$$\begin{aligned}\vec{J}^p(x, y, z_1') &= \vec{e}_x \sin\left(\frac{\pi}{W_{x1}}(x + \frac{W_{x1}}{2})\right), \\ \tilde{J}^p(k_x, k_y, z_1') &= \vec{e}_x \left[\frac{2\pi W_{x1}\cos(k_x W_{x1}/2)}{\pi^2 - (k_x W_{x1})^2}\right] W_{y1}\mathrm{sinc}(k_y W_{y1}/2),\end{aligned} \tag{3.67}$$

where the amplitude of the current has been normalised to 1. The far-field pattern in the E-plane ($\phi = 0^0$) and H-plane ($\phi = 90^0$) can be calculated from the following formulas:
E-plane ($\phi = 0^0$)

$$\vec{\mathcal{E}}(\vec{r}) = \frac{jk_0 e^{-jk_0 r}}{2\pi r} e^{jk_0 h_2 \cos\theta}\left[\frac{2\pi W_{x1} W_{y1}\cos(k_x W_{x1}/2)}{\pi^2 - (k_x W_{x1})^2}\right] Q^E_{2xx}(k_x, k_y, h_2, z_1')\vec{e}_\theta, \tag{3.68}$$

with $k_x = k_0 \sin\theta$, $k_y = 0$,
and in the H-plane ($\phi = 90^0$):

$$\vec{\mathcal{E}}(\vec{r}) = \frac{-jk_0 e^{-jk_0 r}}{2\pi r} e^{jk_0 h_2 \cos\theta}\left[\frac{2W_{x1} W_{y1}}{\pi}\mathrm{sinc}(k_y W_{y1}/2)\right] Q^E_{2xx}(k_x, k_y, h_2, z_1)\cos\theta\,\vec{e}_\phi, \tag{3.69}$$

with $k_x = 0$, $k_y = k_0 \sin\theta$.
Figure 3.13 shows the E-plane radiation pattern at resonance of an electrically thin, single-layer, microstrip antenna ($h_2/\lambda = 0.02$) calculated with approximation (3.68) and with the exact expression (3.64). Clearly, the approximation is quite good in this case. In figure 3.14 the E-plane radiation pattern at resonance is shown of an electrically thick, single-layer, microstrip antenna with $h_2/\lambda = 0.11$. We now see a slightly larger difference between the approximation (3.68) and the exact formula (3.64), which is mainly caused by the currents on the coaxial probe.
Note that the far-field pattern derived in this section is essentially a linearly polarised field, because only one coaxial cable was used to feed the microstrip antenna. If two coaxial cables are used with a 90 degree phase difference, a circularly polarised far field can be obtained. More details on circular polarisation can be found in section 4.6 of this thesis.
An important antenna parameter is the antenna gain. The gain of an antenna is defined as

$$G_e = \eta D_e, \tag{3.70}$$

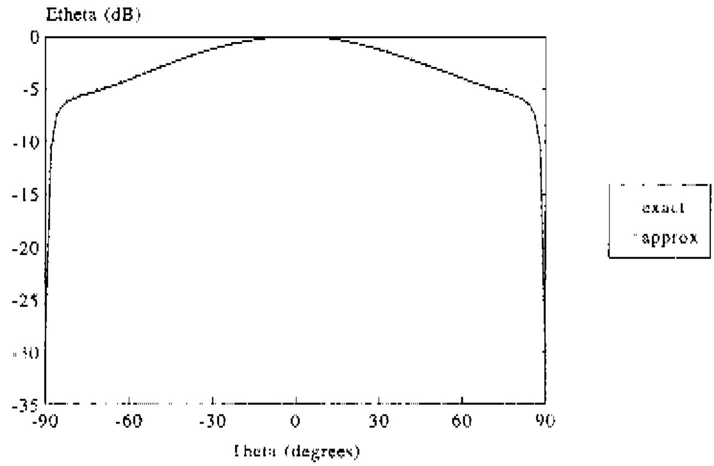

Figure 3.13 *Radiation pattern of an electrically thin microstrip antenna at resonance, with* $z_1' = z_2' = h_1 = h_2 = 0.79$ *mm*, $W_{x1} = W_{y1} = 18.025$ *mm*, $\varepsilon_{r1} = 2.33$, $x_s = 2.75$ *mm and* $y_s = 0$

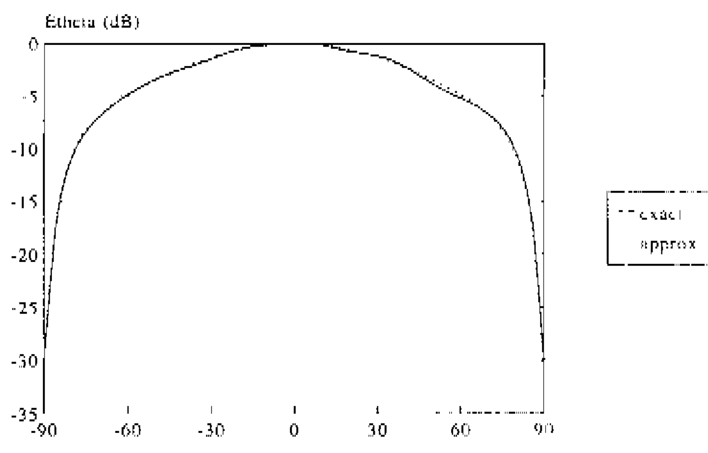

Figure 3.14 *Radiation pattern of an electrically thick microstrip antenna at resonance, with* $z_1' = z_2' = h_1 = h_2 = 3.175$ *mm*, $W_{x1} = 11$ *mm*, $W_{y1} = 17$ *mm*, $\varepsilon_{r1} = 2.33$, $x_s = 4$ *mm and* $y_s = 0$

in which D_e is the directivity of the antenna and where η is the antenna efficiency which accounts for the losses in the antenna. The directivity of a microstrip antenna can be calculated once the far field, given by (3.64), is known:

$$D_e = 4\pi \frac{\max\{|\vec{\mathcal{E}}(\theta,\phi)|^2\}}{\int\limits_0^{\pi/2}\int\limits_0^{2\pi} |\vec{\mathcal{E}}(\theta,\phi)|^2 \sin\theta d\theta d\phi}. \tag{3.71}$$

3.8 Computational and numerical details

3.8.1 Introduction

A major drawback of rigorous numerical procedures such as the method of moments or the finite-element method is the relative long computation time and large memory requirements of the computer on which the code is implemented. The most difficult and computationally intensive part in our method-of-moments procedure is the calculation of the elements of the matrices $[Z]$ and $[V^{ex}]$ of equation (3.15). The elements of these matrices are integrals with infinite boundaries that have to be calculated numerically. Once all elements of $[Z]$ and $[V^{ex}]$ are known, it is relatively easy to solve matrix equation (3.15), because the order of $[Z]$ is usually not very large. If, for example, entire-domain basis functions are used on the patches, only a few of them are needed to obtain accurate results. However, if finite arrays of microstrip antennas are studied, the order of $[Z]$ will be larger and the numerical inversion of this matrix may become a problem (see section 4.7). The numerical inversion of the matrix $[Z]$ is carried out with routines of the LINPACK library [21] for the inversion of complex symmetric matrices. Note that the software is written in FORTRAN-77 and has been implemented on several types of computer workstations (PC-486, VAX, HP). In this section some methods will be discussed that make it possible to calculate the elements of $[Z]$ and $[V^{ex}]$ accurately with an acceptable use of computer time. Each element of $[Z]$ can be represented by an integral of the following form

$$Z_{mn} = \int\limits_0^\infty g_{mn}(\beta)d\beta. \tag{3.72}$$

The elements of $[V^{ex}]$ can also be represented by an integral of the form (3.72). The infinite β-integration interval can be divided into the subintervals $[0,1]$, $[1,\beta_{\varepsilon_r}]$ and $[\beta_{\varepsilon_r},\infty)$, where β_{ε_r} is defined as

$$\beta_{\varepsilon_r} = \begin{cases} \sqrt{Re(\varepsilon_{r1})}, & \text{if } Re(\varepsilon_{r1}) > Re(\varepsilon_{r2}), \\ \sqrt{Re(\varepsilon_{r2})}, & \text{if } Re(\varepsilon_{r2}) > Re(\varepsilon_{r1}). \end{cases} \tag{3.73}$$

and where $Re(\varepsilon_{r1})$ is the real part of the relative permittivity of layer 1.

In the first integration interval, $g_{m,n}(\beta)$ has a branch singularity at $\beta = 1$. In the second integration interval numerical problem occurs due to the presence of poles in the Green's function which are caused by surface waves in the grounded dielectric structure. In the last integration interval no singularities occur. Because of the fact that $g_{m,n}(\beta)$ is a slowly decaying and strongly oscillating function for large β, a so-called asymptotic-form extraction technique is introduced in order to reduce the total computation time and to increase the numerical accuracy. The integration over this extracted part can be carried out in closed form. This results in a substantial reduction of the required computer CPU-time. Techniques that can be used to avoid numerical problems in each of the three integration intervals will be discussed in the following two sections. The remaining integrals are calculated with standard numerical integration routines of the package QUADPACK [52]. These routines use efficient Gauss-Kronrod integration rules and can be used to calculate integrals of real- or complex-valued functions. These routines also give an estimate of the absolute error in the approximated integral.

3.8.2 Surface waves and other singularities

In this section the numerical problems associated with the singularities that occur in the β-integration intervals $[0, 1]$ and $[1, \beta_{\varepsilon_r}]$ are discussed. The first singularity in $g_{m,n}(\beta)$ (see (3.72)) occurs at the branch point $\beta = 1$. At this point, the derivative of $g_{m,n}(\beta)$ is infinite. Consequently, many integration points are needed near this point in order to obtain a good accuracy in the numerical integration. This singularity at $\beta = 1$ can be avoided by introducing the change of variables $\beta = \cos t$ in the interval $[0, 1]$:

$$\int_0^1 g_{m,n}(\beta)d\beta = \int_0^{\pi/2} g_{m,n}(\cos t)\sin t \, dt, \tag{3.74}$$

and the change of variables $\beta = \cosh t$ in the interval $[1, \beta_{\varepsilon_r}]$

$$\int_1^{\beta_{\varepsilon_r}} g_{m,n}(\beta)d\beta = \int_0^{\operatorname{arccosh}(\beta_{\varepsilon_r})} g_{m,n}(\cosh t)\sinh t \, dt \tag{3.75}$$

The first integral (3.74) can now be calculated with a standard numerical integration routine. In the second integration interval $[1, \beta_{\varepsilon_r}]$ poles occur due to surface waves that exist in the grounded dielectric structure. The zeros of the functions T_e and T_m, given by (2.40), correspond to solutions of the characteristic equation for TM and TE surface waves in the dielectric structure. The guiding conditions of these surface waves are given by

$$
\begin{aligned}
T_e &= jk_2k_3\sin(k_1d_1)\cos(k_2d_2) + k_1k_2\cos(k_1d_1)\cos(k_2d_2) \\
&\quad -k_2^2\sin(k_1d_1)\sin(k_2d_2) + jk_1k_3\cos(k_1d_1)\sin(k_2d_2) = 0, \\
T_m &= k_2k_3\varepsilon_{r1}\varepsilon_{r2}\cos(k_1d_1)\cos(k_2d_2) + jk_2^2\varepsilon_{r1}\cos(k_1d_1)\sin(k_2d_2) \\
&\quad -k_1k_3\varepsilon_{r2}^2\sin(k_1d_1)\sin(k_2d_2) + jk_1k_2\varepsilon_{r2}\sin(k_1d_1)\cos(k_2d_2) = 0
\end{aligned}
\tag{3.76}
$$

The zeros of T_m and T_e give rise to poles in the spectral-domain dyadic Green's function. It can be shown that these poles are first-order poles that are located just below the real β-axis if the substrates are lossy. Although the poles are not located exactly on the real β-axis, they do give rise to numerical problems when an integration is carried out along that β-axis. The exact location of the zeros of the complex functions T_m and T_e can only be found with numerical techniques. However, it is possible to say something about which TM- or TE-modes appear in the microstrip structure. For that purpose we will assume that the dielectric losses are negligible, i.e., $\tan\delta_i = 0$. The zeros of T_m and T_e now lie on the real axis of the complex β-plane and they are located within the interval $[1, \beta_{\varepsilon_r}]$. In this interval k_3, defined in (2.23), is imaginary and the z-dependence of the fields in the air region will be of the form $\exp(-k_0z\sqrt{\beta^2-1})$ (see (2.25)). Note that we look only at positive values of β. Not all the TM and TE surface wave modes are excited in the dielectric structure. This depends on the permittivity and thickness of the dielectric layers and on the frequency of operation. Now let β_k be the radial propagation constant for the k-th surface-wave mode. A certain surface-wave mode k turns on when $\beta_k = 1$ [1]. Inserting $\beta_k = 1$ into (3.76) yields

$$
\tan(k_0d_2\sqrt{\varepsilon_{r2}-1}) = -\frac{\varepsilon_{r2}\sqrt{\varepsilon_{r1}-1}}{\varepsilon_{r1}\sqrt{\varepsilon_{r2}-1}}\tan(k_0d_1\sqrt{\varepsilon_{r1}-1}), \tag{3.77}
$$

for TM modes, and

$$
\tan(k_0d_2\sqrt{\varepsilon_{r2}-1}) = \frac{\sqrt{\varepsilon_{r1}-1}}{\sqrt{\varepsilon_{r2}-1}}\cot(k_0d_1\sqrt{\varepsilon_{r1}-1}), \tag{3.78}
$$

for TE surface-wave modes. When we introduce the notation

$$
\begin{aligned}
v_d &= k_0d_2\sqrt{\varepsilon_{r2}-1}, \\
C &= \frac{d_1\sqrt{\varepsilon_{r1}-1}}{d_2\sqrt{\varepsilon_{r2}-1}},
\end{aligned}
\tag{3.79}
$$

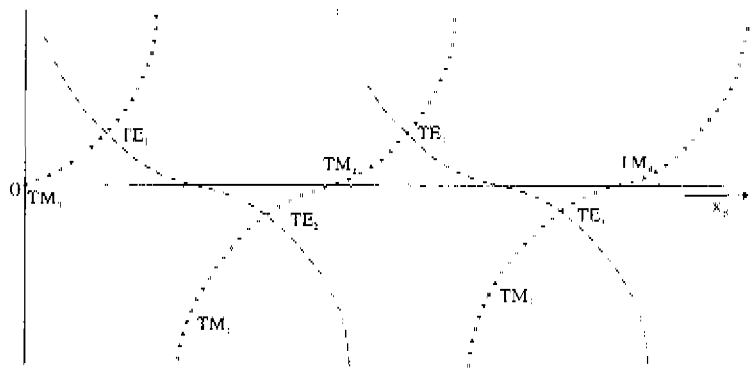

Figure 3.15. *Graphical representation of the TM and TE cut-off conditions, with $a = \varepsilon_{r2}d_2/\varepsilon_{r1}d_1$ and $b = d_2/d_1$*

the equations (3.77) and (3.78) take the following form

$$\tan(x_d) = -\frac{\varepsilon_{r2}d_2}{\varepsilon_{r1}d_1}C\tan(Cx_d), \tag{3.80}$$

for TM modes, and

$$\tan(x_d) = \frac{d_2}{d_1}C\cot(Cx_d), \tag{3.81}$$

for TE surface-wave modes. The cut-off conditions for a certain mode can be made more clear if both sides of equations (3.80) and (3.81) are displayed graphically. Figure 3.15 shows the graphical representation of the TM and TE cut-off conditions for a fixed C and a variable x_d.
The lowest order TM surface-wave mode is always above cut off. This mode is denoted as the TM_0 surface-wave mode with a zero cut-off frequency and with a propagation constant β_0 in the interval $1 \leq \beta_0 \leq \beta_{\varepsilon_r}$. The next surface-wave mode is the TE_1 mode. From figure 3.15 it is clear that if $x_d < x_{d1}$, with x_{d1} being the first root of (3.81), this first TE-mode is below cut off. This implies that, if the condition

$$\tan(x_d) < \frac{d_2}{d_1}C\cot(Cx_d), \tag{3.82}$$

is fulfilled, only the TM_0-mode exists in the layered structure. In almost all practical microstrip configurations, condition (3.82) is satisfied.

If dielectric losses are introduced, the values of β for which the functions T_e and T_m are zero will be complex:

$$\beta_k = \chi_k + j\nu_k, \tag{3.83}$$

where $\nu_k < 0$. So the $\{\beta_k\}$ are located just below the real axis of the complex β-plane. The exact location of a zero β_k is determined with a numerical routine of the library MINPACK [50], which is a very robust routine based on the Powell-hybrid method. Now let us assume that only T_m has one zero, located at $\beta = \beta_0 = \chi_0 + j\,\nu_0$ with $1 \leq \chi_0 \leq \beta_{\varepsilon_r}$ and $\nu_0 \leq 0$. The β-integrand in (3.72) may be written in the form

$$g_{m,n}(\beta) = \frac{h(\beta)}{T_m(\beta)}, \tag{3.84}$$

where $h(\beta)$ is an analytical function in the interval $1 \leq \beta \leq \beta_{\varepsilon_r}$. Because the function T_m has a first-order zero at $\beta = \beta_0$, $g_{m,n}(\beta)$ will have a first-order pole at this point. In the neighbourhood of this pole, $g_{m,n}(\beta)$ can be expanded in a Laurent series. The singular part of this series is given by

$$g_{m,n}^{sing}(\beta) = \frac{R_0}{\beta - \beta_0}, \tag{3.85}$$

where R_0 is the residue of $g_{m,n}$ at $\beta = \beta_0$

$$R_0 = \lim_{\beta \to \beta_0} (\beta - \beta_0) g_{m,n}(\beta) = h(\beta_0) \lim_{\beta \to \beta_0} \frac{\beta - \beta_0}{T_m(\beta)} = \frac{h(\beta_0)}{T'_m(\beta_0)}, \tag{3.86}$$

with

$$T'_m(\beta_0) = \left. \frac{d(T_m(\beta))}{d\beta} \right|_{\beta=\beta_0}$$

Numerical problems associated with surface waves can be avoided by extracting the singular part, denoted by $g_{m,n}^{sing}$, from the original integrand $g_{m,n}$:

$$\int_1^{\beta_{\varepsilon_r}} g_{m,n}(\beta)d\beta = \left\{ \int_1^{\beta_{\varepsilon_r}} (g_{m,n}(\beta) - g_{m,n}^{sing}(\beta))d\beta + \int_1^{\beta_{\varepsilon_r}} g_{m,n}^{sing}(\beta)d\beta \right\} \tag{3.87}$$

The integration over β of $g_{m,n}^{sing}$ can be performed analytically

$$\begin{aligned} \int_1^{\beta_{\varepsilon_r}} g_{m,n}^{sing}(\beta)d\beta &= \frac{R_0}{2} \ln \left[\frac{(\beta_{\varepsilon_r} - \chi_0)^2 + \nu_0^2}{(1 - \chi_0)^2 + \nu_0^2} \right] \\ &+ jR_0 \arctan \left[\frac{\beta_{\varepsilon_r} - \chi_0}{\nu_0} \right] + jR_0 \arctan \left[\frac{\chi_0 - 1}{\nu_0} \right] \end{aligned} \tag{3.88}$$

In the case of a lossless substrate ($\nu_0 \uparrow 0$) the integral of $g_{m,n}^{sing}$ takes the form

$$\int_1^{\beta_{\varepsilon_r}} g_{m,n}^{sing}(\beta)d\beta = R_0 \ln\left[\frac{\beta_{\varepsilon_r} - \chi_0}{(\chi_0 - 1)}\right] - j\pi R_0 \tag{3.89}$$

The remaining integral over β in (3.87) is well-behaved and can be calculated by standard numerical integration. This is illustrated in figure 3.16 where the real part of the original integrand $g_{m,n}(\beta)$ and of the modified integrand $g_{m,n}(\beta) - g_{m,n}^{sing}(\beta)$ are shown for the interval $1 \leq \beta \leq \beta_{\varepsilon_r}$ for a typical microstrip configuration.

3.8.3 Asymptotic-form extraction technique

In the third β-integration interval, i.e., $[\beta_{\varepsilon_r}, \infty)$, no singularities occur in the integrand $g_{m,n}(\beta)$ of (3.72). It is therefore possible to perform this integration numerically up to a certain upper limit β_{max}. The upper limit β_{max} has to be chosen carefully to ensure that the relative error of the calculated numerical approximation of the integral (3.72) is sufficiently small. A great disadvantage of this direct integration strategy is the fact that $g_{m,n}(\beta)$ is a slowly decaying and strongly oscillating function. This means that a lot of computer time is needed to obtain accurate results. This situation becomes even worse if one wants to analyse arrays of microstrip antennas, because the frequency of oscillations in $g_{m,n}(\beta)$ increases if the distance between the two basis functions under consideration increases (arrays are discussed in chapter 4).

These numerical problems can be avoided if the so-called asymptotic-form extraction technique is used. The asymptotic form of $g_{m,n}(\beta)$ for large β-values is substracted from the original integrand, which results in a rapidly converging integral. The infinite integration over the extracted asymptotic part of $g_{m,n}(\beta)$ can be evaluated in closed form. This leads to a significant reduction of the required computer time (CPU time) needed to calculate the elements of $[Z]$ and $[V^{ex}]$. From numerical tests, we found that the total computer time for a typical microstrip configuration is reduced by a factor 20 or more when this method is applied. In the spatial domain, i.e. the (x, y, z)-domain, the dyadic Green's function in the dielectric structure has a $\mu_0/4\pi|\vec{r} - \vec{r}_0|$-singularity, where $\vec{r}_0$ is a source point. This source singularity is responsible for the asymptotic behavior of the dyadic Green's function in the spectral domain. If the z-coordinates of the two basis functions of the element $Z_{m,n}$ intersect each other, the spectral-domain Green's function decreases slowly ($\sim 1/\beta^2$) for large values of β. On the other hand, if the z-coordinates of these two basis functions do not intersect, the asymptotic form of $g_{m,n}(\beta)$ will decrease exponentially for large β. In the latter case, the asymptotic-form extraction technique obviously need not be used. Now let $\bar{g}_{m,n}(\beta)$ be the asymptotic form of $g_{m,n}(\beta)$. Then an element of the method-of-moments

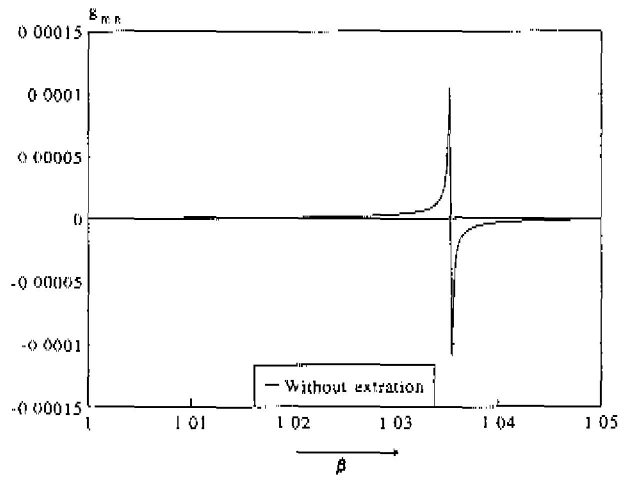

a) no extraction

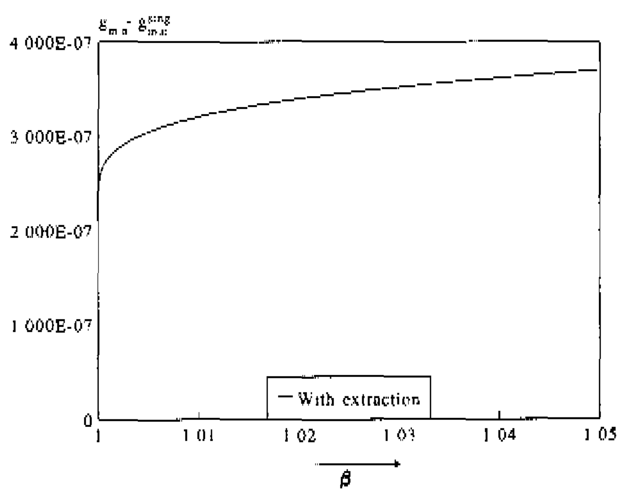

b) with extraction

Figure 3.16: *Real part of $g_{m,n}(\beta)$ and $g_{m,n}(\beta) - g_{m,n}^{sing}(\beta)$, with $h_2 = 6.08$ mm, $\varepsilon_{r1} = \varepsilon_{r2} = 2.94$ and $f = 3$ GHz.*

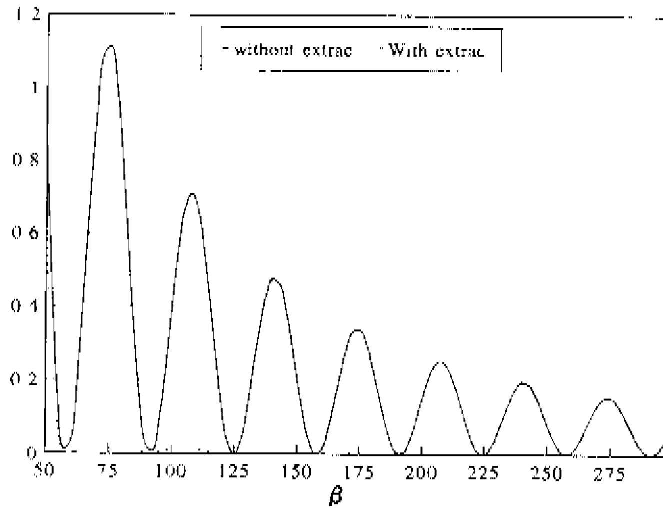

Figure 3.17: *Real part of original integrand $g_{m,n}(\beta)$ and modified integrand $g_{m,n}(\beta) - \tilde{g}_{m,n}(\beta)$, with $h_2 = 6.08$ mm, $\varepsilon_{r1} = \varepsilon_{r2} = 2.94$ and $f = 3$ GHz*

matrix $[Z]$ may be written as

$$
\begin{aligned}
Z_{m,n} &= \int_0^\infty g_{m,n}(\beta)d\beta \\
&= \int_0^\infty \left[g_{m,n}(\beta) - \tilde{g}_{m,n}(\beta)\right] d\beta + \int_0^\infty \tilde{g}_{m,n}(\beta)d\beta \\
&= (Z_{m,n} - \tilde{Z}_{m,n}) + \tilde{Z}_{m,n}
\end{aligned}
\tag{3.90}
$$

with

$$\tilde{Z}_{m,n} = \int_0^\infty \tilde{g}_{m,n}(\beta)d\beta$$

The improved convergence of the integrand of the first integral in (3.90) is illustrated in figure 3.17. In this figure the real part of $g_{m,n}(\beta)$ is compared with the real part of the modified integrand $g_{m,n}(\beta) - \tilde{g}_{m,n}(\beta)$ for the case of two z-directed subdomain rooftop basis functions on the coaxial probe ($m = n = 2$, $N_z = 8$). From this figure we may conclude that, with the asymptotic-form extraction technique, the number of integration points which are needed to calulate the β-integral with a numerical integration procedure, is much lower than the number of points that would be required for an accurate numerical evaluation of the original integrand. In the following part of this section we will discuss how this asymptotic-form extraction technique can be applied to the calculation of the elements of each of the submatrices of $[Z]$ and of $[V^{ex}]$, given by (3.17) and (3.18). It should be noted that we will only consider the case of entire-domain sinusoidal basis functions on the patches, given by (3.30) and (3.31). From convergence tests (see also section 3.9) it was shown that with this set of basis functions very accurate results can be obtained even if only a few basis functions are used in a method-of-moments procedure. The asymptotic-form extraction technique can, of course, also be applied if different sets of basis functions on the patches are used. In the following part of this section it is assumed that the length of the coaxial probe is not longer than the height of the first layer, i.e., $z_1' \leq h_1$. An extension to the more general case is straightforward.

i. $[\mathbf{Z^{pp}}]$: patch modes $\longleftrightarrow$ patch modes

In section 3.4, several types of basis functions that can be used on the patches were discussed. Further on, in section 3.9, it will be shown that very good results can be obtained if the set of basis functions given by (3.30) and (3.31) is used. Normally, only a few modes of this set are needed in the method-of-moments procedure to obtain fairly good results. This is essential when we are going to look at arrays of microstrip antennas in chapter 4. We will therefore present the extraction technique only for this set of basis functions. Note that the analytical technique presented in this section for the case of isolated microstrip antennas can easily be extended to the case of an array of microstrip antennas.

The extracted part $\tilde{Z}^{pp}_{m,n}$ of the asymptotic-form extraction technique is in this case given by (see also (A.13) of appendix A)

$$\begin{aligned}\tilde{Z}^{pp}_{m,n} &= \int_0^{\frac{\pi}{2}}\int_0^{\infty} \left[\bar{\bar{\tilde{Q}}}_2^{E}(\beta,\alpha,z_m,z_n)\cdot\vec{\tilde{J}}^p_n(\beta,\alpha,z_n)\right] \\ &\quad \cdot\vec{\tilde{J}}^{p*}_m(\beta,\alpha,z_m)\,S_{pp}(m,1,n,1,\beta,\alpha)k_0^2\beta d\beta d\alpha,\end{aligned} \tag{3.91}$$

with

$$z_m = \begin{cases} z_1', & \text{if domain } m \text{ is located on the lower patch,} \\ z_2', & \text{if domain } m \text{ is located on the upper patch,} \end{cases}$$

where $\bar{\bar{\tilde{Q}}}_2^{E}$ is the asymptotic form of the dyadic Green's function $\bar{\bar{Q}}_2^{E}$ for large-valued β, i.e., k_1, k_2 and k_3 replaced by $-jk_0\beta$. The numbering of the elements of the submatrix $[Z^{pp}]$ is now

$m = 1, 2, \ldots, N_1 + N_2$ and $n = 1, 2, \ldots, N_1 + N_2$. The function $S_{pp}(m, 1, n, 1, \beta, \alpha)$ is given by (A.14) in appendix A. Both patches are located in layer 2. Note that $\bar{\bar{Q}}_2^E$ is extracted from the original integrand for all values of β. We are only interested in x- and y-directed basis functions on the patches. Therefore, the following asymptotic Green's function $\bar{\bar{Q}}^E$ is used here

$$\bar{\bar{Q}}_2^E(\beta, \alpha, z_m, z_n) = \begin{pmatrix} \bar{Q}^E_{2xx} & \bar{Q}^E_{2xy} & 0 \\ \bar{Q}^E_{2yx} & \bar{Q}^E_{2yy} & 0 \\ 0 & 0 & 0 \end{pmatrix}, \tag{3.92}$$

with

$$\bar{Q}^E_{2xx} = \begin{cases} \dfrac{-j\omega\mu_0}{2k_0\beta}\left[1 - \dfrac{\beta^2\cos^2\alpha}{\varepsilon_{rh}}\right], & z_m = z_n, \\ 0, & z_m \neq z_n, \end{cases}$$

$$\bar{Q}^E_{2yy} = \begin{cases} \dfrac{-j\omega\mu_0}{2k_0\beta}\left[1 - \dfrac{\beta^2\sin^2\alpha}{\varepsilon_{rh}}\right], & z_m = z_n, \\ 0, & z_m \neq z_n, \end{cases}$$

$$\bar{Q}^E_{2yx} = \bar{Q}^E_{2xy} = \begin{cases} \dfrac{j\omega\mu_0\beta\sin 2\alpha}{4k_0\varepsilon_{rh}}, & z_m = z_n, \\ 0, & z_m \neq z_n. \end{cases}$$

with

$$\varepsilon_{rh} = \begin{cases} (\varepsilon_{r1} + \varepsilon_{r2})/2, & \text{if } z_m = z_n = h_1, \\ \varepsilon_{r2}, & \text{if } h_1 < z_m = z_n < h_2, \\ (\varepsilon_{r2} + 1)/2, & \text{if } z_m = z_n = h_2 \end{cases}$$

From (3.92) it is clear that $\tilde{Z}^{pp}_{mn}$ is nonzero only if the basis functions $\vec{J}^p_m(\beta, \alpha, z_m)$ and $\vec{J}^p_n(\beta, \alpha, z_n)$ are located both at the same z-coordinate, i.e., if $z_m = z_n$. Our task is now to find a closed-form expression for the infinite integration over β of the extracted part of the integrand. The integral over β in (3.91) depends on the type of basis function used on the patches. Now let us consider two x-directed basis functions of the set (3.30), both located on the lower patch or both located on the upper patch, with m_p and n_p both odd. In the following part of this section we will present an analytical method to determine $\tilde{Z}^{pp}_{m,n}$, for these two basis functions. The procedure for the calculation of $\tilde{Z}^{pp}_{m,n}$ for the remaining basis functions of the set (3.30) and (3.31), on both the lower and upper patch, is analogous. Substitution of (3.32) and (3.92) in expression (3.91) yields

$$\tilde{Z}^{pp}_{m,n} = 4A \int_0^{\frac{\pi}{2}} \frac{1}{\sin^2\alpha} \int_0^{\infty} \left[1 - \frac{\beta^2\cos^2\alpha}{\varepsilon_{rb}}\right] \frac{\cos^2(\beta\gamma/2)\sin^2(\beta\xi/2)}{(n_p\pi - \beta\gamma)(n_p\pi + \beta\gamma)(m_p\pi - \beta\gamma)(m_p\pi + \beta\gamma)\beta^2} d\beta d\alpha, \tag{3.93}$$

with m_p and n_p both odd and with

$$A = \frac{-8j\omega\mu_0\pi^2 m_p n_p W_{xt}^2}{k_0},$$

$$\gamma = k_0\cos\alpha W_{xt}, \quad \xi = k_0\sin\alpha W_{yt},$$

$$W_{xt} = \begin{cases} W_{x1}, & \text{if } z_m = z_n = z_1', \\ W_{x2}, & \text{if } z_m = z_n = z_2', \end{cases}$$

$$W_{yt} = \begin{cases} W_{y1}, & \text{if } z_m = z_n = z_1', \\ W_{y2}, & \text{if } z_m = z_n = z_2' \end{cases}$$

The term $\cos^2(\beta\gamma/2)\sin^2(\beta\xi/2)$ in (3.93) can be written as a sum of exponential functions.

$$\cos^2(\beta\gamma/2)\sin^2(\beta\xi/2) = \frac{1}{16}\left\{g(\beta) + g(-\beta)\right\}, \tag{3.94}$$

with

$$g(\beta) = -2 - 2e^{j\beta\gamma} + 2e^{j\beta\xi} + e^{j\beta(\gamma+\xi)} + e^{j\beta(\gamma-\xi)}$$

Since the integrand of $\tilde{Z}^{pp}_{m,n}$ is an even function of β, the integration over β can be extended to the

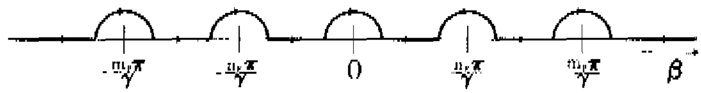

Figure 3.18. *Modified integration contour if $m_p \neq n_p$.*

interval $(-\infty, \infty)$. This results in

$$
\begin{aligned}
\tilde{Z}^{pp}_{mn} &= 2A \int_0^{\frac{\pi}{2}} \frac{1}{\sin^2\alpha} \int_{-\infty}^{\infty} \left[1 - \frac{\beta^2\cos^2\alpha}{\epsilon_r h}\right] \\
&\quad \frac{\cos^2(\beta\gamma/2)\sin^2(\beta\xi/2)}{(n_p\pi - \beta\gamma)(n_p\pi + \beta\gamma)(m_p\pi - \beta\gamma)(m_p\pi + \beta\gamma)\beta^2}\, d\beta\, d\alpha \\
&= 2A \int_0^{\frac{\pi}{2}} \frac{1}{\sin^2\alpha} I_\beta(\alpha)\, d\alpha,
\end{aligned}
\tag{3.95}
$$

with

$$
I_\beta(\alpha) = \int_{-\infty}^{\infty} \frac{\left[1 - \frac{\beta^2\cos^2\alpha}{\epsilon_r h}\right]\cos^2(\beta\gamma/2)\sin^2(\beta\xi/2)}{(n_p\pi - \beta\gamma)(n_p\pi + \beta\gamma)(m_p\pi - \beta\gamma)(m_p\pi + \beta\gamma)\beta^2}\, d\beta \tag{3.96}
$$

The integral I_β can be calculated analytically. First, the integration contour will be deformed such that values of β for which the denominator of the β-integrand is zero are avoided. The second step is the expansion of the term $\cos^2(\beta\gamma/2)\sin^2(\beta\xi/2)$ into exponential functions, given by (3.94). The integral I_β is then written as a sum of 10 integrals. Each of these 10 integrals can be calculated by closing the integration contour with a semi circle and applying Cauchy's Theorem and Jordan's Lemma. The location of the semi circle, i.e. above or below the β-axis, depends on the argument of the exponential function.
Two situations can be distinguished: 1) $m_p \neq n_p$ and 2) $m_p = n_p$. We shall take a closer look at both situations.

1. $m_p \neq n_p$

The integrand of $I_\beta(\alpha)$ is analytic for all complex β. We may, therefore, deform the β-integration contour as illustrated in figure 3.18. This figure shows the modified integration contour in the complex β-plane.

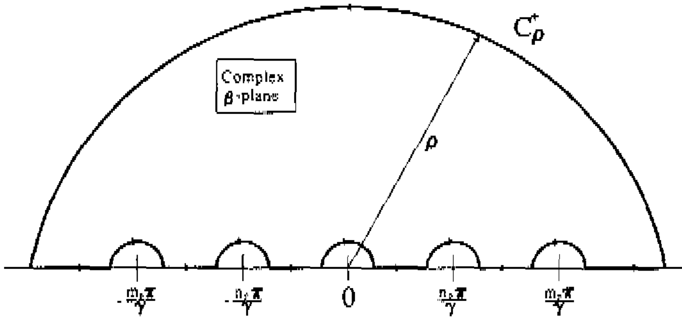

Figure 3.19: *Integration contour for $t \geq 0$*

Based on this modified integration contour, the integral $I_\beta(\alpha)$ is given by

$$I_\beta(\alpha) = \oint_{-\infty}^{\infty} \frac{\left[1 - \frac{\beta^2 \cos^2\alpha}{\epsilon_{rk}}\right] \cos^2(\beta\gamma/2)\sin^2(\beta\xi/2)}{(n_p\pi - \beta\gamma)(n_p\pi + \beta\gamma)(m_p\pi - \beta\gamma)(m_p\pi + \beta\gamma)\beta^2} d\beta, \tag{3.97}$$

where $\oint_{-\infty}^{\infty}$ denotes that the integration is along the contour shown in figure 3.18. If we substitute (3.94) in expression (3.97), $I_\beta(\alpha)$ can be written as a sum of 10 integrals of the general form

$$G_1(t) = \oint_{-\infty}^{\infty} \frac{\left[1 - \frac{\beta^2 \cos^2\alpha}{\epsilon_{rk}}\right] e^{j\beta t}}{(n_p\pi - \beta\gamma)(n_p\pi + \beta\gamma)(m_p\pi - \beta\gamma)(m_p\pi + \beta\gamma)\beta^2} d\beta. \tag{3.98}$$

The integrand of the above integral has four poles of order 1 at $\beta = \pm(m_p\pi/\gamma)$ and $\beta = \pm(n_p\pi/\gamma)$ and a pole of order 2 at $\beta = 0$. A closed-form expression for the integral $G_1(t)$ can be found by using Cauchy's theorem and Jordan's Lemma [78]. Two subcases have to be distinguished, namely i) $t \geq 0$ and ii) $t < 0$.

$\underline{t \geq 0}$

The original integration contour of figure 3.18 is closed by the semi-circle C_ρ^+ of radius ρ, shown in figure 3.19. If $t > 0$ the integral over C_ρ^+ tends to 0 as $\rho \longrightarrow \infty$ according to Jordan's Lemma. If $t = 0$ the integral over C_ρ^+ also tends to 0 as $\rho \longrightarrow \infty$, because the integrand is of $\mathcal{O}(\beta^{-4})$ as $|\beta| \longrightarrow \infty$. The integral $G_1(t)$ is equal to zero for $t \geq 0$, because no singularities are located in the region enclosed by the integration contour of figure 3.19:

$$G_1(t) = 0 \quad \text{for} \quad t \geq 0 \tag{3.99}$$

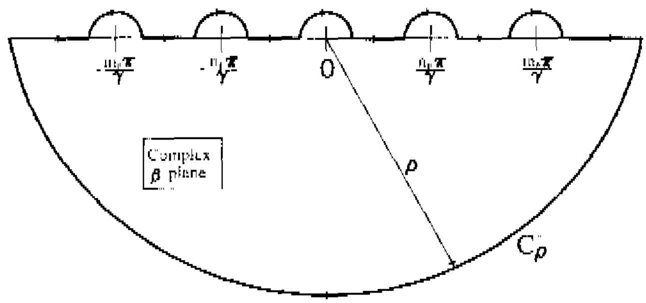

Figure 3.20: *Integration contour for $t < 0$*

<u>$t < 0$</u>

Our integration contour is now closed with the semi-circle C_ρ^-, shown in figure 3.20. In the region enclosed by the integration contour 5 poles are located. According to Jordan's Lemma the integral over C_ρ^- tends to 0 as $\rho \longrightarrow \infty$. Then $G_1(t)$ can be expressed in terms of the 5 residues:

$$\begin{aligned} G_1(t) = \; & -2\pi j \left(\operatorname*{Res}_{\beta = -\frac{m_p\pi}{\gamma}} f_1(\beta, t) + \operatorname*{Res}_{\beta = -\frac{n_p\pi}{\gamma}} f_1(\beta, t) + \operatorname*{Res}_{\beta = 0} f_1(\beta, t) \right. \\ & \left. + \operatorname*{Res}_{\beta = \frac{n_p\pi}{\gamma}} f_1(\beta, t) + \operatorname*{Res}_{\beta = \frac{m_p\pi}{\gamma}} f_1(\beta, t) \right), \end{aligned} \tag{3.100}$$

where the function $f_1(\beta, t)$ is given by

$$f_1(\beta, t) = \frac{\left[1 - \frac{\beta^2 \cos^2\alpha}{k_0^2}\right] e^{j\beta t}}{(n_p\pi - \beta\gamma)(n_p\pi + \beta\gamma)(m_p\pi - \beta\gamma)(m_p\pi + \beta\gamma)\beta^2} \tag{3.101}$$

The residues in (3.100) are given by

$$
\begin{aligned}
\operatorname*{Res}_{\beta=-\frac{m_p\pi}{\gamma}} f_1(\beta,t) &= \frac{\gamma e^{-\frac{jm_p\pi t}{\gamma}}}{2\pi^5 m_p^3[n_p^2-m_p^2]}\left[1-\frac{m_p^2\pi^2\cos^2\alpha}{\gamma^2\varepsilon_{rh}}\right],\\
\operatorname*{Res}_{\beta=-\frac{n_p\pi}{\gamma}} f_1(\beta,t) &= \frac{\gamma e^{\frac{jn_p\pi t}{\gamma}}}{2\pi^5 n_p^3[m_p^2-n_p^2]}\left[1-\frac{n_p^2\pi^2\cos^2\alpha}{\gamma^2\varepsilon_{rh}}\right],\\
\operatorname*{Res}_{\beta=0} f_1(\beta,t) &= \frac{jt}{m_p^2 n_p^2\pi^4},\\
\operatorname*{Res}_{\beta=\frac{n_p\pi}{\gamma}} f_1(\beta,t) &= \frac{-\gamma e^{\frac{jn_p\pi t}{\gamma}}}{2\pi^5 n_p^3[m_p^2-n_p^2]}\left[1-\frac{n_p^2\pi^2\cos^2\alpha}{\gamma^2\varepsilon_{rh}}\right],\\
\operatorname*{Res}_{\beta=\frac{m_p\pi}{\gamma}} f_1(\beta,t) &= \frac{-\gamma e^{\frac{jm_p\pi t}{\gamma}}}{2\pi^5 m_p^3[n_p^2-m_p^2]}\left[1-\frac{m_p^2\pi^2\cos^2\alpha}{\gamma^2\varepsilon_{rh}}\right].
\end{aligned}
\tag{3.102}
$$

Substituting these results in expression (3.100) gives a closed-form expression for the integral $G_1(t)$:

$$
\begin{aligned}
G_1(t) = {} & \frac{2t}{m_p^2 n_p^2\pi^3}-\frac{2\gamma}{m_p^3\pi^4[n_p^2-m_p^2]}\left[1-\frac{m_p^2\pi^2\cos^2\alpha}{\gamma^2\varepsilon_{rh}}\right]\sin\frac{m_p\pi t}{\gamma}\\
&-\frac{2\gamma}{n_p^3\pi^4[m_p^2-n_p^2]}\left[1-\frac{n_p^2\pi^2\cos^2\alpha}{\gamma^2\varepsilon_{rh}}\right]\sin\frac{n_p\pi t}{\gamma}, \qquad t<0
\end{aligned}
\tag{3.103}
$$

Define an auxiliary function $F_1(t)$ with $F_1(t)=G_1(t)+G_1(-t)$. Then according to (3.103) and (3.99) $F_1(t)$ is given by

$$
\begin{aligned}
F_1(t) = {} & \frac{-2|t|}{m_p^2 n_p^2\pi^3}+\frac{2\gamma}{m_p^3\pi^4[n_p^2-m_p^2]}\left[1-\frac{m_p^2\pi^2\cos^2\alpha}{\gamma^2\varepsilon_{rh}}\right]\sin\frac{m_p\pi|t|}{\gamma}\\
&+\frac{2\gamma}{n_p^3\pi^4[m_p^2-n_p^2]}\left[1-\frac{n_p^2\pi^2\cos^2\alpha}{\gamma^2\varepsilon_{rh}}\right]\sin\frac{n_p\pi|t|}{\gamma}
\end{aligned}
\tag{3.104}
$$

Now that $F_1(t)$ is known, we can also calculate the original integral I_β. I_β can be written in terms

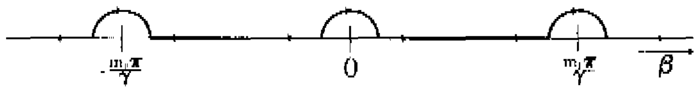

Figure 3.21: *Modified integration contour for the case that $m_p = n_p$.*

of the function $F_1(t)$:

$$I_\beta(\alpha) = \oint_{-\infty}^{\infty} \frac{\left[1 - \frac{\beta^2\cos^2\alpha}{\varepsilon_{rh}}\right]\cos^2(\beta\gamma/2)\sin^2(\beta\xi/2)}{(n_p\pi - \beta\gamma)(n_p\pi + \beta\gamma)(m_p\pi - \beta\gamma)(m_p\pi + \beta\gamma)\beta^2}d\beta$$

$$= \frac{1}{16}\left\{ 2F_1(0) - 2F_1(\gamma) + 2F_1(\xi) + F_1(\gamma + \xi) + F_1(\gamma - \xi)\right\}, \tag{3.105}$$

with $m_p \neq n_p$

2. $m_p = n_p$

The same procedure as presented in the case when $m_p \neq n_p$ is used now. The integrand of I_β, given by (3.96), is also in this case analytic for all complex β. We may therefore use the modified integration contour of figure 3.21 to determine I_β. I_β is then given by

$$I_\beta(\alpha) = \oint_{-\infty}^{\infty} \left[1 - \frac{\beta^2\cos^2\alpha}{\varepsilon_{rh}}\right] \frac{\cos^2(\beta\gamma/2)\sin^2(\beta\xi/2)}{(m_p\pi - \beta\gamma)^2(m_p\pi + \beta\gamma)^2\beta^2}d\beta, \tag{3.106}$$

where the symbol $\oint_{-\infty}^{\infty}$ is used to indicate that the integration contour of figure 3.21 is used. Now substitute (3.94) in expression (3.106). The integral $I_\beta(\alpha)$ can then be written as a sum of 10 integrals with the general form:

$$G_2(t) = \oint_{-\infty}^{\infty} \left[1 - \frac{\beta^2\cos^2\alpha}{\varepsilon_{rh}}\right] \frac{e^{j\beta t}}{(m_p\pi - \beta\gamma)^2(m_p\pi + \beta\gamma)^2\beta^2}d\beta. \tag{3.107}$$

The integrand of $G_2(t)$ has three poles of order 2 at $\beta = \pm m_p\pi/\gamma$ and $\beta = 0$. Again two subcases can be distinguished, i.e., i) $t > 0$ and ii) $t < 0$

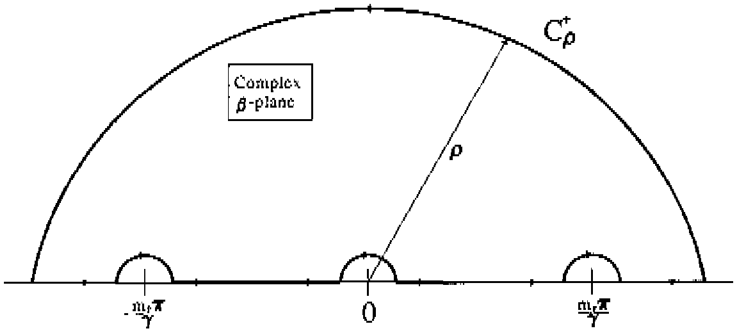

Figure 3.22: *Modified integration contour if $t \geq 0$.*

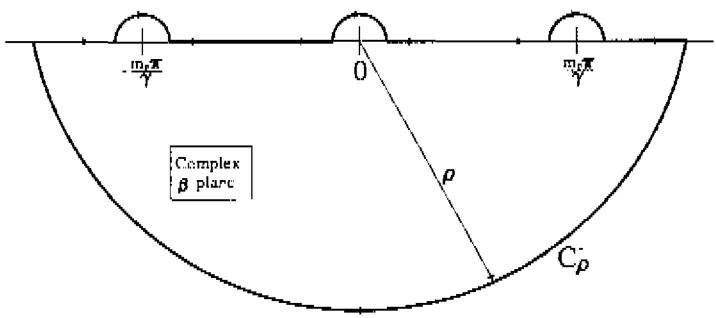

Figure 3.23: *Modified integration contour if $t < 0$.*

$t \geq 0$

The integration contour is closed with C_ρ^+, shown in fig. 3.22. According to Jordan's Lemma the integral over C_ρ^+ tends to 0 as $\rho \longrightarrow \infty$. There are no singularities located in the region enclosed by the integration contour of figure 3.22, so $G_2(t)$ will be zero in this case:

$$G_2(t) = 0 \quad \text{for} \quad t \geq 0 \tag{3.108}$$

$t < 0$

The integration contour is closed with the semi-circle C_ρ^- as shown in figure 3.23. Again Jordan's Lemma can be used to show that the contribution of the integral over C_ρ^- tends to 0 as $\rho \longrightarrow \infty$

Now let

$$f_2(\beta,t) = \frac{\left[1 - \dfrac{\beta^2\cos^2\alpha}{\varepsilon_{rh}}\right] e^{j\beta t}}{(m_p\pi - \beta\gamma)^2(m_p\pi + \beta\gamma)^2\beta^2}, \tag{3.109}$$

then $G_2(t)$ is calculated from

$$\begin{aligned} G_2(t) &= -2\pi j\left(\operatorname*{Res}_{\beta = \frac{m_p\pi}{\gamma}} f_2(\beta,t) + \operatorname*{Res}_{\beta = 0} f_2(\beta,t) + \operatorname*{Res}_{\beta = \frac{-m_p\pi}{\gamma}} f_2(\beta,t)\right) \\ &\quad - \frac{2t}{m_p^4\pi^3} + \frac{t}{m_p^4\pi^3}\left[1 - \frac{m_p^2\pi^2\cos^2\alpha}{\gamma^2\varepsilon_{rh}}\right]\cos\frac{m_p\pi t}{\gamma} \\ &\quad - \frac{\gamma}{m_p^5\pi^4}\left[3 - \frac{m_p^2\pi^2\cos^2\alpha}{\gamma^2\varepsilon_{rh}}\right]\sin\frac{m_p\pi t}{\gamma}, \qquad t < 0 \end{aligned} \tag{3.110}$$

If we define an auxiliary function $F_2(t)$ with $F_2(t) = G_2(t) + G_2(-t)$ then I_β can be expressed in terms of this function F_2 as

$$\begin{aligned} I_\beta(\alpha) &= \oint_{-\infty}^{\infty}\left[1 - \frac{\beta^2\cos^2\alpha}{\varepsilon_{rh}}\right]\frac{\cos^2(\beta\gamma/2)\sin^2(\beta\xi/2)}{(m_p\pi - \beta\gamma)^2(m_p\pi + \beta\gamma)^2\beta^2}\,d\beta \\ &= \frac{-1}{16}\left\{-2F_2(0) - 2F_2(\gamma) + 2F_2(\xi) + F_2(\gamma + \xi) + F_2(\gamma - \xi)\right\}, \end{aligned} \tag{3.111}$$

with $m_p = n_p$. The remaining integral over α in (3.95) has to be evaluated numerically. If one properly divides the α-integration interval into two subintervals, only a few integration points are needed to obtain an acceptable accuracy. These two intervals are $[0, \alpha_0]$ and $[\alpha_0, \pi/2]$, where α_0 is the value of α for which $\gamma - \xi = 0$. Fortunately, the integration over α only needs to be carried out for one frequency point.

ii. $\mathbf{Z^{aa}}$: attachment mode $\longleftrightarrow$ attachment mode

A detailed expression of Z^{aa} is given by formula (A.2) of appendix A, where it was assumed that the lower patch is located at the interface between layer 1 and layer 2 ($z_1' = h_1$). Now let Z^{aa} be represented by the following integral

$$Z^{aa} = \int_0^\infty g^{aa}(\beta)\,d\beta \tag{3.112}$$

This can also be written in the form

$$
\begin{aligned}
Z^{aa} &= \int_0^\infty g^{aa}(\beta)d\beta = \int_0^v g^{aa}(\beta)d\beta + \int_v^\infty g^{aa}(\beta)d\beta \\
&= \int_0^v g^{aa}(\beta)d\beta + \int_v^\infty \left[g^{aa}(\beta) - \tilde{g}^{aa}(\beta)\right] d\beta + \int_v^\infty \tilde{g}^{aa}(\beta)d\beta \\
&= \left[Z^{aa} - \tilde{Z}^{aa}\right] + \tilde{Z}^{aa},
\end{aligned}
\tag{3.113}
$$

with

$$
\tilde{Z}^{aa} = \int_v^\infty \tilde{g}^{aa}(\beta)d\beta,
$$

where $\tilde{g}^{aa}(\beta)$ is the asymptotic form of the original β-integrand $g^{aa}(\beta)$ for large-valued β. Note that in this case the extraction technique is only used when $\beta > v$, because the asymptotic form $\tilde{g}^{aa}(\beta)$ has a $1/\beta^2$-dependence for $\beta \downarrow 0$. The exact value of v is not very critical. In our simulations, we have used $v = 50$. The asymptotic form of $g^{aa}(\beta)$ can be found by substituting $k_1 = -jk_0\beta$, $k_2 = -jk_0\beta$ and $k_3 = -jk_0\beta$ in the original expression. We then finally arrive at

$$
\begin{aligned}
\tilde{Z}^{aa}(\beta) = \int_v^\infty \frac{j\omega\mu_0\pi}{k_0} & \left(\frac{8J_1^2(k_0\beta b_a)}{(\varepsilon_{r1}+\varepsilon_{r2})b_a^2 k_0^2\beta^2} - \frac{16J_1(k_0\beta b_a)J_0(k_0\beta a)}{(\varepsilon_{r1}+\varepsilon_{r2})b_a h k_0^2\beta^2} \right. \\
& + \frac{2\varepsilon_{r1}^2 J_0^2(k_0\beta a)}{(\varepsilon_{r1}+\varepsilon_{r2})\beta^4} + \frac{4J_0^2(k_0\beta a)}{\varepsilon_{r1} h k_0\beta} - \frac{k_0 h\, J_0^2(k_0\beta a)}{3\beta} \\
& \left. - \frac{(4\varepsilon_{r1}+12\varepsilon_{r2})\, J_0^2(k_0\beta a)}{\varepsilon_{r1}(\varepsilon_{r1}+\varepsilon_{r2})h^2 k_0^2\beta^2} \right) d\beta, \qquad z_1' = h_1
\end{aligned}
\tag{3.114}
$$

The above integral contains four types of infinite integrals. All of them can be evaluated analytically or can be approximated by a closed-form expression. These five integrals have the form

$$
\begin{aligned}
I_1 &= \int_{\nu}^{\infty} \frac{J_1^2(k_0\beta b_a)}{\beta^2}\,d\beta, \\
I_2 &= \int_{\nu}^{\infty} \frac{J_0^2(k_0\beta a)}{\beta}\,d\beta, \\
I_3 &= \int_{\nu}^{\infty} \frac{J_0^2(k_0\beta a)}{\beta^2}\,d\beta, \\
I_4 &= \int_{\nu}^{\infty} \frac{J_1(k_0\beta b_a)\,J_0(k_0\beta a)}{\beta^2}\,d\beta, \\
I_5 &= \int_{\nu}^{\infty} \frac{J_0^2(k_0\beta a)}{\beta^4}\,d\beta
\end{aligned}
\tag{3.115}
$$

The first type of integral can be evaluated analytically if we choose $\nu = 0$.

$$
I_1 = \int_{0}^{\infty} \frac{J_1^2(k_0\beta b_a)}{\beta^2}\,d\beta = \frac{4k_0 b_a}{3\pi}
\tag{3.116}
$$

The second integral cannot be evaluated analytically, but can be reduced to an integral over a finite interval for $\nu > 0$ [7]:

$$
\begin{aligned}
I_2 &= \int_{\nu}^{\infty} \frac{J_0^2(k_0\beta a)}{\beta}\,d\beta \\
&= -\log\frac{1}{2}k_0\nu a - C - \int_{0}^{k_0\nu a} \frac{J_0^2(x) - 1}{x}\,dx,
\end{aligned}
\tag{3.117}
$$

where $C = 0.577215\ldots$ is Euler's constant. The third integral I_3 can be evaluated in closed form [27, p. 634]:

$$
\begin{aligned}
I_3 &= \int_{\nu}^{\infty} \frac{J_0^2(k_0\beta a)}{\beta^2}\,d\beta \\
&= \frac{J_0^2(k_0\nu a)}{\nu} - \frac{4k_0 a}{\pi} + 2k_0^2 a^2 \nu\left[J_1^2(k_0\nu a) + J_0^2(k_0\nu a)\right] \\
&\quad - 2k_0 a\, J_0(k_0\nu a)\, J_1(k_0\nu a)
\end{aligned}
\tag{3.118}
$$

The integrals I_4 and I_5 cannot be evaluated analytically, but can be approximated by a closed-form expression For large-valued β, the Bessel functions can be replaced by their asymptotic forms, so

$$J_0(x) = \sqrt{\frac{2}{\pi x}}\left\{\cos(x-\frac{\pi}{4}) + \frac{\sin(x-\frac{\pi}{4})}{8x} + \mathcal{O}(\frac{1}{x^2})\right\}. \tag{3.119}$$

For the sake of simplicity, only the first term in the above expansion will be used here. A better approximation can, of course, be obtained if more terms of the asymptotic expansion of the Bessel functions are used. Considering only the first term of (3.119), we get

$$\begin{aligned} I_4 &= \int_v^\infty \frac{J_1(k_0\beta b_a)J_0(k_0\beta a)}{\beta^2}d\beta \\ &\approx \int_v^\infty \frac{2}{\pi k_0\sqrt{b_a a}}\frac{\cos(k_0\beta b_a - \frac{3\pi}{4})\cos(k_0\beta a-\frac{\pi}{4})}{\beta^3}d\beta \\ &= -\frac{k_0}{\pi\sqrt{b_a a}}\left((a+b_a)^2\left[\frac{\cos k_0 v(a+b_a)}{2k_0^2v^2(a+b_a)^2} - \frac{\sin k_0 v(a+b_a)}{2k_0 v(a+b_a)} + \frac{1}{2}ci(k_0v(a+b_a))\right]\right. \\ &\left.+ (a-b_a)^2\left[\frac{\sin k_0v(a-b_a)}{2k_0^2v^2(a-b_a)^2} + \frac{\cos k_0 v(a-b_a)}{2k_0v(a-b_a)} + \frac{1}{2}si(k_0v(a-b_a))\right]\right), \end{aligned} \tag{3.120}$$

where $ci(x)$ and $si(x)$ are the cosine and sine integral, respectively, defined by

$$\begin{aligned} ci(x) &= -\int_x^\infty \frac{\cos t}{t}dt, \\ si(x) &= -\int_x^\infty \frac{\sin t}{t}dt \end{aligned} \tag{3.121}$$

The integral I_5 is calculated by a similar procedure

iii. $[\mathbf{Z}^{\mathrm{fa}}]$: feed modes $\longleftrightarrow$ attachment mode

The extracted part $\tilde{Z}_m^{fa}$ can be found by substituting $k_1 = k_2 = k_3 = jk_0\beta$ in the integrand of the expression of Z_m^{fa}, given by formula (A.5) of appendix A. The extracted part $\tilde{Z}_m^{fa}$ is only nonzero if subdomain m on the coaxial probe touches or overlaps the attachment mode.

$$\tilde{Z}_m^{fa} = \frac{2j\omega\mu_0\pi}{\varepsilon_{r1}} \times \begin{cases} \displaystyle\int_v^\infty \frac{-2J_0^2(k_0\beta a)}{h^2k_0^3\beta^2}d\beta, & m = N_z - 1, \\ \displaystyle\int_v^\infty \left(-\frac{\varepsilon_{r1}hJ_0^2(k_0\beta a)}{12\beta} + \frac{4\varepsilon_{r1}J_1(k_0\beta b_a)J_0(k_0\beta a)}{b_a h\beta^2k_0^3(\varepsilon_{r1}+\varepsilon_{r2})}\right. & \\ \displaystyle\left.+\frac{(4\varepsilon_{r1}+8\varepsilon_{r2})J_0^2(k_0\beta a)}{h^2\beta^2k_0^3(\varepsilon_{r1}+\varepsilon_{r2})} - \frac{2J_0^2(k_0\beta a)}{h\beta k_0^2}\right)d\beta, & m = N_z, \end{cases} \tag{3.122}$$

with $m = 1, 2, \ldots, N_z$ and where it is again assumed that the lower patch is located at the interface between layer 1 and layer 2, i.e., $z_1' = h_1$. The three types of integrals in (3.122) have already been discussed in the previous part of this section and are given by (3.117), (3.118) and (3.120).

iv. $[\mathbf{Z}^{\mathbf{ff}}]$: feed modes $\longleftrightarrow$ feed modes

The numbering of the elements of the submatrix $[Z^{ff}]$ is now $m = 1, 2, \ldots, N_z$ and $n = 1, 2, \ldots, N_z$. In this case, three situations can be distinguished, namely $m = n$, $n = m - 1$ and $n \leq m - 2$. In the first two cases, there is an overlap between subdomain m and subdomain n. The extracted part $\tilde{Z}^{ff}_{m,n}$ is again found by substituting $k_1 = k_2 = k_3 = -jk_0\beta$ in expression (A.9) of appendix A. We then get (with $z_1' = h_1$):

$$\tilde{Z}^{ff}_{m,n} = 2\pi \int_0^\infty J_0^2(k_0\beta a) k_0^2 \beta \tilde{I}^{ff}_{m,n}(\beta) d\beta, \tag{3.123}$$

with for $m = n$,

$$\tilde{I}^{ff}_{m,m} = \frac{j\omega\mu_0}{\varepsilon_{r1}\beta^2} \times \begin{cases} \dfrac{1}{h^2 k_0^4}\left(\dfrac{12}{k_0\beta} - 4h\right) + \dfrac{h\varepsilon_{r1}}{3k_0^2}, & m > 2 \wedge z_{m+1} < h_1, \\[2ex] \dfrac{1}{h^2 k_0^4}\left(\dfrac{10\varepsilon_{r1} + 14\varepsilon_{r2}}{k_0\beta(\varepsilon_{r1} + \varepsilon_{r2})} - 4h\right) + \dfrac{h\varepsilon_{r1}}{3k_0^2}, & m > 2 \wedge z_{m+1} = h_1 \\[2ex] \dfrac{1}{h^2 k_0^4}\left(\dfrac{14}{k_0\beta} - 4h\right) + \dfrac{h\varepsilon_{r1}}{3k_0^2}, & m = 2 \wedge z_{m+1} < h_1, \\[2ex] \dfrac{1}{h^2 k_0^4}\left(\dfrac{12\varepsilon_{r1} + 16\varepsilon_{r2}}{k_0\beta(\varepsilon_{r1} + \varepsilon_{r2})} - 4h\right) + \dfrac{h\varepsilon_{r1}}{3k_0^2}, & m = 2 \wedge z_{m+1} = h_1, \\[2ex] \dfrac{1}{h^2 k_0^4}\left(\dfrac{6}{k_0\beta} - 2h\right) + \dfrac{h\varepsilon_{r1}}{6k_0^2}, & m = 1 \wedge z_{m+1} < h_1 \\[2ex] \dfrac{1}{h^2 k_0^4}\left(\dfrac{4\varepsilon_{r1} + 8\varepsilon_{r2}}{k_0\beta(\varepsilon_{r1} + \varepsilon_{r2})} - 2h\right) + \dfrac{h\varepsilon_{r1}}{6k_0^2}, & m = 1 \wedge z_{m+1} = h_1 \end{cases}$$

and for $n = m - 1$,

$$\tilde{I}^{ff}_{m,m-1}(\beta) = \frac{-j\omega\mu_0}{\varepsilon_{r1}\beta^2}\left\{\frac{1}{h^2 k_0^4}\left[2h - \frac{8}{k_0\beta}\right] + \frac{h\varepsilon_{r1}}{12k_0^2}\right\},$$

and for $n \leq m - 2$,

$$\tilde{I}^{ff}_{m,n}(\beta) = \begin{cases} -\dfrac{2j\omega\mu_0}{\varepsilon_{r1} h^2 k_0^5 \beta^3}, & n = m - 2, \\[2ex] 0, & \text{otherwise} \end{cases}$$

Consequently, $\tilde{Z}^{ff}_{m,n}$ is nonzero only if subdomain m intersects subdomain n. Note that we have assumed that the length of the probe is not longer than the height of the first layer, i.e., $z_f \leq h_1$. The same assumption was made in appendix A. Apparently, two types of integrals have to be calculated. They are of the same type as integral I_2 and I_3 given by (3.117) and (3.118), respectively.

v. $[\mathbf{Z}^{pa}]$: patch modes $\longleftrightarrow$ attachment mode

The extracted part $\tilde{Z}^{pa}_m$ is only nonzero if basis function m is located on the lower patch, i.e., if $z_m = z_1'$. The extracted part can be found by substituting $k_1 = k_2 = k_3 = -jk_0\beta$ in expression (A.17) of appendix A. This gives

$$\tilde{Z}^{pa}_m = \begin{cases} \dfrac{j\omega\mu_0}{\varepsilon_{rh}} \displaystyle\int_0^{\frac{\pi}{2}}\int_0^{\infty} \left(-\dfrac{jJ_1(k_0\beta b_a)}{k_0 b_a} + \dfrac{jJ_0(k_0\beta a)}{k_0 h}\right. \\ \qquad\qquad \left. -\dfrac{j\varepsilon_{r1} J_0(k_0\beta a)}{2\beta}\right) S_{pf}(m,1,1,\beta,\alpha)\,d\beta\, d\alpha, & z_m = z_1', \\ 0, & z_m = z_2', \end{cases} \tag{3.124}$$

with

$$\varepsilon_{rh} = \frac{\varepsilon_{r1} + \varepsilon_{r2}}{2}, \quad \text{for } z_1' = h_1$$

Note that $m = 1, 2, \ldots, N_1 + N_2$. The function $S_{pf}(m, 1, 1, \beta, \alpha)$ is given by (A.18) in appendix A. We have three different types of integrals in (3.124)

$$\begin{aligned} I_1(\alpha) &= \int_0^{\infty} J_1(k_0\beta b_a) S_{pf}(m,1,1,\beta,\alpha)\, d\beta, \\ I_2(\alpha) &= \int_0^{\infty} J_0(k_0\beta a) S_{pf}(m,1,1,\beta,\alpha)\, d\beta, \\ I_3(\alpha) &= \int_0^{\infty} \frac{J_0(k_0\beta a)}{\beta} S_{pf}(m,1,1,\beta,\alpha)\, d\beta \end{aligned} \tag{3.125}$$

Let us first take a closer look at the integrals $I_1(\alpha)$ and $I_3(\alpha)$. The integrands of both integrals are even functions of β. They can therefore be evaluated by a similar technique as used for the calculation of the extracted part of the elements of $[Z^{pp}]$. The only additional factors are the zero-order and first-order Bessel functions in the integrands of $I_1(\alpha)$ and $I_3(\alpha)$, respectively. The Bessel functions can be represented by an integral as

$$J_n(z) = \frac{1}{2\pi}\int_0^{2\pi} e^{jz\sin\theta} e^{-jn\theta}\, d\theta. \tag{3.126}$$

This integral representation is used to write the numerator of the integrand of $I_1(\alpha)$ and $I_3(\alpha)$ as a sum of exponential functions, similar to (3.94). As a result, a sum of integrals with a similar form as (3.98) is obtained.

The second integral in (3.125) is an integration over an odd function with respect to β. We will present a method to calculate I_2 for the case of a x-directed basis function of the set (3.30) pertaining to the lower patch, with m_p odd. The procedure for the other basis functions of this set is analogous to the one presented here. Substitution of (3.32) and (A.18) into expression (3.125) gives

$$I_2(\alpha) = \frac{A\cos\alpha}{\sin\alpha}\int_0^\infty J_0(k_0\beta a)\frac{\cos(\beta\gamma/2)\sin(\beta\xi/2)\sin(\beta\nu)\cos(\beta\mu)}{(m_p\pi - \beta\gamma)(m_p\pi + \beta\gamma)\beta}d\beta, \tag{3.127}$$

with

$$A = \frac{16j\pi m_p W_{x1}}{k_0},$$

$$\gamma = k_0\cos\alpha W_{x1},\ \xi = k_0\sin\alpha W_{y1},$$

$$\nu = k_0\cos\alpha x_c,\ \mu = k_0\sin\alpha y_c.$$

Using the integral representation (3.126) of the Bessel function $J_0(k_0\beta a)$ we may write

$$J_0(k_0\beta a)\cos(\beta\gamma/2)\sin(\beta\xi/2)\sin(\beta\nu)\cos(\beta\mu) = \frac{-1}{32\pi}\int_0^{2\pi}\{q_2(\beta,\theta) + q_2(-\beta,\theta)\}\,d\theta, \tag{3.128}$$

with

$$\begin{aligned} q_2(\beta,\theta) = {} & \left(e^{j\beta(\gamma/2+\xi/2+\nu+\mu+\tau)} - 1\right) + \left(e^{j\beta(\gamma/2+\xi/2+\nu-\mu+\tau)} - 1\right) \\ & - \left(e^{j\beta(\gamma/2+\xi/2-\nu+\mu+\tau)} - 1\right) - \left(e^{j\beta(\gamma/2+\xi/2-\nu-\mu+\tau)} - 1\right) - \left(e^{j\beta(\gamma/2-\xi/2+\nu+\mu+\tau)} - 1\right) \\ & - \left(e^{j\beta(\gamma/2-\xi/2+\nu-\mu+\tau)} - 1\right) + \left(e^{j\beta(\gamma/2-\xi/2-\nu+\mu+\tau)} - 1\right) + \left(e^{j\beta(\gamma/2-\xi/2-\nu-\mu+\tau)} - 1\right), \end{aligned} \tag{3.129}$$

where $\tau = k_0 a\sin\theta$. Cauchy's theorem will now be applied to find a closed-form expression for $I_2(\alpha)$. The modified integration path of figure 3.24 will be used here. The integral $I_2(\alpha)$ is then given by

$$I_2(\alpha) = \frac{A\cos\alpha}{\sin\alpha}\int_0^\infty J_0(k_0\beta a)\frac{\cos(\beta\gamma/2)\sin(\beta\xi/2)\sin(\beta\nu)\cos(\beta\mu)}{(m_p\pi - \beta\gamma)(m_p\pi + \beta\gamma)\beta}d\beta, \tag{3.130}$$

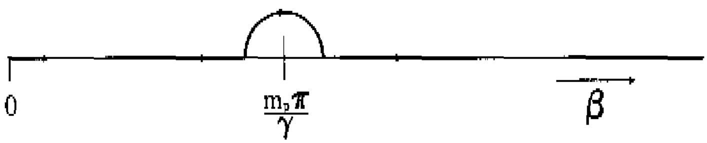

Figure 3.24: *Modified integration path for $I_2(\alpha)$.*

where $\int_0^{\infty}$ denotes the integration path of figure 3.24. If we substitute (3.129) in (3.130) we can write I_2 as a sum of 16 integrals of the general form:

$$G(t) = \int_0^{\infty} \frac{e^{j\beta t} - 1}{(m_p\pi - \beta\gamma)(m_p\pi + \beta\gamma)\beta} d\beta \tag{3.131}$$

Two subcases can be distinguished, namely i) $t \geq 0$ and ii) $t < 0$

$t \geq 0$

The original integration path is closed with the contours C_ρ^+ and C_γ^+ as shown in figure 3.25. If $t \geq 0$ the integral over C_ρ^+ tends to 0 as $\rho \longrightarrow \infty$, because the integrand behaves as $O(\beta^{-3})$ as $\beta \longrightarrow \infty$. Furthermore, there are no singularities located in the area enclosed by the integration contour of figure 3.25. So the only contribution to the integral $G(t)$ is the integration over C_γ^+:

$$G(t) = -\int_{j\infty}^{0} \frac{e^{j\beta t} - 1}{(m_p\pi - \beta\gamma)(m_p\pi + \beta\gamma)\beta} d\beta \tag{3.132}$$

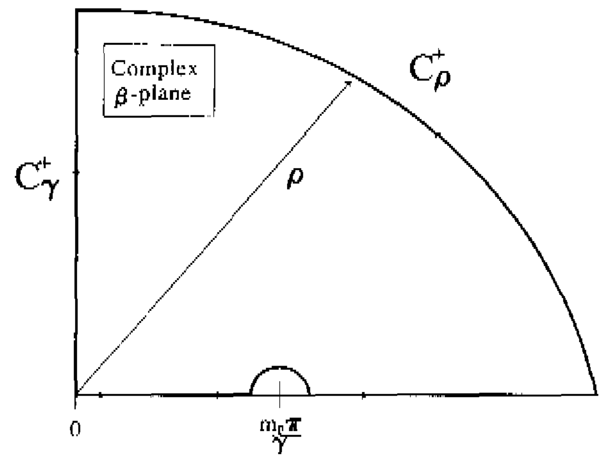

Figure 3.25 *Integration contour for $t \geq 0$.*

This integral may also be written in the form

$$
\begin{aligned}
G(t) &= -\int_{j\infty}^{0} \frac{e^{j\beta t}-1}{(m_p\pi-\beta\gamma)(m_p\pi+\beta\gamma)\beta}\,d\beta \\
&= -\int_{0}^{j\infty} \frac{1-e^{j\beta t}}{(m_p\pi-\beta\gamma)(m_p\pi+\beta\gamma)\beta}\,d\beta \\
&= -\int_{0}^{\infty} \frac{1-e^{-ty}}{(m_p\pi-jy\gamma)(m_p\pi+jy\gamma)y}\,dy \\
&= \frac{1}{\gamma^2}\int_{0}^{\infty} \frac{1-e^{-ty}}{\left(\frac{m_p\pi}{\gamma}-jy\right)\left(\frac{m_p\pi}{\gamma}+jy\right)y}\,dy
\end{aligned}
\tag{3.133}
$$

Divide the integrand of the above integral into two parts and use relation 3.4.3.5 of [27] gives

$$
\begin{aligned}
G(t) &= \frac{-1}{\gamma^2}\int_0^\infty \frac{1-e^{-ty}}{\left(\frac{m_p\pi}{\gamma}-jy\right)\left(\frac{m_p\pi}{\gamma}+jy\right)y}dy \\
&= \frac{-1}{\gamma^2}\left\{\frac{\gamma}{2m_p\pi}\int_0^\infty \frac{1-e^{-ty}}{y\left(\frac{m_p\pi}{\gamma}+jy\right)}dy+\frac{\gamma}{2m_p\pi}\int_0^\infty \frac{1-e^{-ty}}{y\left(\frac{m_p\pi}{\gamma}-jy\right)}dy\right\} \\
&= \frac{-1}{2m_p^2\pi^2}\left\{2C+\ln(-\frac{jm_p\pi t}{\gamma})+\ln(\frac{jm_p\pi t}{\gamma})\right. \\
&\quad \left. -e^{-\frac{jm_p\pi t}{\gamma}}Ei(\frac{jm_p\pi t}{\gamma})-e^{\frac{jm_p\pi t}{\gamma}}Ei(-\frac{jm_p\pi t}{\gamma})\right\} \\
&= \frac{-1}{m_p^2\pi^2}\left\{C+\ln\left|\frac{m_p\pi t}{\gamma}\right|-ci\left(\frac{m_p\pi t}{\gamma}\right)\cos\left(\frac{m_p\pi t}{\gamma}\right)\right. \\
&\quad \left. -si\left(\frac{m_p\pi t}{\gamma}\right)\sin\left|\frac{m_p\pi t}{\gamma}\right|\right\},
\end{aligned}
\tag{3.134}
$$

for $t \geq 0$, where C is Euler's constant and where $Ei(x)$ is the exponential-integral function defined as

$$
Ei(x) = -\int_x^\infty \frac{e^{-t}}{t}dt,
\tag{3.135}
$$

and where $si(x)$ and $ci(x)$ are the sine and cosine integrals, respectively, given by (3.121). The exponential-integral function $Ei(x)$ can be expressed in terms of the sine and cosine integral:

$$
Ei(\pm jx) = ci(x) \pm jsi(x)
\tag{3.136}
$$

This property has been used in (3.134).

$\underline{t < 0}$

The integration contour for this situation is shown in figure 3.26. There is one singularity located inside the integration contour. The contribution of the integral over C_ρ^- tends to 0 as $\rho \longrightarrow \infty$. So $G(t)$ can in this case be expressed in terms of the residue at $\beta = m_p\pi/\gamma$ and the integral over C_γ^-:

$$
\begin{aligned}
G(t) = & -2\pi j \operatorname*{Res}_{\beta=\frac{m_p\pi}{\gamma}}\left(\frac{e^{j\beta t}-1}{(m_p\pi-\beta\gamma)(m_p\pi+\beta\gamma)\beta}\right) \\
& -\int_{-j\infty}^{0}\frac{e^{j\beta t}-1}{(m_p\pi-\beta\gamma)(m_p\pi+\beta\gamma)\beta}d\beta.
\end{aligned}
\tag{3.137}
$$

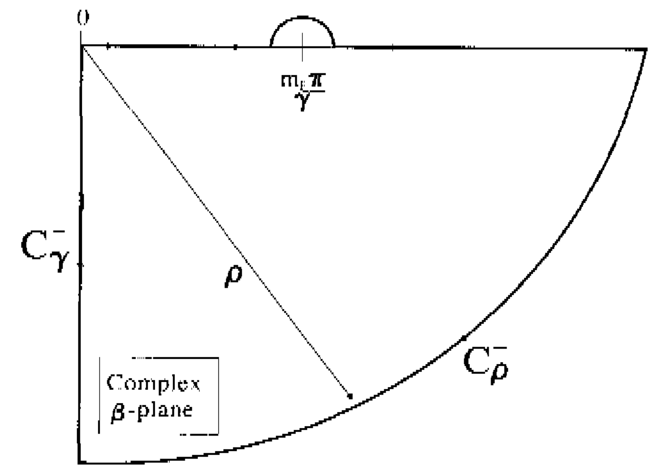

Figure 3.26. *Integration contour for $t < 0$*

The residue at $\beta = m_p\pi/\gamma$ is given by

$$\operatorname*{Res}_{\beta=\frac{m_p\pi}{\gamma}} \left(\frac{e^{j\beta t} - 1}{(m_p\pi - \beta\gamma)(m_p\pi + \beta\gamma)\beta} \right) = \frac{1}{2m_p^2\pi^2} \left(e^{\frac{jm_p\pi t}{\gamma}} - 1 \right) \tag{3.138}$$

The integration over C_γ^- can be rewritten in the following form

$$-\int_{-j\infty}^{0} \frac{e^{j\beta t} - 1}{(m_p\pi - \beta\gamma)(m_p\pi + \beta\gamma)\beta} d\beta = \frac{-1}{\gamma^2} \int_0^\infty \frac{1 - e^{yt}}{\left(\frac{m_p\pi}{\gamma} - jy\right)\left(\frac{m_p\pi}{\gamma} + jy\right) y} dy \tag{3.139}$$

This is exactly the same integral as in (3.133), because in this case $t < 0$. So we can use (3.134) as a result of the integral over C_γ^-. Combining (3.138) and (3.134) with (3.137) gives

$$\begin{aligned} G(t) = & \frac{j}{m_p^2\pi}\left(e^{\frac{jm_p\pi t}{\gamma}} - 1\right) - \frac{1}{m_p^2\pi^2}\left\{C + \ln\left|\frac{m_p\pi t}{\gamma}\right|\right. \\ & \left. - \operatorname{ci}\left(\frac{m_p\pi t}{\gamma}\right)\cos\left(\frac{m_p\pi t}{\gamma}\right) - \operatorname{si}\left(\frac{m_p\pi t}{\gamma}\right)\sin\left|\frac{m_p\pi t}{\gamma}\right|\right\}, \end{aligned} \tag{3.140}$$

for $t < 0$

Define an auxiliary function $F(t) = G(t) + G(-t)$. The original integral $I_2(\alpha)$, given by (3.127), can now be expressed in terms of $F(t)$

$$
\begin{aligned}
I_2(\alpha) &= \frac{A\cos\alpha}{\sin\alpha}\int_0^{\infty} J_0(k_0\beta a)\frac{\cos(\beta\gamma/2)\sin(\beta\xi/2)\sin(\beta\nu)\cos(\beta\mu)}{(m_p\pi-\beta\gamma)(m_p\pi+\beta\gamma)\beta}d\beta \\
&= \frac{-A\cos\alpha}{32\pi\sin\alpha}\int_0^{2\pi}\{F(\gamma/2+\xi/2+\nu+\mu+\tau)+F(\gamma/2+\xi/2+\nu-\mu+\tau) \\
&\quad -F(\gamma/2+\xi/2-\nu+\mu+\tau)-F(\gamma/2+\xi/2-\nu-\mu+\tau) \\
&\quad -F(\gamma/2-\xi/2+\nu+\mu+\tau)-F(\gamma/2-\xi/2+\nu-\mu+\tau) \\
&\quad +F(\gamma/2-\xi/2-\nu+\mu+\tau)+F(\gamma/2-\xi/2-\nu-\mu+\tau)\}\,d\theta,
\end{aligned}
\tag{3.141}
$$

with m_p odd. The θ-integration interval can be reduced to $[-\frac{\pi}{2}, \frac{\pi}{2}]$. The θ-integration in (3.141) can be eliminated if we assume that the radius of the coaxial probe a is equal to zero. This saves some computation time while the final results do not change significantly, because in almost all practical configurations $a \ll \lambda_0$. Now that we have found a way to calculate the three integrals I_1, I_2 and I_3, we can determine $\tilde{Z}^{pa}_{m}$ by evaluating the remaining integration over α in (3.124) numerically. This can be done very efficiently if the α-integration interval is divided properly into subintervals such that the boundaries of these subintervals correspond with values of α for which the derivative of the integrand is discontinuous. The integrations over these subintervals can be carried out with standard numerical integration routines of the package QUADPACK [52]. An advantage of the asymptotic-form extraction technique is the fact that the integrals in $\tilde{Z}^{pa}_{m}$ need to be evaluated for one frequency point only, because these integrals are frequency-independent.

vi. $[\mathbf{Z}^{\mathrm{pf}}]$: patch modes $\longleftrightarrow$ feed modes

The numbering of the elements of $[Z^{pf}]$ is $m = 1, 2, \ldots, N_1 + N_2$ and $n = 1, 2, \ldots, N_z$. The extracted part $\tilde{Z}^{pf}_{m,n}$ is non-zero only if the domain of basis function m is located on the lower patch and if the domain of basis function n on the coaxial probe touches the lower patch, i.e., if $n = N_z$ and if $z_F = z_1'$. If we assume that the length of the coaxial probe is not larger than the height of the first layer, the extracted part is given by

$$
\tilde{Z}^{pf}_{m,n} = \begin{cases} 0, & z_{n+1} < z_m, \\ \dfrac{\omega\mu_0}{h\varepsilon_{r,h}k_0}\displaystyle\int_0^{\frac{\pi}{2}}\int_0^{\infty} J_0(k_0\beta a)S_{pf}(m,1,1,\beta,\alpha)\,d\beta\, d\alpha, & z_{n+1} = z_1', \end{cases}
\tag{3.142}
$$

with

$$\varepsilon_{rh} = \frac{\varepsilon_{r1} + \varepsilon_{r2}}{2} \quad \text{if } z_1' = h_1.$$

The integral over β in (3.142) has exactly the same form as integral $I_2(\alpha)$ in (3.125). So we can use the same methods to calculate the above integral over β. The remaining integration over α is again divided into properly chosen subintervals.

vii. $V^{ex,a}$: attachment mode

The expression for $V^{ex,a}$ is given by formula (B.1) of appendix B. The integral over β converges quickly in most practical situations. However, if the probe part of the attachment mode intersects with the ground plane, i.e., if $h/2 = z_1'$ ($N_z = 1$), the integral over β converges very slowly. For this situation, the asymptotic-form extraction technique will be used to speed up the convergence. Substitution of $k_1 = k_2 = k_3 = -jk_0\beta$ into (B.1) of appendix B, gives the extracted part $\tilde{V}^{ex,a}$:

$$\tilde{V}^{ex,a} = \begin{cases} 0, & h/2 < z_1', \\ \dfrac{-4\pi^2 k_0^2}{\ln(b/a)} \displaystyle\int_0^\infty \dfrac{2\, J_0(k_0\beta a)}{h k_0^3 \beta^2} \left[J_0(k_0\beta b) - J_0(k_0\beta a)\right] d\beta, & h/2 = z_1' \end{cases} \tag{3.143}$$

The above integral can be calculated with the same methods that were used to arrive at (3.115).

viii. $[V^{ex,f}]$: feed modes

The asymptotic form of the original β-integrand can be found by inserting $k_1 = k_2 = k_3 = -jk_0\beta$ into (B.4) or (B.3) of appendix B. With some algebraic manipulations, it is easily shown that the extracted part $\tilde{V}_m^{ex,f}$ is given by

$$\begin{aligned} \tilde{V}_m^{ex,f} &= -\frac{4\pi^2 k_0^2}{\ln(b/a)} \int_0^\infty J_0(k_0\beta a)\left[J_0(k_0\beta b) - J_0(k_0\beta a)\right] \\ &\times \begin{cases} \left(\dfrac{1}{k_0^2\beta} - \dfrac{2}{k_0^3\beta^2 h}\right) d\beta, & m = 1, \\ \dfrac{2}{k_0^3\beta^2 h}\, d\beta, & m = 2, \\ d\beta, & m \geq 3, \end{cases} \end{aligned} \tag{3.144}$$

with $m = 1, 2, \ldots, N_z$. The extracted part differs from zero only if the subdomain m touches the ground plane. The type of integrals that occur in (3.144) have the same form as the integrals discussed in (3.115) and can therefore be evaluated analytically.

ix. $[\mathbf{V}^{\mathbf{ex,p}}]$: patch modes

In this case the asymptotic-form extraction technique need not be used, because the β-integrand of $V_m^{ex,p}$ (see expression (B.5) of appendix B) decays exponentially for large values of β ($\sim e^{-\beta}$).

x. $[\mathbf{V}_\mathbf{t}^{\mathbf{ex}}]$: thin-substrate model

The expression for an element of the vector $[V_t^{ex}]$ when the thin-substrate model of section 3.2.2 is used is given by (B.6) of appendix B. Again the asymptotic-form extraction technique can be applied to speed up the convergence of the integral over β. The extracted part $\tilde{V}_{t,m}^{ex}$ differs from zero in this case only if the domain of the basis function m is located on the lower patch of the antenna and is given by

$$\tilde{V}_{t,m}^{ex} = \frac{-\omega\mu_0}{k_0^2(\varepsilon_{r1}+\varepsilon_{r2})} \int_0^{\frac{\pi}{2}} \int_0^{\infty} J_0(k_0\beta a) S_{pf}^*(m,1,1,\beta,\alpha) k_0^2 \beta d\beta d\alpha, \tag{3.145}$$

with $m = 1, 2, \ldots, N_1 + N_2$, in which it is again assumed that $z_1' = h_1$ and where $S_{pf}(m,1,1,\beta,\alpha)$ is given by expression (A.18) in appendix A. The integral over β that appears in the extracted term $\tilde{V}_{t,m}^{ex}$ is of the same type as the integral I_3 given by (3.125), and can therefore be evaluated in closed form.

3.9 Results

The calculated results presented in this section are obtained by using the thick-substrate model of section 3.2.3. The antenna characteristics are found by solving the matrix equation (3.15).

3.9.1 Validation of the model

In section 3.4 of this thesis several types of basis functions were discussed that can be used in a method-of-moments procedure for the analysis of microstrip antennas. The question is now: which set of basis functions and how many of them must be used on the patches and on the coaxial probe to obtain accurate results with a minimum use of computer time and computer memory? And, when is a solution accurate enough? This last question may be answered if we take a closer look at the tolerances of the materials and at the production techniques of microstrip antennas. If, for example, Duroid 6002 with $\varepsilon_r = 2.94$ is used, a typical error of $\pm 1\frac{1}{2}\%$ in the nominal value of the permittivity ε_r occurs, and an error of $\pm 3\%$ in the thickness of the substrate. The patches can usually be etched with an accuracy of $\pm 1\%$. Other errors that can be made are an inaccurate positioning of the coaxial cable and a misalignment of the patches in a stacked configuration. In addition to these construction errors, errors will be made in the measurements. We have done our measurements in the Compact Antenna Test Range of the Eindhoven University of Technology. A HP 8510 B network analyser was used to perform the actual measurements. Errors in the measurements can be minimized if a proper calibration set is used. For an accurate measurement of the input impedance, one has to be sure that the reference plane is positioned very accurately. In summary, a number of errors can occur when a microstrip antenna is constructed and measured. It is therefore useless to put much effort in the development of an extremely accurate model for the analysis of microstrip antennas. A certain error level in the predicted characteristics of a microstrip antenna is acceptable.

Table 3.1 shows the calculated resonant frequency and the corresponding maximum input resistance R_{in} for three single-layer, linearly polarised ($y_s = 0$) microstrip antennas with varying thickness. The resonant frequency is defined as the frequency for which the real part of the input impedance, i.e., R_{in}, has its maximum. The calculations were made with the thick-substrate model of section 3.2.3 with rooftop basis functions on the coaxial probe. The dimensions of the antennas are given in table 3.2. The calculations were done with each of the three sets of basis functions of section 3.4.1. The first two sets consist of entire-domain basis functions, where the first set (set 1) is given by expressions (3.30) and (3.31) and the second set (set 2) is given by (3.33) and (3.34) and includes the behaviour of the current near the edges of the patches. In [44] it was shown that with 14 x-directed basis functions and 4 y-directed basis functions of set 2, accurate results can be obtained. The third set (set 3), given by (3.36) and (3.37), contains subsectional rooftop basis functions.

	Number of modes	*Antenna 1*	*Antenna 2*	*Antenna 3*
f_r, set 1	$N_x = 4, N_y = 1$	0.623 GHz	1.875 GHz	6.1 GHz
R_{in}, set 1	$N_x = 4, N_y = 1$	86Ω	58Ω	50Ω
f_r, set 2	$N_x = 14, N_y = 4$	0.624 GHz	1.865 GHz	6.1 GHz
R_{in}, set 2	$N_x = 14, N_y = 4$	80Ω	50Ω	56Ω
f_r, set 3	15 subsections	0.623 GHz	1.872 GHz	6.15 GHz
R_{in}, set 3	15 subsections	86Ω	57Ω	58Ω

Table 3.1: *Calculated resonant frequency f_r and input resistance R_{in} for three sets of basis functions*

Antenna	h_2 *(mm)*	h_2/λ_ε	z_F *(mm)*	ε_r	W_{x1} *(mm)*	W_{y1} *(mm)*	x_s *(mm)*
1 [56]	3.175	0.01	3.175	2.56	150	75	15
2 EUT	3.175	0.03	3.175	2.33	49.6	49.6	7.25
3 EUT	6.61	0.22	6.36	2.33	11.5	11.5	4.6

Table 3.2: *Dimensions of antennas 1,2 and 3, with $h_2 = z_1' = z_2'$ and* $\tan\delta \approx 0.001$.

The differences between the calculated results with the three types of patch basis functions are in most cases smaller than the material tolerances of a typical microstrip structure and the expected error of the measurements. The resonant frequency can be calculated with a better accuracy than the resonant resistance. From an engineering point of view we may conclude that each of the sets of basis functions of section 3.4.1 gives acceptable results. From a computational point of view, however, it is recommended to use the first set of basis functions given by (3.30) and (3.31). Usually only a few modes of this set are needed to obtain fairly accurate results. From convergence tests in [19] and [57] it was also concluded that with the x-directed basis functions with $(m_p, m_q) = (1,0), (3,0), (5,0), (7,0)$ and with the y-directed basis function with $(m_p, m_q) = (0,2)$ from set 1, accurate results can be obtained for a linearly polarised microstrip antenna or microstrip array. This is especially important when arrays of microstrip antennas are considered (see chapter 4).

Antenna	h_2 *(mm)*	h_2/λ_0	ε_r	W_{x1} *(mm)*	W_{y1} *(mm)*	x_s *(mm)*	*Ref*
4	3.175	0.07	2.33	11	17	4	[11]
5	21.8	0.09	2.05	67.9	67.9	22	EUT [67]
6	1.27	0.01	10.2	20	30	3.5	[62]
7	1.27	0.06	10.2	9.5	15	1.55	[62]
8	2.54	0.06	10.2	19	30	3	[62]
9	0.79	0.01	2.22	25	40	8.5	[62]
10	0.79	0.02	2.22	12.5	20	4.25	[62]
11	1.52	0.02	2.22	25	40	8.5	[62]

Table 3.3 *Dimensions of antennas 4 to 11, with* $h_2 = z_1' = z_2' - z_f$

We have compared our calculations with experimental data from several publications in the literature [69]. In table 3.3 eight microstrip antennas with varying thickness are given. All antennas are linearly polarised and are constructed on a single substrate layer ($h_2 = z_1' - z_2'$). Figure 3.27 shows the relative difference between the calculated and measured resonant frequencies of the antennas of table 3.2 and 3.3. In figure 3.28 the corresponding relative differences between the predicted and measured maximum value of the input resistance R_{in} is shown. The agreement between the calculated and measured results is in almost all cases

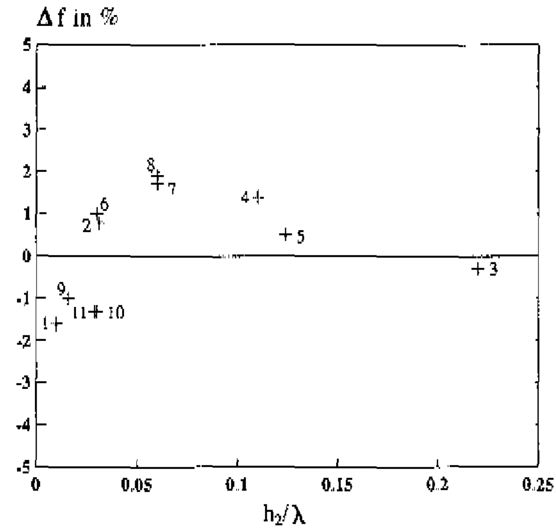

Figure 3.27: *Relative difference between calculated and measured resonant frequency.*

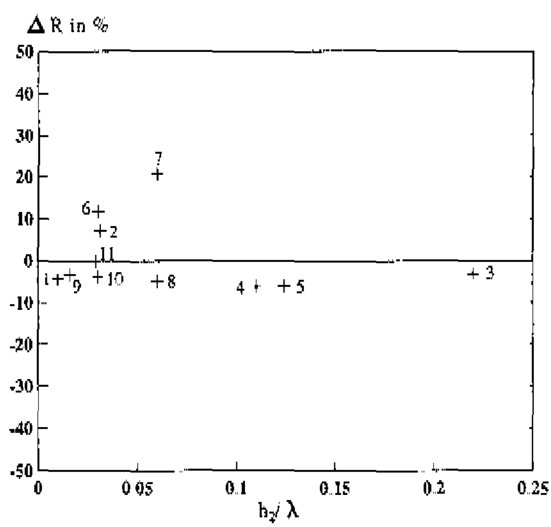

Figure 3.28: *Relative difference between calculated and measured resonant input resistance R_{in}.*

quite acceptable. The calculated results of antenna 6 to 11 are in much better agreement with the experiments of reference [62] than the calculated results presented in [62]. For example, the relative difference between the predicted resonant resistance (calculated with a method-of-moments procedure) in [62] and the measured resonant resistance of antenna 11 is more than 46%! The relative differences in figures 3.27 and 3.28 are in most cases not larger than the total error which could be caused by material tolerances, construction errors and errors made during the measurements. The relative differences for the resonant resistance are significantly larger than the relative differences for the resonant frequency. One of the reasons for this larger difference is the fact that the measured resonant resistance is more sensitive to errors made during the measurements. In addition, from table 3.1 it was already concluded that some error in the predicted resonant resistance can be expected. Other authors [62] have observed the same phenomena. From an engineering point of view, one may conclude that the model presented in this chapter is very suitable for an efficient and accurate analysis of microstrip antennas with electrically thin or with electrically thick substrates. Note that all the calculations were done with the thick-substrate model. On the patch sinusoidal entire-domain basis functions were used.

3.9.2 Single-layer microstrip antennas

In chapter 1 of this thesis, it was concluded that for many applications of microstrip antennas, a relative large impedance bandwidth is required. It is therefore interesting to investigate the bandwidth of a basic single-layer microstrip antenna. For that purpose, three configurations have been analysed constructed on three different substrates with a permittivity of $\varepsilon_r = 1.07$ (foam), $\varepsilon_r = 2.33$ (Duroid 5870) and $\varepsilon_r = 10.5$ (Duroid 6010), respectively. In each configuration a square patch was used, i.e. $W_{x1} = W_{y1}$. The feeding coaxial cable has a inner conductor with $a = 0.635$ mm and an outer conductor with $b = 2.1$ mm. Figure 3.29 shows the calculated relative bandwidth versus electrical substrate thickness h_2/λ, where λ is the wavelength in the dielectric material. The relative bandwidth is defined as the frequency band relative to the centre frequency for which the VSWR is lower than 2. The excitation point is located on the x-axis ($y_s = 0$). The location of the coaxial cable on the x-axis is chosen such that a maximum bandwidth is obtained. The characteristic impedance of the coaxial cable is $Z_0 = 50\Omega$ and the design frequency is approximately 5 GHz. From figure 3.29 it can be seen that the bandwidth increases with increasing substrate thickness. However, there appears to be a certain maximum bandwidth. This is caused by the fact that with increasing electrical thickness of the substrate, the inductance also increases. The maximum bandwidth obtained with foam is about 12% and is obtained for a substrate thickness of $h_2/\lambda = 0.085$. If a substrate with $\varepsilon_r = 2.33$ is used, a maximum bandwidth of approximately 15% can be obtained for $h_2/\lambda = 0.15$. Microstrip antennas on a high-permittivity material with $\varepsilon_r = 10.5$ are usually narrow band, except when very thick substrates are used.

Note that square patches were used, because they offer the opportunity to create a circularly polarised far-field pattern when the patch is excited with two coaxial cables. Circular polarisation

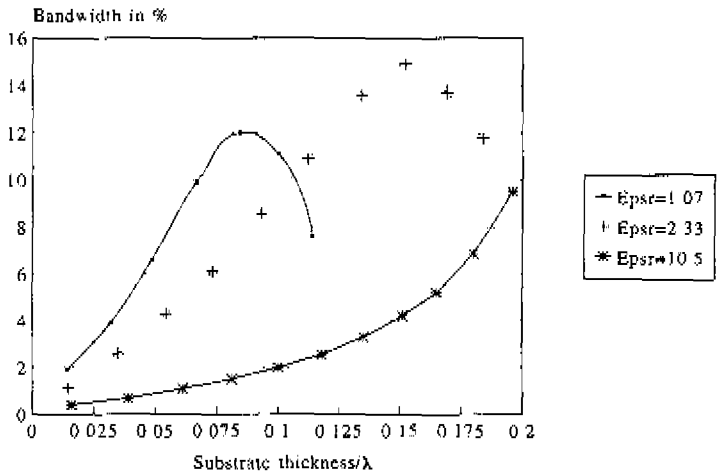

Figure 3.29: *Relative bandwidth of single-layer microstrip antennas, with* $Z_0 = 50\Omega$

is discussed in section 4.6 . Furthermore, the width of the patch (here denoted by W_y) has only a minor influence on the bandwidth of a microstrip antenna.

3.9.3 Stacked microstrip antennas

A stacked microstrip antenna usually has two closely spaced resonant frequencies. This results in a larger bandwidth or in dual-frequency operation. Two stacked microstrip configurations were built and measured. The first antenna is made on a Duroid 6002 dielectric substrate with design frequency of approximately 3.1 GHz Figure 3.30 shows the calculated bandwidth of such a stacked microstrip antenna versus the thickness of the second layer (d_2) and versus the dimensions of the upper square patch ($W_{x1} = W_{y1}$). The other dimensions of this antenna are given in table 3.4 The upper patch is located on top of the second layer, i.e. $z_2' = h_2 = d_1 + d_2$

Ant	$d_1 = z_1'$ (mm)	ε_r	$\tan\delta$	W_{x1} (mm)	(x_s, y_s) (mm)
12	3.04	2.94	0 0012	25 3	(8.5,0)

Table 3.4 *Dimensions of stacked microstrip antenna 12, with* $W_{x1} = W_{y1}$, $a = 0.635$ *mm and* $b = 2.1$ *mm.*

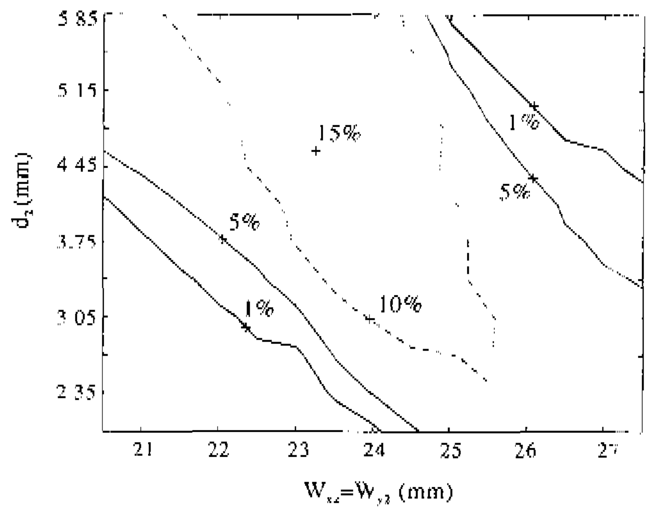

Figure 3.30: *Contour plot of the relative bandwidth of a stacked microstrip antenna, with* $Z_0 = 50\Omega$.

Note that linear interpolation was used between the calculated points in figure 3.30. With the configuration of table 3.4 a bandwidth ranging from 10% to 15% can easily be obtained. The maximum bandwidth is approximately 16.5%. A stacked microstrip antenna on Duroid 6002 was constructed with $d_2 = 3.04$ mm and with $W_{x2} = W_{y2} = 25$ mm. The other dimensions are the same as in table 3.4. In figure 3.31 the calculated and measured input impedance of this antenna are plotted in a Smith chart. The curl that appears in the Smith chart illustrates that the antenna has two closely spaced resonances, resulting in a relatively large bandwidth. Figures 3.32 and 3.33 show the corresponding plots of the measured and predicted amplitude and phase of the reflection coefficient. The agreement between the measured and the predicted reflection coefficient is good. The bandwidth of this stacked antenna is approximately 13%. Figure 3.34 shows the corresponding measured and calculated radiation pattern of this antenna in the E-plane ($\varphi = 0^0$) and in the H-plane ($\varphi = 90^0$) for $f = 3.1$ GHz. The agreement between the predicted and measured H-plane far-field pattern is quite good, except for $\theta \approx \pm 90^0$. The measured pattern in the E-plane shows a certain fluctuation. In [76] the Uniform Theory of Diffraction (UTD) was used to show that these fluctuations in the measured far-field pattern of this antenna are caused by diffraction of the field at the edges of the ground plane. The influence of diffraction from the edges of the ground plane can also be seen from the relative large difference between the calculated and measured far-field patterns of figure 3.34 for $\theta = \pm 90^0$. In our calculations an infinite ground plane and substrate are assumed. The size of the rectangular ground plane on

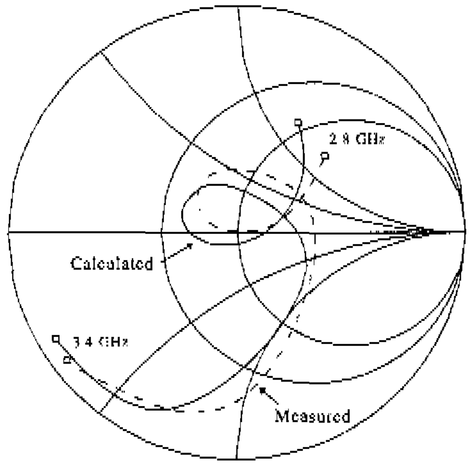

Figure 3.31 *Measured and calculated input impedance of antenna 12, with* $d_2 = 3.04$ *mm and with* $W_{x2} = W_{y2} = 25$ *mm*

which the antenna was made is 46 cm ×31 cm (length × width).

Another stacked microstrip antenna which has been built consists of two different dielectric layers. The first dielectric layer is made of Duroid 5870 with a relative permittivity of 2.33, and the top layer is made of foam with a relative permittivity of approximately 1.07. The other dimensions of this configuration are given in table 3.5. Figure 3.35 shows the measured and

Ant	$h_1 = z_1'$ (mm)	$h_2 = z_2'$ (mm)	ε_{r1}	ε_{r2}	W_{x1} (mm)	W_{x2} (mm)	x_s (mm)
13	1.57	6.28	2.33	1.07	29.5	35.4	13

Table 3.5 *Dimensions of stacked microstrip antenna 13, with* $W_{x1} = W_{y1}$, $W_{x2} = W_{y2}$, $x_s = y_s$, $\tan\delta_1 = 0.0012$, $\tan\delta_2 = 0.0008$, $a = 0.635$ *mm and* $b = 2.1$ *mm.*

predicted reflection coefficient. The calculations were performed with the thick-substrate model of section 3.2.3. The agreement between the calculated data and the measured data is fairly good. There is a difference of 3% between the measured and calculated resonant frequency, which is probably due to material and fabrication tolerances. In addition, the model for the attachment mode will not be very accurate in this configuration, because the coaxial probe is connected

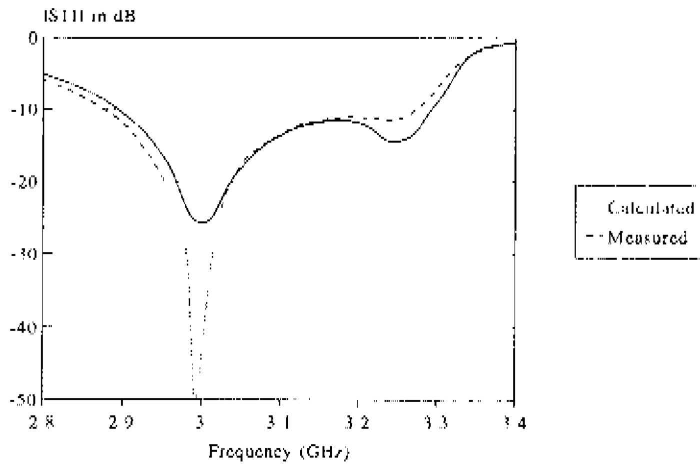

Figure 3.32: *Measured and calculated amplitude of the reflection coefficient of antenna 12, with* $d_2 = 3.04$ *mm and with* $W_{x2} = W_{y2} = 25$ *mm.*

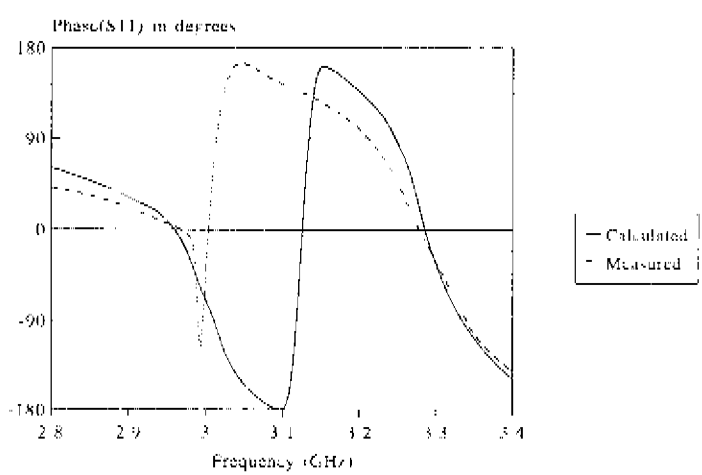

Figure 3.33: *Measured and calculated phase of the reflection coefficient of antenna 12, with* $d_2 = 3.04$ *mm and with* $W_{x2} = W_{y2} = 25$ *mm.*

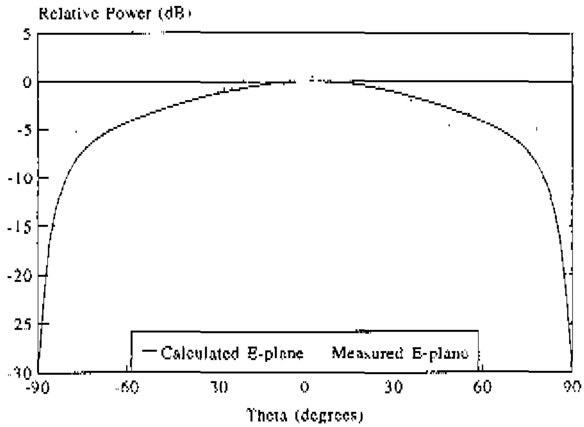

a) E-plane,

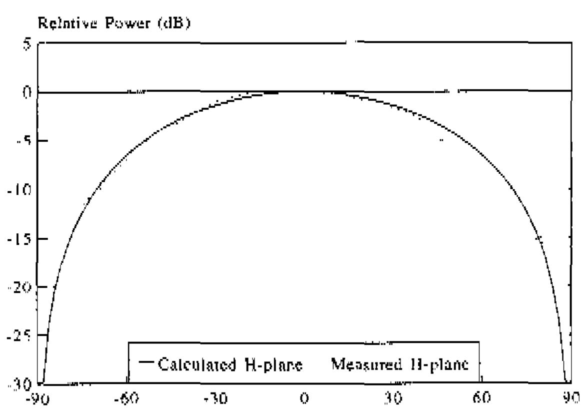

b) H-plane,

Figure 3.34: *Measured and calculated far-field pattern in the E- and H-plane of antenna 12, with* $d_2 = 3.04$ *mm and with* $W_{x2} = W_{y2} = 25$ *mm, and* $f = 3.1$ *GHz.*

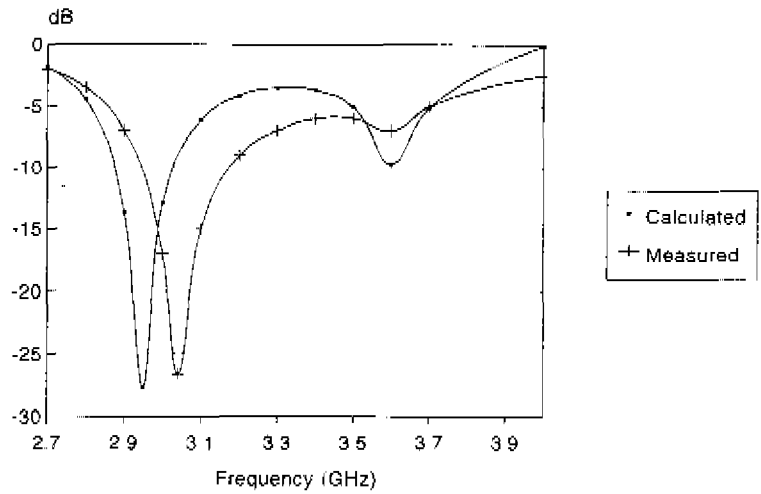

Figure 3 35: *Measured and calculated reflection coefficient*

near the edge of the lower patch. The antenna was originally designed with the thin-substrate model of section 3 2 2 using only 2 entire-domain sinusoidal modes on each patch, i.e with $N_{x1} = N_{y1} = N_{x2} = N_{y2} = 1$ [20] The predicted relative bandwidth with this model was approximately 19%, where the achieved (and also measured) bandwidth is approximately 7%.

3.9.4 Broadband multilayer structures

The second stacked microstrip antenna presented in the previous section was made on a multilayer structure with foam ($\varepsilon_r \approx 1$) as a top layer. The measured relative bandwidth of this antenna was about 7%, which is of course not very spectacular It is, however, possible to obtain a larger impedance bandwidth with multilayer structures. In the literature some designs of broadband stacked multilayer microstrip antennas have been presented [39, 75], where a relatively thick foam layer was used A serious drawback of these foam-based antennas is the fact that they have a high mutual-coupling level when used in an array configuration Because of the low permittivity of foam, the length of the upper patch is approximately equal to $\lambda_0/2$ This means that in an array configuration, where usually an element spacing of $\lambda_0/2$ is used, the distance between the edges of two adjacent array elements will be very small. This results in a high mutual coupling level We have studied another multilayer configuration with broadband characteristics and with a low mutual coupling level in an array configuration Figure 3 36 shows the side view of such a stacked two-layer configuration. The bottom layer is made of Duroid 6010 with a high relative

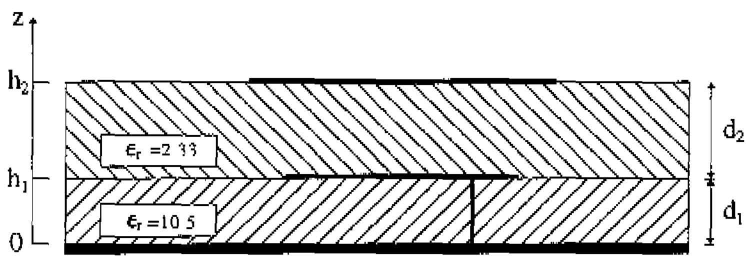

Figure 3 36: *Stacked two-layer microstrip antenna.*

permittivity of $\varepsilon_{r1} = 10.5$ and $\tan\delta_1 = 0.0023$. The top layer is made of Duroid 5880 with $\varepsilon_{r2} = 2\ 33$ and $\tan\delta_2 = 0\ 0012$. Due to the high permittivity of the first layer, the dimensions of both the lower and the upper patch will be much smaller than $\lambda_0/2$. Therefore, one could expect that this type of microstrip antenna will have a relatively low mutual coupling level in an array configuration. A drawback of high-permittivity materials is that more power will be lost in surface waves. More details about arrays of multilayer microstrip elements can be found in chapter 4. Bandwidths ranging from 15% to 25% can easily be achieved with these microstrip antennas. The bandwidth can be maximised if an optimal set of parameters is selected As an example we will take a closer look at the optimisation of an antenna with $d_1 = 1\ 27$ mm, $W_{x1} = W_{y1} = 11$ mm and $x_s = y_s = 4$ mm, fed by a coaxial cable with dimensions $a = 0\ 43$ mm and $b = 1.4$ mm Note that the antenna is fed on its diagonal, which reduces the cross-polarisation level of the antenna [35]. The first dielectric layer is electrically thin, so the length of the coaxial probe is small compared to the wavelength. The optimisation is done by varying the dimensions of the square upper patch ($W_{x2} = W_{y2}$) and by changing the thickness of the second layer (d_2) Figure 3.37 shows a contour plot of the predicted bandwidth (VSWR< 2) as a function of the thickness of the second layer (vertical axis) and as a function of the dimension of the upper patch (horizontal axis) The centre frequency is approximately 4.3 GHz. The maximum relative bandwidth is approximately 23% and is obtained for $d_2 = 4\ 5$ mm and for $W_{x2} = W_{y2} = 18\ 7$ mm.

Note that the high-permittivity material with $\varepsilon_r = 10\ 5$ could be replaced by a GaAs substrate

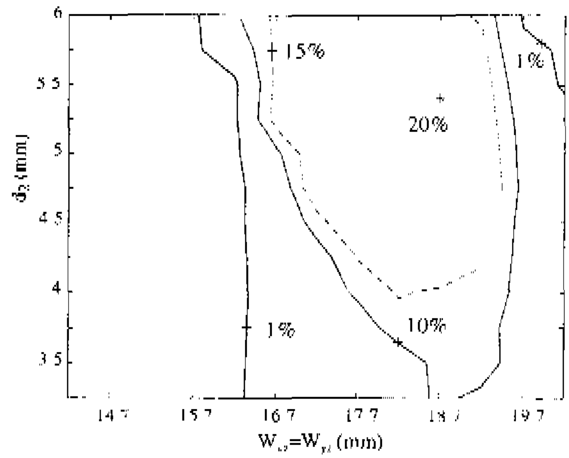

Figure 3.37: *Contour plot of the predicted relative bandwidth (VSWR< 2) of a stacked multilayer microstrip antenna, with $Z_0 = 50\Omega$.*

with a relative permittivity of $\varepsilon_r = 13$ and with a loss factor $\tan\delta = 0.006$. The use of GaAs offers the opportunity to integrate the antenna with the transmitter and receiver modules (T/R modules) if MMIC fabrication techniques are used. This would result in a large reduction of the total production costs of a phased-array microstrip antenna.

3.9.5 Dual-frequency/dual-polarisation microstrip antennas

Dual-frequency operation of a microstrip antenna can be obtained with at least two configurations. The first configuration is a stacked microstrip antenna of which the dimensions of the lower and upper patches are chosen such that the antenna is matched to 50Ω in two different frequency bands. Another way to obtain dual-frequency operation is shown in figure 3.38. In this case

Ant	$h_2 = z_1'$ (mm)	ε_r	$\tan\delta$	W_x (mm)	W_y (mm)	x_{f1} (mm)	y_{f2} (mm)
14	2.36	2.33	0.0012	23.2	14.65	2.5	5.25

Table 3.6: *Dimensions of dual-frequency, dual-polarisation, microstrip antenna 14 with a = 0.635 mm and b = 2.1 mm.*

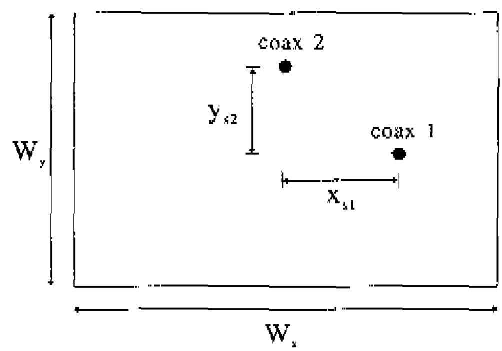

Figure 3.38: *Dual-polarised microstrip antenna for dual-frequency operation*

two coaxial cables are connected to a rectangular patch. This configuration can only be used if one wants to obtain both dual-frequency operation as well as dual polarisation. As an example, we will take a closer look at the single-layer configuration of table 3.6. Figure 3.39 shows the calculated VSWR at port 1 and at port 2 of the antenna. The antenna is matched to 50Ω in a frequency band of 2.6% around $f = 4$ GHz and in a frequency band of 7.2% around $f = 6$ GHz. With this type of microstrip antenna a dual-frequency, circularly polarised 2×2 subarray can be constructed. Such subarrays are investigated in section 4.8.8.

3.9.6 Broadband EMC microstrip antennas

The bandwidth of microstrip antennas can be improved if electrically thick substrates are used. This was already shown in chapter 1, where the bandwidth of several microstrip antennas was given as a function of the electrical thickness h_2/λ_ε. A drawback of thick substrates is the fact that the inductive part of the input impedance is usually very high, which means that a good impedance match with the feeding coaxial cable can only be achieved if a compensating input network is used. This input network increases the complexity and the overall costs of the antenna. A solution for this problem could be the so-called electromagnetically coupled (EMC) microstrip structure. The patch is now not physically connected to the coaxial cable. This configuration is shown in figure 3.2. The dimensions of the EMC microstrip antenna that we have designed are given in table 3.7. The gap between the top of the coaxial probe and the patch is 0.25 mm. In figure 3.40 the calculated and measured input impedance of the EMC microstrip antenna is shown. The calculations were done with 9 entire-domain basis functions on the patch and with 5 rooftop basis functions on the coaxial probe. The agreement between calculated and measured

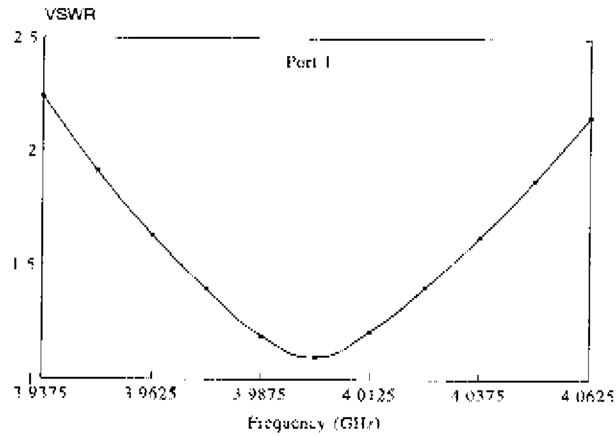

a) low-frequency operation.

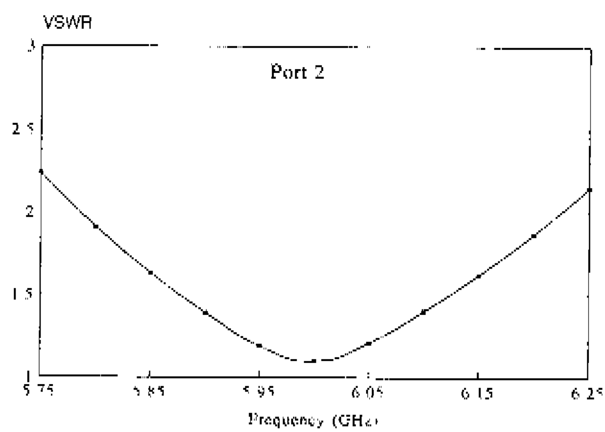

b) high-frequency operation.

Figure 3.39 *Calculated VSWR at port 1 and port 2 of a dual-frequency, dual polarisation microstrip antenna, with $Z_0 = 50\Omega$*

Ant	$h_2 = z'_1$ (mm)	z_f (mm)	ε_r	$\tan\delta$	W_{x1} (mm)	(x_s, y_s) (mm)
15	6.61	6.36	2.33	0.0012	11.5	(4 6,0)

Table 3.7: *Dimensions of an EMC microstrip antenna, with a = 0 635 mm, b = 2.1 mm and $W_{x1} = W_{y1}$*

data is quite good. The relative bandwidth is approximately 50% (VSWR< 2). Similar results

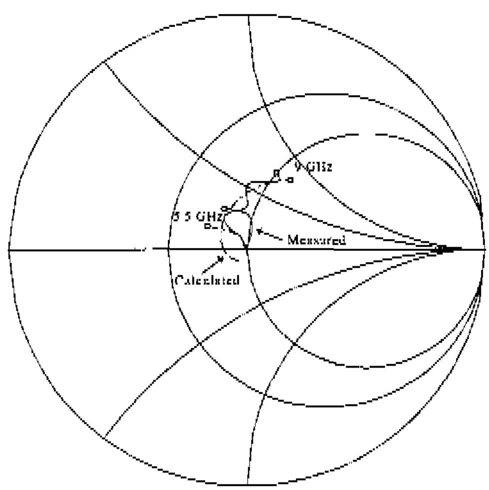

Figure 3 40 *Measured and calculated input impedance of the EMC antenna, $Z_0 = 50\Omega$.*

have been reported in [42]. Therefore, the EMC microstrip antenna seems to be an interesting candidate for future broadband phased-array antennas. In chapter 4, the behaviour of the EMC microstrip antenna in an array environment will be investigated. The predicted and measured far-field pattern in the E- and H-plane are plotted in figure 3 41, with f = 6 GHz The fluctuations in the measured patterns are caused by constructive and destructive interference of the diffracted fields from the edges of the ground plane [76]. The EMC microstrip antenna is made on an electrically thick substrate It is therefore expected that the antenna efficiency will be reduced due to the loss of power in surface waves. In [36] it was shown that about 22% of the total input power is lost in surface waves for the configuration of table 3.7. This corresponds with an efficiency of about 78%.

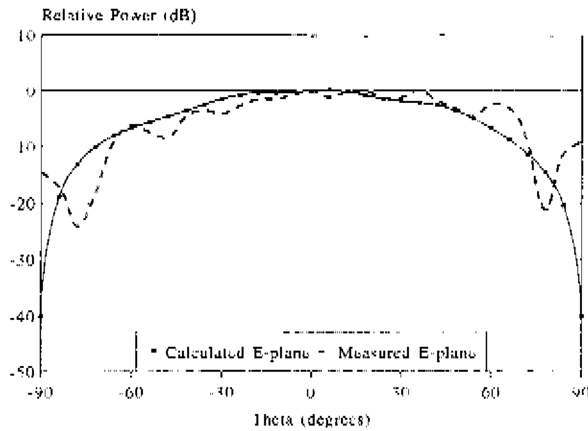

a) E-plane,

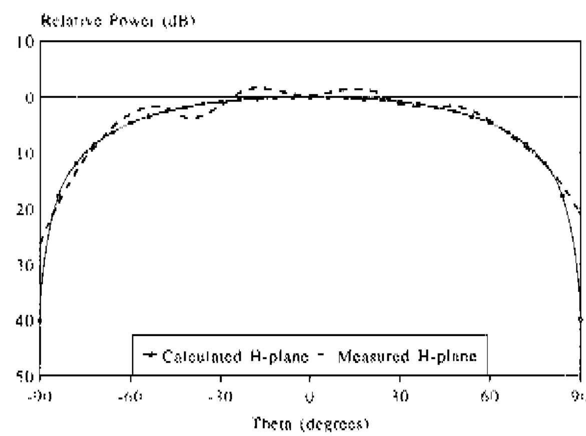

b) H-plane,

Figure 3.41 *Measured and calculated far-field pattern in the E- and H-plane of antenna 15, with $f = 6$ GHz*

Chapter 4

Finite arrays of microstrip antennas

4.1 Introduction

In chapter 1 of this thesis several applications of microstrip antennas have been discussed. Table 1.1 shows the corresponding antenna requirements of these applications. From this table it is obvious that the gain requirement cannot be fulfilled if only a single microstrip element is used, because the gain of one microstrip antenna is usually in the range between 5 and 9 dB. In most applications it will therefore become necessary to use more antenna elements, i.e., to use an array of microstrip antennas. The more elements used in an array, the higher the total antenna gain will be. To illustrate the principle of operation of an array antenna, the linear phased-array antenna of figure 4.1 with K elements will be investigated in more detail. The array consists of K identical,

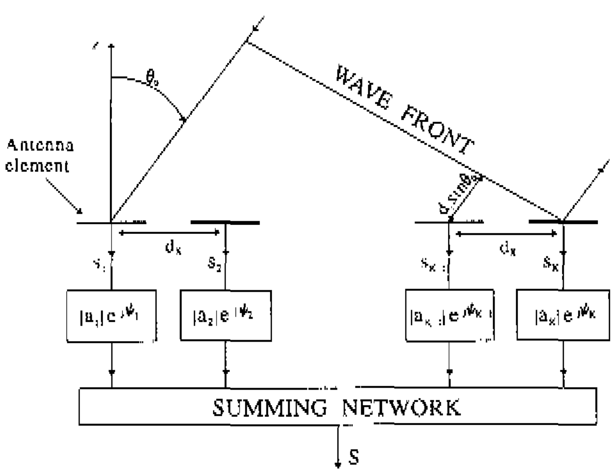

Figure 4.1: *Linear phased-array antenna.*

isotropic, radiating elements equally spaced with a distance d_x. Note that in a "real" microstrip phased-array antenna, the electromagnetic behaviour of the array elements will not be identical (due to mutual coupling) and they will also not have an isotropic radiation pattern. An incident wave arrives at an angle θ_0. The received signal at element k is then given by

$$s_k = \exp[jk_0(k-1)d_x \sin\theta_0], \quad \text{with } k_0 = 2\pi/\lambda_0, \tag{4.1}$$

where the received signal at array element 1 is normalised to $s_1 = 1$. The received signals are multiplied in the network layer with a so-called excitation vector $[a]$ of which the elements are given by

$$a_k = |a_k| \exp(-j\psi_k). \tag{4.2}$$

The received signal after summation is now given by

$$S(\theta_0) = \sum_{k=1}^{K} |a_k| \exp[jk_0(k-1)d_x \sin\theta_0] \exp(-j\psi_k) \tag{4.3}$$

$S(\theta_0)$ is the so-called array factor. The array factor is a periodic function of $\sin\theta_0$ with a period of λ_0/d_x. The array factor $S(\theta_0)$ can be maximised if the phase shift ψ_k of each element equals the phase of the received signal:

$$\psi_k = k_0(k-1)d_x \sin\theta_0 \tag{4.4}$$

If not all the array elements have the same electromagnetical properties (due to mutual coupling for example) the received signal will deteriorate. The linear array of figure 4.1 can, of course, also be used as a transmitting antenna. The angle of maximum radiation is equal to θ_0 if the elements of the excitation vector $[a]$ have the phase given by (4.4). If the phase ψ_k is varied, the main beam of the array will *scan*. The array factor $S(\theta_0)$ can have more maxima for $-\pi/2 \leq \theta_0 \leq \pi/2$, due to the periodic nature of $S(\theta_0)$. These additional maxima are called *grating lobes*. They occur whenever the argument of $S(\theta_0)$ is a multiple of 2π. The larger the spacing between the array elements, the smaller the separation between two grating lobes. Grating lobes are unwanted, which implies that the element spacing has to be chosen such that grating lobes do not occur. Grating lobes can be avoided if the following condition is satisfied

$$d_x/\lambda_0 \leq \frac{1}{1 + |\sin\theta_0^{max}|}, \tag{4.5}$$

in which θ_0^{max} is the maximum angle to which the main beam of the antenna can be scanned without causing the appearance of a grating lobe.

The theory of linear arrays can easily be extended to the case of a two-dimensional planar phased array. Figure 4.2 shows a planar array of radiating elements, along with the notation to be used. The elements are placed on a rectangular grid. The distance between two array elements in the

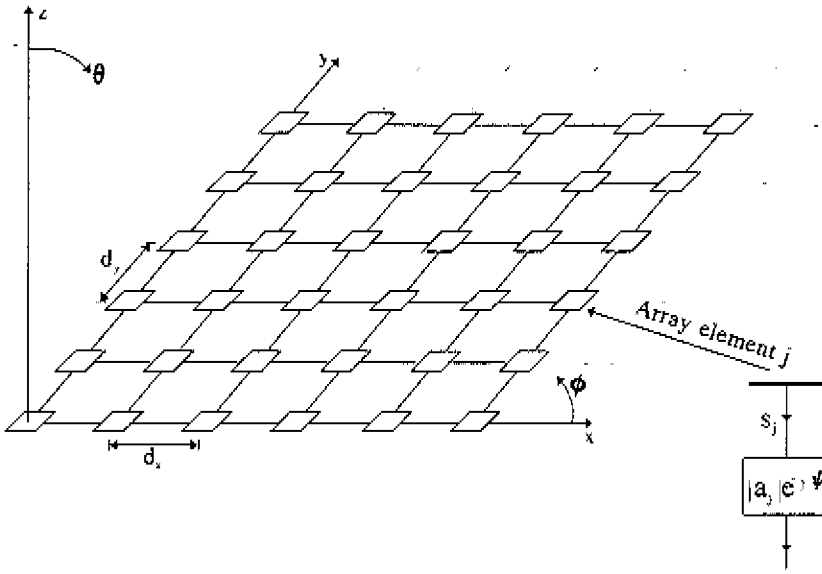

Figure 4.2: *Planar $K \times L$ phased-array antenna, with $k = 1, 2, \ldots K$ elements in the x-direction and $l = 1, 2, \ldots L$ elements in the y-direction and with $j = (l-1)K + k$*

x and y-direction is d_x and d_y, respectively. When the main beam of the array is directed to a certain angle (θ_0, ϕ_0), the elements of the excitation vector $[a]$ should have the form

$$a_j = |a_j| \exp\{-jk_0[(k-1)d_x u + (l-1)d_y v]\}, \tag{4.6}$$

with

$$u = \sin\theta_0 \cos\phi_0, \quad v = \sin\theta_0 \sin\phi_0, \quad j = (l-1)K + k$$

Often a so-called uniform amplitude taper is used to excite the array, which means that the amplitudes of the input signals of the array elements are all the same, so $|a_j| = 1$ for $j = 1, 2, \ldots K \times L$ [8]. It is, of course, also possible to use different amplitudes for each array element, in which case one speaks of an amplitude tapering or weighted illumination. The sidelobe level of an array can be lowered if a properly chosen amplitude taper is used. With an amplitude taper not all the elements are fed with the same energy, which results in a loss of antenna gain. Some frequently used tapers are the cosine-squared weigthing, the tapered-Taylor weighting and the Dolph-Chebyshev weighting [8]. A special form of tapering is space tapering. In this method, every active array element is fed with full power ($|a_j| = 1$), but now not all the array elements are made active, some are made passive (dummy elements).

There are several ways to design microstrip phased-array antennas. The first and commonly used design procedure is to use radiating elements which have been optimised with one of the models for isolated microstrip antennas. By doing this, mutual coupling effects between array elements are neglected. Mutual coupling deteriorates the (active) input impedance of each element and affects the radiation pattern and the polarisation characteristics of the total array. This becomes even more important if electrically thick, i.e. broadband, microstrip antennas are used, because it is expected that these thick elements will have a high mutual coupling level. A better way to design a microstrip phased-array antenna is by using a model that includes the mutual coupling between array elements. Two approaches can be distinguished. The first method is a very rigorous finite-array approach or element-by-element approach and the second method is an infinite-array approach [3, 4, 55, 57, 74]. Small arrays and elements near the edge of an array can only be properly analysed with a rigorous finite-array approach.

In this chapter, the model of chapter 2 for the analysis of isolated antennas is extended to the case of a finite microstrip phased-array antenna with $K \times L$ elements. The array elements are placed on a rectangular grid and can be linearly or circularly polarised (see section 4.6). The array elements are fed with coaxial cables. The thick-substrate model of section 3.2.3 is used, which means that the magnetic current distributions (3.3) in the coaxial apertures are used as sources.

Finally, in section 4.9 another type of antennas is investigated, namely finite arrays of monopoles embedded in a grounded dielectric slab. This type of array antenna can also be analysed with the methods presented in this thesis.

4.2 Configuration

The geometry of a finite array of identical microstrip elements is shown in figure 4.3, along with the notation to be used. Figure 4.4 shows a cross section of the configuration. The array elements are placed on a rectangular grid, and the array elements are uniformly spaced by distances d_x in the x-direction and d_y in the y-direction. The structure consists of two dielectric layers backed by a perfectly conducting infinite ground plane. Each array element may have two rectangular patches (stacked configuration), which are both located in layer 2, so $h_1 < z_1' < z_2' \leq h_2$. The geometry of a single array element is the same as the configuration shown in figure 3.1. So, the x- and y-dimensions of the lower patches are denoted by W_{x1} and W_{y1}, respectively, and the x- and y-dimensions of the upper patches denoted by W_{x2} and W_{y2}. The number of array elements in the x- and the y-direction is K and L, respectively. j is the array element index with $j = (l-1) \times K + k$. The centres of both the lower and upper patch of antenna element 1 ($k = l = 1$) are located at the coordinates $(x, y) = (0, 0)$. Each array element is fed by a coaxial

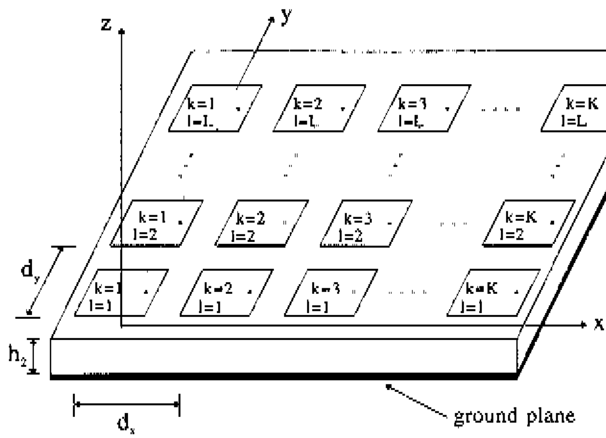

Figure 4.3: *Geometry of a finite microstrip array with $K \times L$ elements.*

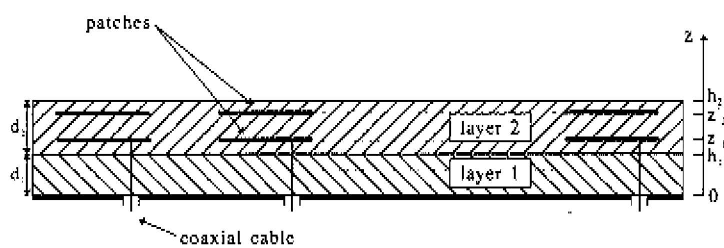

Figure 4.4: *Side view of the array configuration*

cable placed at the coordinates (x_s, y_s) relative to the centre of each array element. In this way, the far-field pattern will be linearly polarised. Circular polarisation is discussed in section 4.6. The feeding coaxial cables are modelled according to the thick-substrate model of section 3.2.3

4.3 Method-of-moments formulation

The same method as discussed in section 3.3 will be used in this chapter to find a solution for the unknown current distribution on each element of the finite microstrip array. Each array element will be treated in the same way. So, on every array element the same number of basis functions will be used to approximate the current distribution. The magnetic current distributions in the coaxial apertures act as sources, which corresponds to the thick-substrate model presented in section 3.2.3. The thin-substrate model can, of course, also be used to describe the feeding coaxial cables. More details about the implementation of the thin-substrate model to the case of a microstrip array can be found in references [3, 68]. The boundary conditions on all the patches and on all the coaxial probes are now used to obtain a system of integral equations for the unknown currents on each array element. These integral equations can be transformed into a set of linear equations by applying the method of moments. The only difference with the isolated microstrip-antenna problem of chapter 3 is the number of unknowns. We will again start with the boundary condition that on each patch and on each coaxial probe the total tangential electric field has to be zero

$$\vec{e}_\nu \times (\vec{\mathcal{E}}^{ex}(\vec{r}) + \vec{\mathcal{E}}^{s}(\vec{r})) = \vec{0}, \quad \vec{r} \in S_0, \tag{4.7}$$

where the surface S_0 denotes the surface of the patches and the probes and where $\vec{\mathcal{E}}^{ex}(\vec{r})$ is the excitation field which is generated by the magnetic current distribution at the coaxial apertures. The vector $\vec{e}_\nu$ is the unit normal vector on the surface S_0. The term $\vec{\mathcal{E}}^{s}(\vec{r})$ represents the scattered field that results from the induced currents on all the patches and probes of the array. Similar to the case of an isolated microstrip antenna, the unknown currents on each array element are expanded into a set of basis functions. The unknown current distribution on the array is then given by

$$\begin{aligned}
\vec{\mathcal{J}}(x, y, z) &= \sum_{i=1}^{K\times L} \vec{\mathcal{J}}_i(x, y, z) = \sum_{i=1}^{K\times L} \sum_{n=1}^{1+N_s+N_1+N_2} I_{in}\vec{\mathcal{J}}_{in}(x, y, z) \\
&= \sum_{i=1}^{K\times L} \left\{ I_{i1}\vec{\mathcal{J}}_i^{a}(x, y, z) + \sum_{n=2}^{N_s+1} I_{in}\vec{\mathcal{J}}_{in}^{f}(x, y, z) \right. \\
&\qquad \left. + \sum_{n=N_s+2}^{1+N_s+N_1+N_2} I_{in}\vec{\mathcal{J}}_{in}^{p}(x, y, z_n) \right\}
\end{aligned} \tag{4.8}$$

with

$$z_n = \begin{cases} z_1, & N_s + 2 \le n \le N_s + 1 + N_1, \\[2ex] z_2', & n > N_s + 1 + N_1, \end{cases}$$

where basis function $\vec{\mathcal{J}}_i^{a}$ represents the attachment mode on array element i, $\vec{\mathcal{J}}_{in}^{f}$ is a basis function on the feeding coaxial probe of array element i and $\vec{\mathcal{J}}_{in}^{p}$ represents one of the basis functions on the lower patch or on the upper patch of array element i. On each array element we will use 1 attachment mode, N_z basis functions on the coaxial probe, N_1 basis functions on the lower patch, and N_2 basis functions on the upper patch. The total number of basis functions is $N_{max} = K \times L \times (1 + N_z + N_1 + N_2)$. Possible types of basis functions that can be used have already been discussed in section 3.4. With the procedure described in section 3.3 we finally obtain a set of linear equations of the form

$$[Z][I] + [V^{ex}][V^p] = [0], \tag{4.9}$$

in which the elements of the matrices $[Z]$ and $[V^{ex}]$ are given by

$$\begin{aligned} Z_{jm,in} &= 4\pi^2 \iint_{S_{jm}} \vec{\mathcal{E}}^s_{in}(x,y,z) \cdot \vec{\mathcal{J}}_{jm}(x,y,z)\, dS, \\ V^{ex}_{jm,i} &= \frac{4\pi^2}{V^p_i} \iint_{S_{jm}} \vec{\mathcal{E}}^{ex}_i(x,y,z) \cdot \vec{\mathcal{J}}_{jm}(x,y,z)\, dS \\ &= -4\pi^2 \iint_{frill\ i} \vec{\mathcal{H}}^s_{jm}(x,y,0) \cdot \vec{\mathcal{M}}_{frill\ i}(x,y,0)\, dx dy, \end{aligned} \tag{4.10}$$

where S_{jm} denotes the surface on which basis function m on array element j is nonzero and where $\vec{\mathcal{M}}_{frill\ i}(x,y,0)$ is the magnetic current distribution in the coaxial aperture of array element i, given by expression (3.3). $\vec{\mathcal{E}}^s_{in}(x,y,z)$ is the electric field due to the n-th current basis function on array element i and $\vec{\mathcal{H}}^s_{jm}(x,y,0)$ is the magnetic field caused by the m-th basis function on antenna element j. The symmetric matrix $[Z]$ contains $N_{max} \times N_{max}$ elements, $[I]$ is a vector with the N_{max} unknown mode coefficients, $[V^{ex}]$ is a $N_{max} \times (K \times L)$ matrix and $[V^p]$ is the $K \times L$-element vector of port voltages. The general structure of the method-of-moments matrices $[Z]$ and $[V^{ex}]$ is similar to that of (3.17) and (3.18):

$$[Z] = \begin{pmatrix} [Z^{aa}] & [Z^{af}] & [Z^{ap}] \\ [Z^{fa}] & [Z^{ff}] & [Z^{fp}] \\ [Z^{pa}] & [Z^{pf}] & [Z^{pp}] \end{pmatrix}; \tag{4.11}$$

and

$$[V^{ex}] = \begin{pmatrix} [V^{ex\ a}] \\ [V^{ex\ f}] \\ [V^{ex\ p}] \end{pmatrix}, \tag{4.12}$$

where the superscript a denotes an attachment mode, f a basis function on one of the coaxial probes, and p a basis function on one of the patches. The elements of $[Z]$ and $[V^{(i)}]$ can again be expressed in terms of the spectral-domain dyadic Green's functions $\bar{\bar{Q}}^{E}_{\nu}$ and $\bar{\bar{Q}}^{H}_{\nu}$ of chapter 2. We finally obtain the following expressions for the elements of $[Z]$ (extensions of expressions (3.19) and (3.20))

$$
\begin{aligned}
Z^{aa}_{ji} &= 4\pi^2 \iint_{S_{j1}} \vec{\mathcal{E}}^{s\,a}_{i}(x,y,z) \cdot \vec{\mathcal{J}}^{a}_{j}(x,y,z)\, dS \\
&= \int_{-\infty}^{\infty}\int_{-\infty}^{\infty}\int_{0}^{z_1}\int_{0}^{z_1} \left[\bar{\bar{Q}}^{E}_{\nu}(k_x,k_y,z,z_0) \cdot \vec{J}^{a}_{i}(k_x,k_y,z_0)\right] dz_0 \cdot \vec{J}^{a*}_{j}(k_x,k_y,z)\, dz\, dk_x\, dk_y \\
&= \int_{-\infty}^{\infty}\int_{-\infty}^{\infty}\int_{0}^{z_1}\int_{0}^{z_1} \left[\bar{\bar{Q}}^{E}_{\nu}(k_x,k_y,z,z_0) \cdot \vec{J}^{a}_{1}(k_x,k_y,z_0)\right] dz_0 \\
&\qquad \cdot \vec{J}^{a*}_{1}(k_x,k_y,z)\, dz\, e^{-jk_x s_{xji}} e^{-jk_y s_{yji}}\, dk_x\, dk_y, \\
Z^{fa}_{jm,i} &= \int_{-\infty}^{\infty}\int_{-\infty}^{\infty}\int_{0}^{z_1}\int_{0}^{z_1'} \left[\bar{\bar{Q}}^{E}_{\nu}(k_x,k_y,z,z_0) \cdot \vec{J}^{a}_{1}(k_x,k_y,z_0)\right] dz_0 \\
&\qquad \cdot \vec{J}^{f*}_{1m}(k_x,k_y,z)\, dz\, e^{-jk_x s_{xji}} e^{-jk_y s_{yji}}\, dk_x\, dk_y, \\
Z^{ff}_{jm,in} &= \int_{-\infty}^{\infty}\int_{-\infty}^{\infty}\int_{0}^{z_1}\int_{0}^{z_1} \left[\bar{\bar{Q}}^{E}_{\nu}(k_x,k_y,z,z_0) \cdot \vec{J}^{f}_{1n}(k_x,k_y,z_0)\right] dz_0 \\
&\qquad \cdot \vec{J}^{f*}_{1m}(k_x,k_y,z)\, dz\, e^{-jk_x s_{xji}} e^{-jk_y s_{yji}}\, dk_x\, dk_y, \\
Z^{pa}_{jm,i} &= \int_{-\infty}^{\infty}\int_{-\infty}^{\infty}\int_{0}^{z_1} \left[\bar{\bar{Q}}^{E}_{2}(k_x,k_y,z_m,z_0) \cdot \vec{J}^{a}_{1}(k_x,k_y,z_0)\right] dz_0 \\
&\qquad \cdot \vec{J}^{p*}_{1m}(k_x,k_y,z_m)\, e^{-jk_x s_{xji}} e^{-jk_y s_{yji}}\, dk_x\, dk_y, \\
Z^{pf}_{jm,in} &= \int_{-\infty}^{\infty}\int_{-\infty}^{\infty}\int_{0}^{z_1'} \left[\bar{\bar{Q}}^{E}_{2}(k_x,k_y,z_m,z_0) \cdot \vec{J}^{f}_{1n}(k_x,k_y,z_0)\right] dz_0 \\
&\qquad \cdot \vec{J}^{p*}_{1m}(k_x,k_y,z_m)\, e^{-jk_x s_{xji}} e^{-jk_y s_{yji}}\, dk_x\, dk_y, \\
Z^{pp}_{jm,in} &= \int_{-\infty}^{\infty}\int_{-\infty}^{\infty} \left[\bar{\bar{Q}}^{E}_{2}(k_x,k_y,z_m,z_n) \cdot \vec{J}^{p}_{1n}(k_x,k_y,z_n)\right] \\
&\qquad \cdot \vec{J}^{p*}_{1m}(k_x,k_y,z_m)\, e^{-jk_x s_{xji}} e^{-jk_y s_{yji}}\, dk_x\, dk_y.
\end{aligned}
\tag{4.13}
$$

with

$$\nu = 1, \quad \text{if } 0 \le z \le h_1,$$

$$\nu = 2, \quad \text{if } h_1 \le z \le h_2,$$

and the elements of the matrix $[V^{ex}]$ can be rewritten to the following form:

$$
\begin{aligned}
V^{ex\,a}_{j\,i} &= -\int_{-\infty}^{\infty}\int_{-\infty}^{\infty}\left[\int_0^{z_1}\bar{\bar{Q}}_1^H(k_x,k_y,0,z_0)\cdot\vec{J}^a_j(k_x,k_y,z_0)dz_0\right]\cdot\vec{M}^*_{frill\,i}(k_x,k_y)dk_xdk_y \\
&= -\int_{-\infty}^{\infty}\int_{-\infty}^{\infty}\left[\int_0^{z_1}\bar{\bar{Q}}_1^H(k_x,k_y,0,z_0)\cdot\vec{J}^a_1(k_x,k_y,z_0)dz_0\right] \\
&\qquad\cdot\vec{M}^*_{frill\,1}(k_x,k_y)e^{jk_xS_{xji}}e^{jk_yS_{yji}}dk_xdk_y, \\
V^{ex,f}_{jm,i} &= -\int_{-\infty}^{\infty}\int_{-\infty}^{\infty}\left[\int_0^{z_1}\bar{\bar{Q}}_1^H(k_x,k_y,0,z_0)\cdot\vec{J}^f_{1m}(k_x,k_y,z_0)dz_0\right] \\
&\qquad\cdot\vec{M}^*_{frill\,1}(k_x,k_y)e^{jk_xS_{xji}}e^{jk_yS_{yji}}dk_xdk_y, \\
V^{ex,p}_{jm\,i} &= -\int_{-\infty}^{\infty}\int_{-\infty}^{\infty}\left[\bar{\bar{Q}}_1^H(k_x,k_y,0,z_m)\cdot\vec{J}^p_{1m}(k_x,k_y,z_m)\right] \\
&\qquad\cdot\vec{M}^*_{frill\,1}(k_x,k_y)e^{jk_xS_{xji}}e^{jk_yS_{yji}}dk_xdk_y,
\end{aligned}
\tag{4.14}
$$

where $\vec{J}^a_1(k_x,k_y,z)$ is the Fourier transform of the attachment mode on antenna element 1, $\vec{J}^f_{1n}(k_x,k_y,z)$ is the Fourier transform of the n-th basis function on the probe of antenna element 1, $\vec{J}^p_{1m}(k_x,k_y,z_m)$ is the Fourier transform of a basis function on one of the patches of antenna element 1, and $\vec{M}_{frill\,1}(k_x,k_y)$ is the Fourier transform of the magnetic current distribution in the coaxial aperture of antenna element 1, given by (3.22). S_{xji} and S_{yji} are the distances in the x- and the y-direction between the centres of antenna element j and antenna element i, respectively. The integrations over z and z_0 in (4.13) and (4.14) can be carried out analytically. It can also be shown that the two-dimensional integral over k_x and k_y in $Z^{aa}_{j\,i}$, $Z^{fa}_{jm,i}$, $Z^{ff}_{jm,in}$, $V^{ex\,a}_{j\,i}$ and $V^{ex\,f}_{jm\,i}$ can be reduced to a single, one-dimensional integral. The detailed expressions for the elements of the matrix $[Z]$ and of the matrix $[V^{ex}]$ are given in appendix A and appendix B, respectively. The computational and numerical details are discussed in section 4.7.

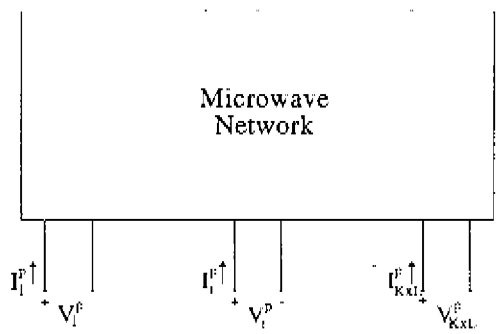

Figure 4.5 *$K \times L$-port network.*

4.4 Port admittance matrix and scattering matrix

One of the advantages of a rigorous finite-array approach is the fact that the complete port admittance matrix $[Y^p]$ and the port scattering matrix $[S]$ are known once the elements of the method-of-moments matrices $[Z]$ and $[V^{ex}]$ have been determined. This means that the array is characterised for all scan angles. If, on the other hand, an infinite-array approach is used [3, 57], the method-of-moments procedure has to be carried out for each possible scan angle. Figure 4.5 shows the finite $K \times L$-element array represented by a $K \times L$-port microwave network. The theory presented in this section is an extension of the theory of section 3.6. The relation between the port currents $[I^p]$ and port voltages $[V^p]$ is defined by

$$[I^p] = [Y^p][V^p] \tag{4.15}$$

The relation between port current I_i^p and port voltage V_i^p can also be characterised by [32, p. 393] (see section 3.6)

$$I_i^p = \frac{P_{in}^{i*}}{V_i^{p*}} - -\iint_{feed\,i} \vec{\mathcal{H}} \cdot \vec{\mathcal{M}}^*_{feed\,i}\, dS_i \tag{4.16}$$

in which $\vec{\mathcal{H}}$ is the total magnetic field and $\vec{\mathcal{M}}^*_{feed\,i}$ is the complex conjugate of the magnetic current distribution in the coaxial aperture of array element i. P_{in}^i is the total complex power supplied by source i. Note that $\vec{\mathcal{H}}$ is the magnetic field due to the currents on all the patches and probes of the array. We can therefore write the magnetic field $\vec{\mathcal{H}}$ in terms of the N_{max} unknown mode coefficients $[I]$:

$$\vec{\mathcal{H}}(x,y,z) = \sum_{j=1}^{K\times L}\left\{I_{j1}\vec{\mathcal{H}}_j^a(x,y,z) + \sum_{m=2}^{1+N_z} I_{jm}\vec{\mathcal{H}}_{jm}^f(x,y,z) + \sum_{m=N_z+2}^{1+N_z+N_1+N_2} I_{jm}\vec{\mathcal{H}}_{jm}^p(x,y,z)\right\}, \tag{4.17}$$

in which $\vec{\mathcal{H}}_j^a$, $\vec{\mathcal{H}}_{jm}^f$ and $\vec{\mathcal{H}}_{jm}^p$ are the magnetic fields due to the attachment mode, an expansion function on the coaxial probe, and a mode on one of the patches of array element j, respectively. Substitution of (4.17) in (4.16) gives the relation

$$[I^p] = \frac{1}{4\pi^2}[V^{ex}]^T[I] = -\frac{1}{4\pi^2}[V^{ex}]^T[Z]^{-1}[V^{ex}][V^p], \tag{4.18}$$

where matrix equation (4.9) was used. The port admittance matrix can now be calculated from

$$[Y^p] = -\frac{1}{4\pi^2}[V^{ex}]^T[Z]^{-1}[V^{ex}]. \tag{4.19}$$

Note that expression (4.19) has the same form as (3.49) when the number of array elements is equal to 1. The scattering matrix $[S]$ can be calculated by means of the well-known relation [2]

$$[S] = \{Y_0[U] - [Y^p]\}\{Y_0[U] + [Y^p]\}^{-1}, \tag{4.20}$$

where $[U]$ is the unity matrix and where Y_0 is the characteristic admittance of the coaxial cables. Usually $Y_0 = 1/Z_0 = 1/50$ (Ω^{-1}). Another important parameter of a phased-array antenna is the so-called active reflection coefficient. The active reflection coefficient R_i is defined as the reflection coefficient at the terminals of array element i when the main beam of the array is scanned at a certain scan angle (θ_0, ϕ_0). The active reflection coefficient can be written in terms of the elements of the scattering matrix $[S]$ and the elements of the excitation vector $[a]$ (see (4.6)) as

$$R_i(\theta_0,\phi_0) = \sum_{j=1}^{K\times L} S_{ij}a_j \tag{4.21}$$

The active reflection coefficient R_i will be different for each array element in a finite array, because the array elements are not affected by mutual coupling in the same way.

4.5 Radiation characteristics

The far-field pattern of an array of microstrip antennas can be calculated with the same method as discussed in section 3.7 for isolated microstrip antennas. The only difference with the situation of section 3.7 is that we now have to sum all the contributions to the total far-field pattern of the currents on the $K \times L$ array elements. The main beam of the array can be scanned at a certain direction (θ_0, ϕ_0) by adjusting the amplitude and phase of the input signals. The far-field pattern of an array can according to formula (3.64) be written in terms of the spectral-domain electric field at the surface $z = h_2$, with $k_x = k_0 \sin\theta\cos\phi$ and $k_y = k_0 \sin\theta\sin\phi$, as

$$\vec{\mathcal{E}}(\vec{r}) = \frac{j k_0 e^{-jk_0 r}}{2\pi r} e^{jk_0 h_2 \cos\theta} \vec{e}_r \times \left[\vec{E}(k_x, k_y, h_2) \times \vec{e}_z\right], \tag{4.22}$$

in which $\vec{E}(k_x, k_y, h_2)$ is the spectral-domain electric field at the interface between region 2 and region 3, due to the currents on all the $K \times L$ array elements, so

$$\begin{aligned}\vec{E}(k_x, k_y, h_2) = \sum_{j=1}^{K \times L} \Bigg\{ & I_{j1} \int_0^{z_1} \bar{\bar{Q}}_2^{r}(k_x, k_y, h_2, z_0) \cdot \vec{J}_j^{r}(k_x, k_y, z_0) dz_0 \\ & + \sum_{m=2}^{N_z+1} I_{jm} \int_0^{z_1} \bar{\bar{Q}}_2^{F}(k_x, k_y, h_2, z_0) \cdot \vec{J}_{jm}^{f}(k_x, k_y, z_0) dz_0 \\ & + \sum_{m=N_z+2}^{1+N_z+N_1+N_2} I_{jm} \bar{\bar{Q}}_2^{P}(k_x, k_y, h_2, z_m) \cdot \vec{J}_{jm}^{p}(k_x, k_y, z_m) \Bigg\},\end{aligned} \tag{4.23}$$

with

$$z_m = \begin{cases} z_1', & \text{if } N_z + 2 \le m \le N_z + 1 + N_1, \\ z_2', & \text{if } m > N_z + 1 + N_1 \end{cases}$$

The integrations over z_0 in (4.23) can be carried out analytically (in the same way as done in appendix A). The mode coefficients of the basis functions, i.e. the vector $[I]$, can be determined from the matrix equation (4.9), in which the input port voltage vector $[V^p]$ is given by

$$[V^p] = \{[U] + [S]\}[a], \tag{4.24}$$

where $[U]$ is again the unity matrix. The elements of the excitation vector $[a]$ are given by (4.6) and depend on the required scan angle (θ_0, ϕ_0). The gain of an array, when the main beam is directed to the angle (θ_0, ϕ_0), can be calculated with formula (3.70) in which the electric field is given by expression (4.22). The gain of an array can be approximated with the formula

$$G_t = 10\log_{10}(K \times L) + G_e \qquad \text{(dB)}, \tag{4.25}$$

in which G_e is the gain of a single array element. The above approximation is exact if all array elements are identical and if there is no mutual coupling between the array elements.

4.6 Circular polarisation

Many practical antenna applications require circularly polarised antennas. In mobile satellite communications, for example, a convenient way to maintain communication between the mobile user and the satellite under all circumstances is to use circularly polarised receive and transmit antennas. In radar applications, circular polarisation is often used during periods of rain. The electric field of a circularly polarised field can be divided into two components, i.e. a Right-Hand-Circularly (RHC) polarised wave and a Left-Hand-Circularly (LHC) polarised wave. So, the total electric field is divided into the following two components

$$\vec{\mathcal{E}} = \mathcal{E}_\theta \vec{e}_\theta + \mathcal{E}_\phi \vec{e}_\phi = \mathcal{E}_L \vec{e}_L + \mathcal{E}_R \vec{e}_R, \tag{4.26}$$

in which the unit vectors $\vec{e}_L$ and $\vec{e}_R$ are defined as

$$\begin{aligned} \vec{e}_L &= \frac{1}{\sqrt{2}}(\vec{e}_\theta + j\vec{e}_\phi), \\ \vec{e}_R &= \frac{1}{\sqrt{2}}(\vec{e}_\theta - j\vec{e}_\phi), \end{aligned} \tag{4.27}$$

and where the LHC- and RHC-components $\vec{\mathcal{E}}_L$ and $\vec{\mathcal{E}}_R$, respectively, are given by

$$\begin{aligned} \mathcal{E}_L &= \frac{1}{\sqrt{2}}(\mathcal{E}_\theta - j\mathcal{E}_\phi), \\ \mathcal{E}_R &= \frac{1}{\sqrt{2}}(\mathcal{E}_\theta + j\mathcal{E}_\phi) \end{aligned} \tag{4.28}$$

If one of these two components vanishes, the far field will be perfectly circularly polarised. Practical antenna systems, however, will always transmit or receive power from the unwanted component. Therefore, a quantity called axial ratio (AR) is introduced to describe the polarisation mismatch of the far field. The axial ratio is defined by

$$\mathrm{AR} = \left| \frac{|\mathcal{E}_L| + |\mathcal{E}_R|}{|\mathcal{E}_L| - |\mathcal{E}_R|} \right| \tag{4.29}$$

So if AR $= 1$ (=0 dB), the fields are perfectly circularly polarised. A circularly polarised far-field pattern can be created with one of the two microstrip configurations shown in figure 4.6. The most common method to create a circularly polarised field with square microstrip patches is shown in figure 4.6a, where two coaxial cables are connected to the microstrip antenna. The input signals have a relative phase difference of 90^0. If such an element is placed in an array of which the beam is scanned to an angle (θ_0, ϕ_0), the excitation vector $[a]$ should have the following form

$$a_{j\nu} = |a_j| \begin{cases} \exp\{-jk_0[(k-1)d_x u + (l-1)d_y v]\}, & \text{if } \nu = 1, \\ \exp\{-jk_0[(k-1)d_x u + (l-1)d_y v] + j\frac{\pi}{2}\}, & \text{if } \nu = 2, \end{cases} \tag{4.30}$$

with $u = \sin\theta_0 \cos\phi_0$ and $v = \sin\theta_0 \sin\phi_0$. The second configuration of figure 4.6 is a 2×2 subarray of which the elements and the phases of the input signals are sequentially rotated [37]. Each element of the subarray is fed with only one coaxial cable, with orientation and phasing according to figure 4.6b. The distance between the elements in both the x and y direction is d_x. When such a subarray is placed in an array configuration with scan angle (θ_0, ϕ_0), the excitation vector $[a]$ should have the form

$$\begin{aligned} a_{j\nu} = \; & |a_j| \exp\{-jk_0[(k-1)2d_x u + (l-1)2d_x v]\} \\ & \times \begin{cases} 1, & \text{if } \nu = 1, \\ \exp(-jk_0 d_x u + j\dfrac{\pi}{2}), & \text{if } \nu = 2, \\ \exp(-jk_0 d_x v + j\dfrac{3\pi}{2}), & \text{if } \nu = 3, \\ \exp(-jk_0[d_x u + d_x v] + j\pi), & \text{if } \nu = 4, \end{cases} \end{aligned} \tag{4.31}$$

where the x and y-coordinates of subarray j are $(k-1)2d_x$ and $(l-1)2d_x$, respectively. A combination of the two techniques of figure 4.6 is also possible. This configuration is shown in figure 4.7. Due to the symmetry of this configuration, the influence of mutual coupling (between the eight input ports) on the polarisation characteristics for $\theta_0 = 0^0$ is eliminated, resulting in a 0 dB axial ratio for $\theta_0 = 0^0$.

4.7 Computational and numerical details

The expressions for the elements of the method-of-moments matrix $[Z]$ and matrix $[V^{ex}]$ are given in appendix A and appendix B, respectively. They have a similar form as the expressions for $[Z]$ and $[V^{ex}]$ in the case of an isolated microstrip element. So most of the numerical techniques presented in section 3.8 can also be applied here. The only difference is an extra function in the integrand, which depends on the distances in the x- and the y-direction, i.e. S_{xji} and S_{yji}, between

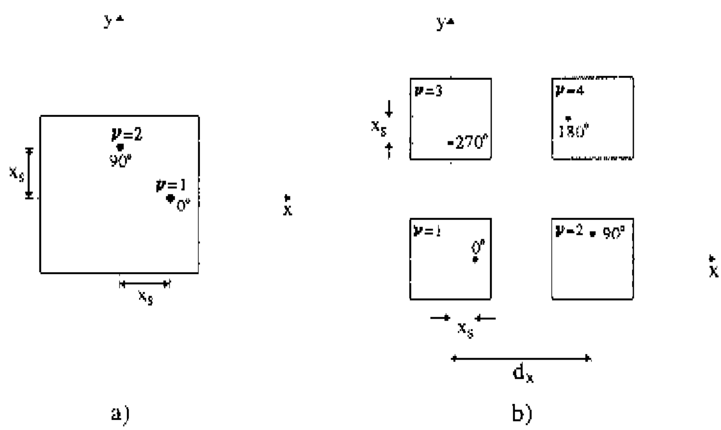

Figure 4.6: *Circularly polarised microstrip configurations*

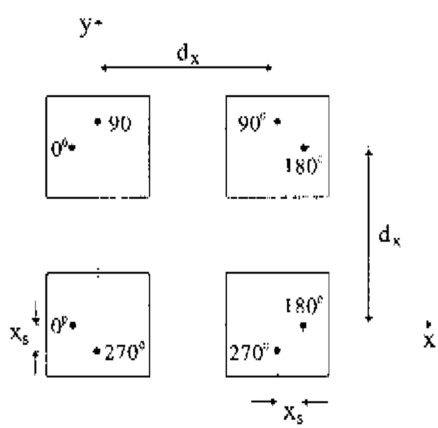

Figure 4.7: *Sequentially rotated subarray with two coaxial cables for each array element.*

array element j and array element i. As an example, let us take a closer look at an element of the submatrix $[Z^{aa}]$. According to (A.2), an element of $[Z^{aa}]$ is given by

$$Z^{aa}_{j,i} = \int_0^\infty f^{iso}(\beta) J_0(k_0 \beta R_{ji}) d\beta, \tag{4.32}$$

in which $R_{ji} = \sqrt{S^2_{xji} + S^2_{yji}}$ is the distance between the centre of array element j and the centre of array element i and where $f^{iso}(\beta)$ is the β-integrand in the case of an isolated microstrip antenna ($R_{ji} = 0$). Four important observations can be made from expression (4.32)

i Numerical problems due to surface waves and other singularities in $f^{iso}(\beta)$ can be eliminated with the analytical techniques presented in section 3.8.2.

ii An element $Z^{aa}_{j,i}$ depends only on the absolute distance between array element j and array element i. This implies that the submatrix $[Z^{aa}]$ has a Toeplitz structure. This saves a lot of computation time, because only the elements of the first row of $[Z^{aa}]$ need to be calculated.

iii Computation time can be saved if all elements of the matrix $[Z^{aa}]$ are calculated simultaneously, because the function $f^{iso}(\beta)$ then needs to be evaluated only once

iv As the distance R_{ji} between the array elements becomes larger, it will take more computation time to calculate the integral over β in (4.32) by direct numerical integration, because the number of oscillations for a certain β interval $(0, \beta_{max})$ in the Bessel function $J_0(k_0 \beta R_{ji})$ increases with increasing R_{ji}. A convenient way to avoid numerical difficulties for large values of R_{ji} is by using the asymptotic-form extraction technique, introduced in section 3.8.3

The above observations are also valid for the other elements of the matrix $[Z]$ and also for the elements of $[V^{e,e}]$. Item iv) leads to the conclusion that an efficient and accurate analysis of finite microstrip arrays is only possible if the asymptotic-form extraction technique is used to calculate the integrals with infinite boundaries. This technique is now even more important than it was for the isolated microstrip antenna case. Similar to (3.90), an element of $[Z]$ is written in the following form

$$\begin{aligned} Z_{jm,in} &= \int_0^\infty g_{jm,in}(\beta) d\beta \\ &= \int_0^\infty \left[g_{jm,in}(\beta) - \tilde{g}_{jm,in}(\beta) \right] d\beta + \int_0^\infty \tilde{g}_{jm,in}(\beta) d\beta \\ &= (Z_{jm,in} - \tilde{Z}_{jm,in}) + \tilde{Z}_{jm,in} \end{aligned} \tag{4.33}$$

in which $\tilde{Z}_{jm,in}$ is the extracted asymptotic part with

$$\tilde{Z}_{jm,in} = \int_0^{\infty} \tilde{g}_{jm,in}(\beta)d\beta$$

We have found a way to evaluate the extracted part analytically for each of the elements of the matrices $[Z]$ and $[V^{ex}]$. To that end, we have used similar analytical techniques as presented in section 3.8.3. The remaining integral in (4.33) can be evaluated numerically with a standard integration routine for complex functions. More details about the asymptotic-form extraction technique for finite microstrip arrays can be found in references [68, 71].
The electromagnetical coupling between two array elements decreases rapidly as the distance between both array elements increases. This phenomenon can be used to speed up the numerical calculations when the direct coupling between array elements which are located far away from each other is neglected. In this way the method-of-moments matrices $[Z]$ and $[V^{ex}]$ become sparse matrices. Three sets of parameters will be distinguished:

- (k_v, l_v): All interactions in the matrix $[V^{ex}]$ between modes and sources for which the distance in the x- and the y-direction is larger than $k_v \times d_x$ and $l_v \times d_y$, respectively, are zero. This affects $[V^{ex,a}]$, $[V^{ex,f}]$ and $[V^{ex,p}]$.
- (k_z^{f+a}, l_z^{f+a}): All interactions in the matrix $[Z]$ with a mode on one of the probes or an attachment mode for which the distance in the x- and the y-direction is larger than $k_z^{f+a} \times d_x$ and $l_z^{f+a} \times d_y$, respectively, are made zero. This affects the submatrices $[Z^{aa}]$, $[Z^{fa}]$, $[Z^{af}]$, $[Z^{pa}]$, $[Z^{ap}]$, $[Z^{pf}]$, $[Z^{fp}]$ and $[Z^{ff}]$.
- (k_z^p, l_z^p): All interactions in the matrix $[Z]$ with a mode on one of the patches for which the distance in the x- and the y-direction is larger than $k_z^p \times d_x$ and $l_z^p \times d_y$, respectively, are made zero. This only affects the submatrix $[Z^{pp}]$

The above technique was tested for an L-band, single-layer, 7×7 microstrip array antenna. The element spacing is approximately $0.5\lambda_0$. The dimensions of the array are given in table 4.1. Figures 4.8, 4.9 and 4.10 show the calculated mutual coupling coefficient $|S_{ji}|$ between the centre element of the array ($j = 25$) and array elements $i = 24$, $i = 18$ and $i = 1$ when one of the three sets of parameters is varied, while the other parameters are all equal to 7. From these three figures it is clear that a considerable amount of CPU time can be saved if not all the direct interactions between the basis functions are calculated. In most cases it will suffice to use $(k_v, l_v) = (1, 1)$, $(k_z^{f+a}, l_z^{f+a}) = (1, 1)$ and $(k_z^p, l_z^p) = (4, 4)$ to calculate the mutual coupling between the centre element and the other elements of a 7×7 array. If one is only interested in the coupling between adjacent array elements, even $(k_v, l_v) = (1, 1)$, $(k_z^{f+a}, l_z^{f+a}) = (1, 1)$ and $(k_z^p, l_z^p) = (2, 2)$ can be used. This method therefore results in a large reduction of the required computation time.

Array	$h_2 = z_1'$ (mm)	ε_r	$\tan\delta$	W_x (mm)	(x_s, y_s) (mm)	d_x (mm)
1	10	1.07	0.0008	97.5	(26,0)	115.3

Table 4.1: *Dimensions of microstrip array 1, with $W_x = W_y$, $d_x = d_y$, $a = 1.5$ mm and $b = 5$ mm*

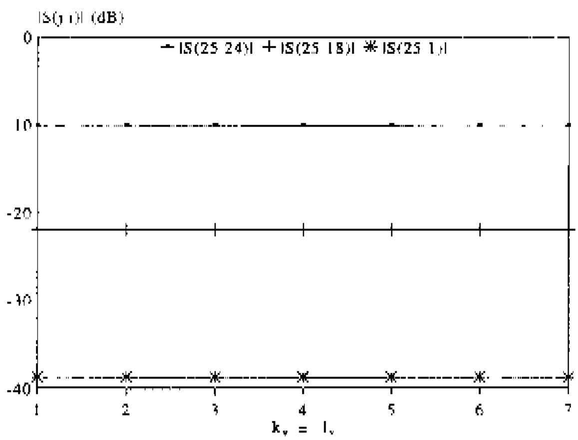

Figure 4.8 *Calculated S_{25i} for various (k_v, l_v) values, $f = 1.3$ GHz.*

In this way large arrays can be analysed while the overall computation time remains relatively short. If one considers the above example with $(k_v, l_v) = (1, 1)$, $(k_z^{f+a}, l_z^{f+a}) = (1, 1)$ and $(k_z^p, l_z^p) = (4, 4)$, the total number of elements of $[Z]$ and $[V^{ex}]$ that have to be calculated is reduced from approximately $49(2 + 2N_z + N_z^2 + 2(N_1 + N_2) + N_z(N_1 + N_2) + (N_1 + N_2)^2)$ to $2 + 2N_z + N_z^2 + 2(N_1 + N_2) + N_z(N_1 + N_2) + 16(N_1 + N_2)^2$. With $N_z = 3$, $N_1 = 5$ and $N_2 = 0$, this corresponds to a reduction of the total number of non-zero elements in $[Z]$ and $[V^{ex}]$ by a factor of $3283/442 \approx 7.5$. The CPU time needed to calculate the elements of $[Z]$ and $[V^{ex}]$, for a 7×7 array with the configuration of table 4.1, takes about 3 minutes and 50 seconds for a single frequency point on a 486PC computer.

Once the elements of $[Z]$ and $[V^{ex}]$ are known, the admittance matrix and the scattering matrix can be determined from (4.19). The inverse of the complex symmetric matrix $[Z]$ is calculated with a routine from the LINPACK library [21]. When small or medium-sized arrays are analysed,

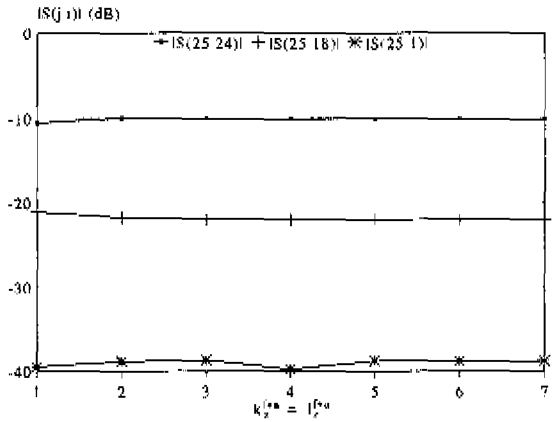

Figure 4.9: *Calculated S_{25i} for various (k_z^{f+a}, l_z^{f+a}) values, $f = 1.3$ GHz.*

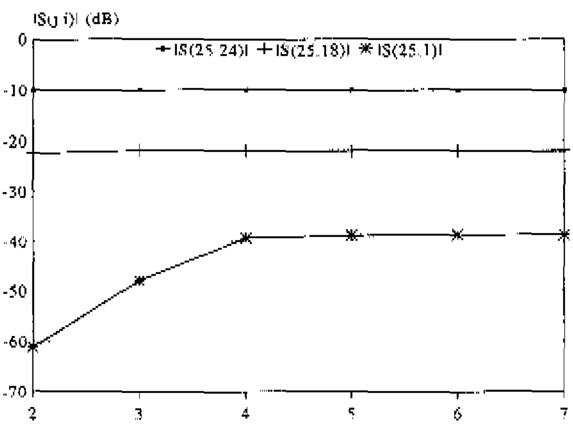

Figure 4.10 *Calculated S_{25i} for various (k_z^p, l_z^p) values, $f = 1.3$ GHz.*

the CPU time required to calculate the elements of $[Z]$ and $\{V^{ea}\}$ will be much longer than the CPU time required for the inversion of $[Z]$. However, if a large number of array elements is used, the inversion of $[Z]$ could require more attention. In that case an iterative method, such as the conjugate gradient method [34], can be employed for the solution of the method-of-moments matrix equation. Mutual coupling in very large microstrip arrays can be analysed by truncating the number of array elements which are used in the analysis In this way, mutual coupling between array elements which are located relatively close to each other can be calculated with a reasonable accuracy In most practical array configurations this will be no real limitation, because of the very low mutual coupling between elements which are located far away from each other. Another way to handle very large microstrip arrays is the infinite-array approach [4, 55, 57, 74] It should be noted, however, that the behaviour of array elements near the edges of a very large array cannot be handled with an infinite-array approach Therefore, the best way to design a very large microstrip array antenna is probably a combination of the finite-array approach and the infinite-array approach [3]

4.8 Results

In this section some microstrip array designs, obtained with the finite-array model, will be presented. In addition, the accuracy of the model is checked by comparing the calculated results with experimental data. Note that our finite-array approach and the corresponding software have also been verified in [3]. In [3] the calculated results from an infinite-array approach were compared with the results from our finite-array approach.

4.8.1 Introduction

When an isolated microstrip element is placed in an array environment, its electromagnetical behaviour is influenced by the presence of the other microstrip elements. The element distance in an array is usually somewhere between $0.5\lambda_0$ and $0.9\lambda_0$, depending on the maximum scan angle. So, the array elements are located close to each other in terms of the wavelength. In section 3.9 the bandwidth of several microstrip configurations was investigated. It was shown that isolated microstrip antennas with a large bandwidth can be constructed. An important question is now: how much will the bandwidth of such a microstrip antenna change if this antenna is placed in an array? Furthermore, each array element will have, in general, a different environment, which implies that each array element will behave differently. In this section our attention will be focused at the following three array characteristics:

- the mutual coupling S_{ji} between the array elements,
- the active reflection coefficient $R_j(\theta_0, \phi_0)$ of each array element,
- the radiation pattern of the array.

Mutual coupling causes the reflection coefficient of an element to differ from its isolated-element value, and to depend on the phasing of the array and on the location of the element in the array. Furthermore, the radiation pattern and the polarisation characteristics deteriorate because of the mutual coupling between the array elements. The bandwidth of an array could be defined as the frequency band for which the active reflection coefficient $R_j(\theta_0, \phi_0)$ is smaller than a certain value R_{max}, for a specified scan volume $0 \leq \theta_0 \leq \theta_{max}$ and $0 \leq \phi_0 \leq \phi_{max}$. Throughout this thesis a value of $|R_{max}| = 1/3$ is used, which corresponds to a VSWR ≤ 2.

The organisation of this section is as follows. In section 4.8.2 three single-layer microstrip arrays will be investigated and the numerical results will be compared with experiments. Next, in section 4.8.3 stacked microstrip arrays are discussed. The broadband multilayer structure with a high-permittivity substrate, presented in section 3.9.4, will be investigated in section 4.8.4. In section 4.8.5 arrays of broadband EMC microstrip antennas are analysed and the results are compared with experimental data. In section 4.8.6 the far-field pattern of finite microstrip arrays is investigated. Microstrip antennas and arrays with a circularly polarised far-field pattern are discussed in section 4.8.7. Finally, in section 4.8.8, a new type of dual-frequency subarrays with a circularly polarised far field is presented.

It should be noted that all mutual-coupling measurements were performed in an anechoic chamber, while the measurements were made with a Hewlett Packard HP8510B network analyser. In this way the effect of reflections against objects in the environment is minimised. While measuring the mutual coupling between two array elements, all the other array elements were terminated with 50Ω loads.

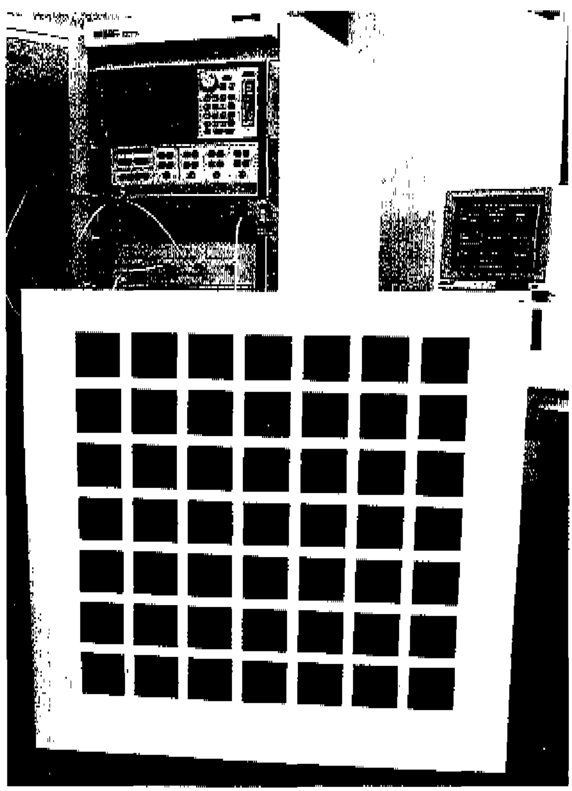

Figure 4.11: *Photograph of the* 7 × 7 *test array*

4.8.2 Single-layer microstrip arrays

The first microstrip array that will be investigated is a linearly polarised, L-band, 7 × 7 array made on a foam substrate with $\varepsilon_r = 1.07$. Foam-based microstrip arrays are easy to manufacture, inexpensive and have a light weight. The dimensions of the 7 × 7 microstrip array which was designed and constructed were given in table 4.1. The distance between the centres of the array

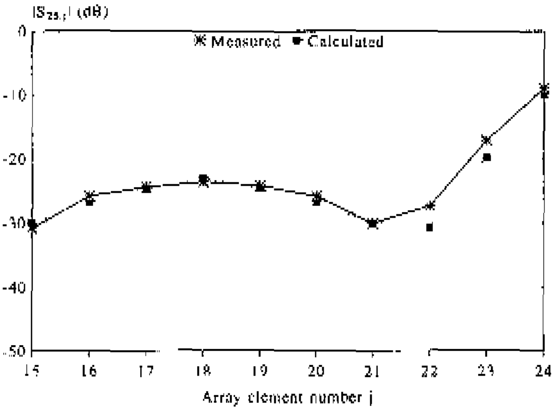

Figure 4.12: *Measured and calculated coupling coefficients between the centre element ($j = 25$) and the elements of the $l = 4$ and $l = 3$ row of 7×7 array I, with $j = (l-1)K + k$ and $f = 1.3$ GHz.*

elements is in both directions approximately $\lambda_0/2$. Due to the low relative permittivity of foam, the length and width of the patches are also approximately equal to $\lambda_0/2$. The spacing between the edges of two adjacent patches is therefore very small, which results in a high mutual-coupling level. Figure 4.11 shows a photograph of the 7×7 test array. The overall size of the array is $1\text{m} \times 1\text{m}$. Figure 4.12 shows the predicted and measured mutual-coupling coefficients at $f = 1.3$ GHz, between the centre element ($k = l = 4, j = 25$) and the elements along the $l = 3$ and $l = 4$ row. The measured resonant frequency is approximately $f = 1.32$ GHz, while the predicted resonant frequency is $f = 1.35$ GHz. The calculations were performed with 5 entire-domain sinusoidal basis functions on each patch and 2 subdomain rooftop basis functions on each coaxial probe. So the total number of basis functions on each array element is equal to 8. The agreement between the measured and the calculated coupling coefficients is fairly good. The disagreement is probably due to the finite size of the ground plane and due to the mismatch in resonant frequency (caused by material tolerances). Furthermore, the inaccuracy of the permittivity and the inaccuracy of the patch dimensions could be a potential source of errors. Figure 4.12 also shows that the coupling between two adjacent array elements, which are located in the same row, is very high. For example $S_{25,24} \approx -9$dB. This implies that the active reflection coefficient of each array element will also be very high. We may therefore conclude that microstrip antennas made on a single foam layer are not a good choice for constructing a microstrip phased-array antenna with an element spacing equal or almost equal to $\lambda_0/2$. Another

Array	h_1 (mm)	$h_2 = z_1'$ (mm)	ε_{r1}	ε_{r2}	W_{x1} (mm)	(x_s, y_s) (mm)	d_x (mm)
2	6.35	6.85	1.03	2.17	31.9	(11,0)	60

Table 4.2 *Dimensions of linear microstrip array 2, with $W_{x1} = W_{y1}$, $a = 0.635$ mm and $b = 2.1$ mm.*

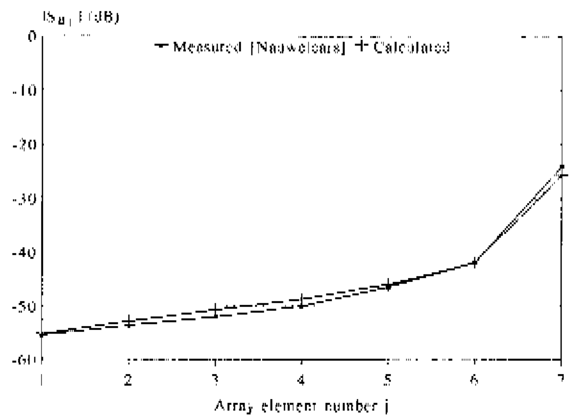

Figure 4.13 *Measured and calculated coupling coefficients between element ($j = 8$) and the other elements of linear array 2 with $f = 3.3$ GHz.*

microstrip array fabricated on a foam substrate is presented in [51]. This linear array consists of 8 single-layer microstrip elements ($K = 8$, $L = 1$). The 8 patches are mounted on a thin top layer with $\varepsilon_{r2} = 2.17$ and with $d_2 = 0.5$ mm. The other dimensions are given in table 4.2. Figure 4.13 shows a plot of the calculated and measured coupling coefficient between the last element ($j = 8$) and the other 7 elements of the linear array. The frequency is $f = 3.3$ GHz. Again 8 basis functions on each array element were used. The agreement between the calculations and measurements is excellent. The mutual coupling is lower than the mutual coupling in array 1 (figure 4.12), because a larger element spacing is used, namely $d_x \approx 0.66\lambda_0$.

Next, a single-layer microstrip array on a Duroid 5870 substrate with $\varepsilon_r = 2.33$ was designed. The thickness of the substrate is $h_2 = 2$ mm and the centre design frequency is $f = 5.4$ GHz. So, according to figure 3.29 of section 3.9.2, the relative bandwidth of an isolated microstrip antenna on this substrate with $h_2/\lambda = 0.055$ would be approximately 4.3%. The other array dimensions

Array	$h_2 = z_1'$ (mm)	ε_r	$\tan\delta$	W_{x1} (mm)	(x_s, y_s) (mm)	d_x (mm)
3	2	2.33	0.0012	17	(3.5,0)	28.3

Table 4.3: *Dimensions of microstrip array 3, with* $W_{x1} = W_{y1}$, $d_x = d_y$, $a = 0.635$ *mm and* $b = 2.1$ *mm.*

are specified in table 4.3. The element spacing is approximately $d_x = d_y = 0.5\lambda_0$. The maximum scan angle in the E- and H-plane is therefore $\theta_0^{max} = \arcsin(\lambda_0/d_x - 1) = 90^0$. In figure 4.14 the input impedance of the centre element is shown for various array sizes, when the main beam of the array is directed at broadside ($\theta_0 = \phi_0 = 0^0$). The dependence of the input impedance on the number of array elements shows the influence of mutual coupling. Another interesting observation from figure 4.14 is that the input impedance of the centre element converges to a certain value as the number of array elements increases. This agrees with the results obtained in [3], where finite arrays were compared with infinite arrays of microstrip antennas. In figures 4.15 and 4.16 the coupling coefficients between the centre element ($k = l = 4, j = 25$) and the other elements in a 7×7 array are plotted for $f = 5.4$ GHz. Figures 4.17, 4.18 and 4.19 show the corresponding active reflection coefficient of the centre element versus scan angle θ_0 for various frequencies, for the $\phi_0 = 0^0$ plane, the $\phi_0 = 45^0$ plane and the $\phi_0 = 90^0$ plane. At this point, it is interesting to take a closer look at the bandwidth of the array. To that end, the active reflection coefficient of the centre element in a 7×7 array is investigated in three planes, namely in the $\phi_0 = 0^0$ plane, the $\phi_0 = 45^0$ plane and the $\phi_0 = 90^0$ plane. The relative bandwidth (BW) with $|R_{25}| \leq 1/3$, is now:

- BW=6.3%, if $\phi_0 = 0^0$ and maximum scan angle $\theta_0 = 0^0$,
- BW=5.7%, if $\phi_0 = 0^0$ and maximum scan angle $\theta_0 = 30^0$,
- BW=3.2%, if $\phi_0 = 0^0$ and maximum scan angle $\theta_0 = 60^0$,
- BW=5.6%, if $\phi_0 = 45^0$ and maximum scan angle $\theta_0 = 30^0$,
- BW=5%, if $\phi_0 = 45^0$ and maximum scan angle $\theta_0 = 60^0$,
- BW=5.7%, if $\phi_0 = 90^0$ and maximum scan angle $\theta_0 = 30^0$,
- BW=0%, if $\phi_0 = 90^0$ and maximum scan angle $\theta_0 = 60^0$.

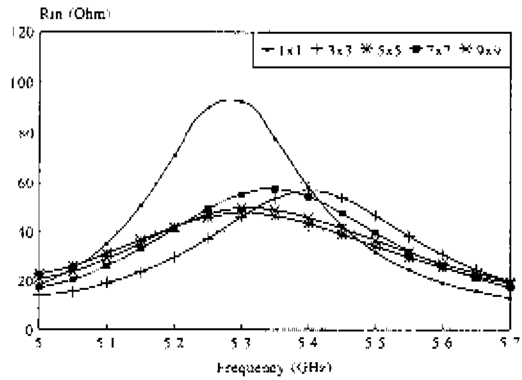

a) real part Z_{in}

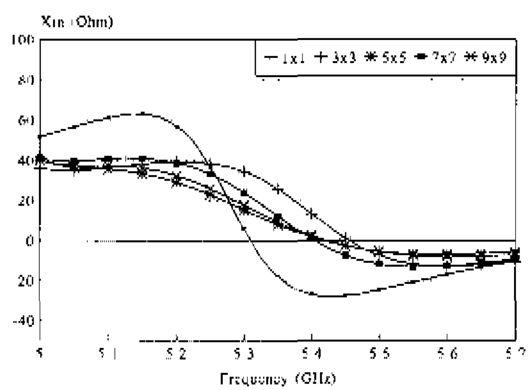

b) imaginary part Z_{in}

Figure 4.14: *Centre-element input impedance for various array sizes for the configuration of array 3, with $\theta_0 = \phi_0 = 0^0$*

As expected, the bandwidth decreases with increasing scan angle. Furthermore, the bandwidth at broadside ($\theta_0 = 0^0$) is larger than the bandwidth of a single element. This is a positive effect of the mutual coupling.

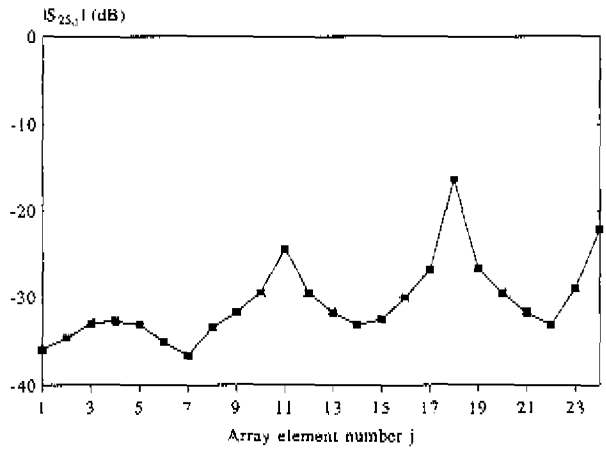

Figure 4.15: *Mutual coupling in a 7 × 7 single-layer array with dimensions of array 3 and f = 5.4 GHz.*

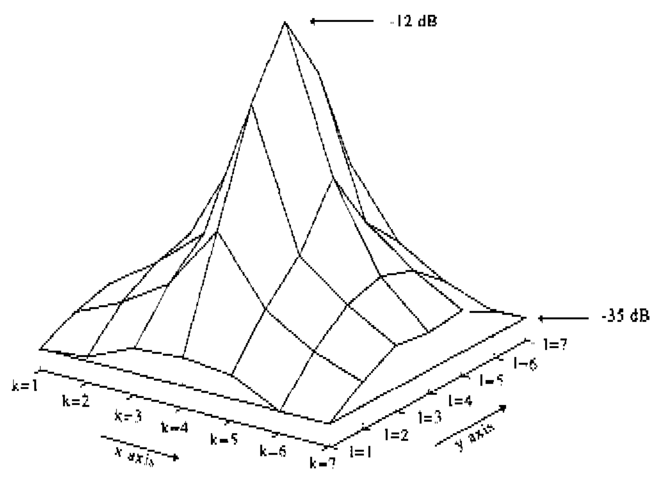

Figure 4.16: *Three-dimensional representation of mutual coupling ($|S_{25,j}|$ in dB) in a 7 × 7 single-layer array with dimensions of array 3 and f = 5.4 GHz.*

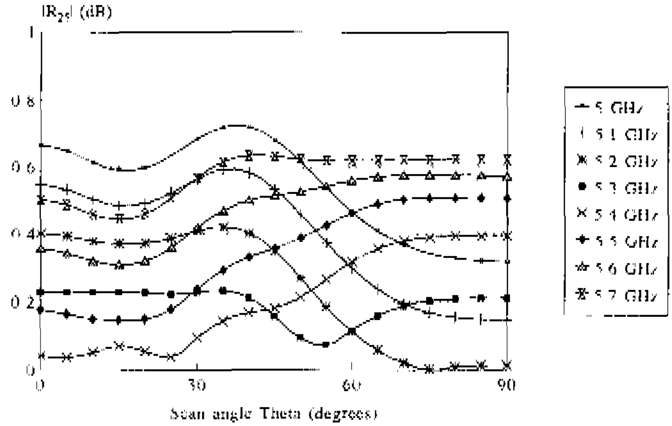

Figure 4.17: *Centre-element active reflection coefficient in a 7 × 7 single-layer array with dimensions of array 3 and* $\phi = 0^0$ *(E-plane).*

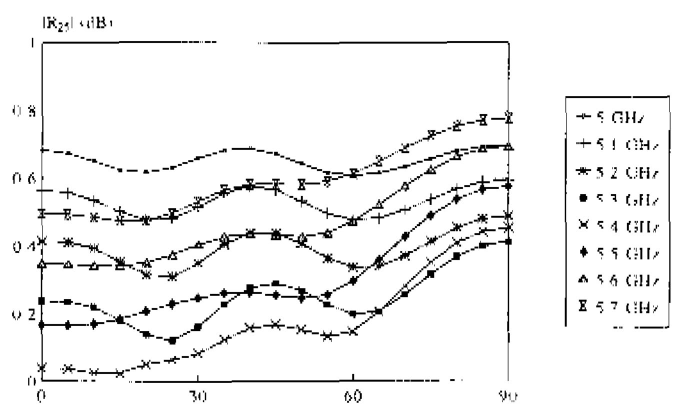

Figure 4.18: *Centre-element active reflection coefficient in a 7 × 7 single-layer array with dimensions of array 3 and* $\phi = 45^0$ *(D-plane).*

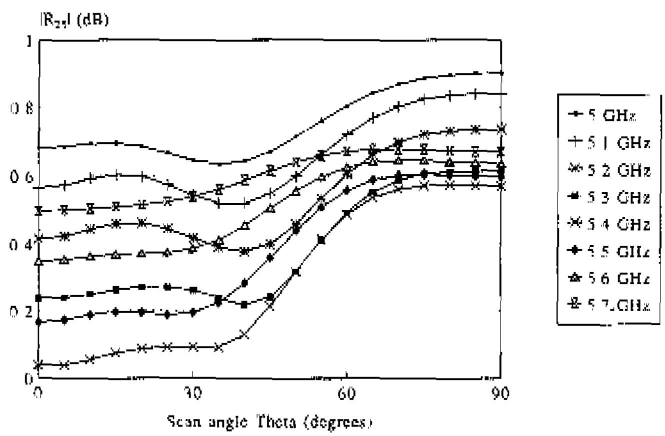

Figure 4.19: *Centre-element active reflection coefficient in a 7 × 7 single-layer array with dimensions of array 3 and $\phi = 90^0$ (H-plane).*

4.8.3 Stacked microstrip arrays

A stacked microstrip antenna has two resonances, that can be used to obtain a larger bandwidth or to obtain dual-frequency operation. In this section a finite array of stacked microstrip antennas with a relative large bandwidth will be investigated. The antenna design of section 3.9.3 with a bandwidth of 13% on Duroid 6002 substrate with $\varepsilon_r = 2.94$ is used as a starting point. The array dimensions are given in table 4.4. Figure 4.20 shows the calculated coupling coefficient between

Array	z_1' (mm)	$h_2 - z_2'$ (mm)	ε_r	$\tan\delta$	W_{x1} (mm)	W_{x2} (mm)	x_s (mm)	d_x (mm)
4	3.04	6.08	2.94	0.0012	25.3	25	8.5	48.5

Table 4.4 *Dimensions of microstrip array 4, with* $W_{x1} = W_{y1}$, $W_{x2} = W_{y2}$, $d_x = d_y$, $y_s = 0$, $a = 0.635$ *mm and* $b = 2.1$ *mm.*

the centre element and the other elements in a 7×7 array configuration. The H-plane coupling (column $k = 4$) seems to be much stronger than the E-plane coupling (row $l = 4$) for this stacked configuration. In figures 4.21, 4.22 and 4.23 the corresponding active reflection coefficient in the three principal planes of the centre element in a 7×7 array is plotted for various frequencies. The relative bandwidth of the centre element is in the three principal planes with $|R_{25}| < 1/3$

- BW=12.4%, if $\phi_0 = 0^0$ and maximum scan angle $\theta_0 = 0^0$,
- BW=12.4%, if $\phi_0 = 0^0$ and maximum scan angle $\theta_0 = 30^0$,
- BW=3.7%, if $\phi_0 = 0^0$ and maximum scan angle $\theta_0 = 60^0$,
- BW=12.4%, if $\phi_0 = 45^0$ and maximum scan angle $\theta_0 = 30^0$,
- BW=11.6%, if $\phi_0 = 45^0$ and maximum scan angle $\theta_0 = 60^0$,
- BW=11.5%, if $\phi_0 = 90^0$ and maximum scan angle $\theta_0 = 30^0$,
- BW=0%, if $\phi_0 = 90^0$ and maximum scan angle $\theta_0 = 60^0$

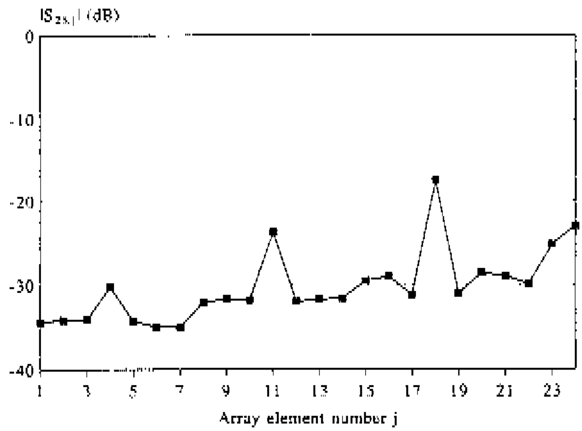

Figure 4.20: *Mutual coupling in the 7 × 7 stacked microstrip array 4 with $f = 3.1$ GHz.*

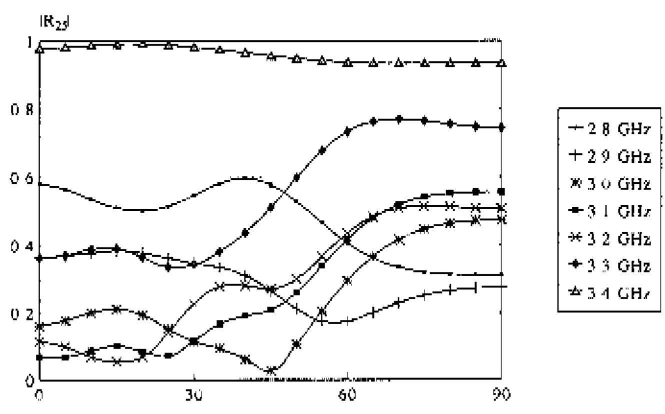

Figure 4.21: *Centre-element active reflection coefficient in the 7 × 7 stacked microstrip array 4 with $\phi = 0^0$ (E-plane).*

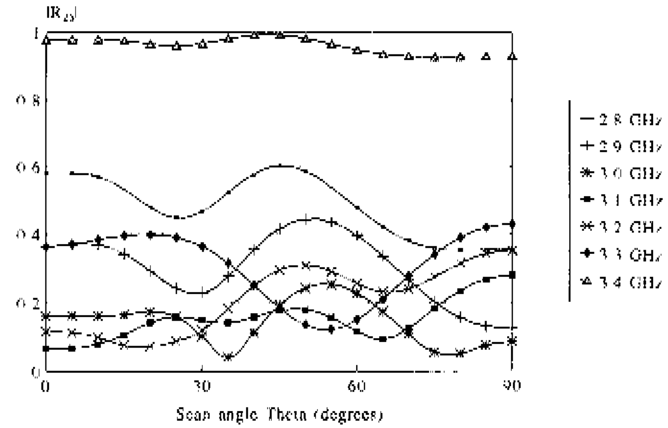

Figure 4.22: *Centre-element active reflection coefficient in the 7 × 7 stacked microstrip array 4 with $\phi = 45^0$ (D-plane).*

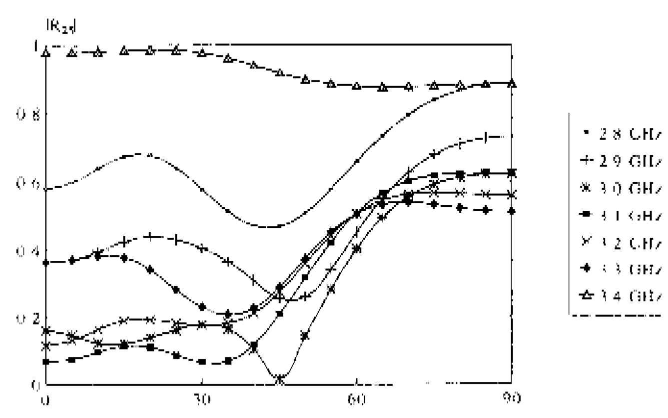

Figure 4.23. *Centre-element active reflection coefficient in a 7 × 7 stacked microstrip array 4 with $\phi = 90^0$ (H-plane).*

4.8.4 Multilayer microstrip arrays

In section 3.9 4 a two-layer microstrip antenna with a high-permittivity substrate was investigated. It was shown that with such microstrip antennas bandwidths up to 25% could easily be obtained. Figure 4 24 shows the top view of a linearly polarised array of $K \times L$ multilayer microstrip elements, which are fed on their diagonal with a coaxial cable. The orientation of the array elements is somewhat different than in a conventional microstrip array, due to the location of the feed point A 7×7 array with centre frequency $f = 4.1$ GHz was investigated Table 4.5 shows

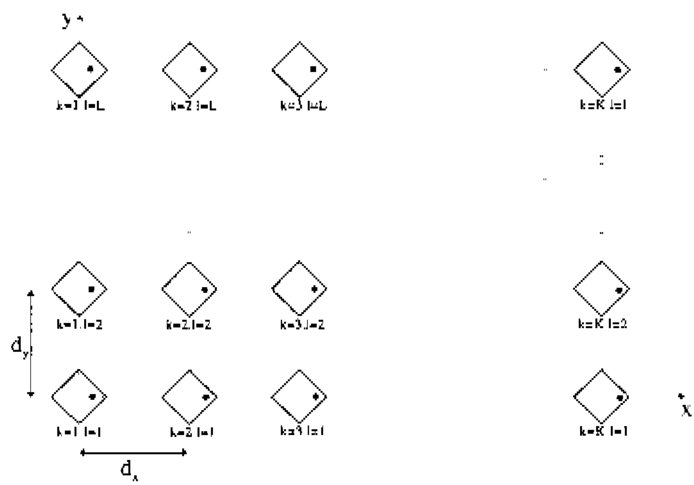

Figure 4.24: *Geometry of a finite array of multilayer stacked microstrip antennas, with* $k = 1, 2, \ldots, K$, $l = 1, 2, \ldots, L$ *and* $j = (l-1) \times K + k$

the dimensions of this array The calculated coupling coefficients between the centre element and the elements of the $l = 1$, $l = 2$, $l = 3$ and $l = 4$ row are plotted in figure 4.25, with $f = 4.1$ GHz. The maximum coupling coefficient is $S_{25\,18} = -17.7$ dB. This maximum mutual-coupling level is much lower than the mutual-coupling level between multilayer microstrip antennas with a foam layer [75] The coupling coefficients can be used to determine the active reflection coefficient. The centre-element active reflection coefficient versus scan angle θ_0 is plotted in figures 4.26, 4 27 and 4.28 for the planes $\phi_0 = 0^0$, $\phi_0 = 45^0$ and $\phi_0 = 90^0$, respectively. The corresponding relative bandwidth of the centre element of this array in these three planes is ($|R_{25}| \leq 1/3$).

- BW=18%, if $\phi_0 = 0^0$ and maximum scan angle $\theta_0 = 0^0$,
- BW=13%, if $\phi_0 = 0^0$ and maximum scan angle $\theta_0 = 30^0$,
- BW=8%, if $\phi_0 = 0^0$ and maximum scan angle $\theta_0 = 60^0$,

Array	$h_1 - z_1'$ (mm)	$h_2 - z_2'$ (mm)	ε_{r1}	ε_{r2}	W_{x1} (mm)	W_{x2} (mm)	x_s (mm)	d_x (mm)
5	1.27	6.27	10.5	2.33	11	18.2	4	35

Table 4.5: *Dimensions of microstrip array 5, with* $tan\delta_1 = 0.0023$, $tan\delta_2 = 0.0012$, $W_{x1} = W_{y1}$, $W_{x2} = W_{y2}$, $d_x = d_y$, $x_s = y_s$, $a = 0.635$ *mm and* $b = 2.1$ *mm*

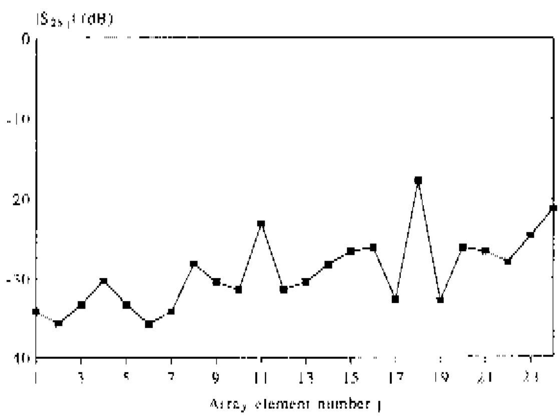

Figure 4.25: *Mutual coupling in a 7 × 7 array of broadband stacked multilayer microstrip antennas (array 5), with* $f = 4.1$ *GHz.*

- BW=16.5%, if $\phi_0 = 45^0$ and maximum scan angle $\theta_0 = 30^0$,
- BW=10%, if $\phi_0 = 45^0$ and maximum scan angle $\theta_0 = 60^0$,
- BW=11%, if $\phi_0 = 90^0$ and maximum scan angle $\theta_0 = 30^0$,
- BW=3.5%, if $\phi_0 = 90^0$ and maximum scan angle $\theta_0 = 60^0$

Compared with the bandwidth of an isolated multilayer microstrip antenna, the bandwidth is reduced significantly. At broadside the available relative bandwidth is still 18%, but when the main beam of the array is scanned to an angle of 60 degrees the available relative bandwidth is reduced to 3.5% in the H-plane. The active reflection coefficient of an array element near the edge of an array will usually differ from the centre-element active reflection coefficient. This phenomenon is illustrated in figure 4.29, where the active reflection coefficient of an edge

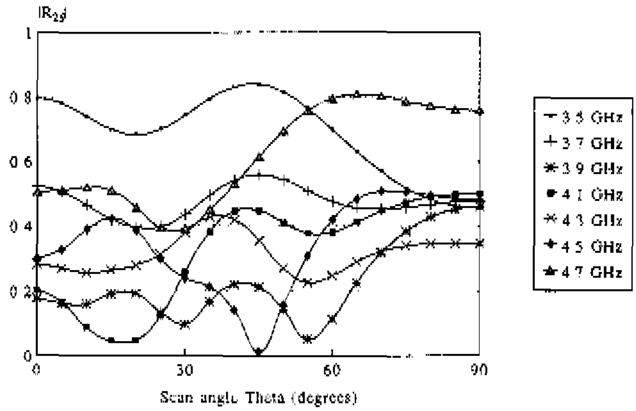

Figure 4.26: *Centre-element active reflection coefficient of a 7 × 7 multilayer microstrip array (array 5), $\phi = 0^0$ (E-plane).*

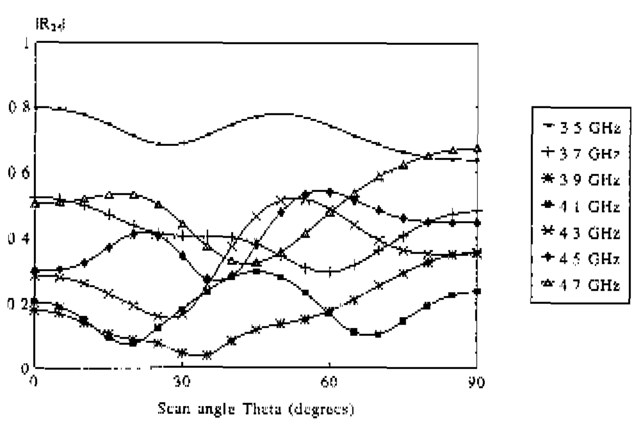

Figure 4.27: *Centre-element active reflection coefficient of a 7 × 7 multilayer microstrip array (array 5), $\phi = 45^0$ (D-plane).*

element ($k = l = 1$, $j = 1$) is compared with the active reflection coefficient of the centre element ($k = l = 4$, $j = 25$) in a 7 × 7 array. The influence of mutual coupling on the electromagnetical behaviour of an edge element of this array appears to be less strong than the influence on the centre element.

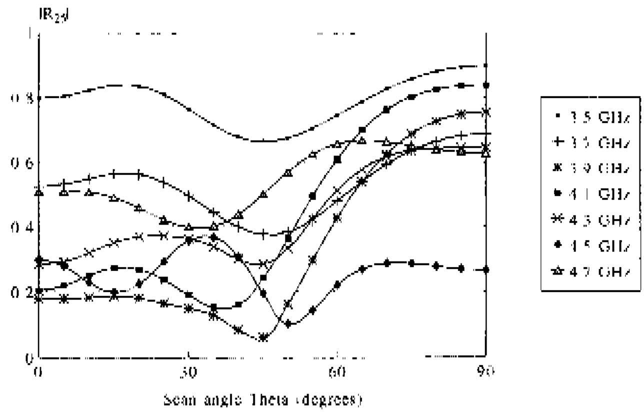

Figure 4.28. *Centre-element active reflection coefficient of a* 7×7 *multilayer microstrip array (array 5),* $\varphi = 90^0$ *(H-plane)*

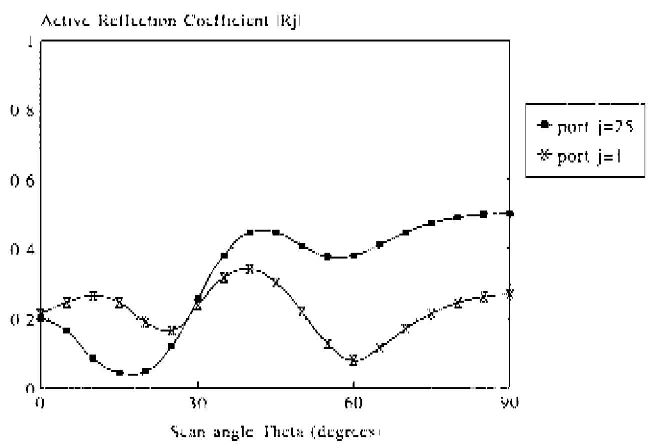

Figure 4.29: *Active reflection coefficient in a* 7×7 *multilayer microstrip array (array 5),* $\phi = 0^0$ *(E-plane) and* $f = 4.1$ *GHz.*

4.8.5 Array of broadband EMC microstrip antennas

Electromagnetically coupled (EMC) microstrip antennas have broadband input characteristics (see section 3.9.6). In these antennas the inner conductor of the feeding coaxial cable is not connected to the patch (see figure 3.2). The measured and predicted relative bandwidth of the configuration discussed in section 3.9.6 is approximately 50%. It is interesting to investigate whether these elements can be used in a practical array antenna. For that purpose, two linear arrays with 7 EMC microstrip elements were designed and built. Both arrays were designed to operate at broadside ($\theta_0 = \phi_0 = 0^0$). A photograph of both antennas is shown in figure 4.30. The array on the left in figure 4.30 has a so-called E-plane configuration of the patches,

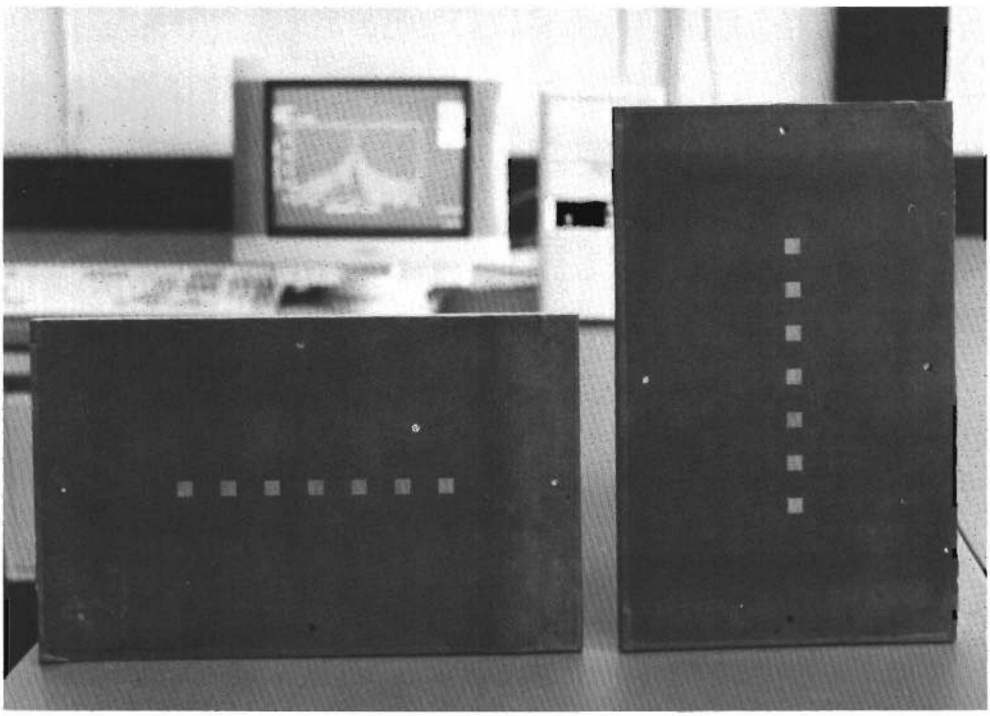

Figure 4.30: *Two linear arrays of EMC microstrip elements.*

i.e. $(K = 7, L = 1)$ and $y_s = 0$, and the array on the right of this photograph has a H-plane configuration of the patches, i.e. $(K = 1, L = 7)$ and $y_s = 0$. The dimensions of both arrays are specified in table 4.6. In figure 4.31 and figure 4.32 the measured and predicted mutual coupling coefficients S_{1i} are plotted for both linear arrays with f = 5.5 GHz. This is the worst-case situation, because the mutual coupling in both arrays decreases with increasing frequency [72]. The difference between the calculated and measured data is probably due to the finite size of the ground plane. The mutual-coupling level is in both arrays lower than -19 dB over a large

Array	$h_2 = z_1^f$ (mm)	z_F (mm)	ε_r	$\tan\delta$	W_{y1} (mm)	x_s (mm)	d_x (mm)
6	6.61	6.36	2.33	0.0012	11.5	4.6	32

Table 4.6: *Dimensions of microstrip array 6, with $y_s = 0$, $W_{x1} = W_{y1}$, $d_x = d_y$, $a = 0.635$ mm and $b = 2.1$ mm*

frequency band. Compared with the single-layer microstrip array of table 4.3, the decrease of

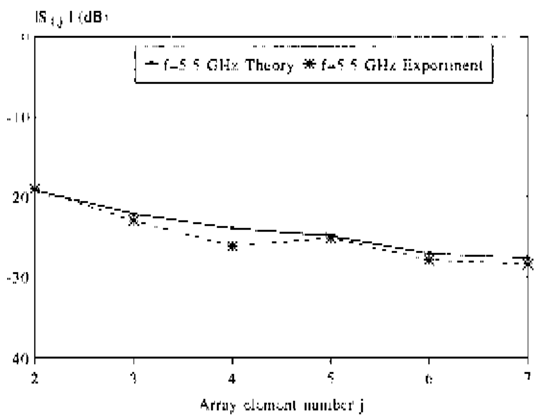

Figure 4.31: *E-plane coupling in a linear 7 × 1 array of EMC microstrip elements (array 6).*

mutual coupling in figure 4.31 with respect to the distance between the elements in the E-plane is much smaller. This is a direct result of the fact that more input power is going into surface waves in case of an electrically thick microstrip configuration. Figure 4.33 shows the centre-element reflection coefficient for various array sizes, when the main beam of the array is directed to broadside ($\theta_0 = \phi_0 = 0^0$). The infinite-array calculations were done with the infinite-array model presented in [74]. This infinite-array model is based on the model described in this thesis. So, the magnetic frill in the coaxial opening is used as a source, the unknown current on the coaxial probe in a unit cell is expanded in rooftop basis functions, and the currents on the patches are written in terms of entire-domain sinusoidal basis functions. In case of an infinite array, the available relative bandwidth is reduced to approximately 23%.

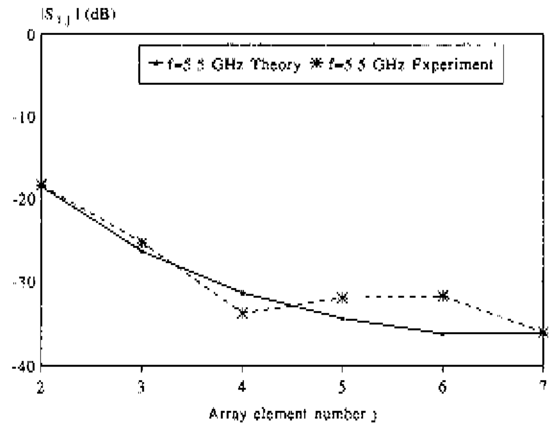

Figure 4.32: *H-plane coupling in a linear* 1×7 *array of EMC microstrip elements (array 6).*

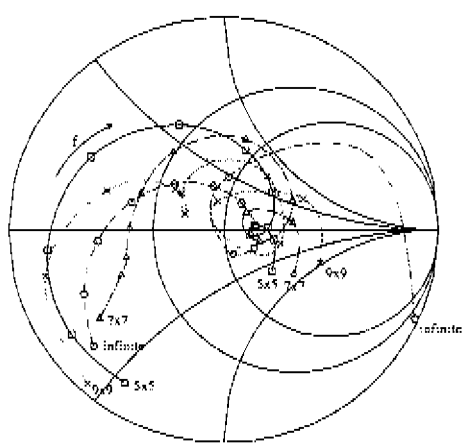

Figure 4.33: *Centre-element reflection coefficient at broadside* $(\theta_0 = \phi_0 = 0^0)$ *of array configuration 6 for various array sizes, with* $5 \leq f \leq 7.75$ *GHz and* $\Delta f = 0.25$ *GHz.*

4.8.6 Far-field pattern of a finite microstrip array

In this section two different approaches are discussed to determine the far-field pattern of an array of microstrip antennas. These two approaches are:

i An approach which includes mutual coupling and edge effects. The current distribution on all array elements is calculated and used to determine the radiation pattern of the array.

ii An approach which neglects mutual coupling. The current distribution and the corresponding element pattern of an isolated microstrip antenna are determined. The element pattern is multiplied with the array factor (=radiation pattern of an array of identical, isotropic radiators) in order to calculate the radiation pattern of the array.

In approach ii), on each array element the same current distribution is used in order to determine the radiation pattern. In approach i) a different current distribution is used for each array element. This is therefore the most rigorous and accurate way to determine the radiation characteristics of finite microstrip arrays. A third approach is discussed in [70], where a periodic-array method (infinite-array approach) was investigated and compared with the results obtained from the approaches i) and ii). As an example, the radiation pattern of the single-layer microstrip configuration of table 4.3 will be investigated. The antenna is fabricated on a substrate with $\varepsilon_r = 2.33$. In figure 4.34 the E-plane ($\phi = 0^0$) radiation pattern is plotted when scanning the array at broadside ($\theta_0 = 0^0, \phi_0 = 0^0$), calculated with approach i) and ii). The array consists of 11×11 elements. A uniform amplitude taper was used. The influence of mutual coupling on the radiation

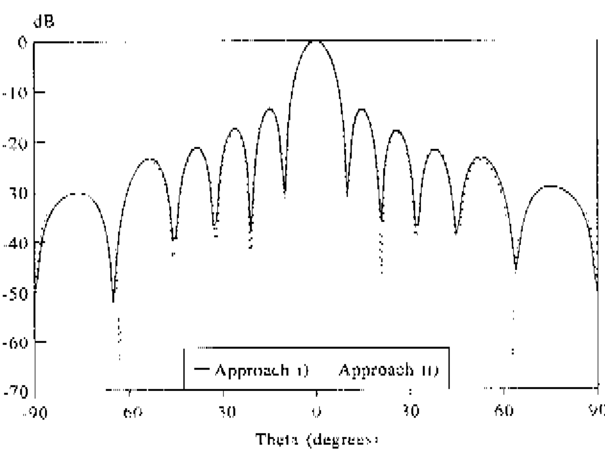

Figure 4.34 *Radiation pattern of a* 11×11 *microstrip array scanned at broadside* ($\theta_0 = 0^0, \phi_0 = 0^0$)*, with dimensions of array 3 and* $f = 5.4$ *GHz.*

characteristics of a microstrip array is far less than the influence of mutual coupling on the active reflection coefficient. Therefore, during the design of a microstrip array, the attention has to be focussed on the optimisation of the active reflection coefficient of each array element. The radiation pattern of the array can be optimised by chosing a proper amplitude and phase taper. In figure 4.35 the E-plane pattern of the 11×11 array is shown when the main beam of the antenna is scanned to the angle ($\theta_0 = -30^0, \phi_0 = 0^0$). Again, the array is illuminated with a uniform amplitude taper

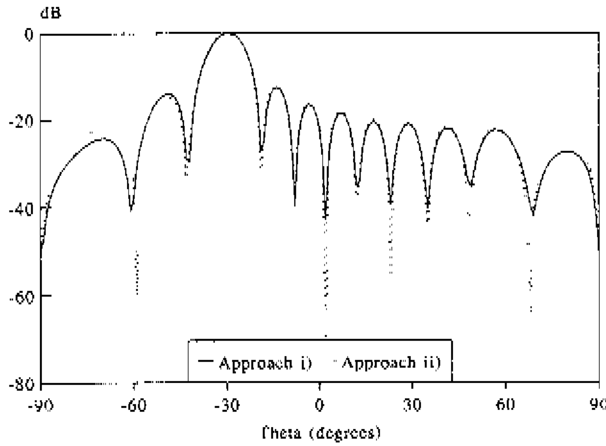

Figure 4.35: *Radiation pattern of a* 11 × 11 *microstrip array scanned at* ($\theta_0 = -30^0, \phi_0 = 0^0$), *with dimensions of array 3 and* $f = 5.4$ *GHz.*

4.8.7 Circular polarisation

In section 4.6 of this thesis three microstrip configurations have been presented that generate a circularly polarised far-field pattern. Each configuration will be discussed in more detail in this section. A circularly polarised stacked microstrip antenna, fed by two coaxial probes with a phase difference of 90^0 (see configuration a of figure 4.6), was designed and built. The dimensions of this antenna are shown in table 4.7. In figure 4.36 the calculated and measured scattering coefficients

Ant	z_1' (mm)	$h_2 = z_2'$ (mm)	ϵ_r	$\tan\delta$	W_{x1} (mm)	W_{x2} (mm)	x_s (mm)
16	3.04	6.08	2.94	0.0012	25.3	25	8.5

Table 4.7: *Dimensions of circularly polarised microstrip antenna 16, with* $W_{x1} = W_{y1}$, $W_{x2} = W_{y2}$, $a = 0.635$ *mm and* $b = 2.1$ *mm*

S_{11} and S_{12} are plotted versus frequency. The agreement between theory and experiment turns out to be quite good. The coupling between both input ports is lower than -19.5 dB in the frequency band of interest. The predicted and measured axial ratio of this antenna in the E-plane ($\phi = 0^0$)

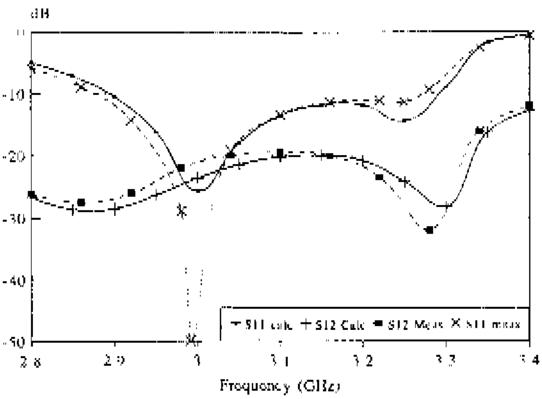

Figure 4.36: *Measured and calculated S_{11} and S_{12} of the circularly polarised microstrip antenna 16 fed with 2 coaxial cables.*

can be found in figure 4.37, with $f = 3.1$ GHz. Measurements were made in the Compact Antenna Test Range at EUT. Note that the axial ratio for $\theta = 0^0$ is not equal to zero, due to the asymmetric orientation of the two coaxial cables. The axial ratio of this antenna can be improved if 4 coaxial cables are used to feed the antenna [6]. The dimensions of the ground plane on which the antenna was built is length × height=31 cm × 46 cm. The asymmetrical ground plane is probably one of the causes of the difference between the measured and calculated axial ratio.

Next, a 2 × 2 subarray was investigated with a sequentially rotated orientation of the patches (configuration of figure 4.6b). Circular polarisation is obtained with 4 linearly polarised elements. The dimensions of the subarray are given in table 4.8. The predicted coupling coefficients between

Array	$h_2 = z_1^i$ (mm)	ε_r	$\tan\delta$	W_{x1} (mm)	x_s (mm)	d_x (mm)
7	1.588	2.53	0.0012	60.2	9.5	110

Table 4.8: *Dimensions of microstrip* 2 × 2 *subarray 7, with $W_{x1} = W_{y1}$, $d_x = d_y$, $a = 0.635$ mm and $b = 2.1$ mm.*

the 4 input ports are plotted in figure 4.38. Figure 4.39 shows a plot of the axial ratio of this

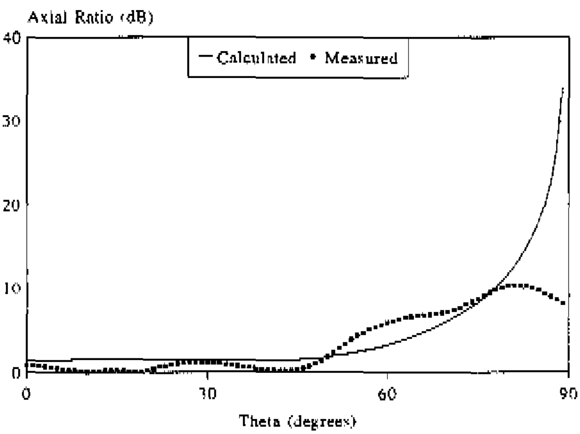

Figure 4.37. *Measured and calculated axial ratio of the circularly polarised microstrip antenna 16, fed with 2 coaxial cables and with $f = 3.1$ GHz.*

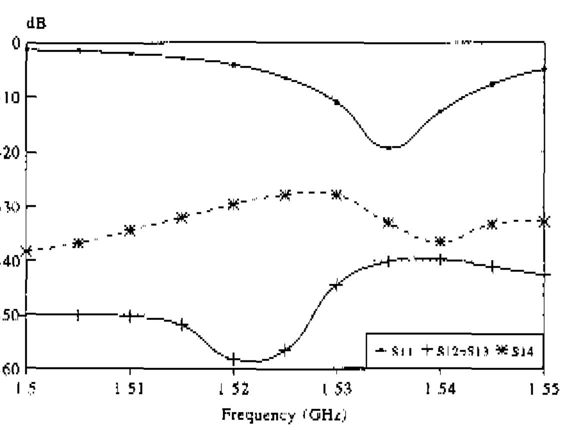

Figure 4.38: *Calculated coupling coefficients in a 2×2 subarray with sequentially rotated linearly polarised microstrip elements (array 7)*

subarray in the E-plane, in the diagonal plane and in the H-plane. Note that the scan angle $\theta_0 = \phi_0 = 0^0$. The E- and H-plane patterns are exactly the same. Due to the symmetry of this sequentially rotated configuration, the axial ratio for $\theta = 0^0$ is equal to 0 dB.

The axial ratio can be improved somewhat if circularly polarised elements are used in the subarray. This corresponds to the configuration shown in figure 4.7. A 2×2 array was constructed [70] on

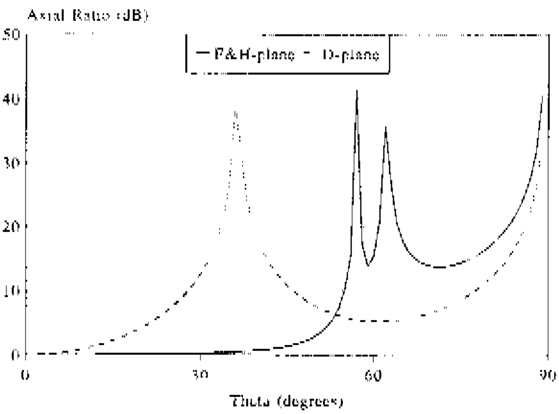

Figure 4.39: *Calculated axial ratio of a 2×2 subarray with sequentially rotated linearly polarised microstrip elements (array 7), with $f = 1.54$ GHz.*

Rexolite 1422 substrate with $\varepsilon_r = 2.53$. The remaining array dimensions are the same as those of array 7. The feeding network of this subarray was mounted on the backside of the ground plane, with Wilkinson splitters serving as power dividers. Figure 4.40 and 4.41 show the measured co-polarisation level and the corresponding axial ratio in the E-plane ($\phi = 0^0$), compared with calculations. The measurements were made in the Compact Antenna Test Range at EUT. The predicted axial ratio for $\theta = 0^0$ is equal to 0 dB, which is due to the symmetry in the 2×2 array.

4.8.8 Dual-frequency circularly polarised microstrip subarray

In section 3.9.5 a dual-frequency, dual-polarisation, microstrip antenna was presented. When such an element is placed in a 2×2 subarray with sequentially rotated elements, a dual-frequency circularly polarised subarray can be constructed. Figure 4.42 shows this configuration along with the phasing of the input ports. The main beam is directed to broadside, i.e., $\theta_0 = \phi_0 = 0^0$. Antenna 14 (table 3.6) was used to construct a 2×2 subarray with an element spacing of $d_x = 35$ mm ($\approx 0.7\lambda_0$ for $f = 6$ GHz). Figure 4.43 shows the coupling coefficients between input port 1 and the other ports for low-frequency operation (a-ports). Figure 4.43 shows the corresponding coupling coefficients at the higher frequency band (b-ports). Finally, in figure 4.45 the predicted axial ratio in the E-plane is plotted for $f = 4$ GHz and $f = 6$ GHz. The axial ratio for $f = 4$ GHz is lower than the axial ratio for $f = 6$ GHz. The dual-frequency circularly polarised subarray is an interesting concept that can be used in future mobile satellite communication [22].

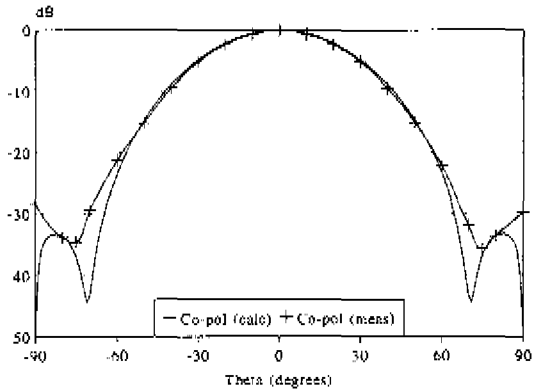

Figure 4.40: *Measured and calculated co-polarisation level ($\phi = 0^0$) of the* 2×2 *subarray with sequentially rotated circularly polarised microstrip elements,* $f = 1.5$ *GHz*

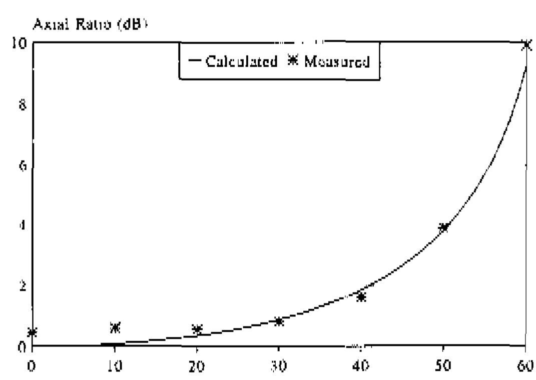

Figure 4.41: *Measured and calculated axial ratio of a* 2×2 *subarray with sequentially rotated circularly polarised microstrip elements,* $f = 1.5$ *GHz.*

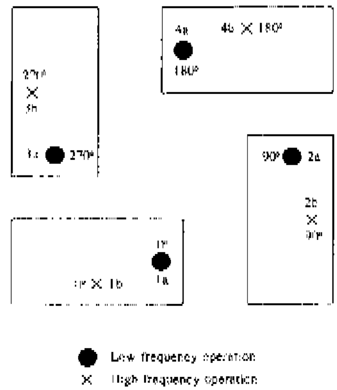

Figure 4.42: *Dual-frequency circularly polarised* 2 × 2 *subarray with sequentially rotated elements.*

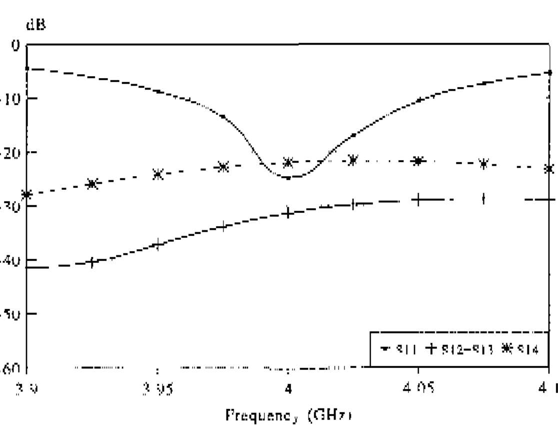

Figure 4.43: *Calculated coupling coefficients in a dual-frequency circularly polarised* 2 × 2 *subarray, low-frequency operation (a ports).*

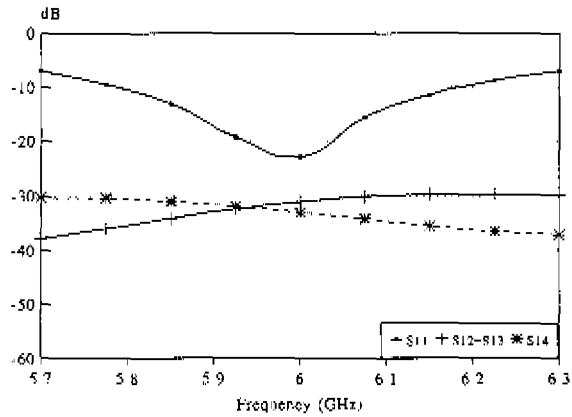

Figure 4.44: *Calculated coupling coefficients in a dual-frequency circularly polarised* 2 × 2 *subarray, high-frequency operation (b-ports)*

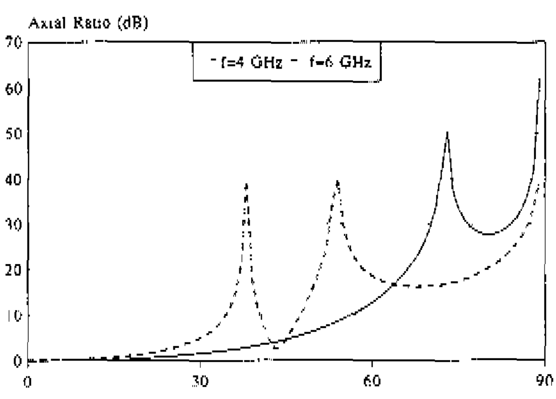

Figure 4.45 *Calculated axial ratio in the E-plane of a dual-frequency circularly polarised* 2 × 2 *subarray*

4.9 Finite array of monopoles embedded in a grounded dielectric slab

A finite array of monopoles embedded in a dielectric slab is studied [1] using a rigorous yet efficient spectral-domain moment method. Computed input impedance data are compared with data from an infinite-array analysis. Significant differences are observed, even for relatively large arrays.

Introduction

In this section a method is presented for the analysis of finite two-dimensional arrays of vertical monopoles embedded in a grounded dielectric slab. The radiation pattern of such an array has a null at broadside. Previously, this type of arrays has been investigated by Pozar [58], who analysed an infinite array of monopoles. Fenn [23] studied a finite array of monopoles in free space. We have investigated finite arrays of monopoles embedded in a dielectric slab by using a spectral-domain moment method. A sophisticated magnetic-frill source model is used in order to account for the feeding coaxial cables. Both Pozar [58] and Fenn [23] use a more simple and less accurate source model.

Theory

In figure 4.46 the geometry of a finite two-dimensional array of monopoles embedded in a grounded dielectric slab is shown. The length of a monopole is d.
An antenna element is represented by a cylinder with radius a and with perfectly conducting walls. It is assumed that the z-directed surface current on this cylinder only depends on the z-coordinate. The fields corresponding to the TEM-mode in the coaxial aperture act as a source. The electric field in the coaxial aperture of antenna element 1 then takes the form [32, 67]:

$$\vec{E}_r^1(\vec{r}) = \frac{V_1^p}{r\ln(b/a)}\vec{e}_r, \quad a < r \leq b, \tag{4.34}$$

where V_1^p represents the impressed port voltage at monopole 1 (=port 1). The unknown currents on the antenna elements can be found by applying the well known method of moments. The problem is formulated in the spectral domain, i.e. all quantities are transformed according to $\{x, y\} \longrightarrow \{k_x, k_y\}$. This finally results in the matrix equation:

$$[Z][I] + [V^{ex}][V^p] = [0], \tag{4.35}$$

[1] *This section was published as a paper in Electronics Letters, Vol. 28 (1992), p. 2079-2080. The numbering of its equations and references has been changed, so that they correspond with the numbering of the previous part of this thesis.*

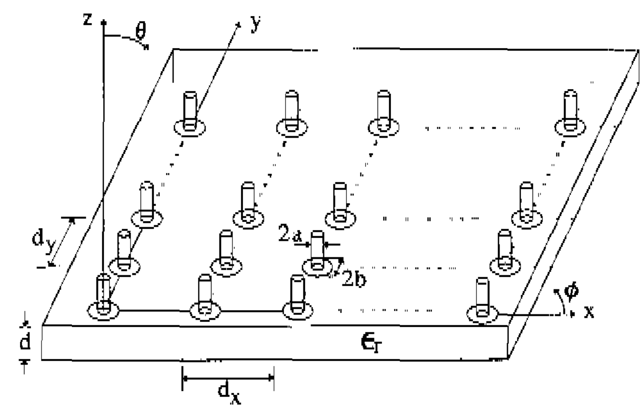

Figure 4.46: *Geometry of a finite array of vertical monopoles embedded in a grounded dielectric slab.*

with

$$
\begin{aligned}
Z_{jm\,in} = {} & 2\pi \int_0^\infty k_0^2 \beta J_0(k_0\beta R_{ji}) J_0^2(k_0\beta a)\cdot \\
& \int_z \left[\int_{z_0} Q^E_{zz}(\beta, z, z_0) g_{in}(z_0) dz_0\right] g_{jm}(z) dz d\beta, \\
V^{ex}_{jm\,i} = {} & -\frac{4\pi^2 k_0^2}{\ln(b/a)} \int_0^\infty \frac{\beta}{k_1 T_m} J_0(k_0\beta R_{ji}) J_0(k_0\beta a)\left[J_0(k_0\beta b) - J_0(k_0\beta a)\right]\cdot \\
& \int_{z_0} g_{jm}(z_0)[\varepsilon_r k_2 \sin k_1(d - z_0) - jk_1 \cos k_1(d - z_0)] dz_0 d\beta,
\end{aligned}
$$

$$
\begin{aligned}
Q^E_{zz}(\beta, z, z_0) = {} & \frac{j\omega\mu_0}{\varepsilon_r k_0^2}\delta(z - z_0) \\
& -\frac{j\omega\mu_0\beta^2}{\varepsilon_r k_1 T_m}\begin{cases} \cos(k_1 z_0)\,[\varepsilon_r k_2 \sin k_1(d - z) - jk_1 \cos k_1(d - z)] & z_0 \le z, \\ \cos(k_1 z)\,[\varepsilon_r k_2 \sin k_1(d - z_0) - jk_1 \cos k_1(d - z_0)] & z_0 \ge z, \end{cases}
\end{aligned}
$$

$$T_m = k_2\varepsilon_r \cos k_1 d + jk_1 \sin k_1 d,$$

$$k_1^2 = \varepsilon_r k_0^2 - k_x^2 - k_y^2,$$

$$k_2^2 = k_0^2 - k_x^2 - k_y^2,$$

$$k_0^2\beta^2 = k_x^2 + k_y^2, \qquad k_0^2 = \omega^2\varepsilon_0\mu_0.$$

R_{ji} is the distance between monopole j and i. $g_{jm}(z)$ represents the z-dependent part of the m-th basis function on monopole j. Subdomain rooftop basis functions are used. The two integrations over z can be performed analytically for this type of basis function. The mode coefficients $[I]$ are found by solving equation (4.35). The main disadvantage of the spectral-domain moment method for the analysis of finite arrays is the long computation time needed to evaluate the elements of $[Z]$ and $[V^{ex}]$, especially when the distance between monopole j and i is large. This problem is mainly due to the numerical evaluation of infinite integrals over slowly decaying and strongly oscillating functions. Fortunately, we have found a way to rewrite these infinite integrals as a sum of a closed-form expression and a relatively fast converging integral. In Smolders [72] this approach was used for the analysis of microstrip patch antennas. By using this analytical method, the computation time can be reduced significantly. Once the elements of $[Z]$ and $[V^{ex}]$ are known, the port admittance matrix $[Y^p]$ can easily be calculated. An element of the port admittance matrix is given by:

$$Y_{ji}^p = \frac{I_j^p}{V_i^p}, \quad \text{with } V_\nu^p = 0 \text{ for } \nu \neq i, \tag{4.36}$$

where I_j^p is the current at the base of monopole j and is calculated with (4.36), V_i^p is the impressed port voltage at monopole i. Once the port admittance matrix is known, the scattering matrix $[S]$ and the active reflection coefficient can be determined. Note that with the infinite-array approach of [58], the scattering matrix cannot be calculated.

Results

We have checked our method and computer program with the results obtained by Fenn [23], who analysed finite arrays of monopoles in free space ($\varepsilon_r = 1$). The agreement between our calculations and the measurements of Fenn [23] is excellent. Next we considered the array configuration of Pozar ([58], fig. 4), with $\varepsilon_r = 2.5$, $d = 10$ mm, $a = 0.565$ mm, $d_x = d_y = 60.6$ mm and $\phi_0 = 45^o$. Pozar [58] measured the input impedance using a waveguide simulator in the TM_{11} mode, with $\theta_0 = \arcsin[\lambda/(\sqrt{2}d_x)]$. In figure 4.47 the calculated centre-element reflection coefficient against frequency for this configuration is shown for three array sizes. The characteristic impedance is 50Ω. Note that the reflection coefficient of the centre element can become larger than 1 for a finite array.

A significant difference can be observed between the calculated reflection coefficient of figure 4.47 and the results obtained by Pozar ([58], fig. 4) using an infinite-array approach, even for relatively large arrays. In figure 4.48, the corresponding calculated coupling coefficients between the centre element and the elements of row 5 (see fig. 4.46) of a 9×9 array are given

Conclusion

A rigorous yet efficient method is presented for the analysis of a finite array of monopoles embedded in a dielectric slab. Significant differences in calculated input impedance data between our finite-array method and the infinite-array approach of Pozar [58] are observed, even for relatively large arrays

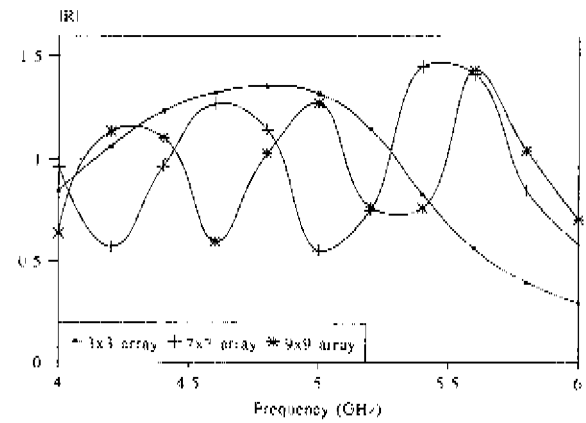

Figure 4.47: *Calculated centre-element reflection coefficient magnitude versus frequency for three finite arrays of monopoles embedded in a dielectric slab*

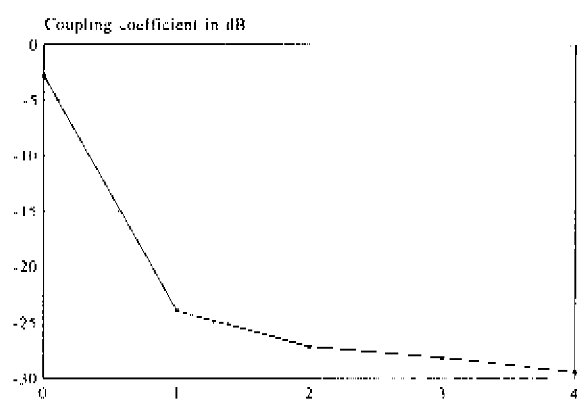

Figure 4.48 *Coupling coefficient of centre element and the elements of row 5 in a 9 × 9 array of monopoles embedded in a dielectric slab, f = 4 GHz.*

Chapter 5

Summary and conclusions

Microstrip antennas and microstrip phased-array antennas have several practical features, including light weight, conformability and low production costs, which make them interesting candidates for several (future) telecommunication applications and radar systems. Accurate theoretical models and corresponding software are critical, since experimental design approaches are usually too time-consuming and expensive. In this thesis an accurate theoretical model is developed for both isolated microstrip elements as well as finite arrays of microstrip antennas. Most applications require a large bandwidth. We have developed our model such that electrically thick, and therefore broadband, microstrip configurations can be analysed. The current distribution on a microstrip array antenna is found by solving the integral equation for the currents with the method of moments. The method of moments transforms an integral equation into a matrix equation by expanding the unknown current distribution on the antenna into a set of basis functions and by weighting the integral equation with a set of testing functions. The resulting matrix equation can be solved with standard numerical techniques. The electromagnetic field which appears in the integral equation is written in terms of the spectral-domain dyadic Green's function of the layered medium on which the microstrip antenna is fabricated. In this way, mutual coupling between array elements and surface-wave effects are accounted for in a rigorous manner

In *chapter 2*, the exact spectral-domain dyadic Green's function is determined for the point-source problem for a grounded three-layer medium. Vertical as well as horizontal electric dipoles are investigated. First, the magnetic vector potential is calculated. The general solution in each of the three regions is written as a sum of an upgoing wave and a downgoing wave. The amplitudes of these waves can be found by applying the boundary conditions at the interfaces between the layers Once the magnetic vector potential is known, the electric field and the magnetic field in each region can be determined

Chapter 3 deals with the analysis of isolated linearly polarised microstrip antennas. The antenna is constructed on a grounded two-layer substrate, and has one or two (stacked configuration) rectangular metallic patches. The antenna is fed with a coaxial cable. The current distribution on the patches and on the coaxial cable is determined by applying a Galerkin-type method-of-moments procedure. The electromagnetic fields are expressed in terms of the spectral-domain dyadic Green's functions of chapter 2. Once the current distribution on the antenna is known, the input impedance and the radiation pattern can be determined. A sophisticated model for the feeding coaxial cable is used, which accounts for the variation of the current along the coaxial probe, and ensures continuity of the current at the patch-probe transition. In this way electrically thick microstrip antennas can be analysed. The current distribution on the coaxial probe is expanded into subdomain rooftop basis functions. On the patches, several types of basis functions have been investigated. It is shown that by choosing a proper set of entire-domain basis functions, only a few of such functions are needed in the analysis to obtain accurate results. Some analytical and numerical techniques to improve the numerical accuracy and to reduce the required CPU time have been discussed. One of these techniques is the asymptotic-form extraction technique presented in section 3.8. It is shown that the integration over the extracted part can be evaluated in closed form. This analytical technique reduces the required CPU time by a factor 20 or more. The theoretical model and the corresponding software were validated by comparing calculated results with measured data from several experiments. In all cases considered good agreement between theory and experiment was obtained, for electrically thin as well as electrically thick substrates. In addition, the bandwidth of several microstrip configurations was investigated. With single-layer microstrip antennas a relative bandwidth upto 15% can be realised, whereas with a multilayer configuration a relative bandwidth of 25% can be obtained. The largest bandwidth was achieved with a new concept, namely the ElectroMagnetically Coupled (EMC) microstrip antenna. We have achieved a (measured and calculated) relative bandwidth of approximately 50% with an EMC microstrip antenna. A dual-frequency dual-polarisation microstrip antenna can be obtained if two coaxial cables are used to feed a rectangular patch.

In *chapter 4*, the model of chapter 3 is extended to the case of a finite array of linearly or circularly polarised microstrip antennas. Mutual coupling and surface waves are rigorously accounted for in the model. In general, there are two ways to analyse microstrip arrays with a method-of-moments procedure: (1) element-by-element approach (finite-array approach) and (2) infinite-array approach. However, elements near the edge of an array or elements in small arrays can only be properly analysed with an element-by-element approach. In this thesis we have therefore used the element-by-element approach. The required CPU time can be reduced by using the analytical and numerical techniques of chapter 3. In this way, arrays with hundred elements or more can be analysed within acceptable CPU times. Several designs of finite microstrip arrays

are discussed in chapter 4. Calculated mutual-coupling coefficients are compared with measured data. The measurements showed good agreement with theoretically predicted results. The effect of mutual coupling on the active reflection coefficient of each array element and the influence on the radiation pattern were investigated for various array sizes. The active reflection coefficient is strongly affected by mutual coupling whereas mutual coupling has only a minor effect on the radiation pattern of the total array. One of the configurations which is investigated in chapter 4 is a two-layer stacked microstrip array of which the lower layer is made of a high-permittivity material. If this configuration is used to construct an isolated microstrip antenna, a relative bandwidth of approximately 23% can be obtained. However, in an array environment the available bandwidth of this configuration is reduced significantly, especially at large scan angles. At broadside, the available relative bandwidth in a 7×7 array is still 18%, but when the main beam of the array is scanned to an angle of 60 degrees the available bandwidth is reduced to 3.5%. Another 7×7 array configuration, constructed on a single substrate layer, showed an improvement of the available bandwidth compared with the bandwidth of an isolated microstrip antenna. This is a positive effect of mutual coupling. It is therefore concluded that an optimal finite microstrip phased-array antenna can only be designed when mutual coupling is included in the analysis.
Some methods to obtain a circularly polarised far field with a microstrip antenna or with a subarray of microstrip antennas are discussed. It is shown that mutual coupling between the input ports deteriorates the axial ratio. A new dual-frequency circularly polarised 2×2 subarray is presented with a bandwidth of a few percent around both resonant frequencies (4 GHz and 6 GHz).

Appendix A

Expressions for the elements of $[Z]$

In this appendix the expressions for the elements of the method-of-moments matrix $[Z]$ are given for the case of an array of stacked microstrip antennas fed by coaxial cables. If the array indices j and i are both equal to 1, we obtain the expressions for a single, isolated, stacked microstrip antenna, with $S_{xji} = S_{yji} = 0$ The general structure of the symmetric matrix $[Z]$ is given by (3 17) and (4.11) for the case of an isolated microstrip antenna and for the case of an array of microstrip antennas, respectively. The matrix $[Z]$ has a Toeplitz-type symmetry (see section 4.7), so only a limited number of elements need to be evaluated It is assumed that all patches are located in layer 2 and that the length of the coaxial probes is not longer than the height of the first dielectric layer (see figure 3.1), so $z_1' = h_1$ Extension to the more general case with $z_1' \geq h_1$ is straightforward.

The elements of $[Z]$ can be calculated from (3.19) and (3.20) or from (4.13), depending on whether an isolated microstrip antenna or an array of microstrip antennas is considered The electric-field dyadic Green's function $\bar{\bar{Q}}_{\nu}^{E}$ that appears in these expressions is given in chapter 2 by (2.59). All integrations over z and z_0 can be carried out analytically. Furthermore, a change to cylindrical coordinates is introduced with

$$
\begin{aligned}
k_x &= k_0\beta \cos\alpha, \\
k_y &= k_0\beta \sin\alpha,
\end{aligned}
\qquad \text{(A.1)}
$$

$$\text{with } 0 \leq \beta \leq \infty \quad \text{and} \quad -\pi \leq \alpha \leq \pi$$

The absolute distance between the centres of two array elements is equal to R_{ji}, with $R_{ji} = \sqrt{S_{xji}^2 + S_{yji}^2}$. So if only isolated microstrip antennas are considered ($j = i = 1$), we have $R_{ji} = 0$ Note that j and i are array-element counters with $j = 1, 2, \ldots, K \times L$ and $i = 1, 2, \ldots, K \times L$

(see figure 4.3). After some algebraic manipulations, we obtain the following expressions for the elements of the matrix $[Z]$

Elements of the submatrix $[Z^{aa}]$

$$
\begin{aligned}
Z_{ji}^{aa} &= \int_{-\infty}^{\infty}\int_{-\infty}^{\infty}\int_{0}^{z_1'}\int_{0}^{z_1}\left[\bar{Q}_1^{E}(k_x,k_y,z,z_0)\cdot\vec{J}_1^{a}(k_x,k_y,z_0)\right]dz_0 \\
&\quad \vec{J}_1^{a*}(k_x,k_y,z)dz\,e^{-jk_x S_{xji}}e^{-jk_y S_{yji}}dk_x dk_y \\
&= 2\pi\int_0^{\infty}\left\{\frac{-j\omega\mu_0}{\varepsilon_{r2}}G_{pa}^2\left[j\beta^2\partial_z g_4+g_2(\varepsilon_{r2}-\beta^2)\right]\Big|_{z=z_0=h_1}\right. \\
&\quad +\frac{2j\omega\mu_0\beta k_2 G_{pa}J_0(k_0\beta a)}{hk_0T_m}\left[\varepsilon_{r2}k_3\cos(k_2d_2)+jk_2\sin(k_2d_2)\right] \\
&\quad \left.\left[\frac{h\sin(k_1h_1)}{2k_1}+\frac{\cos(k_1h_1)}{k_1^2}-\frac{\cos[k_1(h_1-h/2)]}{k_1^2}\right]+I_{ff}^{aa}(\beta)J_0^2(k_0\beta a)\right\} \\
&\quad J_0(k_0\beta R_{ji})k_0^2\beta d\beta,
\end{aligned}
\tag{A.2}
$$

for $z_1' = h_1$, with

$$
\begin{aligned}
I_{ff}^{aa}(\beta) &= -\frac{j\omega\mu_0 h}{6k_0^2(\beta^2-\varepsilon_{r1})}-\frac{4j\omega\mu_0\beta^2}{\varepsilon_{r1}h^2k_1^3T_m}\left\{\varepsilon_{r1}k_2(k_3\varepsilon_{r2}\cos(k_2d_2)+jk_2\sin(k_2d_2))\right. \\
&\quad \left(-\frac{h\cos[k_1(h_1-h/2)]}{k_1}+\frac{\sin(k_1h/2)\cos[k_1(h_1-h/2)]}{k_1^2}\right. \\
&\quad \left.+\frac{h\cos(k_1h_1)}{2k_1}+\frac{h^2\sin(k_1h_1)}{4}\right) \\
&\quad -jk_1(k_2\varepsilon_{r2}\cos(k_2d_2)+jk_3\varepsilon_{r2}^2\sin(k_2d_2))\left(-\frac{2\cos[k_1(h_1-h/2)]}{k_1^2}\right. \\
&\quad \left.\left.+\frac{\cos(k_1h/2)\cos[k_1(h_1-h/2)]}{k_1^2}+\frac{h\sin(k_1h_1)}{2k_1}+\frac{\cos(k_1h_1)}{k_1^2}\right)\right\},
\end{aligned}
$$

where G_{pa} is defined by

$$
G_{pa} = \frac{1}{k_0\beta}\left[\frac{2J_1(k_0\beta b_a)}{b_a k_0\beta}-J_0(k_0\beta a)\right],
\tag{A.3}
$$

and where h is the height of a subdomain on the probe (see figure 3.8).

In the derivation of (A.2) the following relation was used

$$\int_{-\pi}^{\pi} e^{jk_0\beta R_{ji}\sin\alpha}d\alpha = 2\int_{0}^{\pi}\cos(k_0\beta R_{ji}\sin\alpha)d\alpha = 2\pi J_0(k_0\beta R_{ji}). \tag{A.4}$$

Elements of the submatrix $[Z^{fa}]$

$$\begin{aligned} Z^{fa}_{jm,i} &= \int_{-\infty}^{\infty}\int_{-\infty}^{\infty}\int_{0}^{z_1'}\int_{0}^{z_1'} \left[\bar{\bar{Q}}_1^{E}(k_x,k_y,z,z_0)\cdot \vec{J}_1^{a}(k_x,k_y,z_0)\right]dz_0 \\ &\quad \vec{J}^{f*}_{1m}(k_x,k_y,z)dz e^{-jk_xS_{xji}}e^{-jk_yS_{yji}}dk_xdk_y \\ &= 2\pi\int_{0}^{\infty} J_0(k_0\beta R_{ji})J_0(k_0\beta a)\left(I_m^{fap}(\beta)+I_m^{faf}(\beta)J_0(k_0\beta a)\right)k_0^2\beta d\beta, \end{aligned} \tag{A.5}$$

with $m = 1, 2, \ldots, N_z$ and with

$$\begin{aligned} I_m^{fap}(\beta) = &\ \frac{j\omega\mu_0\beta k_2}{k_0 T_m}\left[\varepsilon_{r2}k_3\cos(k_2d_2)+jk_2\sin(k_2d_2)\right]G_{pa} \\ &\ \frac{2}{hk_1^2}\left[2\cos(k_1z_m)-\cos(k_1z_{m+1})-\cos(k_1z_{m-1})\right], \end{aligned} \tag{A.6}$$

and for $m \le N_z - 1$

$$\begin{aligned} I_m^{faf}(\beta) = &\ \frac{-2j\omega\mu_0\beta^2}{\varepsilon_{r1}h^2k_1^4T_m}\left\{\varepsilon_{r1}k_2(k_3\varepsilon_{r2}\cos(k_2d_2)+jk_2\sin(k_2d_2))\left[h-\frac{2\sin(k_1h/2)}{k_1}\right]\right. \\ &\left. +jk_1(k_2\varepsilon_{r2}\cos(k_2d_2)+jk_3\varepsilon_{r2}^2\sin(k_2d_2))\left[-\frac{2}{k_1}+\frac{2\cos(k_1h/2)}{k_1}\right]\right\} \\ &\ \left[2\cos(k_1z_m)-\cos(k_1z_{m+1})-\cos(k_1z_{m-1})\right], \end{aligned} \tag{A.7}$$

and for $m = N_z$ (overlap between feed mode m and the attachment mode)

$$
\begin{aligned}
I_m^{faf}(\beta) = \frac{j\omega\mu_0}{\varepsilon_{r1}} \Bigg\{ & \frac{h\varepsilon_{r1}}{12k_0^2(\beta^2 - \varepsilon_{r1})} - \frac{2\beta^2}{h^2 k_1^5 T_m} \times \\
& \big[\varepsilon_{r1} k_2 (k_1 \varepsilon_{r2} \cos(k_2 d_2) + j k_2 \sin(k_2 d_2)) \\
& (2\cos[k_1(z_1' - h)]\sin(k_1 h/2) - 4\cos[k_1(z_1' - h/2)]\sin(k_1 h/2) \\
& - k_1 h \cos[k_1(z_1' - h)] + 2k_1 h \cos[k_1(z_1' - h/2)]) \\
& - j k_1 (k_2 \varepsilon_{r2} \cos(k_2 d_2) + j k_1 \varepsilon_{r2}^2 \sin(k_2 d_2))(-2\cos(k_1 z_1') \\
& + 2\cos[k_1(z_1' - h)]\cos(k_1 h/2) - 4\cos[k_1(z_1' - h/2)]\cos(k_1 h/2) \\
& - k_1 h \sin(k_1 z_1') - 2\cos[k_1(z_1' - h)] + 6\cos[k_1(z_1' - h/2)])\big] \Bigg\},
\end{aligned}
\tag{A.8}
$$

where z_m, z_{m-1} and z_{m+1} are the z-coordinates of subdomain m on the probe of antenna element j (see section 3.4.2). If $m = 1$ and $N_z > 1$ then z_m and z_{m-1} should be made zero in (A.6) and in (A.7), and $z_{m+1} = h/2$. If $m = N_z = 1$ then $z_1' = h$ and $z_1' = h/2$ should be set to zero in the (A.8).

Elements of the submatrix $[Z^{ff}]$

Note that $[Z^{ff}]$ is a symmetrical matrix. More information about the notation can be found in figure 3.8.

$$
\begin{aligned}
Z^{ff}_{jm,in} = & \int_{-\infty}^{\infty}\int_{-\infty}^{\infty}\int_{0}^{z_1}\int_{0}^{z_1} \left[\bar{\bar{Q}}_1^{fz}(k_x, k_y, z, z_0) \cdot \bar{J}^f_{in}(k_x, k_y, z_0)\right] dz_0 \\
& \bar{J}^{f*}_{1m}(k_x, k_y, z)\, dz\, e^{jk_x x_{ji}} e^{-jk_y y_{ji}}\, dk_x\, dk_y \\
& - 2\pi \int_{0}^{\infty} J_0(k_0\beta R_{ji}) J_0^2(k_0\beta a) k_0^2 \beta I^{ff}_{mn}(\beta)\, d\beta,
\end{aligned}
\tag{A.9}
$$

with $m = 1, 2, \ldots, N_z$ and $n = 1, 2, \ldots, N_z$ and where $I^{ff}_{mn}(\beta)$ depends on m and n. If $m = n$, then $I^{ff}_{m\,n}(\beta)$ is given by

$$
\begin{aligned}
I^{ff}_{m\,m} = {} & \frac{j\omega\mu_0}{\varepsilon_{r1}}\{ \left(-\frac{h\varepsilon_{r1}}{3k_0^2(\beta^2-\varepsilon_{r1})} + \frac{4\beta^2}{hk_1^4} \right) \epsilon_m \\
& - \frac{4\beta^2}{h^2 k_1^5 T_m} \left[\varepsilon_{r1} k_2 (k_3 \varepsilon_{r2} \cos(k_2 d_2) + j k_2 \sin(k_2 d_2)) \times \right. \\
& (\cos(k_1 z_{m-1}) \sin[k_1(h_1 - z_{m-1})] - 4\cos(k_1 z_{m-1}) \sin[k_1(h_1 - z_m)] \\
& + 2\cos(k_1 z_{m-1}) \sin[k_1(h_1 - z_{m+1})] + 4\cos(k_1 z_m) \sin k_1(h_1 - z_m) \\
& - 4\cos(k_1 z_m) \sin[k_1(h_1 - z_{m+1})] + \cos(k_1 z_{m+1}) \sin[k_1(h_1 - z_{m+1})]) \\
& - jk_1(k_2 \varepsilon_{r2} \cos(k_2 d_2) + j k_3 \varepsilon_{r2}^2 \sin(k_2 d_2)) \times \\
& (\cos(k_1 z_{m-1}) \cos[k_1(h_1 - z_{m-1})] - 4\cos(k_1 z_{m-1}) \cos[k_1(h_1 - z_m)] \\
& + 2\cos(k_1 z_{m-1}) \cos[k_1(h_1 - z_{m+1})] + 4\cos(k_1 z_m) \cos[k_1(h_1 - z_m)] \\
& \left. - 4\cos(k_1 z_m) \cos[k_1(h_1 - z_{m+1})] + \cos(k_1 z_{m+1}) \cos[k_1(h_1 - z_{m+1})]) \right] \},
\end{aligned}
\tag{A.10}
$$

with $\epsilon_m = 1$ for $m \geq 2$ and $\epsilon_m = 1/2$ for $m = 1$. In the $m = 1$ case (half rooftop basis function), z_m and z_{m-1} should be made zero in (A.10) and $z_{m+1} = h/2$. If basis function m overlaps basis function n, i.e., if $n = m - 1$, $I^{ff}_{m\,n}$ is given by

$$
\begin{aligned}
I^{ff}_{m\,m-1} = \frac{j\omega\mu_0}{\varepsilon_{r1}} \Bigg\{ & \left(-\frac{h\varepsilon_{r1}}{12k_0^2(\beta^2 - \varepsilon_{r1})} - \frac{2\beta^2}{h k_1^4} \right) \\
& - \frac{4\beta^2}{h^2 k_1^5 T_m} \Big[\varepsilon_{r1} k_2 (k_3 \varepsilon_{r2} \cos(k_2 d_2) + j k_2 \sin(k_2 d_2)) \times \\
& (\cos(k_1 z_{m-2}) \sin[k_1(h_1 - z_{m-1})] - 2\cos(k_1 z_{m-2}) \sin[k_1(h_1 - z_m)] \\
& + \cos(k_1 z_{m-2}) \sin[k_1(h_1 - z_{m+1})] + 5\cos(k_1 z_{m-1}) \sin[k_1(h_1 - z_m)] \\
& -2\cos(k_1 z_{m-1}) \sin[k_1(h_1 - z_{m-1})] - 2\cos(k_1 z_{m-1}) \sin[k_1(h_1 - z_{m+1})] \\
& -2\cos(k_1 z_m) \sin[k_1(h_1 - z_m)] + \cos(k_1 z_m) \sin[k_1(h_1 - z_{m+1})]) \\
& - jk_1 (k_2 \varepsilon_{r2} \cos(k_2 d_2) + j k_3 \varepsilon_{r2}^2 \sin(k_2 d_2)) \times \\
& (\cos(k_1 z_{m-2}) \cos[k_1(h_1 - z_{m-1})] - 2\cos(k_1 z_{m-2}) \cos[k_1(h_1 - z_m)] \\
& + \cos(k_1 z_{m-2}) \cos[k_1(h_1 - z_{m+1})] + 5\cos(k_1 z_{m-1}) \cos[k_1(h_1 - z_m)] \\
& -2\cos(k_1 z_{m-1}) \cos[k_1(h_1 - z_{m-1})] - 2\cos(k_1 z_{m-1}) \cos[k_1(h_1 - z_{m+1})] \\
& -2\cos(k_1 z_m) \cos[k_1(h_1 - z_m)] + \cos(k_1 z_m) \cos[k_1(h_1 - z_{m+1})]) \Big] \Bigg\}
\end{aligned} \tag{A.11}
$$

If $m - 1 = 1$, i.e. $m = 2$, z_{m-2} and z_{m-1} should be set to zero in (A.11). Finally, if the two basis functions do not overlap, i.e. if $n < m - 2$, we get

$$
\begin{aligned}
I^{ff}_{m\,n} = -\frac{j\omega\mu_0}{\varepsilon_{r1}} \frac{4\beta^2}{h^2 k_1^5 T_m} & [2\cos(k_1 z_n) - \cos(k_1 z_{n-1}) - \cos(k_1 z_{n+1})] \\
& [\varepsilon_{r1} k_2 (k_3 \varepsilon_{r2} \cos(k_2 d_2) + j k_2 \sin(k_2 d_2)) \times \\
& (2\sin[k_1(h_1 - z_m)] - \sin[k_1(h_1 - z_{m-1})] - \sin[k_1(h_1 - z_{m+1})]) \\
& - jk_1 (k_2 \varepsilon_{r2} \cos(k_2 d_2) + j k_3 \varepsilon_{r2}^2 \sin(k_2 d_2)) \times \\
& (2\cos[k_1(h_1 - z_m)] - \cos[k_1(h_1 - z_{m-1})] - \cos[k_1(h_1 - z_{m+1})])] \,.
\end{aligned} \tag{A.12}
$$

If $n = 1$, z_n and z_{n-1} should be made zero in (A.12)

Elements of the submatrix $[Z^{pp}]$

The numbering of the elements of the submatrix $[Z^{pp}]$ is now $m = 1, 2, \ldots, N_1 + N_2$ and $n = 1, 2, \ldots, N_1 + N_2$. If entire-domain basis functions are used on the patches, we get

$$\begin{aligned} Z^{pp}_{jm,in} &= \int_{-\infty}^{\infty}\int_{-\infty}^{\infty} \left[\bar{\bar{Q}}_2^E(k_x, k_y, z_m, z_n) \cdot \vec{J}^p_{1n}(k_x, k_y, z_n)\right] \\ &\quad \cdot \vec{J}^{p*}_{1m}(k_x, k_y, z_m) e^{-jk_x S_{xji}} e^{-jk_y S_{yji}} dk_x dk_y \\ &= \int_0^{\frac{\pi}{2}}\int_0^{\infty} \left[\bar{\bar{Q}}_2^E(\beta, \alpha, z_m, z_n) \cdot \vec{J}^p_{1n}(\beta, \alpha, z_n)\right] \\ &\quad \cdot \vec{J}^{p*}_{1m}(\beta, \alpha, z_m)\, S_{pp}(m, j, n, i, \beta, \alpha) k_0^2 \beta d\beta d\alpha, \end{aligned} \tag{A.13}$$

with

$$z_m = \begin{cases} z_1', & \text{if domain } m \text{ on lower patch,} \\ z_2', & \text{if domain } m \text{ on upper patch,} \end{cases}$$

and where $\vec{J}^p_{1m}(\beta, \alpha, z_m)$ is the Fourier transform of the m-th basis function on antenna element 1 (see section 3.4). The function $S_{pp}(m, j, n, i, \beta, \alpha)$ is given by

$$S_{pp}(m, j, n, i, \beta, \alpha) = \Psi_{pp}(k_x, S_{xji}, m_p, n_p)\Psi_{pp}(k_y, S_{yji}, m_q, n_q), \tag{A.14}$$

with

$$\Psi_{pp}(k_x, S_{xji}, m_p, n_p) = \begin{cases} 2\cos(k_x S_{xji}), & mod(m_p, n_p) = 0, \\ -2j\sin(k_x S_{xji}), & mod(m_p, n_p) \neq 0 \end{cases}$$

Note that the combination (m_p, m_q) corresponds with the m-th basis function and the combination (n_p, n_q) corresponds with the n-th basis function on one of the patches (see section 3.4.1). If rooftop subdomain basis functions are used on the patches, we obtain

$$Z^{pp}_{jm,in} = \int_0^{\frac{\pi}{2}}\int_0^{\infty} \left[\bar{\bar{Q}}_2^E(\beta, \alpha, z_m, z_n) \cdot \hat{e}_{mn}\right] S_{pp}(m, j, n, i, \beta, \alpha) k_0^2 \beta d\beta d\alpha, \tag{A.15}$$

where

$$
\hat{e}_{mn} = \begin{cases} \hat{e}_{xx}, & \text{basis function } m \text{ and } n \text{ both } x\text{-directed}, \\ \hat{e}_{xy}, & \text{basis function } m\ x\text{-directed}, n\ y\text{-directed}, \\ \hat{e}_{yx}, & \text{basis function } m\ y\text{-directed}, n\ x\text{-directed}, \\ \hat{e}_{yy}, & \text{basis function } m \text{ and } n \text{ both } y\text{-directed} \end{cases}
$$

The Fourier transform of a subdomain rooftop basis function is given by (3 36) and (3 37). $S_{pp}(m, j, n, i, \beta, \alpha)$ therefore takes the form

$$
\begin{aligned}
&S_{pp}(m, j, n, i, \beta, \alpha) \\
&= a_s^2 b_s^2 \times \begin{cases} 4\cos(k_x\Delta_{xmn})\cos(k_y\Delta_{ymn})\operatorname{sinc}^4(k_x a_s/2)\operatorname{sinc}^2(k_y b_s/2), \\ \qquad \text{basis function } m \text{ and } n \text{ both } x\text{-directed}, \\ -4\sin(k_x\Delta_{xmn})\sin(k_y\Delta_{ymn})\operatorname{sinc}^3(k_x a_s/2)\operatorname{sinc}^3(k_y b_s/2), \\ \qquad \text{basis function } m\ x\text{-directed}, n\ y\text{-directed}, \\ -4\sin(k_x\Delta_{xmn})\sin(k_y\Delta_{ymn})\operatorname{sinc}^3(k_x a_s/2)\operatorname{sinc}^3(k_y b_s/2), \\ \qquad \text{basis function } m\ y\text{-directed}, n\ x\text{-directed}, \\ 4\cos(k_x\Delta_{xmn})\cos(k_y\Delta_{ymn})\operatorname{sinc}^2(k_x a_s/2)\operatorname{sinc}^4(k_y b_s/2), \\ \qquad \text{basis function } m \text{ and } n \text{ both } y\text{-directed}, \end{cases}
\end{aligned}
\tag{A 16}
$$

where Δ_{xmn} and Δ_{ymn} represent the distance in the x- and the y-direction, respectively, between the centres of subdomain m on antenna element j and of subdomain n on antenna element i.

Elements of the submatrix $\lfloor Z^{pa} \rfloor$

$$
\begin{aligned}
Z^{pa}_{jm\,i} &= \int_{-\infty}^{\infty}\int_{-\infty}^{\infty}\int_{0}^{z_1'} \left[\bar{\bar{Q}}^{E}_{2}(k_x,k_y,z_m,z_0)\;\; \vec{J}^{a}_{1}(k_x,k_y,z_0)\right] dz_0 \\
&\quad \cdot \vec{J}^{p*}_{1m}(k_x,k_y,z_m) e^{jk_x S_{xji}} e^{-jk_y S_{yji}} dk_x dk_y \\
&= \omega\mu_0 \int_0^{\frac{\pi}{2}}\int_0^{\infty} \left\{ \frac{-\beta G_{pa}}{\varepsilon_{r2}} \left[k_2^2 g_2 + jk_0^2\beta^2\partial_z g_4\right]\Big|_{z=z_m, z_0=h_1} \right. \\
&\quad + \frac{2k_0k_2\beta^2}{hk_1T_m}\left(\frac{h}{2}\sin(k_1h_1) + \frac{\cos(k_1h_1)}{k_1} - \frac{\cos[k_1(h_1-h/2)]}{k_1}\right) J_0(k_0\beta a) \\
&\quad \left. (k_1\varepsilon_{r2}\cos[k_2(h_2-z_m)] + jk_2\sin[k_2(h_2-z_m)])\right\} S_{pf}(m,j,i,\beta,\alpha)\,d\beta\, d\alpha,
\end{aligned}
\tag{A.17}
$$

with $m = 1, 2, \ldots, N_1 + N_2$ and with

$$
z_m = \begin{cases} z_1', & \text{if domain } m \text{ on lower patch,} \\ z_2', & \text{if domain } m \text{ on upper patch,} \end{cases}
$$

and where G_{pa} is given by (A.3) and the functions g_2 and g_4 are given in (2.35). The function $S_{pf}(m,j,i,\beta,\alpha)$ depends on the type of basis function that is being used. In the case of entire-domain basis functions this functions is given by

$$
\begin{aligned}
S_{pf}(m,j,i,\beta,\alpha) &= \cos\alpha\Psi_{pf}(k_x,S_{xji},m_p)\Psi_{pf}(k_y,S_{yji},m_q)\vec{J}^{p*}_{1m}(\beta,\alpha,z_m)\cdot\vec{e}_x, \\
&\quad \text{for } x\text{-directed basis functions,} \\
S_{pf}(m,j,i,\beta,\alpha) &= \sin\alpha\Psi_{pf}(k_x,S_{xji},m_p)\Psi_{pf}(k_y,S_{yji},m_q)\vec{J}^{p*}_{1m}(\beta,\alpha,z_m)\cdot\vec{e}_y, \\
&\quad \text{for } y\text{-directed basis functions.}
\end{aligned}
\tag{A.18}
$$

with

$$
\Psi_{pf}(k_x,S_{xji},m_p) = \begin{cases} 2j\sin[k_x(x_s - S_{xji})], & \text{if } m_p \text{ odd,} \\ 2\cos[k_x(x_s - S_{xji})], & \text{if } m_p \text{ even.} \end{cases}
$$

If subdomain rooftop basis functions are used on the patches, $S_{pf}(m, j, i, \beta, \alpha)$ takes the form

$$
\begin{aligned}
S_{pf}(m, j, i, \beta, \alpha) = {} & 4j \cos\alpha\, a_s b_s \operatorname{sinc}^2(k_x a_s/2) \operatorname{sinc}(k_y b_s/2) \times \\
& \sin[k_x(x_s - S_{xji} - x_{k_m})] \cos[k_y(y_s - S_{yji} - y_{l_m} + b_s/2)],
\end{aligned}
\tag{A.19}
$$

for the case of x-directed rooftop basis functions and

$$
\begin{aligned}
S_{pf}(m, j, i, \beta, \alpha) = {} & 4j \sin\alpha\, a_s b_s \operatorname{sinc}(k_x a_s/2) \operatorname{sinc}^2(k_y b_s/2) \times \\
& \cos[k_x(x_s - S_{xji} - x_{k_m} + a_s/2)] \sin[k_y(y_s - S_{yji} - y_{l_m})],
\end{aligned}
\tag{A.20}
$$

for the case of y-directed rooftop basis functions. The x-and y-dimensions of a subdomain are denoted by a_s and b_s, respectively. The coordinates of subdomain m, denoted by x_{k_m} and y_{l_m}, are shown in figure 3.7.

Elements of the submatrix $[Z^{pf}]$

$$
\begin{aligned}
Z^{pf}_{jm,m} = {} & \int_{-\infty}^{\infty}\int_{-\infty}^{\infty}\int_{0}^{z_1} \left[\bar{\bar{Q}}_2^{E}(k_x, k_y, z_m, z_0) \cdot \vec{J}^{f}_{1n}(k_x, k_y, z_0)\right] dz_0 \\
& \cdot \vec{J}^{p*}_{1m}(k_x, k_y, z_m)\, e^{-jk_x S_{xji}} e^{-jk_y S_{yji}}\, dk_x\, dk_y \\
& - \int_{0}^{\frac{\pi}{2}}\int_{0}^{\infty} \frac{2\omega\mu_0 k_0 \beta^2 k_2}{h k_1^2 T_m} \left(k_1\varepsilon_{r2}\cos[k_2(h_2 - z_m)] + jk_2 \sin[k_2(h_2 - z_m)]\right) J_0(k_0\beta a) \times \\
& S_{pf}(m, j, i, \beta, \alpha) \times \begin{cases} [1 - \cos(k_1 h/2)]\, d\beta\, d\alpha, & n = 1, \\ [2\cos(k_1 z_n) - \cos(k_1 z_{n-1}) - \cos(k_1 z_{n+1})]\, d\beta\, d\alpha & n \geq 2, \end{cases}
\end{aligned}
\tag{A.21}
$$

with $m = 1, 2, \ldots, N_1 + N_2$ and where $n = 1, 2, \ldots, N_z$ and where

$$
z_m = \begin{cases} z_1', & \text{if domain } m \text{ on lower patch,} \\ z_2', & \text{if domain } m \text{ on upper patch} \end{cases}
$$

The function $S_{pf}(m, j, i, \beta, \alpha)$ is given by (A.18) (entire-domain basis functions) or by (A.19) and (A.20) (subsectional basis functions).

Appendix B

Expressions for the elements of $[V^{ex}]$

In this appendix the expressions for the elements of the excitation matrix $[V^{ex}]$ are given for an array of stacked microstrip antennas, fed by coaxial cables. The final expressions for the case of an isolated microstrip antenna can be obtained by substituting $j = i = 1$ and inserting $S_{xji} = S_{yji} = 0$ in the formulas. The general structure of $[V^{ex}]$ is given by (3.18), if the thick-substrate model of section 3.2.3 is used. The matrix $[V^{ex}]$ has a Toeplitz-type of symmetry, so not all the elements need to be calculated. More details about this symmetry can be found in section 4.7. The elements of $[V^{ex}]$ can be calculated from (3.21) or from (4.14). The magnetic-field dyadic Green's function $\bar{\bar{Q}}_1^H$ that appears in these expressions is given in chapter 2 by (2.60). The integration over z in the integral representation of V_m^{ex} can be carried out analytically. Again, a change to cylindrical coordinates (A.1) is introduced. We will also assume that the length of the coaxial probes is not longer than the height of the first dielectric layer, i.e. $z_F \leq h_1$. The numbering of the array elements is $j = 1, 2, \ldots, K \times L$ and $i = 1, 2, \ldots, K \times L$ (see figure 4.3). This results in the following expressions for the elements of $[V^{ex}]$

Elements of the submatrix $\underline{[V^{ex\,a}]}$

An element of the submatrix $[V^{ex\,a}]$ is according to expression (4.14) given by

$$V_{ji}^{ex\,a} = -\int_{-\infty}^{\infty}\int_{-\infty}^{\infty}\left[\int_0^{z_1^i}\bar{\bar{Q}}_1^H(k_x, k_y, 0, z_0) \cdot \vec{J}_1^a(k_x, k_y, z_0)dz_0\right] \cdot \vec{M}_{frill\,1}^*(k_x, k_y)e^{jk_x S_{xji}}e^{jk_y S_{yji}}dk_x dk_y \tag{B.1}$$

After some algebraic manipulations, one finally gets:

$$V_{ji}^{ex,a} = \frac{4\pi^2 k_0}{\ln(b/a)} \int_0^\infty \frac{J_0(k_0 \beta R_{ji})}{T_m} \left[J_0(k_0\beta b) - J_0(k_0\beta a)\right] \times$$

$$\left[\frac{-2\beta k_0 J_0(k_0\beta a)}{k_1^3 h} \left\{\varepsilon_{r1} k_2 (k_3 \varepsilon_{r2} \cos(k_2 d_2) + j k_2 \sin(k_2 d_2))[h k_1/2 - \sin(k_1 h/2)]\right.\right.$$

$$\left. j k_1 (k_2 \varepsilon_{r2} \cos(k_2 d_2) + j k_3 \varepsilon_{r2}^2 \sin(k_2 d_2))[1 - \cos(k_1 h/2)]\right\}$$

$$\left. + j \left\{\frac{-2 j J_1(k_0 \beta b_a)}{b_a k_0^2 \beta^2} + \frac{j J_0(k_0 \beta a)}{k_0 \beta}\right\} \left\{\frac{k_1 T_m N_{e1}(h_1) - j k_0^2 \beta^2 N_{e2}(h_1)}{T_e}\right\}\right] d\beta,$$

where relation (A.4) has been used and where the functions N_{e1} and N_{e2} are given by

$$
\begin{aligned}
N_{e1}(z) &= k_2 \cos[k_2(h_2 - z)] + j k_3 \sin[k_2(h_2 - z)], \\
N_{e2}(z) &= \varepsilon_{r1} k_2 \left[-k_2 \sin(k_1 h_1) \cos[k_2(h_1 - z)] + k_1 \cos(k_1 h_1) \sin[k_2(h_1 - z)]\right] (1 - \varepsilon_{r2}) \\
&\quad + (\varepsilon_{r1} - \varepsilon_{r2}) \left[k_2 \cos(k_2 d_2) + j \varepsilon_{r2} k_3 \sin(k_2 d_2)\right] \\
&\quad \left[j k_3 \sin[k_2(h_2 - z)] + k_2 \cos[k_2(h_2 - z)]\right] \sin(k_1 h_1)
\end{aligned}
\qquad \text{(B 2)}
$$

Elements of the submatrix $[V^{ex,f}]$

The numbering of the basis functions on each probe is $m = 1, 2, \ldots, N_z$. For basis functions on the coaxial probes for which $m \geq 2$ we get

$$
\begin{aligned}
V_{jmi}^{ex,f} &= -\int_{-\infty}^{\infty}\int_{-\infty}^{\infty}\left[\int_{0}^{t_i}\bar{\bar{Q}}_1^H(k_x,k_y,0,z_0)\cdot\vec{J}_{1m}^f(k_x,k_y,z_0)dz_0\right] \\
&\qquad \vec{M}_{fridi}^*(k_x,k_y)e^{jk_xS_{xji}}e^{jk_yS_{yji}}dk_xdk_y \\
&= -\frac{4\pi^2k_0^2}{\ln(b/a)}\int_0^\infty\frac{2\beta J_0(k_0\beta a)J_0(k_0\beta R_{ji})}{hk_1^3T_m}\left[J_0(k_0\beta b)-J_0(k_0\beta a)\right]\times \\
&\{\varepsilon_{r1}k_2(k_3\varepsilon_{r2}\cos(k_2d_2)+jk_2\sin(k_2d_2))\times \\
&[2\sin[k_1(h_1-z_m)]-\sin[k_1(h_1-z_{m-1})]-\sin[k_1(h_1-z_{m+1})]] \\
&-jk_1(k_2\varepsilon_{r2}\cos(k_2d_2)+jk_3\varepsilon_{r2}^2\sin(k_2d_2))\times \\
&[2\cos[k_1(h_1-z_m)]-\cos[k_1(h_1-z_{m-1})]-\cos[k_1(h_1-z_{m+1})]]\}d\beta,
\end{aligned}
\tag{B.3}
$$

and for $m = 1$ we obtain

$$
\begin{aligned}
V_{j1i}^{ex,f} &= -\frac{4\pi^2k_0^2}{\ln(b/a)}\int_0^\infty\frac{\beta J_0(k_0\beta a)J_0(k_0\beta R_{ji})}{k_1^2}\left[J_0(k_0\beta b)-J_0(k_0\beta a)\right]\times \\
&\left\{-1+\frac{2}{k_1hT_m}\left(\varepsilon_{r1}k_2(k_3\varepsilon_{r2}\cos(k_2d_2)+jk_2\sin(k_2d_2)\right)\times\right. \\
&(\sin(k_1h_1)-\sin[k_1(h_1-h/2)])-jk_1(k_2\varepsilon_{r2}\cos(k_2d_2)+jk_3\varepsilon_{r2}^2\sin(k_2d_2))\times \\
&\left.(\cos(k_1h_1)-\cos[k_1(h_1-h/2)]))\right\}d\beta,
\end{aligned}
\tag{B.4}
$$

where z_m, z_{m-1} and z_{m+1} are the z-coordinates of subdomain m (see figure 3.8).

Elements of the submatrix $[V^{ex,p}]$

$$
\begin{aligned}
V^{ex,p}_{jm,i} &= -\int_{-\infty}^{\infty}\int_{-\infty}^{\infty}\left[\bar{Q}^{H}_{1}(k_x,k_y,0,z_m)\cdot \vec{J}^{p}_{1m}(k_x,k_y,z_m)\right] \\
&\qquad \cdot \vec{M}^{*}_{frill,i}(k_x,k_y)e^{jk_x S_{xi}}e^{jk_y S_{yi}}\,dk_x dk_y \\
&= \frac{2j\pi k_0}{\ln(b/a)}\int_{0}^{\infty}\int_{0}^{\frac{\pi}{2}}\left[J_0(k_0\beta b) - J_0(k_0\beta a)\right] S^{*}_{pf}(m,j,i,\beta,\alpha) \\
&\quad \times \left\{\frac{k_1 T_m N_{e1}(z_m) - jk_0^2\beta^2 N_{e2}(z_m)}{T_e T_m}\right\} d\alpha d\beta,
\end{aligned}
\tag{B.5}
$$

with $m = 1, 2, \ldots, N_1 + N_2$ and with

$$
z_m = \begin{cases} z_1', & \text{if domain } m \text{ on lower patch,} \\ z_2', & \text{if domain } m \text{ on upper patch.} \end{cases}
$$

The function $S_{pf}(m,j,i,\beta,\alpha)$ is given by (A.18) or by (A.19) and (A.20). The functions N_{e1} and N_{e2} are defined in (B.2).

If the thin-substrate model of section 3.2.2 is used, we only have to calculate the interaction between the sources, i.e. the probes, and the basis functions on the patches. An element of the matrix $[V_t^{ex}]$ can now be calculated from (3.26). Performing the integration over z analytically and using a change to cylindrical coordinates, finally gives

$$
\begin{aligned}
V^{ex}_{t,jm,i} &= -\int_{0}^{\frac{\pi}{2}}\int_{0}^{\infty}\frac{j\omega\mu_0\beta\sin(k_1 h_1)}{k_0 k_1 \varepsilon_{r1} T_e T_m}\left[k_0^2\beta^2 N_{e2}(z_m) + jk_1 N_{e1}(z_m) T_m\right] \\
&\qquad J_0(k_0\beta a)\, S^{*}_{pf}(m,j,i,\beta,\alpha)k_0^2\beta d\beta d\alpha,
\end{aligned}
\tag{B.6}
$$

with $m = 1, 2, \ldots, N_1 + N_2$ and where

$$
z_m = \begin{cases} z_1', & \text{if domain } m \text{ on lower patch,} \\ z_2', & \text{if domain } m \text{ on upper patch.} \end{cases}
$$

Bibliography

[1] Alexopoulos, N.G. and D.R. Jackson
FUNDAMENTAL SUPERSTRATE (COVER) EFFECTS ON PRINTED CIRCUIT ANTENNAS.
IEEE Transactions on Antennas and Propagation, Vol. AP-32 (1984), p.807-816.

[2] Altman, J.L.
MICROWAVE CIRCUITS.
New York: Van Nostrand, 1964

[3] Arts, M.J. and A.B. Smolders
STUDY OF STACKED MICROSTRIP PHASED ARRAYS.
Microwave and Optical Technology Letters, vol 6 (1993), p.466-471.

[4] Arts, M.J.
ANALYSE VAN EEN ONEINDIG ARRAY BESTAANDE UIT MEERLAGEN MICROSTRIPANTENNES.
M.Sc Thesis, Eindhoven University of Technology, Department of Electrical Engineering, Electromagnetics Division, 1992, no. EM-14-92 (in Dutch).

[5] Bailey, D.M. and M.D. Deshpande
INTEGRAL EQUATION FORMULATION OF MICROSTRIP ANTENNAS.
IEEE Transactions on Antennas and Propagation, Vol. AP-30 (1982), p 651-656

[6] Bauer, R.L. and J.J. Schuss
AXIAL RATIO OF BALANCED AND UNBALANCED FED CIRCULARLY POLARISED PATCH RADIATOR ARRAYS.
Proc. IEEE Int. Conference on Antennas and Propagation 1987, Blacksburg, p.286-289.

[7] Boersma, J.
Private communication, 28-9-1991.

[8] Brookner, E.
PRACTICAL PHASED ARRAY ANTENNA SYSTEMS.
Norwood. Artech House, 1991.

[9] Capelle, A. van de
TRANSMISSION-LINE MODEL FOR RECTANGULAR MICROSTRIP ANTENNAS.
In Handbook of microstrip antennas, Vol. 1, Edited by J.R. James and P.S. Hall.
London: Peregrinus, 1989, p.527-578.

[10] Carver, K.R. and J.W. Mink
MICROSTRIP ANTENNA TECHNOLOGY.
IEEE Transactions on Antennas and Propagation, Vol. AP-29 (1981), p.2-24

[11] Chang, E and S.A. Long, W.F. Richards
AN EXPERIMENTAL INVESTIGATION OF ELECTRICALLY THICK RECTANGULAR MICROSTRIP ANTENNAS.
IEEE Transactions on Antennas and Propagation, Vol. AP-34 (1986), p.767-772.

[12] Chew, W.C.
WAVES AND FIELDS IN INHOMOGENEOUS MEDIA.
New York: Van Nostrand Reinhold, 1990.

[13] Collin, R.E
FIELD THEORY OF GUIDED WAVES.
New York: IEEE Press (2nd ed), 1991.

[14] Da Silva Curiel, A.
INMARSAT'S PRESENT AND FUTURE MARITIME COMMUNICATIONS SYSTEMS
Tijdschrift van het NERG, Vol. 51 (1986), p.128.

[15] Davidovitz, M.D. and Y.T. Lo
INPUT IMPEDANCE OF A PROBE-FED CIRCULAR MICROSTRIP ANTENNA WITH THICK SUBSTRATE
IEEE Transactions on Antennas and Propagation, Vol. AP-34 (1986), p.905-911

[16] Derneryd, A.G. and I. Karlsson
BROADBAND MICROSTRIP ANTENNA ELEMENTS AND ARRAY
IEEE Transactions on Antennas and Propagation, Vol. AP-29 (1981), p.140-141

[17] Derneryd, A.G
A THEORETICAL INVESTIGATION OF THE RECTANGULAR MICROSTRIP AN-

TENNA ELEMENT
IEEE Transactions on Antennas and Propagation, Vol AP-26 (1978), p.532-535

[18] Deschamps, G.A.
MICROSTRIP MICROWAVE ANTENNAS.
Third U.S.A.F. Symposium on antennas, USA, 1953.

[19] Deshpande, M.D. and P.D. Rufus Prabhakar
ANALYSIS OF DIELECTRIC COVERED INFINITE ARRAY OF RECTANGULAR MICROSTRIP ANTENNAS.
IEEE Transactions on Antennas and Propagation, Vol. AP-35 (1987), p.732-736.

[20] Dolmans, W.M.C.
STACKED MICROSTRIP ANTENNAS EMBEDDED IN A TWO-LAYER SUBSTRATE.
M.Sc. Thesis, Eindhoven University of Technology, Department of Electrical Engineering, Electromagnetics Division, 1992, no. EM-11-92.

[21] Dongara, J.J. and C.B. Moler, J.R. Bunch
LINPACK USERS' GUIDE.
Philadelphia: SIAM, 1984.

[22] Estabrook, P. and J. Huang, W. Rafferty, M.K. Sue
A 20/30 GHZ PERSONAL ACCESS SATELLITE SYSTEM DESIGN.
Proc. IEEE Int. Conference on Communications Boston, 1989, p 216-222.

[23] Fenn, A.J.
THEORETICAL AND EXPERIMENTAL STUDY OF MONOPOLE PHASED ARRAY ANTENNAS.
IEEE Transactions on Antennas and Propagation, Vol. AP-33 (1985), p. 1118-1126.

[24] Fitch, J.P.
SYNTHETIC APERTURE RADAR.
New York: Springer-Verlag, 1988.

[25] Fong, K.S. and H.F. Pues, M.J. Withers
WIDEBAND MULTILAYER COAXIAL-FED MICROSTRIP ANTENNA ELEMENT.
Electronics Letters, Vol. 21 (1985), p.497-498.

[26] Goyal, R.
MONOLITHIC MICROWAVE INTEGRATED CIRCUITS: TECHNOLOGY AND DESIGN.
Norwood: Artech House, 1989

[27] Gradsteyn, I.S. and I.M. Ryzhik
TABLE OF INTEGRALS, SERIES AND PRODUCTS.
New York: Academic Press, 1965.

[28] Gronau, G.
THEORETISCHE UND EXPERIMENTELLE UNTERSUCHUNG DER VERKOPPLUNG IN STREIFENLEITUNGSANTENNEN.
Ph.D. Thesis, Duisburg University, 1987.

[29] Hall, P.S.
PROBE COMPENSATION IN THICK MICROSTRIP PATCHES.
Electronics Letters, Vol. 23 (1987), p.606-607

[30] Hall R.C. and J.R. Mosig
THE ANALYSIS OF COAXIALLY FED MICROSTRIP ANTENNAS WITH ELECTRICALLY THICK SUBSTRATES
Electromagnetics, vol. 9 (1989), p.367-384.

[31] Harrington, R.F.
FIELD COMPUTATION BY MOMENT METHODS
New York: IEEE Press, 1993

[32] Harrington, R.F.
TIME HARMONIC FIELDS
New York: McGraw-Hill, 1961

[33] Hertz, H.
GESAMMELTE WERKE VON HEINRICH HERTZ.
Leipzig: J.A. Barth, 1895

[34] Hestenes, M.R. and E. Stiefel
METHOD OF CONJUGATE GRADIENTS FOR SOLVING LINEAR SYSTEMS
Journal Res. Nat. Bur. Standards, Vol. 49 (1952), p.409-436

[35] Hooijen, O.G.
DE DUBBEL GEVOEDE MICROSTRIPANTENNE MET RECHTHOEKIGE PATCH
Report of Training Work, Eindhoven University of Technology, Department of Electrical Engineering, Electromagnetics Division, 1992, no. EM-6-92 (in Dutch)

[36] Hosca, E.
OPPERVLAKTEGOLVEN IN EEN MICROSTRIPSTRUCTUUR.

Report of Training Work, Eindhoven University of Technology, Department of Electrical Engineering, Electromagnetics Division, 1993, no. EM-79-3 (in Dutch).

[37] Huang, J.
A TECHNIQUE FOR AN ARRAY TO GENERATE CIRCULARLY POLARISATION WITH LINEARLY POLARISED ELEMENTS.
IEEE Transactions on Antennas and Propagation, Vol. AP-34 (1986), p.1113-1124.

[38] Kong, J.A.
ELECTROMAGNETIC WAVE THEORY.
New York: John Wiley and Sons, 1986.

[39] Kossiavas, G. and F. Croq, D.L. Sun Luk, A. Papiernik
LARGE BANDWIDTH L-BAND RADIATING ELEMENT.
Archive Electronische Ubertragungen, Vol. 45 (1991), p.191-193.

[40] Krier, P.
MICROSTRIP PATCH ANTENNAS ON GALLIUM ARSENIDE SUBSTRATES.
Ph.D. Thesis, University of Leeds, 1990.

[41] Kumar, A.
FIXED AND MOBILE TERMINAL ANTENNAS.
Norwood: Artech House, 1991.

[42] Laheurte, J.M. and J.R. Mosig
EFFECTS OF PROBE FEED AND SOLDERING POINT ON THICK MICROSTRIP ANTENNAS.
In: Proc. 21th European Microwave Conf., Stuttgart: University of Stuttgart, 1991, p.1179-1184.

[43] Levine, E. and G. Malamud, D. Treves
HIGH GAIN MODULAR MICROSTRIP ANTENNAS
Proceedings European Microwave Conference 1986, p.665-660.

[44] Liu, C.C. and A. Hessel, J. Shmoys
PLANE WAVE REFLECTION FROM MICROSTRIP-PATCH ARRAYS: THEORY AND EXPERIMENT.
IEEE Transactions on Antennas and Propagation, Vol. AP-33 (1985), p.426-435.

[45] Lo, Y.T. and D. Solomon, W.F. Richards
THEORY AND EXPERIMENT ON MICROSTRIP ANTENNAS.
IEEE Transactions on Antennas and Propagation, Vol. AP-27 (1979), p.137-145

[46] Marconi, D
MY FATHER, MARCONI
London: McGraw-Hill, 1962

[47] Meixner, J.
THE BEHAVIOUR OF ELECTROMAGNETIC FIELDS AT EDGES.
IEEE Transactions on Antennas and Propagation, Vol. AP-20 (1972), p.442-446

[48] Montecchia, F
MICROSTRIP-ANTENNA DESIGN FOR HYPERTHERMIA TREATMENT OF SUPERFICIAL TUMORS.
IEEE Transactions on Biomedical Engineering, Vol 39 (1992), p 580-588.

[49] Mosig J.R. and F.E. Gardiol
A DYNAMICAL RADIATION MODEL FOR MICROSTRIP ANTENNAS
In: Advances in Electronics and Electron Physics, edited by P Hawkes, New York. Academic Press, 1982, Vol. 59, p.139-237.

[50] More, J.J. and B.S Garbow, K.E Hillstrom
USER GUIDE FOR MINPACK-1
Argonne Argonne National Laboratory, ANL-80-74

[51] Nauwelears, B and A van de Capelle
DEVELOPMENT OF AN ANALYSIS TOOL FOR MICROSTRIP (PHASED) ARRAY ANTENNAS WITH RECTANGULAR ELEMENTS.
Report of ESA Contract No 8593/89/NL/PB(SC), 1991

[52] Piessens, R. and E. de Doncker-Kapenga, C.W. Uberhuber, D.K. Kahaner
QUADPACK.
Berlin. Springer Verlag, 1983

[53] Pinhas, S. and S Shtrikman, D Treves
MOMENT-METHOD SOLUTION OF THE CENTER-FED MICROSTRIP DISK ANTENNA INVOKING FEED AND EDGE CURRENT SINGULARITIES
IEEE Transactions on Antennas and Propagation, Vol. AP-37 (1989), p.1516-1522.

[54] Popovic, B D. and M.B. Dragovic, A.R Djordjevic
ANALYSIS AND SYNTHESIS OF WIRE ANTENNAS
Chichester John Wiley and Sons, 1982.

[55] Pouwels, A.J H.
ANALYSIS OF AN INFINITE MICROSTRIP ARRAY

M.Sc. Thesis, Eindhoven University of Technology, Department of Electrical Engineering, Electromagnetics Division, 1992, no. EM-2-92.

[56] Pozar, D M.
INPUT IMPEDANCE AND MUTUAL COUPLING OF RECTANGULAR MICROSTRIP ANTENNAS.
IEEE Transactions on Antennas and Propagation, Vol. AP-30 (1982), p.1191-1196.

[57] Pozar, D M.
ANALYSIS OF INFINITE ARRAYS OF PROBE-FED RECTANGULAR MICROSTRIP ANTENNAS USING A RIGOROUS FEED MODEL.
IEE Proceedings-H, Vol 136 (1989), p.110-119.

[58] Pozar, D.M.
PERFORMANCE OF AN INFINITE ARRAY OF MONOPOLES IN A GROUNDED DIELECTRIC SLAB.
IEE Proceedings H, Vol. 137 (1990), p.117-120.

[59] Rumsey, V H
THE REACTION CONCEPT IN ELECTROMAGNETIC THEORY.
Physics Rev , Vol. 94 (1954), p 1483-1491.

[60] Sabban, A.
A NEW BROADBAND STACKED TWO LAYER MICROSTRIP ANTENNA.
Proc. IEEE Int. Conference on Antennas and Propagation, 1983, Houston, p.63-66.

[61] Schaik, H.J. van
THEORY AND PERFORMANCE OF A SPACE-FED, PLANAR, PHASED ARRAY ANTENNA WITH 849 IRIS-LOADED RECTANGULAR WAVEGUIDE ELEMENTS AND EXTERNAL MATCHING SHEET.
Ph D Thesis, Delft University of Technology, 1979.

[62] Schaubert, D.H. and D.M. Pozar, A. Adrian
EFFECT OF MICROSTRIP ANTENNA SUBSTRATE THICKNESS AND PERMITTIVITY: COMPARISON OF THEORIES AND EXPERIMENT
IEEE Transactions on Antennas and Propagation, Vol. AP-37 (1989), p.677-682

[63] Shaeffer, J.H. and L N. Medgyesi-Mitschang
RADIATION FROM WIRE ANTENNAS ATTACHED TO BODIES OF REVOLUTION: THE JUNCTION PROBLEM.
IEEE Transactions on Antennas and Propagation, Vol. AP-29 (1981), p.479-487

[64] Sommerfeld, A.
PARIAL DIFFERENTIAL EQUATIONS IN PHYSICS.
New York. Academic Press Inc, 1949.

[65] Smolders, A.B. and H.J. Visser
TRACKING PHASED-ARRAY ANTENNAS IN THE NETHERLANDS.
Microwaves & RF, Vol 33, no. 5 (may 1994), p.65-75.

[66] Smolders, A.B
FINITE ARRAY OF MONOPOLES EMBEDDED IN A GROUNDED DIELECTRIC SLAB
Electronics Letters, Vol 28 (1992), p 2079-2080.

[67] Smolders, A.B
RIGOROUS ANALYSIS OF THICK MICROSTRIP ANTENNAS AND WIRE ANTENNAS EMBEDDED IN A SUBSTRATE
Eindhoven Faculty of Electrical Engineering, Eindhoven University of Technology, 1992, EUT Report 92-E-263.

[68] Smolders, A.B.
FINITE STACKED MICROSTRIP ARRAYS WITH THICK SUBSTRATES
Eindhoven: Faculty of Electrical Engineering, Eindhoven University of Technology, 1993, EUT Report 93-E-273.

[69] Smolders, A.B and M.E.J Jeuken
EFFICIENT AND RIGOROUS ANALYSIS OF BROADBAND MICROSTRIP PATCH ANTENNAS USING A SPECTRAL DOMAIN MOMENT METHOD.
Proc JINA'92 Int. Symp. Antennas, Nice (France), Nice: Nice University, 1992, p 75-78

[70] Smolders, A.B.
RADIATION PATTERN OF FINITE (STACKED) MICROSTRIP PHASED ARRAYS
Proc. Third Int. Conf on Electromagnetics in Aerospace Applications, Torino (Italy), Torino: Politecnico di Torino, 1993, p.355-358.

[71] Smolders, A.B
EFFICIENT ANALYSIS OF FINITE MICROSTRIP PHASED-ARRAY ANTENNAS.
Proc. IEEE Int. Conference on Antennas and Propagation 1994, Seattle, p. 1836-1839

[72] Smolders, A.B.
BROADBAND MICROSTRIP ARRAY ANTENNAS.
Proc IEEE Int Conference on Antennas and Propagation 1994, Seattle, p 1832-1835

[73] Smolders, A.B
EFFICIENT ANALYSIS OF MICROSTRIP ANTENNAS USING A SPECTRAL DOMAIN MOMENT METHOD
Proc. COST 223 Workshop on Active antennas, Noordwijk (Netherlands), Noordwijk: ESA-ESTEC, 1992, p. 11.1-11.8.

[74] Tangdiongga, E.
ANALYSIS OF AN INFINITE ARRAY OF MICROSTRIP ANTENNAS EMBEDDED IN A THICK SUBSTRATE.
M.Sc. Thesis, Eindhoven University of Technology, Department of Electrical Engineering, Electromagnetics Division, 1994, no. EM-7-94

[75] Terret, C. and A. Edimo, A. Papiernik, G. Kossiavas
PROBE-FED STACKED MICROSTRIP ANTENNAS: DESIGN AND MUTUAL COUPLING.
In: Proc. COST 223 workshop on active antennas, Noordwijk (Netherlands) 11-12 June 1992, Noordwijk: ESTEC, 1992, p. 8.1-8.5.

[76] Tinnemans, P.A.J.
INFLUENCE OF A FINITE GROUND PLANE ON THE RADIATION PROPERTIES OF MICROSTRIP ANTENNAS
M.Sc. Thesis, Eindhoven University of Technology, Department of Electrical Engineering, Electromagnetics Division, 1994, no. EM-8-94.

[77] Visser, H.J.
PLANAIRE MICROSTRIPANTENNES VOOR MOBIELE SATELLIETCOMMUNICATIE. Tijdschrift van het NERG, Vol. 54 (1989), p 61-69 (in dutch)

[78] Watson, G.N.
COMPLEX INTEGRATION AND CAUCHY'S THEOREM
New York: Hafner, 1914.

Samenvatting

Microstripantennes en array's van microstripantennes hebben verschillende voordelen t.o.v. conventionele antennetypes, zoals bijvoorbeeld zeer lage produktiekosten, een laag gewicht en een dunne en dus platte structuur. Microstripantennes zijn daarom erg interessant voor een variëteit aan toepassingen, waarvan mobiele (satelliet-) communicatie en radar de belangrijkste zijn. Vooral mobiele (satelliet-) communicatie kan op termijn een zeer grote markt worden waar goedkoop en eenvoudig te produceren microstripantennes gebruikt kunnen worden. Door hun platte structuur is het bovendien erg eenvoudig om deze antennes te monteren op het dak van vrachtwagens, personenwagens of op vliegtuigen. Het grootste nadeel van de meeste microstripantennes is dat ze slechts bruikbaar zijn voor een kleine frequentieband. Het verbeteren van deze bandbreedte is dan ook een van de belangrijkste doelstellingen van dit onderzoek geweest. In dit proefschrift wordt een theoretisch model gepresenteerd waarmee op een nauwkeurige wijze geïsoleerde microstripantennes alsmede eindige array's van microstripantennes geanalyseerd en ontworpen kunnen worden. De eigenschappen van een microstripantenne of van een microstriparray kunnen bepaald worden zodra de stroomverdeling op ieder arrayelement bekend is. Uit de randvoorwaarden voor het elektrische veld volgt een integraalvergelijking voor de stroomverdeling op de antenne. Deze integraalvergelijking kan opgelost worden met behulp van de momentenmethode. Hierbij worden de nog onbekende stromen ontwikkeld in zogenaamde basisfuncties en wordt het elektromagnetisch veld uitgedrukt in termen van de Greense functie van het gelaagde medium. De keuze van het soort basisfuncties dat gebruikt wordt is daarbij essentieel. Met de basisfuncties die in dit proefschrift gebruikt worden kunnen ook microstripconfiguraties met een elektrisch dik substraat geanalyseerd worden. Er worden in dit proefschrift een aantal nieuwe analytische methodes gepresenteerd waardoor het mogelijk wordt om met de momentenmethode microstrip array's met een groot aantal elementen te analyseren, waarbij de benodigde CPU tijd beperkt blijft.

Teneinde het ontwikkelde model inclusief de daarbij behorende programmatuur te verifiëren, zijn de berekende resultaten vergeleken met metingen van een groot aantal experimenten. In het algemeen kan gesteld worden dat er zowel bij enkele microstripantennes alsmede bij microstrip-array's een goede overeenstemming was tussen theorie en experiment. De bandbreedte van verschillende microstripconfiguraties is onderzocht. In het algemeen geldt dat de bandbreedte toeneemt naarmate een dikker substraat gebruikt wordt. Hieraan is echter een maximum verbon-

den, hetgeen voornamelijk komt door de toenemende probe-inductiviteit van de coaxiale kabels bij een toenemende substraatdikte. Indien de antenne bestaat uit een enkele diëlectrische laag met daarboven een enkele rechthoekige patch, kan een relatieve bandbreedte tot maximaal 15% gerealiseerd worden. Gestapelde structuren, waarbij twee diëlectrische lagen gebruikt worden, hebben breedbandigere eigenschappen. Hiermee kan gemakkelijk een relatieve bandbreedte tot 25% gerealiseerd worden. Voorwaarde hierbij is wel dat de relatieve diëlectrische constante van de onderste laag erg hoog moet zijn. Een nieuwe structuur met een erg breedbandig karakter is de zogenaamde EMC-microstripantenne. De binnengeleider van de voedende coaxiale kabel is nu niet rechtstreeks verbonden met de patch, maar er is een kleine opening tussen beide aangebracht. Het capacitieve effect dat hierdoor optreedt compenseert de inductiviteit van de coaxiale kabel. Met dit type antenne kan een relatieve bandbreedte van ongeveer 50% behaald worden.

Indien een microstripantenne geplaatst wordt in een array, zal in het algemeen de beschikbare bandbreedte afnemen door de mutuele koppelingen tussen de array-elementen. Deze afname zal groter zijn naarmate de hoofdbundel van het array over een grotere hoek afgebogen wordt. Een goed ontwerp van een microstriparray is daarom alleen mogelijk door het gedrag van het totale array te optimaliseren, dus inclusief mutuele koppelingen. Het model dat in dit proefschrift beschreven is kan hiervoor gebruikt worden.

Verder worden er een aantal microstripconfiguraties besproken waarmee een circulair gepolariseerd verre veld kan worden verkregen. Een van deze configuraties betreft een nieuw type subarray welke bij een tweetal frequentiebanden (rond 4 GHz en rond 6 GHz) tegelijkertijd gebruikt kan worden.

Curriculum Vitae

Bart Smolders werd geboren op 1 december 1965 te Hilvarenbeek. Na het succesvol doorlopen van de lagere school slaagde hij in 1984 voor het examen Atheneum-B aan de Rijksscholengemeenschap Koning Willem II te Tilburg. Vervolgens studeerde hij elektrotechniek aan de Technische Universiteit Eindhoven, waar hij in 1989 afstudeerde als elektrotechnisch ingenieur. Tijdens zijn studie was hij onder andere bestuurslid van de studentenorganisatie StIK en was hij twee jaar student-assistent bij het practicum Digitale Technieken. Na zijn studie werd hij als Reserve Officier van de Koninklijke Luchtmacht gedetacheerd bij FEL-TNO in Den Haag. Zijn werk aldaar betrof het ontwerpen van hoogfrequente analoge schakelingen (MMIC's) voor phased-array radars. Sinds 1 februari 1991 werkt hij als toegevoegd onderzoeker bij de vakgroep Elektromagnetisme van de Technische Universiteit Eindhoven. Dit werk is uitgevoerd in het kader van het project "Breedbandige microstripantennas" van de Stichting voor de Technische Wetenschappen (STW). Dit laatste onderzoek heeft geleid tot het schrijven van dit proefschrift.

Dankwoord

Alle leden en ex-studenten van de vakgroep Elektromagnetisme van de Technische Universiteit Eindhoven, die hebben bijgedragen aan het tot stand komen van dit proefschrift, wil ik hierbij bedanken. Verder ben ik prof.dr. J. Boersma van de faculteit Wiskunde erkentelijk voor zijn bijdrage inzake een aantal wiskundige problemen. Ook wil ik ir. P. Giesselink van HSA bedanken voor de produktie van de antennes.

Mijn dank gaat uiteraard vooral uit naar dr. M.E.J. Jeuken die behalve initiatiefnemer van dit onderzoek ook een zeer waardevolle begeleider en collega is geweest.

Stellingen behorende bij het proefschrift

Microstrip Phased-Array Antennas: A Finite-Array Approach

door

A.B. Smolders

Eindhoven, 5 oktober 1994

1. Ondanks het feit dat microstripantennes goedkoop, licht en eenvoudig produceerbaar zijn, worden ze nog maar op een zeer beperkte schaal daadwerkelijk toegepast, omdat de meeste bedrijven niet beschikken over voldoende fundamentele kennis inzake microstripantennes

2. Het ontwerp van toekomstige generaties phased-array antennes zal moeten gebeuren op basis van computersimulaties, teneinde te voorkomen dat niet-optimale en dus te dure oplossingen worden gekozen en om de ontwikkelingstijd te beperken.

   - A B Smolders en H J Visser Tracking Phased-Array Antennas in the Netherlands Microwaves & RF Vol 33 (1994) p 65-75

3. Het vakgebied Elektromagnetisme zal ook in de computertechniek een steeds belangrijkere rol gaan spelen indien de trend om steeds hogere klokfrequenties te gebruiken zich voortzet

4. Een ingenieur die besluit om te gaan promoveren verkleint daarmee zijn mogelijkheden om na zijn promotie een baan te vinden op de Nederlandse arbeidsmarkt.

   - A C v d Neut, J F M de Jonge De Meerwaarde van een Promotie Leiden Research voor beleid oktober 1993

5. De Jeugd-Werk Garantiewet (JWG) zal niet leiden tot een significante vergroting van de kansen van jongeren op de reguliere arbeidsmarkt zolang de garantiebanen zich voornamelijk in de collectieve sector bevinden

   -Gelderse Stuurgroep Werkgelegenheid Werkconferentie experiment ter bevordering uitstroom JWG" 24 maart 1994

6. De discussie omtrent welke computer en bijbehorend besturingssysteem het meest ideaal zou zijn voor een onderzoeker wordt sterk vertroebeld doordat veel onderzoekers de computer niet zien als een hulpmiddel maar als een doel op zich.

   -Cursor Wetenschappers doen zich te kort met PC s , nr 12 jaargang 36 1993

7. Het vaak gehoorde bezwaar tegen microstripantennes dat ze erg smalbandig zijn is onterecht. Het is zeer wel mogelijk om microstripantennes met een breedbandig karakter te ontwerpen.

- A.B. Smolders, Breedbandige microstripantennes, Tijdschrift van het NERG, deel 59, nr 1, 1994, p. 27-32

8. Eventuele blinde scanhoeken in een phased array van rechthoekige golfpijpstralers kunnen experimenteel al duidelijk waargenomen worden bij arrays bestaande uit 15×15 elementen.

-W.P.M. Keizer, A.P. de Hek en A.B. Smolders, "Theoretical and experimental performance of a wideband wide-scan angle rectangular waveguide phased array", IEEE Antennas and Propagation Society Symposium Digest, Vol 3, Ontario, Canada, 1991, p. 1724-1727

9. Microstripantennes op een substraat met een zeer lage relatieve permittiviteit kunnen niet gebruikt worden als element in een breedbandige phased-array antenne met een groot scanbereik, omdat de onderlinge koppelingen tussen de elementen veel te groot zijn.

- Dit proefschrift, par. 4.8

10. Echte kattenliefhebbers zijn geduldige mensen.